Dissertation
submitted to the
Combined Faculties for the Natural Sciences
and for Mathematics
of the Ruperto-Carola University of Heidelberg,
Germany
for the degree of
Doctor of Natural Science

presented by
Dipl.-Phys. Sebastian Hofferberth
born in: Herford, Germany
Oral examination: July 4$^{\text{th}}$, 2007

Coherent manipulation of Bose-Einstein condensates with radio-frequency adiabatic potentials on atom chips

Referees: Prof. Dr. Jörg Schmiedmayer
Prof. Dr. Markus Oberthaler

Zusammenfassung

Kohärente Kontrolle von Bose-Einstein Kondensaten durch adiabatische Radiofrequenz-Potentiale auf Atomchips

In dieser Arbeit wurde eine neuartige Technik zum Fangen und Manipulieren von neutralen Atomen auf Atomchips entwickelt und experimentell umgesetzt. Das Koppeln interner Zustände von magnetisch gefangenen Atomen durch Radio-Frequenz (RF) Felder führt zu vielseitigen mikroskopischen Fallenpotentialen, die verschiedene Einschränkungen konventioneller magnetischer Fallen überwinden. Eine ausführliche experimentelle Untersuchung dieser neuen Fallenart wurde durchgeführt, um die Zustandsabhängingkeit dieser RF Potentiale und die möglichen Realisierungen nicht-trivialer Fallengeometrien zu erforschen. Aufbauend auf diesen Ergebnissen wurde der erste kohärente Materiewellen-Strahlteiler auf einem Atomchip demonstriert, wodurch zum ersten Mal das komplett auf Magnetfeldern basierte Aufteilen eines Bose-Einstein-Kondensats realisiert wurde. Dieses neue atom-optische Element wurde dann zur Untersuchung der Phasen-Eigenschaften von eindimensionalen Bose-Einstein-Kondensaten benutzt. Die in dieser Arbeit entwickelte Fallengeometrie gibt direkten Zugang zu den Phasenfluktuationen in diesen Systemen. Dadurch war erstmalig eine zeitaufgelöste Untersuchung der Gleichgewichtseigenschaften und der Nicht-Gleichgewichts-Dynamik ein-dimensionaler Bose-Gase möglich.

Abstract

Coherent manipulation of Bose-Einstein condensates with radio-frequency adiabatic potentials on atom chips

During this thesis a novel trapping and manipulation technique for neutral atoms on atom chips has been developed and experimentally implemented. Radio-frequency (rf) coupling of internal states of magnetically trapped atoms results in versatile microscopic potentials, which overcome various limitations of static magnetic traps. An extensive experimental analysis of this new technique has been carried out, exploring the state-dependency of the rf potentials and the possible realization of non-trivial trapping geometries. Based on these results, the first coherent matter wave beam splitter on an atom chip has been realized, demonstrating for the first time the all-magnetic coherent splitting of a condensate. This new atom optical tool has then been applied to investigate the phase-properties of one-dimensional Bose-Einstein condensates. The potential configuration developed during this thesis provides direct access to the phase fluctuations in the system and has allowed the first time-resolved study of equilibrium properties and non-equilibrium dynamics in a one-dimensional Bose gas.

Contents

1 Introduction

In the last two decades tremendous progress has been made in the field of ultra cold atomic physics. The development of laser and evaporative cooling as well as magnetic and optical trapping techniques has enabled the preparation of confined atomic gases at temperatures in the micro-Kelvin regime and lower [254, 43]. This has eventually led to the experimental observation of Bose-Einstein condensation (BEC) [5, 26, 56] as well as the formation of degenerate Fermi gases [280], confirming theoretical predictions made already in the early days of quantum mechanics [24, 70]. The preparation of these degenerate quantum gases is now a well established procedure employed in many experiments world-wide, and the basic properties of these systems have been studied in great detail [166].

These initial experiments with dilute atomic gases in simple trapping potentials turned out to be only the starting point for a number of highly interesting research fields. The one which attracts probably the most attention at the moment is the study of interacting many-particle systems. From early on it was recognized that weakly interacting bosonic and fermionic quantum gases provide ideal model systems for probing complex condensed matter phenomena. The atomic systems offer an unparalleled degree of controllability over parameters such as density and, via Feshbach resonances [149], the two-body interaction strength. Key properties of the atomic gases are usually directly measurable, in contrast to solid state systems, where quantum effects often can only be inferred indirectly.

A prime example of such an atomic gas "quantum simulation" is the storing of ultra cold atoms in optical lattices, which mimic the periodic potential structure found in crystalline matter [21]. Such atomic crystals are ideal realizations of the Bose-Hubbard-model [150], and have for example been used to observe the Mott insulator quantum phase transition [104]. Other recent experimental simulations of condensed matter systems include the realization of a bosonic Josephson junction and the observation of tunneling and macroscopic self-trapping in this system [1], or the BEC-BCS crossover in gases of fermionic atoms [14]. In particular, these fermionic systems promise to provide new insights in the area of (high-T_C) superconductivity [41, 333].

A similarly interesting area of research is the study of single or few atom quantum systems. Here, the ultimate goal is obtaining full coherent control of all internal and external degrees of freedom of individual atoms. More complex multi-particle systems could then be constructed step by step from the bottom up. A main driving force for this topic is the idea of quantum information processing (QIP) [236], where information is stored in a coherent superposition of two quantum states. The long lifetimes of internal atomic states and the inherently weak coupling of neutral atoms to the environment result in long coherence times, which make such atomic state quantum bits ideally suited for use as quantum memory.

Impressive progress in coherent manipulation and addressing of single neutral atoms has been made in optical resonators, including the trapping of single atoms with single photons in a cavity [255, 145] and the realization of a single-atom laser [215]. Besides realizing first neutral atom QIP applications [264], these cavity quantum electrodynamics (QED) experiments promise new insights into the fundamental physics of (strong) coupling between matter and light [17]. Steps towards QIP with neutral atoms have also been made in optical lattices [279]. While in these systems scalability is intrinsic, as evidenced by the demonstration of a few thousand simultaneous controlled collision phase gates [211], the addressability of individual atoms remains an issue.

A promising approach to gaining full control over neutral atom quantum systems, both small and

large scale, are so-called atom chips [84, 85]. Miniaturized field generating elements integrated on a semiconductor chip provide non-periodic, built-to-purpose trapping potentials on a micrometer scale for the realization of complex atom optical elements [85, 265, 88]. So far, research in this field has mostly focussed on atomic ensembles: Bose-Einstein condensates [124, 240] and, more recently, degenerate fermion gases [11, 12] have been produced in atom chip traps. Guiding and transport of trapped atoms has been demonstrated [125, 206, 30], and atom beam splitters using magnetic [35, 232, 288] and electric [177] fields have been implemented.

The last years have seen significant progress in the coherent control of atomic ensembles on atom chips. Internal state coherence in thermal atoms [302], a magnetic Bragg reflector [114], and different interferometer schemes (one of which is a topic of this thesis) have been demonstrated [284, 309, 156]. Besides addressing fundamental questions in quantum mechanics, these experiments, together with the continued integration and miniaturization of atom chip experiment setups [67], bring technological applications like portable atomic clocks and interferometric precision sensors closer to reality.

Atom chips are also extremely well suited for the study of one-dimensional (1d) Bose gases [316] and the crossover from three-dimensional (3d) to 1d confinement [75, 301]. Reduction of dimensionality is achieved by confining the atoms so strongly in two directions that excitations in these directions are effectively frozen out [251]. The extremely smooth, highly elongated trapping potentials achievable in atom chip traps [176] allowed us to realize for the first time a single weakly interacting 1d Bose gas in a magnetic trap [316]. These one dimensional systems have attracted much theoretical attention over the last decades, as their exact solvability makes them ideal test grounds for interacting many particle theories [121, 260].

The realization of single or few atom systems on atom chips is mainly hindered by the difficulty of detecting small numbers of neutral atoms. This problem has been addressed by using optical resonators [304, 118], which provide detection efficiency on the single atom level [297]. Recent progress in integrating micro resonators directly on the atom chips makes cavity QED experiments with single atoms in chip traps a realistic possibility [292, 320].

In this thesis, a novel trapping and manipulating technique for neutral atoms on atom chips, radio-frequency (rf) adiabatic potentials, is developed and experimentally demonstrated. This new approach greatly enhances the flexibility of atom chip traps and provides novel tools for both the research fields discussed above, cold atomic gas model systems and coherent quantum control, as shown by the experiments presented in this manuscript.

The coupling of internal Zeeman states of magnetically trapped neutral atoms by an rf magnetic field to realize new trapping configurations was first proposed in 2001 by Zobay and Garraway [330, 331]. However, in their original analysis only a spatially homogeneous coupling strength was considered, and the vector nature of the rf magnetic coupling was neglected. We have developed a complete theoretical description of rf adiabatic potentials created by the combination of arbitrary static and oscillating fields, including the correct description of the rf coupling [186, 141], which is presented in this manuscript.

This analysis reveals various advantages of rf adiabatic potentials over conventional static magnetic traps, which are experimentally investigated and verified in this thesis. We show that sub-micron potential modulations on an atom chip are realizable with comparably large wire structures and surface distances ($> 100\,\mu$m), overcoming impedimental scaling laws encountered in static magnetic traps [74]. The rf potentials allow a state-dependent manipulation of trapped atoms, which is of particular interest for QIP applications [33]. This state-dependency is demonstrated experimentally [142]. Furthermore, potential geometry restrictions imposed by Maxwell´s laws on static magnetic fields are circumvented by use of the rf potentials. This opens possibilities for novel non-trivial trapping geometries like for example a ring potential [193].

A precise experimental characterization of the dressed state level structure and the underlying rf potentials was performed by employing spectroscopic methods [141]. The investigations of

dressed Bose-Einstein condensates revealed subtle atomic level shifts caused by the breakdown of the rotating-wave-approximation (RWA) in very good agreement with our calculations of the rf potentials. The RWA is one of the most widely used theoretical frameworks in atomic physics, and effects of its breakdown have been discussed in various contexts [310, 184]. Our spectroscopy experiments have shown that the precise tunability of the rf potentials allows one to accurately control the importance of different effects leading to the violation of the RWA. Consequently, rf dressed atoms in an atom chip trap are an ideally suited model system for studying beyond-RWA effects. Additionally we demonstrated that the spectroscopy rf field can be used for efficient evaporative cooling of rf dressed atoms, enabling robust condensate production in complex potentials, which further enhances the flexibility of rf potentials [142].
The removal of potential geometry restrictions in the rf potential case allows the dynamic transformation of a single (quadrupole) minimum magnetic trap into a double well potential, which cannot be realized with static magnetic fields [293]. This smooth potential transformation was used to implement a condensate splitting scheme, which allowed us to demonstrate for the first time the coherent spatial separation of a single Bose-Einstein condensate into two parts on an atom chip, realizing the analogy of a beam splitter in coherent optics [284]. Coherent splitting of a condensate has previously been achieved only in optical traps [287, 272, 1]. Based on this all-magnetic matter-wave beam splitter an atom interferometer fully integrated on the atom chip was realized, which had been one of the long standing goals of the atom chip community [85]. Our experimental demonstration of coherent splitting of condensates in arbitrary direction and the realization of state-dependent potential modulation [142] make the rf beam splitter configuration presented in this thesis ideally suited for QIP applications [44]. On the other hand, the system opens the possibility for studying fundamental quantum effects in many particle systems like number squeezing and phase diffusion [156].
Based on the rf beam splitter concept a new approach to the study of 1d Bose gases was developed. In the weakly interacting regime, the characteristic feature of 1d systems are enhanced longitudinal phase fluctuations [251], for whose study interferometry is a natural tool. Analysis of the spatially resolved interference pattern enabled us to directly measure the local phase properties in 1d gases, in contrast to previous methods which could only extract averaged information from indirect observations of the phase fluctuations [65, 131]. The successful combination of the rf beam splitter with true 1d confinement allowed the realization of initially phase-coherent as well as completely uncorrelated 1d condensates in the rf double well [142]. We could study the time-evolution of the phase-coherent state, which presents the first investigation of non-equilibrium phase-dynamics in 1d systems [31]. Alternatively, the temperature dependence of the phase fluctuations in the uncorrelated case was shown to provide a possible thermometry method [107, 147] similar to recent experiments on the phase fluctuations of 3d condensates [92]. The richness of the system was further increased by introducing a tunnel coupling between the 1d condensates. Here, a new example of a cold atomic gas model system for other branches of physics was found: A pair of coupled 1d Bose gases provides realization of the quantum Sine-Gordon model, which is of significant importance in such diverse areas of physics as superconductors and quantum gravity [108].

Outline of this thesis

This thesis is organized as follows: In chapter 2, after a brief summary of the theory of magnetic trapping and specific atom chip traps, the theoretical derivation of the rf adiabatic potentials in the second quantization description of the dressed state formalism is presented. It is shown that the application of the rotating-wave-approximation leads to simple analytical formulas for the rf potentials. The beyond-RWA calculation for strong rf dressing or large frequency detuning is also discussed. In chapter 3 the most relevant theory for the experiments discussed in this thesis is summarized. The theory of Bose gases in one and three dimensions is reviewed and the interference of

two condensates is discussed in detail. The experimental apparatus and the procedure of creating Bose-Einstein condensates in atom chip traps in our setup are presented in chapter 4.
Chapter 5 discusses the actual implementation of the rf potentials on our atom chip. A three-wire layout is used to combine a standard Ioffe-Pritchard magnetic trap [261] with two (approximately) linear rf fields, which turns out to be a highly versatile configuration giving access to experimental study of all advantages of the rf potentials [142]. The possible trap geometries are calculated both analytically and numerically, and are then investigated experimentally. In chapter 6 a spectroscopy technique is presented which allows a precise determination of the dressed level structure of the trapped atoms. In particular, the occurrence of beyond-RWA effects for large rf dressing can be directly observed [141].
The dynamic splitting of a Bose-Einstein condensate based on this trap configuration is discussed in chapter 7. A detailed study of the dynamics of the system during and after the splitting process is presented. In particular, the evolution of the relative phase is examined and the observed decoherence process is compared to theoretical predictions.
In chapter 8 the application of the rf beam splitter to the study of phase fluctuations in one-dimensional condensates is presented. It is shown that true 1d-confinement in the rf double well can be realized and how the combination of vertical splitting with transverse imaging allows direct observation of the local phase fluctuations in interferometric measurements. This experimental setup is used for the study of phase dynamics in coherently split coupled and uncoupled condensates and the contrast statistics in the case of two uncorrelated condensates.
The manuscript concludes with a summary of the obtained results and an outlook on future perspectives of the experiment (chapter 9).

2 Radio frequency induced adiabatic potentials

Magnetic trapping in (quasi)-static external fields is one of the key techniques in the field of ultracold neutral atoms [166, 315, 246]. It is based on the coupling of the inherent magnetic moment of the atoms to the external magnetic field, which causes an energy shift of atomic levels, known as the Zeeman effect. The spatial variation of this energy shift in an inhomogeneous magnetic field leads, in the low temperature limit, to a conservative force, which is the basis for confining potentials without a (fundamental) lower temperature limit.
In section 2.1, the derivation of the magnetic potential for (cold) atoms is described. Its application to building traps and its validity conditions are discussed, using as examples two common trap configurations, the *quadrupole* [222, 16] and the *Ioffe-Pritchard* [261] trap.
In section 2.2 the concept of miniaturized planar magnetic field generating structures, so called atom chips, is introduced. The size reduction of the electromagnets producing the magnetic trapping fields is motivated by general scaling laws, and a brief overview on the large number of proposed and/or experimentally realized potential configurations is given. In particular, two trap configurations relevant for the experiments described in this manuscript, the U-trap and the Z-trap are presented, followed by a general model of magnetic field calculation for atom chip wire traps.
The third section of this chapter focusses on radio-frequency adiabatic potentials. The idea of coupling the different magnetic states of a hyperfine level with a radio frequency (rf) oscillating field to modify a static trapping potential was first proposed by Zobay and Garraway [330, 331], but only the complete inclusion of the vector nature of the involved coupling and static fields by M. Andersson in our group lead to the full realization of the flexibility of this trapping technique. In section 2.3.1 the derivation of the rf adiabatic potentials in the dressed state formalism including a second-quantization description of the involved rf fields, is shown. The application of the common rotating wave approximation (RWA) leads to a great simplification of the problem and enables us to develop simple analytical formulas for the effective potentials (section 2.3.2). From the experiments discussed later in this manuscript, we learn that the generally assumed validity of this approximation is not always guaranteed, indeed it fails rather easily in the case of rf dressing. Consequently, in section 2.3.3 the (numerical) solving of the complete dressed state Hamiltonian is discussed.

2.1 Atoms in static magnetic fields

A magnetic field $\mathbf{B}$ interacts with the magnetic moments of the nucleus and the electron(s) (in the alkali atoms, such as Rb, only the single outer electron contributes to the electron magnetic moment) of a neutral atom, which result from the nuclear spin $\mathbf{I}$ and the total electron angular momentum $\mathbf{J}$. This coupling lifts the degeneracy of the different magnetic substates of the atomic energy levels, which is present in the field-free case.

2.1.1 Linear Zeeman effect

The magnetic fields typically used for cold atom magnetic traps are relatively small, usually of the order $10^{-4}...10^{-2}$T. In this regime, the Zeeman energy can be approximated by

$$H_{\mathrm{Zeeman}} = \mu_{\mathrm{F}} \cdot \mathbf{B} = g_{\mathrm{F}} \mu_{\mathrm{B}} \mathbf{F} \cdot \mathbf{B}, \tag{2.1}$$

where $\mathbf{F} = \mathbf{I} + \mathbf{J}$ is the total angular momentum of the atom, g_F is the corresponding Landé factor, $\mu_B = 9.274 \times 10^{-24}$ J/T is Bohr´s magneton, and μ_F is the total magnetic moment of this atomic state. This regime is known as the linear Zeeman shift.
For the typical energy and magnetic field scales used in ultra cold atom experiments, SI units are usually not a natural choice. For the magnetic field strength, a more suitable unit is Gauss, with $1\mathrm{G} = 10^{-4}\mathrm{T}$. Additionally, it is often more convenient to express energies in other units than Joule. Through the relations $E = k_\mathrm{B}T = h\nu = \mu_\mathrm{B}B$, where $k_\mathrm{B} = 1.381 \times 10^{-23}$ J/K is the Boltzmann and $h = 6.626 \times 10^{-24}$ Js the Planck constant, energy can be converted into temperature, frequency, or magnetic field units, respectively. Throughout this manuscript, the most suitable of these units will be used in each given situation.
The linear approximation of the Zeeman energy given in (2.1) is valid as long as the energy shift due to the magnetic field is small compared to the hyperfine splitting. If this is not the case, the magnetic field couples to the nuclear and electron spin independently and the total spin $\mathbf{F}$ no longer has a sensible meaning. Similarly, if the Zeeman splitting becomes comparable to the spin-orbit coupling energy, the electron spin $\mathbf{S}$ and the total angular momentum $\mathbf{L}$ have to be treated separately and $\mathbf{J}$ is no longer well-defined. This is known as the Paschen-Back effect. In the most general case, the components of the atom, the nucleus and the electrons, have to be considered completely independently. This becomes necessary when the magnetic field varies on a length scale typical of the extension of the atom, for example when highly excited Rydberg-atoms are placed in extremely inhomogeneous fields. Such systems have been studied in detail in this group [185, 190, 191, 194, 192, 187, 188, 189]. For this treatment to become necessary, field gradients of $\sim 10^9$ G/cm are needed. While micro-traps such as those used in our experiment offer the most extreme parameters available, the field gradients they produce are orders of magnitude below this regime.

2.1.2 Adiabatic approximation

Consequently, the Hamiltonian describing the motion of a neutral atom in a typical magnetic trapping field can be written as

$$H = E_\mathrm{kin} + H_\mathrm{Zeeman} = \frac{\mathbf{p}^2}{2m} + g_\mathrm{F}\mu_\mathrm{B}\mathbf{F}\cdot\mathbf{B}(\mathbf{r}), \tag{2.2}$$

where $\mathbf{p}$ is the momentum operator and m is the mass of the atom. To solve this Hamiltonian, an unitary transformation U_s is applied, which transforms the total spin operator $\mathbf{F}$ such that two of its three components vanish. It is convention to choose the z-component as the remaining one. In that case such a transformation, which in general depends on the position $\mathbf{r}$, is given by

$$U_\mathrm{S}(\mathbf{r}) = \exp\left[-iF_\mathrm{z}\alpha(\mathbf{r})\right]\exp\left[-iF_\mathrm{y}\beta(\mathbf{r})\right] \tag{2.3}$$

with the angles

$$\alpha(\mathbf{r}) = \arctan\left[\frac{B_\mathrm{y}(\mathbf{r})}{B_\mathrm{x}(\mathbf{r})}\right] \tag{2.4}$$

$$\beta(\mathbf{r}) = \arctan\left[\frac{\sqrt{B_\mathrm{x}^2(\mathbf{r}) + B_\mathrm{y}^2(\mathbf{r})}}{B_\mathrm{z}(\mathbf{r})}\right]. \tag{2.5}$$

This transformation performs a rotation of $\mathbf{F}$, which can be equivalently expressed by rotation matrices $R_i(\phi)$, where ϕ is the rotation angle and the index i specifies the axis around which the rotation is performed:

$$U_{\mathrm{S}}^{\dagger}\mathbf{F}\cdot\mathbf{B}(\mathbf{r}) = [R_y(-\beta)(\mathbf{r})R_z(-\alpha(\mathbf{r}))\mathbf{F}]\cdot\mathbf{B}(\mathbf{r}) = \mathbf{F}\cdot[R_y(\beta)(\mathbf{r})R_z(\alpha(\mathbf{r}))\mathbf{B}(\mathbf{r})] = F_{\mathrm{z}}\left|\mathbf{B}(\mathbf{r})\right|. \quad (2.6)$$

The second equality in the series of equations (2.6) shows that the rotation can also be applied to the magnetic field $\mathbf{B}(\mathbf{r})$ instead, which gives a more intuitive explanation of the performed transformation: The reference system is transformed from the lab frame into a (space-dependent) coordinate system, which z-axis is always parallel to the magnetic field. In the last equality the fact is used that the absolute value of the magnetic field is invariant under rotations.
Applying U_{S} to the whole Hamiltonian (2.2) thus yields

$$U_{\mathrm{S}}^{\dagger}HU_{\mathrm{S}} = U_{\mathrm{S}}^{\dagger}\frac{\mathbf{p}^2}{2m}U_{\mathrm{S}} + m_{\mathrm{F}}g_{\mathrm{F}}\mu_{\mathrm{B}}\left|\mathbf{B}(\mathbf{r})\right| = \frac{1}{2m}\left[\mathbf{p}+A(\mathbf{r})\right]^2 + m_{\mathrm{F}}g_{\mathrm{F}}\mu_{\mathrm{B}}\left|B\mathbf{B}(\mathbf{r})\right|, \quad (2.7)$$

with the "gauge" field $A(\mathbf{r}) = U_{\mathrm{S}}^{\dagger}\mathbf{p}U_{\mathrm{S}}$. In this new reference frame, the Zeeman term of the Hamiltonian is always diagonal by default, the off-diagonal terms coming from the spatial dependence of the magnetic field are transferred to the additional term $A(\mathbf{r})$ in the kinetic energy part of the Hamiltonian.
As a final step, the *adiabatic approximation* is applied, which consists of neglecting of the guage term $A(\mathbf{r})$. This is valid, if the off diagonal elements of $A(\mathbf{r})$ are small compared to the energy scales set by the potential term, in which case the gauge term gives rise only to a geometric phase (or Berry's phase) [139], which usually is of no consequence for experiments [328]. In a semi-classical approach, where the spin is interpreted as a precession of a momentum vector around a (local) quantization axis, the validity condition of the adiabatic approximation can be obtained as

$$\frac{\frac{d}{dt}\mathbf{B}}{|\mathbf{B}|} < \frac{g_{\mathrm{F}}\mu_{\mathrm{B}}}{\hbar}\left|\mathbf{B}(\mathbf{r})\right| = \omega_{Larmor}. \quad (2.8)$$

If the rate of change of the magnetic field is small compared to the precession frequency ω_{Larmor} of the atomic spin, this precession can adiabatically follow the field while the atom moves. In this case, although the quantization axis changes its direction as a function of space, the eigenvalues of F_{z}, the quantum numbers m_{F} can be treated as spatially independent.
After this approximation, the Hamiltonian (2.2) takes the simple form

$$H = \frac{\mathbf{p}^2}{2m} + V_{\mathrm{mag}}, \quad (2.9)$$

where the interaction of the atom with the magnetic field appears now as the potential

$$V_{\mathrm{mag}} = m_{\mathrm{F}}g_{\mathrm{F}}\mu_{\mathrm{B}}\left|\mathbf{B}(\mathbf{r})\right|. \quad (2.10)$$

2.1.3 Magnetic traps for neutral atoms

From (2.9) it follows, that to build a magnetic trap, a field configuration $\mathbf{B}(\mathbf{r})$ is required, such that V_{mag} has a (local) minimum. It can be seen from equation (2.10) that V_{mag} is proportional to the absolute value of the magnetic field. Additionally, the sign of the proportionality constant depends on the product $m_F g_F$, which defines the relative orientation of the atomic spin to the external field. Based on this factor, the magnetic states can be categorized into three groups. Atoms in magnetic states with $g_F m_F < 0$ are drawn towards regions of maximum field strength (*high-field seekers*), while states with $g_F m_F > 0$ are drawn toward minima in the field strength (*low-field seekers*). In the case of $g_F m_F = 0$, the atoms are unaffected by the magnetic field and consequently cannot be trapped magnetically.
An application of the Earnshaw theorem [69] to magnetic fields, the so-called *Wing theorem* [321, 167] shows that Maxwell´s equations allow no field extrema in free space for (quasi-)static fields.

This theorem is a consequence of the fact that the divergence of the electromagnetic fields is zero in source free space. While this forbids maxima in the absolute magnetic field strength, the vector nature of the magnetic field still allows local minima in the absolute value of the field. Therefore it is only possible to create static trapping potentials with external fields for low-field seeking states. Trapping of high-field seekers is also possible when there is a current inside the trapping area. This has been shown for atoms trapped on stable orbits around a current carrying wire [64, 62].

Energy scales

Before considering specific trap configurations, it is interesting to look at the general energy scales of magnetic trapping. The order of magnitude of the Zeeman effect and thus of the energy depth of magnetic traps is given by the Bohr magneton $\mu_B = 9.27 \times 10^{-24}$ J/T= $k_B \times 670$ mK/T. This means that to trap atoms with temperature $T = 1$K, magnetic field variations of the order of 1 T are required. Typical field variations in experiments are of the order $10^0...10^2$ G= $10^{-4}...10^{-2}$ T, so that the trap depth of realistic magnetic traps is of the order $E = k_B \times 10^2\,\mu$K. To magnetically trap atoms therefore substantial pre-cooling of a thermal atomic sample is required. This is usually done in a magneto-optical trap (MOT). How this procedure is implemented in our experiment is described in chapter 4.

2.1.4 Common trapping configurations

As has been explained in the last section the design of a magnetic trap reduces to finding a field configuration whose modulus has a minimum. The resulting traps can be divided into two classes: those with vanishing magnetic field strength at the trap center and those with non-vanishing magnetic field everywhere [16]. The most common traps of each class are the *quadrupole* and the *Ioffe-Pritchard* trap, respectively, which will be introduced in the following.

Quadrupole type traps

In general, all magnetic field configurations can be expressed as a magnetic multipole expansion. Since the dipole term is a constant, the first order that leads to a trapping configuration is the quadrupole one, whose magnetic field has the form

$$\mathbf{B} = (B'_x x, B'_y y, B'_z z). \tag{2.11}$$

The Maxwell equation $\nabla \cdot \mathbf{B} = 0$ requires that $B'_x + B'_y + B'_z = 0$.
An ideal quadrupole field can be realized for example with a pair of coils in 'anti-Helmholtz' configuration. Indeed this was the configuration used for the first magnetic trapping of neutral atoms [222].
It is easy to see that the quadrupole field offers the steepest possible trap gradients, leading to the strongest realizable confinement, as the addition of any other term, constant or higher order, will result in quadratic or higher orders in the modulus of the field. Both this and the simple practical realization make the quadrupole trap appealing for experiments, but the field zero at the center turns out to be a problem which greatly reduces its usability, unless specific care is taken. The adiabatic approximation is only valid when the condition (2.8) is fulfilled. At a point with $|\mathbf{B}| = 0$ this is not the case, because the Lamor frequency is zero. As a consequence, at this point the degeneracy of the magnetic states is not lifted, and transitions between different states occur. In particular atoms in low-field seeking states may be transferred to high-field seeking states, and thereby be ejected from the trap. Such transitions are known as *Majorana spin-flips* [209]. The quadrupole trap effectively has a hole at the field node through which atoms can escape from the trap. The resultant loss rate scales with the temperature as T^{-2} [57, 247], because colder atoms are confined closer to the center and thus to the hole.

Various methods exist to 'plug' the hole to make the quadrupole field useful for magnetic traps, for example by using a dynamic magnetic field (*time-orbiting potential (TOP) trap*) [5] or a laser beam repelling atoms from the trap center [56].

Ioffe-Pritchard traps

The hole present in quadrupole traps can be avoided by using trap configurations with nonzero field at the minimum. It is not possible to simply 'lift' the quadrupole potential without changing its shape, since other multipole expansion terms become important. Even if only the dipole term is comparable to the quadrupole term, the resulting magnetic potential will be harmonic instead of linear. In other words the closing of the hole at the trap center reduces the confinement of the resulting traps, with the harmonic confinement being the steepest possible.
A modification of the quadrupole trap that leads to such a harmonic potential around the minimum was first proposed by Pritchard [261] for neutral atoms, based on the similar Ioffe configuration discussed decades earlier for plasma confinement [101]. Today, the designation 'Ioffe-Pritchard trap' is used in general for traps that are harmonic around their center.
A harmonic potential is fully described by its oscillation frequencies, which are given by the curvature of the field along the main axes of the trap:

$$\omega_i = \sqrt{\frac{1}{m}\frac{d^2V}{dx_i^2}} = \sqrt{\frac{\mu_\mathrm{B} m_\mathrm{F} g_\mathrm{F}}{m}\frac{d^2B}{dx_i^2}}. \tag{2.12}$$

These frequencies give an indication of both the steepness of the potential around the center and the size of the harmonic area. It can be shown, that no isotropic harmonic trap can be realized [16], which is again a direct consequence of the Maxwell equations. In most cases, the used field configurations are such that two of the trapping frequencies are approximately equal and larger than the third, resulting in a "cigar" shaped trap. Alternatively, only a single frequency can be larger than the roughly equal other two, in which case a "pancake" potential is obtained.
At points where the field strength is finite but small, a certain probability of atom loss remains also for Ioffe-Pritchard traps, due to Landau-Zehner tunneling from a trapped to an untrapped state [178, 327]. The rate of such transition is given by [296, 102]

$$\Gamma_M = 4\pi\omega_\mathrm{max}\exp\left(-\frac{\omega_\mathrm{Larmor}}{\omega_\mathrm{ho}}\right), \tag{2.13}$$

where ω_max is the largest of the three trap frequencies. For realistic numbers ($B = 0.1$ G and $\omega_\mathrm{max} = 2\pi \times 1000$ Hz) the flip rate is practically zero. Even small offset fields on the order of 10 mG are enough to prevent atom loss due to spin flips in typical traps.

2.2 Atom chips

In 1995 it was proposed to use current carrying wires directly in vacuum to create magnetic traps [312, 275], which lead to a number of experiments with freestanding macroscopic wires [63, 86, 64, 61, 62]. Soon after, these wire structures were miniaturized and integrated to planar wire patterns [266]. For this, fabrication techniques from semiconductor micro chip fabrication were adapted, which lead to the name *atom chips* for these devices [84]. The first successful realizations of Bose-Einstein condensation in such atom chip traps was achieved in 2001 [124, 240].

2.2.1 Motivation for micro traps

There are two main advantages atom chips have over conventional magnetic traps. For once, they offer more strongly confining potentials than achievable with macroscopic field generating

structures outside the vacuum. Second, they greatly enhance the design flexibility of magnetic trapping potentials. In addition, the integration of other techniques for trapping and manipulating neutral atoms besides magnetic fields can further enhance the flexibility of these devices.

Strong confinement

To realize strongly confining potentials, magnetic fields with large gradients are required, as can be seen from equations (2.11) and (2.12). On the other hand, the actual trapping area scales inversely with the steepness of the potential. Already for weakly confining traps, this area is small, usually on the order of millimeters. Consequently, strong field gradients are needed only in a small area around the trap center.
When macroscopic electromagnets outside the vacuum chamber are used, usually large field gradients have to be provided over lengths of > 10 cm which requires large electric currents, resulting in high power consumption and heat dissipation.
The advantage of bringing the field generating structures close to the trap center can be illustrated by looking at the magnetic field produced by a single straight wire. A current flowing through such a wire generates a circular field whose strength decreases with the distance from the wire:

$$\mathbf{B} = \frac{\mu_0 I}{2\pi r}\mathbf{e}_\varphi = 2 \cdot 10^{-7} \cdot \frac{I}{r}\mathbf{e}_\varphi \tag{2.14}$$

where I is the current through the wire, r the distance from the wire, and $\mu_0 = 4\pi 10^{-7} \frac{\mathrm{V\,s}}{\mathrm{A\,m}}$ is the magnetic field constant. The strength and gradient of the field are given by:

$$B(r) = \frac{\mu_0}{2\pi}\frac{I}{r} \tag{2.15}$$

$$\frac{dB(r)}{dr} = -\frac{\mu_0}{2\pi}\frac{I}{r^2} \tag{2.16}$$

It can be seen that both quantities are limited by the maximum current I_{max} the wire can sustain and the finite size $2R$ of the wire. In particular, the maximum field gradient is proportional to the current density in the wire:

$$\frac{dB(r)}{dr} \propto \frac{I}{R^2} = j \tag{2.17}$$

Because of the quadratic dependence on the wire radius the most efficient way to increase the current density is to reduce the wire size. Hence miniaturization of the current-carrying structures leads to stronger confinement in the traps.
Conventional harmonic traps have typical trap frequencies on the order of $\omega \sim 2\pi \times 10...500$ Hz. In atom chip traps, this can be increased dramatically. For example, standard values in our experiment are $\omega \sim 2\pi \times 1...10$ kHz, with values up to $\omega \sim 2\pi \times 100$ kHz being achievable. A detailed analysis of the maximally achievable trap frequencies in atom chips can be found in [175]. The realization of such large trap frequencies not only enhances the efficiency of BEC production in magnetic traps, it also opens up the possibility of conceptually new experiments, for example traps with reduced dimensionality, as will be discussed in chapters 3 and 8.
To simplify the required wire structures usually a hybrid approach is chosen to create atom chip magnetic traps. The inhomogeneous field of the wires are combined with external homogeneous fields, which are easily generated by pairs of coils in Helmholtz configuration. The advantage of strong confinement is not lost in this approach because the field gradients are determined by the inhomogeneous wire fields. Also because of the relatively low currents in the wires the external fields usually need to be only of the order of a few Gauss, i.e. orders of magnitude smaller than for conventional setups, eliminating the problems of heating and power consumption such macroscopic

experiments have. Alternatively, additional chip wires can be used to create (locally) homogeneous fields in addition to the gradient fields provided by the main trap wires [60, 74].

Design of complex trapping potentials

Besides the realization of tightly confining magnetic traps, atom chips offer another advantage, namely extreme flexibility in designing complex and versatile magnetic traps. At first glance, the restriction of the current carrying structures to two dimensions suggests limitations on the realizable magnetic potentials. But due to the circular magnetic field of current carrying wires, a two-dimensional wire array provides full control over all three directions of the magnetic field, without any loss of flexibility [312]. Indeed, the freedom of building almost arbitrary wire structures on surfaces using established techniques from microelectronics fabrication allows the realization of complex *potential landscapes*, which are not (realistically) achievable with conventional, macroscopic magnetic traps.
The resolution of atom chip potentials is given by the structure size and the atom-surface distance. In current experiments, both these lengths are of the order $1 - 100\,\mu$m, which is comparable to the size of the ground state wave function in the realized potentials. A large variety of atom chip wire configurations for trapping and manipulation of neutral atoms has been proposed and/or demonstrated. The main goal in the field is gaining coherent control over Bose-Einstein condensates or single trapped atoms, for the realization of of atom optical elements, i.e. building blocks like matter wave beam splitters analogous to conventional wave optics [267].
On the other hand, single minimum traps and wave guides can already be created with very simple wire structures. Wire traps are especially suited for the creation of such wave guiding potentials. The most basic of these, the *side guide*, consists of just a single wire and a homogeneous field parallel to the atom chip [276, 136, 117]. Controlled release of atoms into such a guide was first reported in [179].
The direction of the side guide is fixed by the orientation of the homogeneous field. This restriction can be overcome by using two wires combined with a bias field perpendicular to the chip surface, which allows the realization of curved guides [206, 30, 231]. Alternatively, such guides can be completely integrated on the chip, with additional wires replacing the external field [60, 74].
More controlled transport can be achieved by using conveyor belt structures, which can control the speed and the direction of the atoms moving in a wave guide [126, 113, 144]. This allows for example the spatial separation of the area of Bose-Einstein condensate production from actual experimental regions.
One of the most discussed application for atom chips is the realization of a miniaturized matter wave interferometer [232, 138, 126, 7, 74]. One of the goals in this area is the creation of sensitive sensors for acceleration, rotation, and gravity changes. Combined with the ongoing miniaturization of the required experimental apparatus, this may lead to portable devices [67]. So far, due to technical and fundamental problems (loss channels, nonadiabaticity, surface effects) none of the schemes based on (quasi)-static magnetic fields have succeeded so far. However, the combination of atom chip traps with radio-frequency adiabatic potentials, as discussed in this thesis, has lead to the first demonstration of coherent splitting of a Bose-Einstein condensate in 2005 [284].
The realization of a magnetic diffraction grating for atoms is reported in [114]. Coherent scattering of Bose-Einstein condensates from this grating could be observed.
Comprehensive summaries of the trapping geometries realized so far and of future applications of atom chips can be found in these review papers: [137, 85, 265, 88].

Integration of other techniques

Atom chips are well suited for the combination with or the direct integration of other techniques for manipulating trapped atoms, which further enhance the flexibility of these devices.

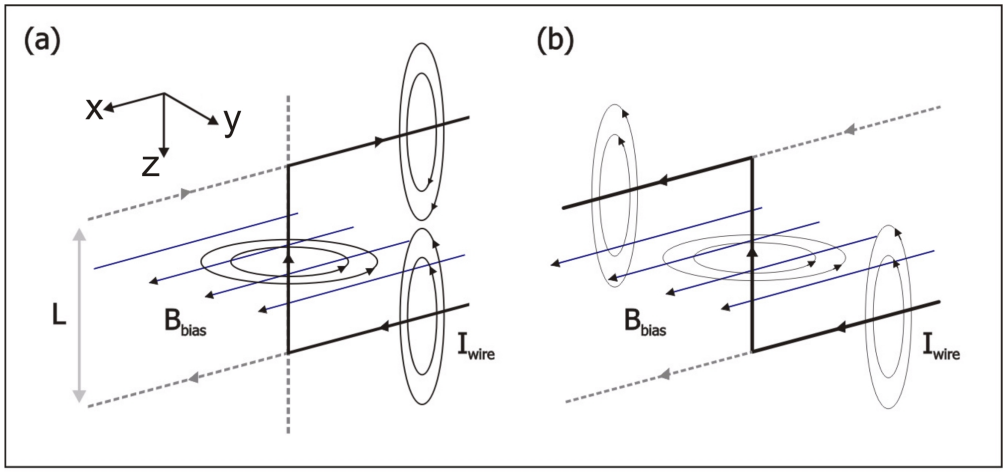

Figure 2.1: Common single wire traps. **(a)** The magnetic field of a single wire bent into a U-shape combined with a homogeneous bias field creates a three dimensional quadrupole trap. The antiparallel currents in the outer leads of the U create fields which compensate each other in the central x-y plane, resulting in a zero field minimum there. **(b)** In the case of a Z-shaped wire, the currents in the outer leads are parallel, hence their fields do not compensate each other at any position. A field minimum still exists at the symmetry point of the wire, around this minimum a Ioffe-Pritchard type trap is created.

Charged pads and wires on the chip have been used to provide electric fields for modification of magnetic potentials [177, 123]. The combination of electric and magnetic trapping fields allows for example the realization of state-dependent potentials.
A highly promising approach is the integration of optical elements on the atom chip. Microscopic cavities can be used for single-atom trapping and detection [304, 292] and possibly for atom-photon entanglement. The integration of optical fibers is also persued in our group [118, 202, 320]. Recently, successful single atom detection with a macroscopic cavity mounted on an atom chip has been reported [297]. In another experiment, optical mirrors on the chip where used to realize a Mach-Zehnder interferometer of the Bragg type [309]. In our setup, we employed a single laser beam using the atom chip as a mirror to create a combined standing light wave-magnetic trap and demonstrated Bragg scattering of magnetically trapped atoms [89, 316].
An alternative approach to single atom detection is laser-induced on-chip ionization and subsequent detection of the produced ions and/or electrons. First results of such a setup are presented in [34].
The integration of radio-frequency oscillating fields on atom chips is the main topic of this thesis and is discussed below. The integration of microwave fields is one of the future goals of this experiment [171]. In [302], the successful application of a macroscopic microwave field for the coherent internal state manipulation of thermal atoms in an atom chip trap is reported.
The realization of superconducting atom chips is technologically extremely challenging, but promises completely new insights into atom-surface interactions. The successful loading of atoms into superconducting wire traps on atom chips has recently been reported [237, 230]. A scheme for integrating a mechanical resonator into a room temperature atom chip is presented in [303], presenting another approach to coherent surface-atom coupling.

2.2.2 Common single wire traps

Single minimum traps of both the quadrupole and the Ioffe-Pritchard type, as discussed in section 2.1.4, can be realized with only one wire and a homogeneous bias field. The two most common single wire traps, the *U-trap* and the *Z-trap* are shown in figure 2.2.2. They form the basis of many atom chip experiments, including the one described in this thesis.

The details of the trapping potentials created with these wire configurations have been studied extensively in various review papers [137, 85, 265, 88]. Further analysis can be found in a number of diploma and PhD thesis from this group [174, 116, 96, 277, 164, 123]. Here, we only briefly discuss how the respective trapping potentials are formed, and list relevant formulas used later in this thesis.
The basic building block of both traps is the *side guide*. When the circular field of a straight wire (equation 2.15) is superimposed by a homogeneous bias field $\mathbf{B}_{\text{bias}}$ a two-dimensional minimum results at the distance

$$d = \frac{\mu_0}{2\pi}\frac{I}{|\mathbf{B}_{\text{bias}}|} \tag{2.18}$$

from the wire, where the two fields compensate each other. Around this minimum, the magnetic field can be well approximated by a quadrupole configuration

$$\begin{aligned} B_x &= G(y-h) \\ B_y &= Gx \end{aligned} \tag{2.19}$$

with the gradient

$$G = \frac{|\mathbf{B}_{\text{bias}}|}{d} = \frac{2\pi}{\mu_0}\frac{B_{\text{bias}}^2}{I} = \frac{\mu_0}{2\pi}\frac{I}{d^2} \tag{2.20}$$

where I is the current in the wire.
This two-dimensional trap is closed in the third direction by bending the wire by 90 degrees at two positions, leading to the U- or Z-shape. These outer leads of the wire now provide an inhomogeneous field parallel to the central wire bar, resulting in a three-dimensional potential minimum. We use the coordinate system shown in figure 2.2.2, with the origin located at the middle point of the central wire part, for the following discussion.

U-trap: Miniaturized quadrupole trap

In the U-configuration, the current in the outer parts of the wire are antiparallel. Consequently, in the (x, y) plane, the z-components of the fields these outer leads generate compensate each other. On the other hand, for any $z \neq 0$ the total field of the two outer wire parts is non-zero.
In the (x, y) plane the field has contributions to the x- and y-direction from the central wire, as well as contribution in y-direction from the outer parts. The two y-components are in opposite direction on the outer side of the U-structure. Hence, if a homogeneous bias field in x-direction is used, the position of the field minimum will be located above and besides the U-structure. It can be rotated back directly over the central bar by adding a y-component to the bias field.
Around the minimum position, at which the total field strength is zero, the resulting magnetic field is well approximated by a pure quadrupole field. In the z-direction, the field gradient is weak, while in the two other directions the gradients are of approximately equal magnitude.
In our experiment such a U-trap provides the magnetic field for the initial magneto-optical trap. As will be discussed in section 4.2.1 we use a modified U-wire with a broadened central part to increase the area where the quadrupole approximation is valid [15, 319].

Z-trap: Miniaturized Ioffe-Pritchard trap

If the wire is bent into a Z-shape, the current in the outer parts is parallel. In this configuration, the z-component of the field is finite everywhere. The field created by the these outer parts in the $(0, y, z)$ plane can be well approximated by a quadrupole field, which primary axes are rotated by 45°

$$\begin{aligned} B_y &= G_{\text{out}} z \\ B_z &= G_{\text{out}} y \end{aligned} \tag{2.21}$$

where $G_{\rm out} = \frac{\mu_0}{\pi}\frac{I}{2L^2}$, and L is the length of the central bar. Usually $d \ll L$, hence this longitudinal gradient is much smaller than the transverse gradient G created by the central wire part and the x-component of the bias field.
The total field of the Z-wire plus bias field reads

$$\begin{aligned} B_x &= G(y-h) \\ B_y &= Gx + G_{\rm out} z \\ B_z &= G_{\rm out} y + B_{0,\rm z}. \end{aligned} \tag{2.22}$$

Here $B_{0,\rm z}$ is an additional homogeneous field in z-direction, which we introduce here for completeness. Although it is not necessary to form a trap, such a field is usually used to modify the longitudinal confinement of the trap.
Because of the symmetry of the wire shape, the field minimum is located above the central bar at equal distance from the two outer leads, i.e. ($x_0 = z_0 = 0$). The absolute value of the field in y-direction at this central position is

$$|\mathbf{B}|^2 = G^2(y-d)^2 + (G_{\rm out} y + B_{0,\rm z})^2. \tag{2.23}$$

This expression has a minimum at

$$y_0 = d - \frac{G_{\rm out}^2 d + G_{\rm out} B_{0,\rm z}}{G^2 + G_{\rm out}^2}. \tag{2.24}$$

Unlike for the pure side guide, the principal axes of the three-dimensional Z-trap are slightly turned in the (x,z) plane with respect to the central wire. To obtain the new symmetry axes, the Hessian of the potential has to be diagonalized, which also yields the field curvature along the new axes [277]. The principal axes $(\mathbf{e'}_x, \mathbf{e'}_z)$ of the Z-trap are obtained by rotating the original axes $(\mathbf{e}_x, \mathbf{e}_z)$ by the angle $\tan\beta = d^2/L^2$. The trapping frequencies can be calculated according to equation (2.12). For the field curvature in transverse direction we find

$$\frac{\partial^2 B}{\partial x'^2} = \frac{\partial^2 B}{\partial y^2} = \frac{G^2}{B_{0,\rm z}} = \frac{4\pi^2 B_{\rm bias}^4}{\mu_0^2 I^2 B_{0,\rm z}}. \tag{2.25}$$

In the longitudinal direction the result is

$$\frac{\partial^2 B}{\partial z'^2} = \frac{6G^2}{B_{\rm bias}} = \frac{3\mu_0^2 I^2}{2\pi^2 B_{\rm bias} L^4}. \tag{2.26}$$

The longitudinal trap frequency is usually much smaller than the transverse frequencies, resulting in highly anisotropic traps. The trap aspect ratio, defined as the ratio of the two trapping frequencies, reads

$$R = \frac{\omega_\perp}{\omega_\parallel} = \sqrt{\frac{B_{\rm bias}}{6B_{0,\rm z}}}\frac{L^2}{d^2}. \tag{2.27}$$

In the experiments described in this thesis, various Z-trap are used for magnetic trapping of precooled atoms. Typical aspect ratios for these traps lie between 10 and 10000. Since d is usually of the order 10μm, while L is of the order 1 mm, the rotation of the principal axis is small, and can in many cases be neglected.

2.2.3 Realistic wires

In the discussions in the last sections, we have used the formula for circular (infinitely long) wires to calculate the magnetic field created by the considered wire geometries, or we have used first order

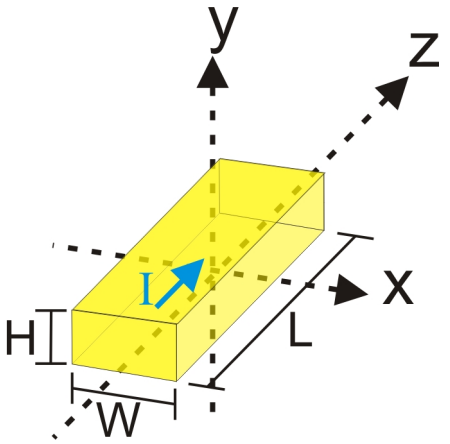

Figure 2.2: Schematic drawing of a rectangular wire of finite length L, defining the coordinate system and current direction used in the calculation in the main text.

(linear) approximations of the resulting fields. While this serves well for illustrating the general scaling laws of wire traps and for understanding basic trap behaviors, for a more quantitative analysis of the resulting magnetic potentials, the actual chip wire shape, which usually is rectangular, has to be considered. Also, the inhomogeneity of the current density at wire bends is of importance for quantitative calculations. In general, these finite size effects become important at distances comparable to the wire size. Since usually the wire width is (much) larger than the wire height, it sets a typical length scale for which the circular wire approximation starts to fail.

Rectangular wires

Consider a rectangular wire of width W and height H with a finite length L, as shown in figure 2.2. We place the origin of the coordinate system at the center of the wire. The magnetic field of such a wire block can be obtained by integration of the Biot-Savart law

$$\mathbf{B}_{\text{wire}}(\mathbf{r}) = \int_{-W/2}^{W/2}\int_{-H/2}^{H/2}\int_{-L/2}^{L/2} \frac{\mu}{4\pi}\frac{\mathbf{j}\times(\mathbf{r}-\mathbf{r}')}{|\mathbf{r}-\mathbf{r}'|^3}d\mathbf{r}' \tag{2.28}$$

with the current density $\mathbf{j} = \frac{I}{WH}\mathbf{e}_z$. The resulting magnetic field components can be written as

$$\begin{aligned} B_{\text{wire,x}} &= \frac{\mu I}{4\pi HW}\left[-f(L,H,W)+f(-L,H,W)\right. && (2.29)\\ &- \left. f(-L,-H,W)+f(L,-H,W)\right] \\ B_{\text{wire,y}} &= \frac{\mu I}{4\pi HW}\left[f(L,W,H)-f(-L,W,H)\right. && (2.30)\\ &+ \left. f(-L,-W,H)-f(L,-W,H)\right] \\ B_{\text{wire,z}} &= 0, && (2.31) \end{aligned}$$

with the auxiliary function

$$\begin{aligned} f(L,W,H) &= y_+ \operatorname{arccoth}\left[\frac{z_+}{\sqrt{x_-^2+y_+^2+z_+^2}}\right] - y_- \operatorname{arccoth}\left[\frac{z_+}{\sqrt{x_-^2+y_-^2+z_+^2}}\right] \\ &+ x_-\left[\arctan\left[\frac{(y_-)(z_+)}{x_-\sqrt{x_-^2+y_-^2+z_+^2}}\right] - \arctan\left[\frac{(y_+)(z_+)}{x_-\sqrt{x_-^2+y_+^2+z_+^2}}\right]\right] \\ &+ z_+ \ln\left[\frac{y_- - \sqrt{x_-^2+y_-^2+z_+^2}}{y_+ - \sqrt{x_-^2+y_+^2+z_+^2}}\right]. \end{aligned} \tag{2.32}$$

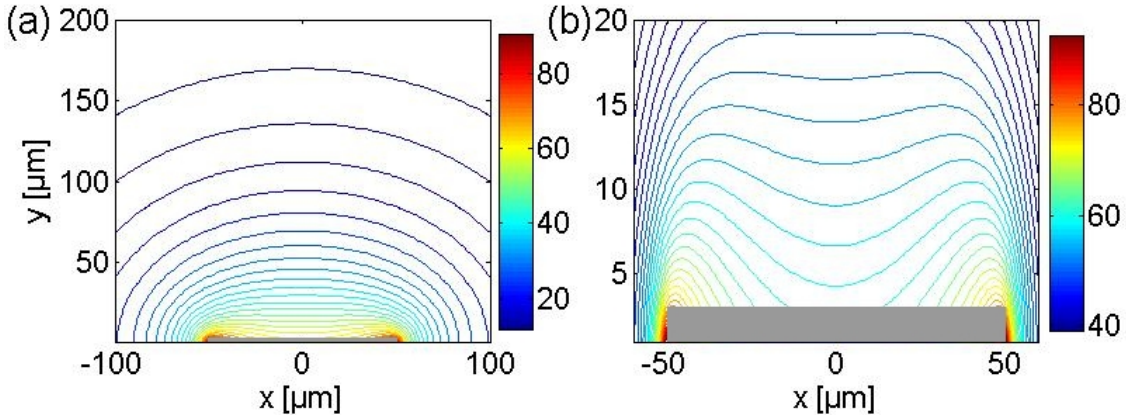

Figure 2.3: Rectangular wire magnetic field. **(a)** The absolute value of the magnetic field in the $(x, y, 0)$-plane of a wire with dimensions $W, H, L = 100, 3, 2000\,\mu$m is shown (in Gauss) for a wire current of 1 A. For distances $d > W$ the resulting field is similar to the circular field of a thin wire. For $d \approx W$ the finite wire size becomes important. In the case of a flat wire $H \ll W$ the circular field are deformed into elliptical ones in this region. **(b)** Zoom in into (a). In the region where $d \ll W$, the rectangular wire cross section leads to strong deviation from the circular field of an elliptical wire. Especially at the corners of the wire, regions of large field strength result.

Here, the abbreviations $x_\pm = x \pm W/2$, $y_\pm = y \pm H/2$, and $z_\pm = z \pm L/2$ have been used.
In figure 2.3 the absolute field strength in the $(x, y, 0)$-plane obtained from equation (2.31) is plotted for wire dimensions $W = 100\,\mu$m, $H = 3\,\mu$m, $L = 2000\,\mu$m. The finite wire width leads to a deformation of the circular field lines into ellipses for distances $d \approx W$. For small distances $d \ll W$, the rectangular wire shape results in more complex field lines, for which the circular wire approximation is completely invalid.

Current flow in realistic wires

The magnetic field of any chip wire configuration can be calculated by dividing the wires into shifted and rotated rectangular blocks for which the field is given by appropriately rotating and shifting equation 2.31. In this block-wise construction of the wires a second finite size effect has to be considered, namely the inhomogeneity of the current density at wire bends and crossings. At such places the current flow deviates from the geometrical outline of the wire. The actual current density distribution can be obtained by (numerically) solving the continuity equation with the wire geometry as boundary conditions [164]. These exact distributions can be well approximated by modeling wire corners with multiple "constant current blocks". How good this approximation is, depends on the number of blocks used and on the distance of the area of interest to wire corners. Usually using a single 45° "binding block" at a 90° bend is sufficient.
Similarly, the distance at which current densities have to be included in the field calculation depends on the desired accuracy. In principle, the complete wire structure, including the atom chip connection pads and the macroscopic current leads to the chip can be incorporated into the current density model. In many cases it is sufficient to consider the central wire parts on the atom chip [123]. We will calculate the magnetic fields of the actual wire structures used in our experiment in chapter 5 using the block model discussed here.

2.3 Radio-frequency adiabatic potentials

As has been discussed in section 2.1, magnetic trapping with static fields is based on the lifting of the degeneracy of the magnetic substates of a hyperfine level. Usually, the energetically highest

state is trapped, the maximally stretched low-field seeker state. When the energy separation is sufficiently large, this state becomes metastable on the timescale of experiments (see equation 2.13), and transitions between the different spin orientation states play no role.
In the following we will discuss what happens when the separated spin states are intentionally coupled by a resonant radiation field. A similar situation occurs for example in optical traps, where a laser beam couples different electronic states of the trapped atoms [106]. A fully quantum mechanical treatment of the problem was developed by S. Haroche and C. Cohen-Tanoudji in the 1960s, the formalism of *dressed states*. Although this formalism is mainly known for its successful explanation of the optical dipole force [54], which is the foundation of optical cooling and trapping techniques [43, 254, 47], it is interesting to note that the original experiments leading to its development considered atoms in microwave or radio-frequency fields, before lasers became widely available in experiments [46]. As will be discussed in the following, radio-frequency dressing of atoms is of renewed interested in the atom chip context, where strong rf (near) fields can be realized.

2.3.1 Dressed state Hamiltonian of an atom in a radio-frequency field

We consider an atom in a static magnetic field $\mathbf{B}_\mathrm{s}(\mathbf{r})$ dressed by an oscillating field $\mathbf{B}_\mathrm{rf}(\mathbf{r})e^{i\omega_\mathrm{rf}t}$ of single (radio) frequency $\nu_\mathrm{rf} = \frac{\omega_\mathrm{rf}}{2\pi}$. The eigenstates of the system are characterized by the magnetic quantum number $\tilde{m}_\mathrm{F}$ of the atom in the total magnetic field, and the rf photon number N. The full Hamiltonian of this configuration reads

$$H = \frac{\mathbf{p}^2}{2m} + g_\mathrm{F}\mu_\mathrm{B}\mathbf{F}\cdot\mathbf{B}_\mathrm{s}(\mathbf{r}) + \hbar\omega_\mathrm{rf}a^\dagger a + \frac{g_\mathrm{F}\mu_\mathrm{B}}{2\sqrt{\langle N\rangle}}\left[\mathbf{B}_\mathrm{rf}(\mathbf{r})a^\dagger + \mathrm{h.c.}\right]\cdot\mathbf{F}, \tag{2.33}$$

where $a^\dagger$ and a are the creation and annihilation operators for quanta of the rf field, defined as

$$a^\dagger\left|m_\mathrm{F}, N\right\rangle = \sqrt{N+1}\left|m_\mathrm{F}, N+1\right\rangle \tag{2.34}$$
$$a\left|m_\mathrm{F}, N\right\rangle = \sqrt{N}\left|m_\mathrm{F}, N-1\right\rangle, \tag{2.35}$$

with N being the numbers of rf photons. $\langle N\rangle$ is the average number of photons in the rf field, which can be identified with the classical amplitude of the field $|\mathbf{B}_\mathrm{rf}|$.
Note that in general the total rf field may be a superposition of different phase shifted components

$$\mathbf{B}_\mathrm{rf}(\mathbf{r})e^{i\omega_\mathrm{rf}t} = \left[\sum_\mathrm{i}\mathbf{B}_\mathrm{i}(\mathbf{r})e^{i\phi_\mathrm{i}t}\right]e^{i\omega_\mathrm{rf}t}, \tag{2.36}$$

in which case the total field vector $\mathbf{B}_\mathrm{rf}(\mathbf{r})$ is complex and has to be included in the hermitian conjugation.
The first term of the Hamiltonian (2.33) describes the kinetic energy of the atom, while the second term comes from the Zeeman shift of the atomic levels due to the static field. This part of the Hamiltonian is identical to the case of purely static fields (equation 2.2). The third term accounts for the energy of the rf field, while the third term describes the coupling of the rf dressing field to the atom. This term accordingly acts on both the atomic and the rf field part of the total quantum state.
To solve this Hamiltonian, we start in the same manner as in the static field case, namely we apply the rotation U_S (equation 2.3), which transforms the coordinate system into one with z-axis parallel to $\mathbf{B}_\mathrm{s}$ everywhere.
The rotated rf field $\tilde{\mathbf{B}}_\mathrm{rf}(\mathbf{r}) = U_\mathrm{S}^\dagger\mathbf{B}_\mathrm{rf}U_\mathrm{S}$ can be decomposed into parts $\tilde{\mathbf{B}}_{\mathrm{rf},\parallel}$ parallel and $\tilde{\mathbf{B}}_{\mathrm{rf},\perp}$ perpendicular to the static field. A second rotation U_rf around the (local) z-axis is applied, such

that $\tilde{\mathbf{B}}_{\mathrm{rf},\perp}$ points into the x-direction of the (space-dependent) coordinate system. This rotation does not affect the static field term, since it already points in the z-direction everywhere after the first rotation. After these two rotations, the total Hamiltonian takes the form

$$\begin{aligned} H &= E_{\mathrm{kin}} + H_{\mathrm{rf}} \\ &= \frac{1}{2m}\left[\mathbf{p} + \tilde{A}(\mathbf{r})\right]^2 + m_{\mathrm{F}} g_{\mathrm{F}} \mu_{\mathrm{B}} \left|\mathbf{B}(\mathbf{r})\right| + \hbar\omega_{\mathrm{rf}} a^\dagger a \\ &\quad + \frac{g_{\mathrm{F}}\mu_{\mathrm{B}}}{2\sqrt{\langle N\rangle}}\left[\left(B_{\mathrm{RF}\perp}(\mathbf{r})a^\dagger + \mathrm{h.c.}\right)F_{\mathrm{x}} + \left(B_{\mathrm{RF}\parallel}(\mathbf{r})a^\dagger + \mathrm{h.c.}\right)F_{\mathrm{z}}\right], \end{aligned} \tag{2.37}$$

with $\tilde{A} = U_{\mathrm{rf}}^\dagger U_{\mathrm{S}}^\dagger \mathbf{p} U_{\mathrm{S}} U_{\mathrm{rf}}$ and the amplitudes of the rf field components being given by

$$\begin{pmatrix} B_{\mathrm{RF}\perp} \\ 0 \\ B_{\mathrm{RF}\parallel} \end{pmatrix} = U_{\mathrm{rf}}^\dagger U_{\mathrm{S}}^\dagger \mathbf{B}_{\mathrm{rf}}(\mathbf{r}) U_{\mathrm{S}} U_{\mathrm{rf}}. \tag{2.38}$$

As in the static field calculation, the Hamiltonian consists of a kinetic energy term including a "gauge" potential $\tilde{A}$ and a potential energy term H_{rf} describing the coupling to the magnetic fields. In the following, we will first obtain the eigenstates of the potential term and then verify that the coupling between these states due to the gauge potential can be neglected in an adiabatic approximation.

2.3.2 Adiabatic rf potentials in the rotating wave approximation

To solve H_{rf}, commonly an approximation know as *rotating wave approximation* (RWA) is applied at this point. The atom-field coupling term in the Hamiltonian contains resonant parts, which involve the creation (annihilation) of an rf photon with the simultaneous lowering (raising) of the spin quantum number, as well as off-resonant terms describing the (virtual) processes of rf photon creation raising (annihilation lowering) the spin state. In the RWA the off-resonant terms are neglected, greatly simplifying the Hamiltonian. The name RWA comes from the classical treatment of an atom in a resonant oscillating field [262]. There, the field is decomposed into one linearly and two circularly polarized components. One then transfers into a frame rotating with the precession frequency of the atomic spin. In this frame, the circular component of same rotational direction becomes (nearly) time independent. The other circular component rotates with the sum of the spin precession and field frequency in the counter direction of the atomic spin precession, and can usually be neglected. The linear component, which points in the same direction as axis around which the atomic spin precesses, can be neglected if its Lamor frequency is small compared to the oscillation frequency. If one looks at how the photon creation and annihilation operators $a^\dagger$ and a are defined in the quantization of classical electromagnetic fields (see e.g. [285]), it can be seen that neglecting the "virtual energy" terms in the fully quantum mechanical treatment is essentially the same, although the meaning of the term rotating-wave is not so obvious anymore.
For the RWA to be applicable the oscillation frequency of the driving field ν_{rf} must be near resonant to the atomic transition frequency ν_0, or more precisely the detuning δ must be small compared to the atomic transition frequency: $\Delta = \nu_{\mathrm{rf}} - \nu_0 \ll \nu_0$. In this case, the off-resonant contributions in the term proportional to F_{x} can be neglected.
The F_{z} term involves only components of $\mathbf{B}_{\mathrm{RF}}(\mathbf{r})$ that oscillate parallel to the static field and can be neglected if $|\mu\mathbf{B}_{\mathrm{RF}\parallel}(\mathbf{r})| \ll h\nu_{\mathrm{rf}}$, i.e. if the Lamor frequency associated with the rf field component parallel to the static field is small compared to the oscillation frequency of the field [243, 186]. In this case the modification of the static field Lamor frequency due to this component can be averaged to zero over an oscillation period.
After these steps, the remaining Hamiltonian can be easily expressed in the bare state basis

$\{|m_\mathrm{F}, N\rangle\}$, $(m_\mathrm{F} = -F, ..., F)$. We group these states into manifolds $\{|m_\mathrm{F}, \kappa - \mathrm{sgn}(g_\mathrm{F})\, m_\mathrm{F}\rangle\}$, which are denoted by the number κ. This sorting of the basis states is convenient, because the complete matrix of the potential energy part of the RWA Hamiltonian now breaks up into a chain of separate $(2F+1) \times (2F+1)$ sub-matrices. In particular, for $F = 2$ these matrices take the form

$$\frac{1}{\hbar} \langle m_\mathrm{F}, \kappa - \mathrm{sgn}(g_\mathrm{F})\, m_\mathrm{F}|\, H_\mathrm{rf,RWA}\, |m_\mathrm{F}, \kappa - \mathrm{sgn}(g_\mathrm{F})\, m_\mathrm{F}\rangle = \tag{2.39}$$
$$\begin{pmatrix} \kappa\omega_\mathrm{rf} + 2\Delta & \Omega_{rf}^* & 0 & 0 & 0 \\ \Omega_{rf} & \kappa\omega_\mathrm{rf} + \Delta & \sqrt{3/2}\Omega_{rf}^* & 0 & 0 \\ 0 & \sqrt{3/2}\Omega_{rf} & \kappa\omega_\mathrm{rf} & \sqrt{3/2}\Omega_{rf}^* & 0 \\ 0 & 0 & \sqrt{3/2}\Omega_{rf} & \kappa\omega_\mathrm{rf} - \Delta & \Omega_{rf}^* \\ 0 & 0 & 0 & \Omega_{rf} & \kappa\omega_\mathrm{rf} - 2\Delta \end{pmatrix},$$

with the detuning $\Delta(\mathbf{r}) = |\mu_\mathrm{B} g_\mathrm{F}||\mathbf{B}_\mathrm{S}(\mathbf{r})| - \hbar\omega_\mathrm{rf}$ and the Rabi frequency $\Omega(\mathbf{r}) = \frac{\mu_\mathrm{B} g_\mathrm{F}}{2}|B_{\mathrm{RF}\perp}(\mathbf{r})|$. We also have used $\sqrt{N+1} = \sqrt{N}$ here. We are dealing with a classical rf field with very large mean photon number $\langle N \rangle$, which justifies this approximation [2].
Apart from the constant offset given by the rf photon energy $\kappa\hbar\omega_\mathrm{rf}$, this matrix is formally equivalent to that of a spin particle in a (static) effective field $\mathbf{B}_\mathrm{eff}(\mathbf{r})$ given by

$$\mathbf{B}_\mathrm{eff}(\mathbf{r}) = \begin{pmatrix} \frac{|B_{\mathrm{RF}\perp}(\mathbf{r})|}{2} \\ 0 \\ |\mathbf{B}_\mathrm{S}(\mathbf{r})| - \frac{\hbar\omega_\mathrm{rf}}{\mu_\mathrm{B}|g_\mathrm{F}|} \end{pmatrix} \tag{2.40}$$

Since we are not interested in the specific quantum state of the rf field, and the different κ-manifolds are decoupled within the RWA, the photon quantum number can be dropped, and we can restrict ourselves to a single manifold. The final Hamiltonian then reads

$$H_\mathrm{final,RWA} = \frac{\mathbf{p}^2}{2m} + g_\mathrm{F}\mu_\mathrm{B}\mathbf{B}_\mathrm{eff}(\mathbf{r}) \cdot \mathbf{F} = \frac{(\mathbf{p} + A(\mathbf{r}))^2}{2m} + g_\mathrm{F}\mu_\mathrm{B}|\mathbf{B}_\mathrm{eff}(\mathbf{r})|F_\mathrm{z}, \tag{2.41}$$

which, in the adiabatic approximation, has the eigenvalues $\tilde{m}_\mathrm{F} g_\mathrm{F}\mu_\mathrm{B}|\mathbf{B}_\mathrm{eff}(\mathbf{r})|$ already known from the static field case (equation 2.10). The $\tilde{m}_\mathrm{F} = -F, ..., F$ numbers can be interpreted as the magnetic quantum number of the atom in regard to the quantization axis defined by $\mathbf{B}_\mathrm{eff}$. Accordingly, we label the obtained eigenstates of the dressed Hamiltonian as $|\tilde{m}_\mathrm{F}\rangle$.

Orientation of the effective field

The field $\mathbf{B}_\mathrm{eff}$ lies in the plane spanned by $\mathbf{B}_\mathrm{s}(\mathbf{r})$ and $\mathbf{B}_\mathrm{rf}(\mathbf{r})$, it is tilted away from the static field by an angle θ, given by

$$\tan\theta = \frac{-\Omega}{\Delta} \qquad 0 \leq \theta \leq \pi. \tag{2.42}$$

In the limiting case of large negative detuning, θ tends to zero and the effective field reduces to the static field. For large positive detuning, θ tends to π and the effective field becomes antiparallel to the static field. If $\Delta = 0$, i.e. on resonance, the effective field becomes perpendicular to the static field, with its length solely determined by the rf field. An alternative interpretation of the situation is to say that the oscillating field modifies the g-factor of the atom, changing its behavior in the static field. Specifically in the case of large detuning, the sign of g_F is flipped, inverting the low- and high-field seeking states.
Just as the effective field is related to the static field by an rotation of angle θ, the dressed states $|\tilde{m}_\mathrm{F}\rangle$ can be obtained by rotating the original undressed spin eigenstates in the static field:

$$|\tilde{m}_\mathrm{F}\rangle = R_\mathrm{y}(\theta)\, |m_\mathrm{F}\rangle \tag{2.43}$$

Again, it can be seen that for large negative detuning, the dressed states are identical to the undressed states, while for positive large detuning, they are the undressed states in reversed order. In between, the dressed states are superpositions of the undressed states, with the coefficients depending on both Δ and Ω.

Adiabaticity of the dressed states

To verify that the adiabatic approximation applied above is valid, one has to check that the coupling between dressed states introduced by the term $\mathbf{A}(\mathbf{r},t)$ is negligible. This is the case if the projection of the time derivative $\partial\left|\tilde{m}_{\mathrm{F}}\right\rangle/\partial t$ of each state on the other dressed states is much smaller than the corresponding energy separation [139]:

$$\left|\left\langle\tilde{n}_{\mathrm{F}}\right|\frac{\partial}{\partial t}\left|\tilde{m}_{\mathrm{F}}\right\rangle\right| \ll \sqrt{\Delta^2+\Omega^2}. \tag{2.44}$$

By expressing the dressed states as rotations of the undressed states according to equation (2.43), and using the fact that the norm of a vector is invariant under rotations, the adiabacity condition can be rewritten as

$$\left|\dot{\theta}\right| \ll \sqrt{\Delta^2+\Omega^2}, \tag{2.45}$$

which is identical to the adiabatic criterium for a spin in a static field, as discussed in section 2.1.2, transferred to the effective field $\mathbf{B}_{\mathrm{eff}}$. If the rate of change of the effective magnetic field is small compared to the associated Lamor frequency $\sqrt{\Delta^2+\Omega^2}$, the $\tilde{m}_{\mathrm{F}}$ become constants of motion and the dressed states can adiabatically follow the effective magnetic field. As for static fields, the adiabatic approximation breaks down at points with $\mathbf{B}_{\mathrm{eff}}=0$. For finite effective fields the Landau-Zener tunneling rate between adiabatic dressed states is given by (2.13), with $\sqrt{\Delta^2+\Omega^2}$ determining the suppression. Similar to the static field case, already small detunings and/or Rabi frequencies reduce the transition rate sufficiently to make the dressed states (meta) stable on experiment time scales, justifying the adiabatic approximation in the case of rf dressed state potentials within the RWA.
As in the static case, the adiabatic approximation gives rise to a geometric phase of the trapped atoms. A detailed calculation and its possible effects especially in the context of rf potential based ring interferometers can be found in [329].

Effective adiabatic rf potential

After the adiabatic approximation, which removes $\mathbf{A}(\mathbf{r},t)$, the local eigenenergies of $H_{\mathrm{final,RWA}}$ give rise to an effective adiabatic potential which can be written as

$$V_{\mathrm{ad,RWA}}(\mathbf{r}) = \mu_{\mathrm{B}}\tilde{m}_{\mathrm{F}}g_{\mathrm{F}}\sqrt{\Delta^2(\mathbf{r})+\Omega^2(\mathbf{r})} \tag{2.46}$$

$$= \mu_{\mathrm{B}}\tilde{m}_{\mathrm{F}}g_{\mathrm{F}}\left[\left(\left|\mathbf{B}_{\mathrm{S}}(\mathbf{r})\right|-\frac{\hbar\omega_{\mathrm{rf}}}{\mu_{\mathrm{B}}\left|g_{\mathrm{F}}\right|}\right)^2+\left(\frac{B_{\mathrm{RF}\perp}(\mathbf{r})}{2}\right)^2\right]^{1/2}. \tag{2.47}$$

We shall call the first term below the square root the *resonance* term, and the second the *coupling* term. The resonance term depends on the coupling field only through its oscillation frequency ω_{rf}. It becomes spatially dependent due to the varying Zeeman shift of the atomic resonance frequency caused by an inhomogeneous static field. The term vanishes at points where the detuning Δ is zero. In principle, this term can be made constant (or zero) by using a homogeneous static field. In that case, the resulting adiabatic potential depends solely on the applied rf field.
The coupling term is proportional to the absolute value of the rf field component perpendicular to the static field. Since, in general, both static and oscillating field are inhomogeneous, this can result in a complex spatial dependence. Unlike the static magnetic field case, where only the modulus

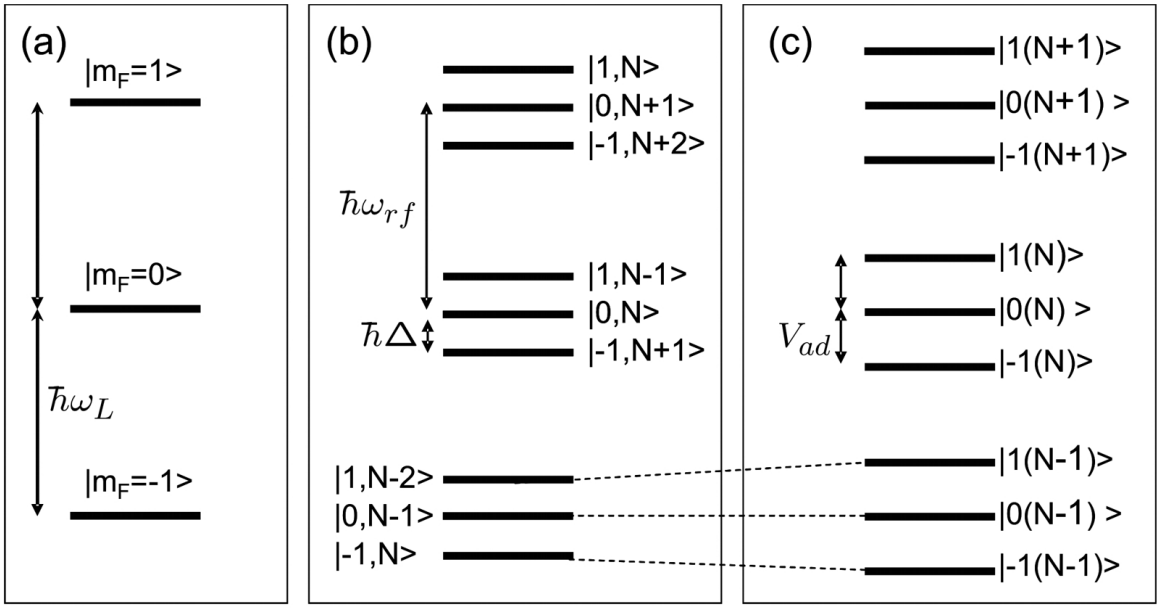

Figure 2.4: Schematic of the dressed state picture for a $F = 1$ system. **(a)** In an external magnetic field, the degeneracy of the magnetic states is lifted due to the Zeeman effect. The energy splitting corresponds to the Larmor frequency ω_{L}. **b** The inclusion of the photon energy of the oscillating field leads to the bare states, which form manifolds separated by the photon energy $\hbar\omega_{\mathrm{rf}}$. Within each manifold the distance between the bare states is given by the detuning $\Delta = \omega_{\mathrm{L}} - \omega_{\mathrm{rf}}$. **c** The dressed states are the eigenstates of the full system (equation 2.33), including the coupling term. For $\Delta, \Omega \ll \omega_{\mathrm{rf}}$the structure of well-separated manifolds is retained. Within the RWA only the coupling within bare states from a single manifolds are considered in the dressed states calculation. The energy splitting is then $V_{\mathrm{ad}}/\hbar = \sqrt{\Delta^2 + \Omega^2}$. If either Δ or Ω becomes comparable to ω_{rf}, the separation between different manifolds becomes comparable to the intra-manifold spacing, and the RWA is no longer applicable.

of the total resulting field determines the potential, here the vector nature of the involved fields remains important. The resulting level structure of the dressed states is illustrated in figure 2.4.

Comparison with static field magnetic traps

In the above derivation we have rewritten the rf adiabatic potential as the potential provided by a "static" effective field $\mathbf{B}_{\mathrm{eff}}$ for an atom with an effective magnetic quantum number $\tilde{m}_{\mathrm{F}}$. But there are a few distinct differences to the case of a "real" static magnetic field, which make the rf potentials more versatile than the static trap counterparts.
First, the effective field $\mathbf{B}_{\mathrm{eff}}$ need not fulfill the Maxwell equations, lifting the restrictions imposed on static fields by the Wing theorem [193] (compare section 2.1.3). An example of this in the context of atom chip wire traps is the reduction of potential minima for a given number of chip wires. In the (quasi)-static field case, it can be shown that the number of (quadrupole) minima in a plane perpendicular to the wires is always equal to the number of involved wires [59] (for a detailed discussion of this proof and its consequences for atom chip traps see for example [96]). Reducing the effective number of potential minima can only be achieved by merging different minima at the same position, which results in a change of this "degenerate" minimum from quadrupole to higher order. This restriction does not apply in the rf potential case, as demonstrated for example by the continuous deformation of a single quadrupole minimum into a double well configuration with two quadrupole minima, which will be discussed in detail in chapters 5 and 7.
A second important difference is that (the x-component of) $\mathbf{B}_{\mathrm{eff}}$ depends on the relative phases of the individual fields in a multi-component rf field case. This can lead to different rf potentials for atoms with same magnetic moment $\mu = \mu_{\mathrm{B}} g_{\mathrm{F}} m_{\mathrm{F}}$, but different hyperfine g-factors g_F [193]. In

contrast, the static trapping potential depends only on the sign of μ (equation 2.10). As will be shown in chapter 5, this can be used for state-selective atom manipulation [142].
Finally, the rf potentials offer a distinct advantage regarding the structure size scaling laws for potential modulations. According to the arguments given in section 2.2.1, in the case of static magnetic (atom chip) traps this length scale is set by the the size d of the field generating structure. Additionally, to fully exploit this scaling, the distance between the atoms and the chip surface has to be of the same order [74]. In contrast, the rf potentials enable the realizing a comparable confinement as the static traps with larger structures and thus farther away from the chip surface. For example, the trap configuration presented in chapter 5 realizes a micrometer potential variation at a distance $d > 100\,\mu$m from the chip surface. This is of particular importance as hereby coherence-destroying surface interactions effects [134, 281, 133] and potential corrugations due to surface roughness [87, 172, 179, 180, 157, 73, 176, 283, 318, 317]are strongly reduced.

2.3.3 Numeric calculation of adiabatic rf potentials

As discussed in the last section, the validity conditions for the RWA can be summarized as

$$\Omega, \Delta \ll \omega_0, \tag{2.48}$$

i.e. both the detuning and the Rabi frequency of the oscillating field must be small compared to the energy difference of the undressed states. From the considerations of the last section, the reasons for these requirements become obvious. In the RWA the dressed states are sorted into manifolds separated by the rf photon energy, between which any coupling is neglected. Within each manifold the states are separated by $\hbar\sqrt{\Delta^2 + \Omega^2}$. If the conditions (2.48) are fulfilled the separation between different manifolds is large compared to the distance between dressed states in each manifold. This justifies the restriction to a single manifold and the neglecting of the off-resonant terms, which introduce a coupling between different manifolds. The RWA obviously begins to fail, once the two different energy distances become comparable, which happens when either the detuning or the Rabi frequency (or both) become comparable to ω_0. Comparison of the full solution and the RWA results allows us to quantify the deviation from the RWA for given parameters, and yield the parameter range in which the analytical formulas of the last section can be safely used.
In most cases, especially in the domain of optical coupling fields, the conditions for the RWA to be valid, are always well fulfilled. This is not necessarily true for rf-dressed atoms, especially in highly inhomogeneous magnetic fields, as present in our experiments. Consequently, some care has to be taken if the RWA is applicable for specific experiment parameters. When the conditions (2.48) are not fulfilled, the complete Hamiltonian (2.37) has to be solved. Although analytical dressed state formalism solutions exist for low order corrections in the case of homogeneous fields [45], in the more general case of arbitrary fields this is best done numerically.

To solve the full Hamiltonian H_{rf} (2.37), we construct its matrix representation in the bare state basis $\{|m_{\mathrm{F}}, N\rangle\}$. We again group these states into κ-manifolds $\{|m_{\mathrm{F}}, \kappa - \mathrm{sgn}(g_{\mathrm{F}})\, m_{\mathrm{F}}\rangle\}$ and use $\sqrt{N+1} = \sqrt{N}$, assuming a large number of rf photons. The classical rf field is best described by a coherent state, which is a superposition of photon number states $|N\rangle$, with a Poissonian distribution of width $\sqrt{\langle N\rangle}$ around the state $|\langle N\rangle\rangle$. Since we are not interested in the change of the photon number or the phase of the rf field, we do not need this complete description, but instead can restrict ourself to the state $|\langle N\rangle\rangle$ and a small number of neighboring states [2]. It is convenient to rescale the photon number of these states $N = \langle N\rangle - \triangle N, ..., \langle N\rangle + \triangle N$ to $-\triangle N, ...\triangle N$ by subtracting the mean photon number, since we are interested only in the relative distance of the dressed states.
Under the assumption that the RF field can be treated as a classical field, the dressed state formalism including the non-RWA terms is equivalent to the theory of Floquet states, as shown in

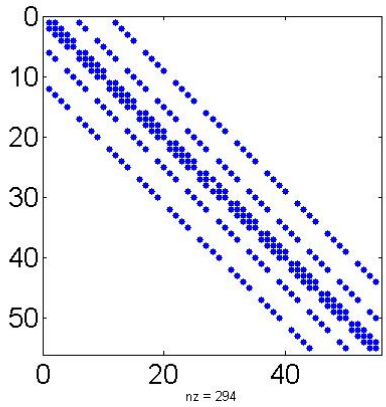

Figure 2.5: Schematic of the matrix representation of the full dressed state Hamiltonian in the basis discussed in the text. Finite entries are shown in blue. On the three central diagonals blocks of finite entries can be seen, which correspond to the terms considered in the RWA. The full Hamiltonian also has off-diagonal elements in the fifth and eleventh diagonal on each side, which are due to the off-resonant terms neglected in the RWA. These terms lead to coupling between different κ-blocks as discussed in the text.

[289]. In this semiclassical approach the quantization of the RF field is not explicitly included, but the Floquet states can be interpreted as quantum states containing a definite, very large, photon number.

Figure 2.5 shows a schematic representation of the resulting matrix for 11 considered manifolds ($\kappa = -5, ..., 5$). In the three center diagonals the blocks of entries also present in the RWA can be seen. Additionally there are now entries in the fifth and 11th off diagonals. The first come from the term proportional to F_z in (2.37), coupling neighboring κ-manifolds, while the latter are the off resonant elements in the F_x term, coupling manifolds with $|\kappa - \kappa'| = 2$. In principle, due to these off-diagonal elements, all considered bare states are coupled to each other. In practise, the coupling becomes negligible for sufficiently large $\triangle N$, so that the calculated dressed states converge for finite matrix sizes. How many manifolds have to be included, depends on the parameters of the magnetic fields used in the calculation. This number should not be chosen too large, as it unnecessarily slows the numeric calculation. On the other hand, it has to be ensured that the calculated states converge. For the calculation of the strongest rf coupling we have used in experiments, 17 manifolds ($\kappa = -8, ..., 8$) were required to reach an accuracy $< 1\%$.

If the off diagonal contributions are small, it is obvious that the full matrix reduces to the independent RWA blocks in the center diagonals. In that case, the numerical calculation should reproduce the analytical RWA results, which can function as a test of the numerical program.

Due to this break-up into identical blocks in the RWA, the system could be reduced to repeating, well-separated groups of $2F + 1$ states, fully characterized by one quantum number $\tilde{m_F}$. When $\sqrt{\Delta^2 + \Omega^2}$ becomes comparable to ω_0, these groups start to overlap. Still, in this regime it remains possible to identify groups of $2F + 1$ dressed states associated with a specific κ, which can be labeled with an effective quantum number $\tilde{m_F}$ (see figure 5.8). We label the dressed states now as $|\tilde{m_F}(\kappa) >$, to show that we now consider multiple κ-manifolds of dressed states. It is important to note that, although dressed states with same κ formally look identical to the RWA case, they are now superpositions of bare states from multiple κ-manifolds. This grouping of states fully breaks down, if $\sqrt{\Delta^2 + \Omega^2}$ becomes large compared to the energy separation of the undressed states. Then all considered bare states contribute equally to each dressed state and association of the dressed states with specific manifolds of bare states becomes meaningless. In the experiments discussed in the following chapters this regime is never reached, so that we can always use the notation introduced above to label the dressed states obtained numerically.

How the beyond-RWA terms modify the resulting adiabatic potentials and at which field parameters they become important, depends greatly on the specific field configuration considered. For quantitative statements, the numerical results have to be compared to the RWA result from case to case, which will be done in chapter 5, where the specific wire configuration used in our experiment are discussed. In general, the RWA begins to fail when $\Omega, \Delta \approx \frac{\omega_0}{3}$, which can be easily reached in experiments. The experimental observation of such beyond-RWA effects will be discussed in

chapter 6.

Adiabaticity of the beyond-RWA dressed states

The adiabaticity criterion remains the same for the numerical dressed states: the off-diagonal elements of the time-derivative operator must be small compared to the energy difference between the dressed states. In contrast to the RWA case, now also transitions between dressed states with different κ, i.e. different rf photon number, have to be considered. Also, each individual dressed state now is a superposition of bare states from multiple manifolds, so they cannot be reduced to simple rotations of one κ-set of bare states anymore. Consequently, the validity of the adiabatic approximation has to be checked individually for each specific field setup, and is best done numerically. For this, we can either explicitly calculate the matrix representation of the time derivative operator, or we can propagate a wave packet in a specific dressed state using the full Hamiltonian (2.33) and verify that no loss into other channels occurs [186]. In these numerical methods, the time-dependence of the involved magnetic fields can be integrated easily.

3 Coherence of one dimensional Bose-Einstein condensates

In this chapter, the most relevant theoretical aspects for the experiments discussed in this thesis are reviewed. In section 3.1 a brief summary of the theory of Bose-Einstein condensation (BEC) in dilute atomic gases is given, with focus on results directly applicable to our experiments.
In the second part (section 3.2), the theory of (no) BEC in one-dimensional (1d) systems is presented. Two different theoretical approaches to 1d Bose gases are discussed, the Bogoliubov framework introduced in section 3.1 and the complimentary Luttinger liquid approach [121, 38].
In sections 3.3 and 3.4 the phenomenon of interference between two BEC is discussed. The description of the interference process in the second-quantization picture is first presented for the case of single-mode condensates, which corresponds to three-dimensional (3d) condensates. This theory is then extended to the case of two interfering 1d BECs in section 3.4. It is shown that the 1d nature of the excitation spectrum of the two condensates requires a multi-mode treatment of the situation. The process of coherently splitting a single condensate is also discussed for both situations, single- and multi-mode BECs, in the respective sections.
In the final section 3.5, the situation of two coupled 1d condensates is studied. This system behaves in many ways like its extensively studied 3d counterpart, the bosonic Josephson junction formed by two coupled single mode condensates [291, 1]. But similar to the interference phenomena studied in section 3.4, the 1d nature of the individual BECs is found to significantly modify the situation. The nonlinear instability and the resulting dynamics in the 1d case are discussed.

3.1 Bose-Einstein condensation in trapped dilute gases

The phenomenon of BEC was first discussed by Einstein in 1924 [70, 71], following ideas of Bose addressing the statistics of photons [24]. Einstein considered a gas of ideal particles obeying Bose statistics in free space and found that below a critical (finite) temperature, a macroscopic population of the ground state of the system occurs.
While this original prediction for a noninteracting gas was considered a peculiarity of an idealized system, soon after the observation of superfluidity in ^{4}He, London suggested that BEC was responsible for the superfluid properties despite the strong interactions in this system [204, 203]. Since then, liquid helium and its connection to BEC has been widely studied, and many of the theoretical concepts used today in the field of ultra cold atomic gases actually predate the first realizations of BEC in these systems [244, 238, 105].
Still, the observation of BEC in dilute atomic vapors in 1995 [5, 26, 56] has led to an explosive increase of interest in the topic, on one hand due to the (relative) experimental ease and flexibility of these systems. Furthermore, the weak atomic interactions in neutral gases greatly facilitate the theoretical treatment of the situation, enabling a quite successful description of many phenomena with low-order mean field approximations.
In this section, key points of the theory of BEC in finite systems of trapped dilute gases are presented, with the focus on concepts relevant to the experiments described in this manuscript. Detailed derivations of the formulas presented here can be found in various review papers on the subject, e.g. [242, 52, 37, 181].

3.1.1 Many-particle Hamiltonian in second quantization

To describe N interacting, identical Bosons trapped in a potential $V_{ext}(\mathbf{r})$, the formalism of second quantization is well suited. Assuming that a complete set $\varphi_\alpha(\mathbf{r})$ of (orthonormal) eigenfunctions of the single-particle states in the potential $V_{ext}(\mathbf{r})$ is known, the annihilation and creation operators a_α and $a_\alpha^\dagger$ are introduced, which annihilate (create) a particle in the state $\varphi_\alpha(\mathbf{r})$:

$$a_\alpha \left|n_0 n_1 ... n_\alpha ...\right\rangle = \sqrt{n_\alpha}\left|n_0 n_1 ... n_\alpha - 1 ...\right\rangle \tag{3.1}$$

$$a_\alpha^\dagger \left|n_0 n_1 ... n_\alpha ...\right\rangle = \sqrt{n_\alpha + 1}\left|n_0 n_1 ... n_\alpha + 1 ...\right\rangle . \tag{3.2}$$

Here, n_α is the eigenvalue of the operator $n_\alpha^\dagger = a_\alpha^\dagger a_\alpha$, giving the number of particles in the single-particle state ϕ_α. The bosonic field operators $\hat{\Psi}(\mathbf{r})$ and $\hat{\Psi}^\dagger(\mathbf{r})$, which create or annihilate particles at position $\mathbf{r}$, can be written as

$$\hat{\Psi}(\mathbf{r}) = \sum_\alpha \varphi_\alpha(\mathbf{r}) a_\alpha. \tag{3.3}$$

The many-body Hamiltonian, including atom-atom interactions, then reads

$$\begin{aligned} \hat{H} &= \int d\mathbf{r}\hat{\Psi}^\dagger(\mathbf{r})\left[-\frac{\hbar^2}{2m}\nabla^2 + V_{ext}(\mathbf{r})\right]\hat{\Psi}(\mathbf{r}) \\ &+ \frac{1}{2}\int d\mathbf{r}d\mathbf{r}'\hat{\Psi}^\dagger(\mathbf{r}')\hat{\Psi}^\dagger(\mathbf{r}')V_{\mathrm{int}}(\mathbf{r}-\mathbf{r}')\hat{\Psi}(\mathbf{r})\hat{\Psi}(\mathbf{r}), \end{aligned} \tag{3.4}$$

where m is the particle mass, and $V_{\mathrm{int}}(\mathbf{r}-\mathbf{r}')$ is the two-body interatomic potential.
The time-evolution of the system is obtained by inserting the Hamiltonian (3.4) and the Heisenberg representation $\hat{\Psi}(\mathbf{r},t)$ of the field operator into the Heisenberg equation:

$$\begin{aligned} i\hbar\frac{\partial}{\partial t}\hat{\Psi}(\mathbf{r},t) &= \left[\hat{\Psi},\hat{H}\right] = \left[-\frac{\hbar^2\nabla^2}{2m} + V_{\mathrm{ext}}(\mathbf{r})\right. \\ &+ \left.\int d\mathbf{r}'\hat{\Psi}^\dagger(\mathbf{r}',t)V_{\mathrm{int}}(\mathbf{r}-\mathbf{r}')\hat{\Psi}(\mathbf{r}',t)\right]\hat{\Psi}(\mathbf{r},t). \end{aligned} \tag{3.5}$$

The one-particle reduced density matrix $\rho(\mathbf{r},\mathbf{r}';t)$ is related to the field operator through the equation

$$\rho(\mathbf{r},\mathbf{r}';t) = \left\langle \hat{\Psi}(\mathbf{r},t)\hat{\Psi}(\mathbf{r}',t)\right\rangle . \tag{3.6}$$

As this matrix is Hermitian, a complete orthonormal basis of single-particles eigenfunctions $\phi(\mathbf{r},t)$ can be found such that

$$\rho(\mathbf{r},\mathbf{r}';t) = \sum_i N_i(t)\phi_i^*(\mathbf{r},t)\phi_i(\mathbf{r}',t). \tag{3.7}$$

In general, the $\phi(\mathbf{r},t)$ are not identical to the original, interaction-free, single-particle solutions $\varphi_\alpha(\mathbf{r})$. BEC occurs when the occupation number N_0 of a particular state ϕ_0 becomes comparable to the total particle number N. A special situation, which we will encounter in the case of the double well potential, is that more than one state is macroscopically occupied at the same time. This is called fragmentation of the BEC [160].
In principle, from the Hamiltonian (3.4) the (time-dependent) many-particle ground state wave function, as well as all thermodynamic properties of the system, can be calculated. Usually, for non-trivial trapping and interaction potentials, this can only be done numerically [173], which quickly becomes impossible for large N. The common approach to circumvent this problem, and to obtain generally applicable analytic formulas for the BEC state, is to resort to mean-field approximations, as will be shown in the following.

Atom-atom interaction in ultra cold gases

The interaction potential $V_{\text{int}}(\mathbf{r}-\mathbf{r}')$ between two neutral atoms is given by the combination of a strong short range ($|\mathbf{r}-\mathbf{r}'| < 5$ Å) repulsive contribution due to Coulomb interaction of the electron clouds and a long range attractive van-der-Waals term, resulting in the existence of bound states [130].
For low temperatures the exact shape of the interaction potential is not important, the only relevant scattering process is s-wave scattering, since the thermal de Broglie wavelength is much larger than the effective extension of the interaction potential. Therefore the exact V_{int} can be replaced with a model potential, which has the same scattering properties in the cold temperature limit, i.e. gives the same result for s-wave scattering, and is treatable in the Born approximation [37]. These requirements are fulfilled by a zero-range pseudo-potential of the form [239, 311]

$$V(\mathbf{r}-\mathbf{r}') = g\delta(\mathbf{r}-\mathbf{r}'), \tag{3.8}$$

where the coupling constant g is related to the s-wave scattering length a_s through

$$g = \frac{4\pi\hbar^2 a_s}{m}. \tag{3.9}$$

The interaction term in the many-body Hamiltonian (3.4) then becomes

$$\frac{4\pi\hbar^2 a_s}{m}\int d\mathbf{r}\hat{\Psi}^\dagger(\mathbf{r})\hat{\Psi}^\dagger(\mathbf{r})\hat{\Psi}(\mathbf{r})\hat{\Psi}(\mathbf{r}) \tag{3.10}$$

In this approximation, all details of the interatomic potential are "hidden" in a single parameter, the scattering length, which can be positive (for repulsive interactions) as well as negative (for attractive interactions). The ^{87}Rb s-wave scattering length for the $|F=1, m_{\text{F}}=-1\rangle$ and $|F=2, m_{\text{F}}=2\rangle$ has been determined experimentally as 5.45 ± 0.26 nm [159].

3.1.2 Mean field theory

A common approach to simplify systems of interacting particles is to adopt a mean-field description of the interatomic forces. The main idea is to replace all interactions to any one body with an effective interaction, i.e. to summarize the interactions felt by each single atom in a (classical) potential field.
The first step of the mean-field treatment of a dilute Bose gas is to decompose the Bosonic field operator is into two parts, one creating particles in the single state into which Bose-Einstein condensation occurs, and another creating the particles in all other states [23]

$$\hat{\Psi}(\mathbf{r},t) = \hat{\Phi}(\mathbf{r},t) + \hat{\Psi}'(\mathbf{r},t). \tag{3.11}$$

Assuming that the condensed fraction of the system is macroscopically large, the ground state operator $\hat{\Phi}(\mathbf{r},t)$ is then replaced by a complex function $\Phi(\mathbf{r},t)$, which is defined as the expectation value of the total field operator

$$\Phi(\mathbf{r},t) = \left\langle \hat{\Psi}(\mathbf{r},t) \right\rangle. \tag{3.12}$$

The function $\Phi(\mathbf{r},t)$ is a classical field, which fixes the density distribution of the BEC through the relation $n_0(\mathbf{r},t) = |\Phi(\mathbf{r},t)|^2$, and can be interpreted as an order parameter for the phase transition from thermal ensemble to BEC. Another important aspect is that the function $\Phi(\mathbf{r},t)$ has a well-defined phase, which is commonly associated with the "macroscopic phase" of the BEC.
At the same time as the condensed fraction becomes large, the contribution of the operator $\hat{\Psi}'(\mathbf{r},t)$, which is called the depletion of the condensate, becomes small. Then the field operator can be expanded around $\hat{\Phi}(\mathbf{r},t)$ and equations for the order parameter $\Phi(\mathbf{r},t)$ for different orders of the expansion can be derived.

Gross-Pitaevskii equation

In the zeroth order the condensate depletion $\hat{\Psi}'(\mathbf{r},t)$ is completely neglected and the total field operator is given by $\hat{\Psi}(\mathbf{r},t) = \Phi(\mathbf{r},t)$. Due to the interactions, this still leads to a non-trivial equation for the order parameter $\Phi(\mathbf{r},t)$. Inserting $\Phi(\mathbf{r},t)$ into (3.5) and using (3.8) yields a closed equation for the condensate wave function

$$i\hbar\frac{\partial}{\partial t}\Phi(\mathbf{r},t) = \left(-\frac{\hbar^2\nabla^2}{2m} + V_{\text{ext}}(\mathbf{r}) + g\left|\Phi(\mathbf{r},t)\right|^2\right)\Phi(\mathbf{r},t), \tag{3.13}$$

which is known as the Gross-Pitaevskii equation (GPE) [110, 256].
Writing $\Phi(\mathbf{r},t) = \phi(\mathbf{r})\exp(-i\mu t/\hbar)$ leads to a time-independent version of the GPE

$$\left(-\frac{\hbar^2\nabla^2}{2m} + V_{\text{ext}}(\mathbf{r}) + g\left|\phi(\mathbf{r})\right|^2\right)\phi(\mathbf{r}) = \mu\phi(\mathbf{r}). \tag{3.14}$$

With the correct normalization $\int d\mathbf{r}\phi = N_0$, the variable μ is the chemical potential of the condensate $\mu = \frac{\partial E}{\partial N_0}$. In the GPE the effective atom-atom interaction is described as a mean field potential $g\left|\phi(\mathbf{r})\right|^2$ proportional to the atom density, which makes the equation non-linear.
The GPE can in general not be solved analytically. In the limiting case of weak atomic interactions, the GPE reduces to the linear Schrödinger equation and the condensate wavefunction is the ground state wavefunction in the external potential times a normalization constant. In the opposite case of dominating mean field energy, we can neglect the kinetic energy term, which is known as Thomas Fermi (TF) approximation. The condensate density distribution is then given by the simple relation

$$n_0(\mathbf{r}) = g^{-1}\left(\mu - V_{\text{ext}}(\mathbf{r})\right)\Theta\left(\mu - V_{\text{ext}}(\mathbf{r})\right) \tag{3.15}$$

where Θ is the unit step function.
The GPE can be seen as the equation of motion of the atomic field in a classical approximation. Consequently, any quantum fluctuations of the field are not described by the GPE. In this sense, the BEC may be regarded as a classical state of the atomic field. This gives a direct indication, that the GPE is only a good approximation if the number of condensed atoms N_0 is large. On the other hand, the density of the BEC must be small enough, so that particle correlations are negligible, which leads to another validity condition of the GPE, namely $n_0 a_s^3 \ll 1$, where n_0 is the condensate density. Finally, the GPE neglects any non-condensed atoms and any interaction of the BEC with these atoms, which is an approximation even at $T = 0$, due to the always present depletion of the condensate due to quantum fluctuations.

Bogoliubov-de Gennes equations

A first order calculation of the excitations of the interacting Bose gas due to quantum fluctuations, is obtained by including the depletion operator $\hat{\Psi}'(\mathbf{r},t)$ written in the form [82]

$$\hat{\Psi}'(\mathbf{r},t) = \sum_j \left[u_j(\mathbf{r})\alpha_j(t)e^{-iE_jt/\hbar} + v_j^*(\mathbf{r})\alpha_j^\dagger(t)e^{iE_jt/\hbar}\right], \tag{3.16}$$

i.e. we expand the depletion operator in the basis of plane waves, with α_j and $\alpha_j^\dagger$ annihilate and create (quasi)-particles in the corresponding states.
Inserting the complete field operator $\hat{\Psi}(\mathbf{r},t) = \Phi(\mathbf{r},t) + \hat{\Psi}'(\mathbf{r},t)$ into the Heisenberg equation (3.5) and keeping only terms linear in the quasiparticle amplitudes u_j and v_j leads to a set of coupled differential equations of the form

$$E_j u_j(\mathbf{r}) = [H_0 - \mu + 2g\phi^2(\mathbf{r})]u_j(\mathbf{r}) + g\phi^2(\mathbf{r})v_j(\mathbf{r}) \tag{3.17}$$

$$-E_j v_j(\mathbf{r}) = [H_0 - \mu + 2g\phi^2(\mathbf{r})]v_j(\mathbf{r}) + g\phi^2(\mathbf{r})u_j(\mathbf{r}), \tag{3.18}$$

the so-called Bogoliubov-de Gennes equations, where $H_0 = -(\hbar^2/2m)\nabla^2 + V_{\text{ext}}(\mathbf{r})$ and $\phi(\mathbf{r})$ is the ground state solution of the stationary GPE. Solving this system of equations yields the energies E_j and the amplitudes u_j, v_j of the elementary excitations. The resulting collective excitations need not only be of single particle character, i.e. excitations into higher trap states, but can also for example be phonon-like excitations of the total system.
Although originally developed for describing the (large) depletion of the ground state in liquid Helium [23] at zero temperature, the formulation of the Bogoliubov approach by Fetter as presented here [82], can be used in the context of dilute Bose gases also for thermal excitations of the system at finite temperature, which is known as the Popov approximation [260, 81]. For $T = (k_{\text{B}}\beta)^{-1}$, the total number density $n(\mathbf{r})$ consists of the condensate contribution $n_0 = |\Phi|^2$ and the noncondensate density

$$n'(\mathbf{r}) = \sum_j \left[f_j |u_j(\mathbf{r})|^2 + (1 + f_j)|v_j(\mathbf{r})|^2 \right], \tag{3.19}$$

where $f_j = [\exp(\beta E_j) - 1]^{-1}$ is the Bose distribution function. The condition $N = \int dV n_0 + \int dV n' = N_0(T) + N'(T)$ determines the temperature dependent condensate fraction N_0/N. At $T = 0$, f_j vanishes, but n' still contains contributions $|v_j|^2$, which shows that also in weakly interacting Bose gases there is a (small) depletion of the ground state due to atomic interactions at zero temperature.

3.1.3 Numeric solution of the GPE

To numerically solve the GPE, we employ a much-used numerical technique known as split-operator method, which allows both the calculation of the static eigenstates as well as the time evolution of the GPE.
In general, the time evolution of an initial state $\Phi(\mathbf{r}, t = 0)$ is given by

$$\Phi(\mathbf{r}, t) = U(t)\Phi(\mathbf{r}, t = 0), \tag{3.20}$$

where $U(t)$ is the time-evolution operator. Assuming that the Hamiltonian of the system is time-dependent but commutes for different times, as is usually the case when solving the GPE, the time-evolution operator is given by

$$U(t) = \exp\left[-i \int_0^t dt' H(t') \right]. \tag{3.21}$$

This continuous propagation can be approximated by a series of small but discrete time evolutions of the form $U(\triangle t) = \exp\left[-iH(t)\triangle t/\hbar\right]$, where $H(t)$ is the Hamiltonian at the moment before the finite time propagation.
In the case of the GPE, $H(t)$ can be separated into a momentum operator part $T(\hat{\mathbf{p}}) = \frac{\hat{\mathbf{p}}^2}{2m}$ and a position operator part $V(\hat{\mathbf{r}}, t) = V_{\text{ext}}(\hat{\mathbf{r}}, t) + g|\Phi(\mathbf{r}, t)|^2$. By using the Baker-Campbell-Hausdorff formula [210], the finite time step operator can be approximated by

$$U(\triangle t) = e^{-iH(t)\triangle t/\hbar} = e^{-iT(\hat{\mathbf{p}})\triangle t/2\hbar} e^{-iV(\hat{\mathbf{x}})\triangle t/\hbar} e^{-iT(\hat{\mathbf{p}})\triangle t/2\hbar} + \mathcal{O}(\triangle t^3). \tag{3.22}$$

Due to the symmetric splitting, this approximation is correct up to quadratic order in $\triangle t$ [77]. Since $V(\hat{\mathbf{r}}, t)$ is time-dependent due to the non-linearity even in the case of a static external potential, the time step operator has to be recalculated after each propagation step. On the other hand, $T(\hat{\mathbf{p}})$ is time independent, so that when performing consecutive propagations the last exponential involving the momentum operator can be combined with the first exponential of the following application of (3.22), simplifying the time step operator to

$$U(\triangle t) = e^{-iT(\hat{\mathbf{p}})\triangle t/\hbar} e^{-iV(\hat{\mathbf{x}},t)\triangle t/\hbar}. \tag{3.23}$$

In principle, when using this form, the first and last time step should have half the length compared to all other steps, but this error can be neglected if the number of time steps is large.
Each time step is applied to the wave function in the following way

$$\Phi(\mathbf{r}, t + \triangle t) = \mathrm{F}^{-1}\left[e^{-iT(\hat{\mathbf{p}})\triangle t/\hbar}\,\mathrm{F}\left[e^{-iV(\hat{\mathbf{x}})\triangle t/\hbar}\Phi(\mathbf{r}, t)\right]\right], \tag{3.24}$$

where F denotes a Fourier transformation. By switching between position and momentum representation of the wave function Φ, the application of both the momentum and the position operator part in the propagator reduce to simple multiplications, as they are diagonal in the momentum and position basis, respectively. In practise the wave function $\Phi(\mathbf{r}, t)$ is calculated on a spatial grid with finite resolution, so that discrete fast Fourier transform (FFT) algorithms can be used. This approach numerically favorable over a calculation in a single basis representation, which involves a (discrete) differentiation of the wave function.
A more detailed discussion of the split operator method, and specifically a discussion of the optimization of the temporal and spatial resolutions used, can be found in [8].

Imaginary time propagation

The split operator propagation method can also be used to find the eigenstates of the time-independent GPE. By changing the time step $\triangle t$ in the propagator to a purely imaginary value $\triangle\tau = i\triangle t$, the GPE turns into a diffusion equation [42], so that consecutive application of the imaginary time propagation leads to a reduction of the total energy of the propagated state.
If an approximative solution of the ground state (either from a single particle solution or the TF approximation) is used as initial state, the propagated wave function quickly converges towards the true ground state of the GPE. The total number of time steps depends on the desired accuracy of the solution. Note that the imaginary time propagation is not norm-conserving, as the time step operator is no longer Hermitian. This problem can be overcome by renormalizing the wave function after each time step.
The first excited state of the GPE can be found by starting with an anti-symmetric initial wave packet. Since the imaginary time propagation cannot change the (anti)-symmetry of the wave function, this results in convergence towards the lowest lying anti-symmetric state, i.e. the first excited state. Alternatively, once the ground state is known, one can project the propagated wave function onto the subspace orthogonal to the ground state wave function after each step, which also results in convergence towards the first excited state. In principal, following this scheme, also higher energy solution can be obtained consecutively, by projecting out all lower lying wave functions after each step.

3.1.4 Three dimensional BEC in harmonic traps

We are specifically interested in Bose gases trapped in three-dimensional harmonic potentials

$$V_{\mathrm{trap}}(\mathbf{r}) = \frac{m}{2}\left(\omega_{\mathrm{x}}^2 x^2 + \omega_{\mathrm{y}}^2 y^2 + \omega_{\mathrm{z}}^2 z^2\right), \tag{3.25}$$

since most of the minima regions of the static and rf magnetic traps used in the experiments discussed in this manuscript are well-described by potentials of this form. For now we focus on the case $\omega_{\mathrm{x}} \approx \omega_{\mathrm{y}} \approx \omega_{\mathrm{z}}$ and $\hbar\omega_{\mathrm{x,y,z}} \ll \mu$. The latter condition ensures the validity of the TF approximation in all dimensions. More specifically, if this condition is fulfilled, the ratio of interaction and kinetic energy is much larger than unity and scales as

$$\frac{E_{\mathrm{int}}}{E_{\mathrm{kin}}} \propto \frac{N a_s}{a_{\mathrm{ho}}} \gg 1. \tag{3.26}$$

Here, we introduced the geometric mean $a_{\rm ho} = (a_x a_y a_z)^{1/3}$ of the single particle oscillator ground state sizes $a_i = \sqrt{\frac{\hbar}{m\omega_i}}$. We shall call the BEC three-dimensional (3d) in this case. In the next section, we will discuss that by breaking the above condition in individual directions, the (effective) dimension of the system can be reduced.
From equation (3.15) it follows that the 3d BEC wave function takes the form

$$\Phi(\mathbf{r}) = \left(\frac{\mu}{N_0 g}\right)^{1/2} \left(1 - \sum_i \frac{r_i^2}{R_i^2}\right)^{1/2}, \tag{3.27}$$

i.e. the boundary of the condensate density is an ellipsoid with half axes

$$R_i = \sqrt{\frac{2\mu}{m\omega_i^2}}. \tag{3.28}$$

The chemical potential can be expressed in terms of N_0 by integrating over the density distribution, which gives

$$\mu = \frac{\hbar\omega_{\rm ho}}{2} \left(\frac{15 N a_s}{a_{\rm ho}}\right)^{2/5}, \tag{3.29}$$

where $\omega_{\rm ho} = (\omega_{\rm x}\omega_{\rm y}\omega_{\rm x})^{1/3}$.
The Bogoliubov formalism can be used to determine the critical temperature T_c at which BEC occurs, giving

$$k_{\rm B} T_c = 0.94\hbar\omega_{\rm ho} N^{1/3} - 1.22 a_s (\hbar m N)^{1/2} \omega_{\rm ho}^{3/2}, \tag{3.30}$$

where the first term is identical to T_c in an ideal gas, while the second term gives a (usually small) correction due to interactions [97].
The TF approximation can be extended to the Bogoliubov-de Gennes equations, which leads to a set of hydrodynamic equations describing the collective excitations of the system [51, 53]. The predictions of the TF mean-field theory are in good quantitative agreement with a large variety of experiments with 3d BECs, successfully describing for example the free expansion [53, 72] and collective oscillations [295].

3.2 BEC in one dimension

The influence of dimensionality on the presence and character of BEC has been extensively studied theoretically. The second quantization formalism presented in the last section can be applied to systems of arbitrary dimension, and not surprisingly, the thermodynamic properties and the elementary excitations of the Bose gas are greatly affected by the dimensionality of the system. Particularly one dimensional (1d) systems have attracted large theoretical interest, as (at least) the spatially homogeneous case for repulsive delta-potential interactions is exactly solvable [200, 199]. Another fundamental result, the Mermin-Wagner-Hohenberg theorem [219, 143] states that BEC does not occur at finite temperature in 1d and two dimensional (2d) homogeneous systems.
Besides being of theoretical interest, low dimensional systems play a role for example in the study of excitons (electron-hole pairs) in semiconductors [55], in high critical temperature superconductivity of monolayer structures [233], or in thin liquid helium films on surfaces [18].
For ultra cold dilute atomic gases, the reduction of dimensionality can be achieved by using highly anisotropic trapping potentials, which have sufficiently strong confinement in one or two directions to restrict the motion of the atoms to zero-point oscillations, in which case the system becomes kinematically 1d or 2d. The presence of a (usually harmonic) trapping potential also in the remaining direction(s) introduces a finite size and changes the level structure of the many body system.

This has important consequences on the occurrence and character of BEC in these systems, as will be discussed in this section. We focus here on the 1d case, a discussion of 2d trapped dilute Bose gases can be found in [250, 249].

3.2.1 Interacting gas in 1d

We first consider a 1d system of N interacting bosons in the absence of a trapping potential. As interaction potential we use a delta function contact potential as in equation (3.8), $V_{\text{int}} = g_{1\text{d}}\delta(z_i - z_j)$, where the 1d coupling constant $g_{1\text{d}} = -2\hbar^2/m/a_{1\text{d}}$ is determined by the 1d s-wave scattering length $a_{1\text{d}}$, just as in the 3d case [68]. We consider only repulsive interaction, so that $a_{1\text{d}} > 0$. The 1d many body Hamiltonian can then directly be written as

$$H^0_{1\text{d}} = -\frac{\hbar}{2m}\sum_{j=1}^{N}\frac{\partial^2}{\partial z_j^2} + g_{1\text{d}}\sum_{i\neq j}^{N}\delta(z_i - z_j). \tag{3.31}$$

This Hamiltonian can be directly solved by using a Bethe ansatz [200]. Consequently the equation of state of the system is known exactly for all densities and temperatures [325]. For example, at zero temperature the resulting energy per particle $\epsilon(n_{1\text{d}})$ is given by

$$\epsilon(n_{1\text{d}}) = \frac{\hbar^2}{2m}n_{1\text{d}}^2 e(\gamma(n_{1\text{d}})), \tag{3.32}$$

where $n_{1\text{d}}$ is the 1d particle density, $\gamma = 2/n_{1\text{d}}a_{1\text{d}}$ is a dimensionless parameter, which is inversly proportional to the 1d gas parameter $n_{1\text{d}}a_{1\text{d}}$, and the function $e(\gamma)$ is given by

$$e(\gamma) = \frac{\gamma^3}{\lambda^3(\gamma)}\int_{-1}^{1} g(x,\gamma)x^2 dx. \tag{3.33}$$

The functions $g(x,\gamma)$ and $\lambda(\gamma)$ are defined by the coupled Lieb-Liniger equations [200]:

$$g(x,\gamma) = \frac{1}{2\pi}\left(1 + \int_{-1}^{1}\frac{2\lambda(\gamma)}{\lambda^2(\gamma) + (y-x)^2}g(y,\gamma)dy\right), \tag{3.34}$$

$$\lambda(\gamma) = \gamma\int_{-1}^{1} g(x,\gamma)dx. \tag{3.35}$$

The parameter γ can also be seen as the ratio of the interaction energy per particle $\epsilon_{\text{int}} = n_{1\text{d}}g_{1\text{d}}$ over a characteristic kinetic energy of particles ϵ_{kin} with a mean separation $\bar{r}$ between them. In 1d $\bar{r} \sim 1/n_{1\text{d}}$, and $\epsilon_{\text{kin}} \approx \frac{\hbar^2 n_{1\text{d}}^2}{m}$, which leads to

$$\frac{\epsilon_{\text{int}}}{\epsilon_{\text{kin}}} = \frac{mg_{1\text{d}}}{\hbar^2 n_{1\text{d}}} = \frac{2}{n_{1\text{d}}a_{1\text{d}}} = \gamma. \tag{3.36}$$

This set of equations shows the surprising fact that in that the 1d Bose gas becomes more interacting with decreasing density [1].

In the limits of small and large γ the energy per particle $\epsilon(n_{1\text{d}})$ can be expressed in closed form as [200]

$$\gamma \gg 1, \quad \epsilon(n_{1\text{d}}) \to \frac{\pi^2\hbar^2}{6m}n_{1\text{d}}^2, \tag{3.37}$$

and

$$\gamma \ll 1, \quad \epsilon(n_{1\text{d}}) \to \frac{g_{1\text{d}}n_{1\text{d}}}{2}. \tag{3.38}$$

[1] To arrive at this conclusion it with assumed that interactions are determined by the s-wave scattering length, which implicitly means one considers a dilute gas. Hence this statement is only valid as long as the mean particle separation $\bar{r} \sim 1/n_{1\text{d}}$ is large compared to the characteristic length of the interatomic potential.

In the large γ (low density) limit (3.37) the energy per particle is identical to the case of free noninteracting fermions. This system of a 1d chain of strongly interacting bosons behaving like fermions is known as Tonks-Girardeau gas [300, 98].
In the opposite regime of weak interactions (small γ), the result (3.38) can be connected to the TF energy functional obtained from the mean-field approach discussed in section 3.1.2 [68]. However, even in the mean-field approach (including first order fluctuations) one does not find a true BEC in 1d, due to low-energy excitations being significantly occupied even at $T = 0$.

Absence of true BEC in 1d

Due to the exact solvability of the system, the absence of BEC in 1d can be proven rigorously for any interaction strength and density, as has been done by Mermin, Wagner, and Hohenberg [219, 143]. We focus here only on the case of weak interactions ($\gamma \ll 1$), where this proof can be obtained from the Bogoliubov mean-field approach discussed in the last section. A highly detailed derivation of this proof, which will be sketched in the following, can be found in [248].
We construct the Bogoliubov approximation here slightly differently compared to equation (3.11), by first writing the total field operators in a density-phase representation

$$\hat{\Psi}(\mathbf{r}) = \exp(i\hat{\phi})\sqrt{\hat{n}},\ \hat{\Psi}^\dagger(\mathbf{r}) = \sqrt{\hat{n}}\exp(-i\hat{\phi}). \tag{3.39}$$

The density and phase operators satisfy the commutation relation

$$\left[\hat{n}(\mathbf{r}), \hat{\phi}(\mathbf{r}')\right] = i\delta(\mathbf{r} - \mathbf{r}'). \tag{3.40}$$

Note, that this rewriting of the field operator is independent from any dimensional restrictions, and can be used to obtain the Bogoliubov spectrum in any dimension. The calculation is equivalent to the one presented in section 3.1.2. The density-phase representation is advantageous here, as it allows a clearer separation of density and phase fluctuations.
To calculate the low-energy excitation spectrum of the 1d system, we now use a Bogoliubov approximation of the field operators in 1d, namely by writing

$$\hat{n}(z) = n_0(z) + \delta\hat{n} \tag{3.41}$$
$$\hat{\phi}(z) = \hat{\phi}_s(z) + \hat{\phi}_p(z), \tag{3.42}$$

i.e. we assume the density to be described by (small) fluctuations around a mean field value and we separate the phase operator in two parts describing the phonon- and particle-like excitations, respectively.
Then, by looking at each contributing operator separately, one shows that only $\hat{\phi}_s$ results in low energy ($\epsilon < \mu$) excitations of the system. For the suppression of density modulations at low T a simple argument can be given: The (mean-field) repulsive interaction makes a uniform density distribution energetically favorable, hence the energetic cost of any deformation due to fluctuations is $\geq \mu$ [161]. Since we are interested only in the low temperature limit of the fluctuations, we rewrite the total field operator as

$$\hat{\Psi} = \sqrt{n_0}\exp(i\hat{\phi}_s). \tag{3.43}$$

To find out if BEC occurs, we consider the 1d reduced one-particle density matrix $\rho(z, z')$ (equation 3.6). In a uniform gas BEC is equivalent to long-range order in the system, which is present if $\rho(\mathbf{r}, \mathbf{r})' = \left\langle \hat{\Psi}(\mathbf{r})\hat{\Psi}(\mathbf{r}') \right\rangle$ remains finite for $|\mathbf{r} - \mathbf{r}'| \to \infty$ [244].
With (3.43) we get

$$\rho(z, z') = n_0 \left\langle e^{-i\left[\hat{\phi}_s(z) - \hat{\phi}_s(z')\right]} \right\rangle = n_o e^{-\frac{1}{2}\left\langle \left[\hat{\phi}_s(z) - \hat{\phi}_s(z')\right]^2 \right\rangle}. \tag{3.44}$$

The calculation of the phase correlator yields a sum of two terms

$$\left\langle \left[\hat{\phi}_s(z) - \hat{\phi}_s(0)\right]^2 \right\rangle \approx \frac{T}{\sqrt{\mu T_\mathrm{d}}} \frac{z}{\xi_\mathrm{h}} + \frac{1}{\pi}\sqrt{\frac{\mu}{T_\mathrm{d}}} \ln\left(\frac{z}{\xi_\mathrm{h}}\right), \tag{3.45}$$

where $\xi_\mathrm{h} = \frac{\hbar}{\sqrt{m n_{1\mathrm{d}} g_{1\mathrm{d}}}}$ is the healing length, and T_d is the degeneracy temperature, i.e. the temperature equal to N times the zero-point energy per particle (3.38). The first term on the right hand side of equation (3.45) corresponds to the (temperature-dependent) contribution of the thermal part of the phase fluctuations, while the second one results from the quantum depletion. Using this result in equation (3.44) gives an exponential decay of the density matrix at finite T due to the thermal fluctuations, while at $T = 0$ there is a power law decay due to the quantum fluctuations, preventing the formation of a true BEC even at zero temperature. This result is consistent with full calculations at $T = 0$ [121] and $T > 0$ [161].
While there is no true BEC due to the phase fluctuations at any temperature, the decay length of the density matrix can become large compared to the healing length for low T. At the same time, as argued above, density fluctuations no longer play a role. This situation was termed quasi-condensate by Popov [260], i.e. the system has the density distribution of a true condensate, but is only (approximately) phase-coherent over lengths determined by the decay length of the density matrix.

3.2.2 Interacting gas in a 1d harmonic trap

The addition of a (weak) confining potential allows one to speak of a trapped 1d gas, but also modifies the possible states of the the system. We consider a harmonic confinement with oscillator frequency ω_z, so that the total Hamiltonian of the system becomes

$$H_{1\mathrm{d}} = H^0_{1\mathrm{d}} + \sum_{j=1}^{N} \frac{m\omega_\mathrm{z}^2 z_i^2}{2}, \tag{3.46}$$

where $H^0_{1\mathrm{d}}$ is the Hamiltonian of the free 1d system (3.31). This system can no longer be solved exactly, but mean-field [251, 227] and beyond mean-field [68] approximations exist. The main change compared the free 1d system, is that in the trapped gas true BEC, i.e. BEC with phase-coherence over the total system length, can occur. This is due to the finite size of the system, which introduces a finite limit for the decay length of the phase fluctuations [251]. One then finds three possible quantum states of the system below the degeneracy temperature $T_\mathrm{d} = N\hbar\omega_\mathrm{z}/k_\mathrm{B}$, the Tonks gas, quasi BEC, and true BEC.
To characterize these states, it is convenient to define a second dimensionless parameter complementary to γ:

$$\alpha = \frac{m g_{1\mathrm{d}} a_\mathrm{z}}{\hbar^2}, \tag{3.47}$$

where $a_\mathrm{z} = \sqrt{\hbar/m\omega_\mathrm{z}}$ is the oscillator length of the confining potential. The parameter α provides a relation between the interaction strength and a characteristic system length introduced by the harmonic trap.

Tonks gas

The finite system size also affects the Tonks gas regime. To achieve $\gamma \gg 1$ in the trapped system, one must have $N < \alpha^2$, i.e. there is a maximum number of atoms for which the Tonks gas can be achieved. This is not surprising, since large γ is achieved in the case of low atomic density, which in a system with finite length directly turns into a restriction on the maximal atom number. Alternatively, γ can be increased for constant atom number by increasing the s-wave scattering

length with the help of a Feshbach resonance [80] or by increasing the effective mass of the particles by introducing a weak periodic modulation to the longitudinal confinement [241]
The chemical potential of a Tonks gas in a harmonic trap is $\mu = N\hbar\omega$ and the density profile is

$$n(z) = \left(\sqrt{2N}/\pi a_\mathrm{z}\right)\sqrt{1-(z/R)^2}, \tag{3.48}$$

with the size $R = \sqrt{2N}a_\mathrm{z}$ of the system [251, 68].

Quasi and true BEC

For weak interactions ($\gamma \ll 1$), similar to the free system, the density fluctuations of the trapped 1d gas are suppressed at sufficiently low temperature and the density distribution takes the shape of a true BEC. In the case of $\alpha \gg 1$, fulfilling the condition of weak interactions requires sufficiently large atom number $N > \alpha^2$. We then always have $\mu \gg \hbar\omega_\mathrm{z}$, and the TF approximation is applicable. The density then takes the form

$$n_0(z) = \frac{\mu}{g_\mathrm{1d}}\left(1 - \frac{z^2}{R_\mathrm{TF}^2}\right), \tag{3.49}$$

with the TF radius $R_\mathrm{TF} = (2\mu/m\omega_\mathrm{z}^2)^{1/2}$. The chemical potential is given by

$$\mu = \hbar\omega_\mathrm{z}(3N\alpha/4\sqrt{2})^{2/3}. \tag{3.50}$$

If $\alpha \ll 1$ one always has $\gamma \ll 1$. The TF approximation then is valid only if $N \ll \alpha^-1$. In the opposite limit the mean-field interaction is negligible and one obtains the Gaussian density profile of an ideal gas in the ground state of the harmonic potential. The situation can be generalized to arbitrary 1d confining potentials, which leads to a form of GPE for 1d [216].
The phase fluctuations can be calculated analogous to the free gas situation, by writing the field operator in the density-phase representation. In the Bogoliubov approximation one finds for the phase operator (only counting the phonon part) [286]

$$\hat{\phi}(z) = (4n_0(z))^{-1/2}\sum_{j=1}^{\infty}(f_j^+(z)\hat{a}_j + h.c.), \tag{3.51}$$

where $f_j^+ = u_j + v_j$ and u_j, v_j are the solutions of the Bogoliubov-de Gennes equations (3.17) and (3.18).
With this the mean square fluctuations of the phase correlation $\delta\hat{\phi}(z,z') = \hat{\phi}(z) - \hat{\phi}(z')$ can be explicitly evaluated as [251]

$$< \delta\hat{\phi}^2(z,z') >= \sum_{j=1}^{\infty}\frac{g_\mathrm{1d}(j+1/2)}{2\epsilon_j R_\mathrm{TF}}[P_j(x) - P_j(x')]^2(1+2N_j), \tag{3.52}$$

where P_j are Legendre polynomials, $x = z/R_\mathrm{TF}$, and $N_j = [\exp(\epsilon_j/T) - 1]^{-1}$ is the occupation number of the excitation with energy ϵ_j. For $T = 0$, the vacuum fluctuations have the form

$$< \delta\hat{\phi}^2(z,z') >_0 \approx (\gamma^{1/2}/\pi)ln(|z-z'|/\xi_\mathrm{h}). \tag{3.53}$$

Assuming an occupation $N_j = T/\epsilon_j$, the thermal phase fluctuations read

$$< \delta\hat{\phi}^2(z,z') >_T = \frac{4T\mu}{3T_\mathrm{d}\hbar\omega_\mathrm{z}}\left|\log\left[\frac{1-x'}{1+x'}\frac{1+x}{1-x}\right]\right|, \tag{3.54}$$

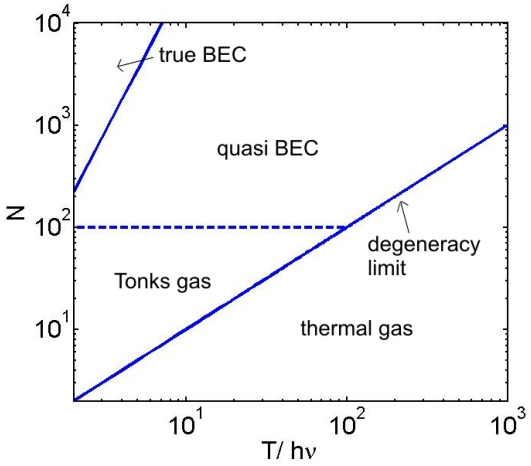

Figure 3.1: Diagram of states for a trapped 1d system with $\alpha = 10$. The degeneracy temperature T_d sets the border for the transition from thermal gas to quantum state. For sufficiently small densities ($N < \alpha^2$), this quantum state is the Tonks gas, while for larger atom numbers the weakly interacting regime is reached. The temperature T_ϕ determines the cross over from quasi to true BEC. Transitions over all of the shown border happen smoothly, there is no sharp phase transition between any of the states of a trapped 1d system.

which usually dominate over the vacuum fluctuations. For $x < 0.4$ the logarithm is of order unity. From this, a characteristic temperature

$$T_\phi = T_\mathrm{d}\hbar\omega_z/\mu \tag{3.55}$$

can be defined, at which $< \delta\hat{\phi}^2(z,z') > \approx 1$ on a length scale $|z-z'| \sim R_\mathrm{TF}$. Below this temperature the characteristic phase coherence length exceeds the size of the system, so that both the density and the phase properties of the system are those of a true BEC. Above T_ϕ, the phase coherence length is given by $R_\phi \approx R_\mathrm{TF}(T_\phi/T) < R_\mathrm{RF}$, so that for $T_\phi \ll T \ll T_\mathrm{d}$ one has a quasi-condensate, which has the same density distribution as a true BEC. Correlation properties at distances smaller than R_ϕ are also the same. However, the phase fluctuations lead to a drastic difference in the phase coherence properties, as will be studied in the experiments described in this manuscript.

Cross over between different phases

In figure 3.1 the regimes discussed above are summarized in the $T-N$ diagram of states for a 1d trapped gas with $\alpha = 10$. For fixed confinement and scattering length, the reachable regimes depend solely on the number of atoms N. The Tonks gas can only be realized for sufficiently low atomic densities. On the other hand, the temperature T_ϕ increases with N, reaching a true, fully phase coherent BEC, becomes easier in the regime of weak interactions, i.e. large atomic densities. It is important to note that all of the transitions between different regimes, from classical gas to quantum, and between different quantum states are smooth. For example, for $N \ll \alpha^2$, the system will continuously change from thermal gas to quasi BEC to true BEC, with no sudden onset of condensation as is present in 3d. The sudden onset of a macroscopic population of the ground state, as discussed in [305], only occurs for a gas with vanishing interactions. Unlike in the 3d case, the critical temperate $T_\mathrm{c}^\mathrm{ideal} = N\hbar\omega_\mathrm{z}/\ln 2N$, at which this transition occurs in the ideal gas, is not a very useful approximation for the onset temperature for a 1d quasi-condensation.

3.2.3 Experimental realization of 1d systems

The actual implementation of 1d systems in cold gases is achieved by using highly anisotropic 3d (harmonic) traps $\omega_\mathrm{z} \ll \omega_\mathrm{x}, \omega_\mathrm{y}$. Most of the times, these traps have cylindrical symmetry in which case $\omega_\mathrm{x} = \omega_\mathrm{y} = \omega_\perp$. If now the chemical potential and the temperature of the system become smaller than the transverse single particle ground state energy $\mu, T \leq \hbar\omega_\perp$, the radial motion of the atoms is "frozen" and governed by the single-particle ground state wave function of the transverse harmonic potential.
Spatially the system still has a finite radial extension, given by the ground state size $a_\perp = \sqrt{\hbar/m\omega_\perp}$.

If this size is much larger than the characteristic length scale of the interatomic potential, the interactions retain a 3d character and are characterized by the 3d scattering length a_s. One can obtain an effective 1d coupling constant [239]

$$g_\mathrm{1d} = \frac{2\hbar^2 a_s}{m a_\perp^2} \tag{3.56}$$

by averaging the 3d interaction over the radial density profile. Similarly, the effective 1d scattering length is given by $a_\mathrm{1d} = a_\perp^2/a_\mathrm{s}$. Such a quasi 1d system has the same statistical properties as a true 1d gas with a 1d contact potential and coupling constant as given above. Its important to note that the transverse confinement still plays a role, as it enters g_1d.
The condition $\mu \approx \hbar\omega_\perp$ for the crossover into the effective 1d regime sets a maximum on the number of particles in a given system

$$N_\mathrm{1d} = \sqrt{\frac{32\hbar}{225 m a_\mathrm{s}^2}}\sqrt{\frac{\omega_\perp}{\omega_\mathrm{z}}}. \tag{3.57}$$

Rewriting this limitation for the linear 1d density yields $n1\mathrm{D} \approx 1/a_\mathrm{s}$, implying that the linear density of a 1D condensate is limited to (approximately) one atom per scattering length independent of the radial confinement. For Rb^{87}, this gives an estimate that the 1d regime is reached when $n_\mathrm{1d} \sim 100$ atoms/μm.

Experiments

Bose gases in 1d have been studied in various groups in the last years. The first realization of $\mu \approx \hbar\omega_\perp$ in a macroscopic magnetic trap is reported in [100], where the cross over to 1d was detected by observing the change of the aspect ratio of the BEC compared to the 3d case. A similar experiment is presented in [280].
The phase fluctuations of a 1d quasi BEC were first observed by Dettmer et al by studying their conversion into density modulations during free expansion of the released quasi BEC [65, 132]. Other techniques employed for investigating the phase fluctuations are condensate focussing [290] and Bragg spectroscopy [268, 95, 146].
More recently, highly elongated atom chip traps have been used to study the density fluctuations present at sufficiently large temperature [75]. Also, deviations from the mean-field predictions for the density profile near the 3d-1d crossover have been observed [301]. In our experiment, the expansion of a quasi BEC in the 1d regime was investigated [316].
A different class of experiments is formed by realizations of 1d systems in 2d optical lattices, first reported in [103] and [100]. In these setups, a large number (usually a few 1000) of 1d systems are realized simultaneously, which allows measurements with a much higher number of involved atoms with respect to a single confining potential. This in turn facilitates much smaller 1d densities in each individual 1d tube, opening the access to the strongly interacting ($\gamma > 1$) regime. In [298], the reduction of losses due to three-body collisions for $\gamma = 0.5$ is reported. The changes in the excitation spectrum between thermal and quantum gas at $\gamma \approx 1$ is investigated in [228]. A first observation of a Tonks gas with $\gamma = 5.5$ is reported in [168], a further increase of γ is achieved by tuning the effective mass of the atoms in an anisotropic 3d lattice [241]. A similar system has been used to observe the superfluid to Mott-insulator transition in 1d [294, 170].
While the optical lattice systems offer the advantage of easy detection, the averaging over many realizations of the same system also results in a loss of information, for example of the phase fluctuations in each individual 1d tube. Here, atom chips, combined with single or few atom detection capability, offer an advantage, as discussed for example in [**?**].

Cross-over from 3d to 1d

Similar to the transitions between different quantum regimes in true 1d, the cross over from 3d to effective 1d turns out to also be very smooth. For example, the phase fluctuations characteristic for systems with reduced dimensionality already appear in very elongated 3d traps [252, 65], even when $\mu, T > \hbar\omega_\perp$.
A mean-field theory based on a local density approximation (LDA) for the cross over regime, smoothly connecting the 3d (valid if $\mu \gg \hbar\omega_\perp$) and 1d TF regime ($\mu \ll \hbar\omega_\perp$), was developed by F. Gerbier [94]. He defines another dimensionless parameter

$$\chi = N a_\mathrm{s} \frac{a_\perp}{a_\mathrm{z}^2}, \tag{3.58}$$

which roughly gives the ratio of the interaction energy to the radial zero-point energy and derives a closed equation

$$\kappa^3(\kappa+5)^2 = (15\chi)^2 \tag{3.59}$$

for the key quantity κ, which can be easily solved numerically. The static properties of the BEC can be expressed as functions of κ at any confinement strength. In the limit $\chi \ll 5$, the mean-field interaction dominates over the transverse confinement, and one recovers 3d TF result, $\kappa \approx \kappa_{3\mathrm{d}} = (15\chi)^{2/5}$. Conversely, if $\chi \ll 5$, the transverse motion is frozen and one finds $\kappa \approx \kappa_{1\mathrm{d}} = (3\chi)^{2/3}$. The crossover between the two regimes occurs approximately for $\kappa_{1\mathrm{d}} = \kappa_{3\mathrm{d}}$, giving a crossover value $\chi_\mathrm{cross} = 5^{3/2}/3 \approx 3.73$.
The chemical potential as function of κ reads

$$\mu = \left(\frac{\kappa}{2} + 1\right) \hbar\omega_\perp, \tag{3.60}$$

while the axial TF radius of the cloud is given by

$$R_\mathrm{TF} = \frac{a_\mathrm{z}^2}{a_\perp}\sqrt{\kappa}. \tag{3.61}$$

The peak density at the trap center is

$$n_0 = \frac{\kappa}{4a_\mathrm{s}}(\kappa+4). \tag{3.62}$$

Finally, the phase coherence temperature reads

$$T_\phi = \frac{\hbar^2}{m k_\mathrm{B}} \frac{n_0}{R_\mathrm{TF}}. \tag{3.63}$$

Since this theory includes both the true 3d and 1d limits, in principle it can be used for all experiments in the weak interactions regime in highly elongated traps. We have used it to study the surface roughness induced potential corrugation in our atom chip traps [318, 317] and the transverse width of an expanding quasi BEC [316]. In practise, we use the true 1d formulas if they are applicable ($\chi \ll 5$), and this approach only in the cross over region.

3.2.4 Luttinger liquid theory

Above, the fluctuations in 1d systems were discussed using the Bogoliubov-Popov approximation presented in section 3.1.2. This theory framework has become the "natural" approach in the cold atoms community, based on its extreme success mainly in describing 3d BECs and their excitations [242, 52, 37, 181]. Also in the weakly interacting regime in 1d systems, it reproduces the exact results with good accuracy in the low temperature limit [251], as discussed above. This has resulted

in the fact that so far all (quasi)-1d experiments with cold atoms have been treated within this model.
An alternative approximative method in 1d is the harmonic-fluid approach. This theory has a long history in the context of 1d fermion systems [299, 214]. In 1981, Haldane realized that this theory can be generalized to a unified treatment of bosons and fermions in 1d [121]. He termed the universality class of systems, for which this generalization holds, as "Luttinger liquids" (LL). The name stems from an analogy with higher dimensional fermionic systems, where the equivalent role is played by the (universality class of) Fermi liquids [207]. This model has found wide-spread application in (mainly fermionic) systems in condensed-matter physics, such as quantum wires, magnetic chain compounds, edge states in the quantum Hall effect, or 1d organic metals (for a review see [38]).
The applicability of the LL theory to effective 1d systems of cold (bosonic) atoms has been suggested as early as 1998 [226], and is discussed in detail in [38]. The LL theory provides a consistent framework for treating strongly and weakly interacting systems bosons and fermions. The Bogoliubov-Popov results in the weakly interacting limit for bosonic systems can be fully recovered and understood within the harmonic-fluid approach. The LL approach is not a mean field theory, and therefore does not break any symmetry. Also, it allows in principle the treatment of more complex atomic interactions than the delta-contact potential. On the other hand, from the condensed-matter physics point of view, cold 1d bosonic gases provide a much cleaner testing ground for the LL concept than most solid state systems [226].
In particular, the LL approach has recently been used in theoretical treatments of situations directly related to the experiments described in this thesis [259, 107, 147, 31, 108, 109]. These specific applications will be discussed in sections 3.4 and 3.5. In the following, a brief summary of the basic concepts of LL theory will be given.

Harmonic fluid approach

The main idea of the LL approach is to transform the 1d system of real particles to a set of 1d harmonic oscillators, whose quanta are understood as phonons corresponding to low-energy phase and density fluctuations of the system [121].
To achieve this, two new operators $\hat{\Pi}$ and $\hat{\Theta}$ are introduced which are defined by the relations

$$\hat{n}_s = n_0 + \hat{\Pi}(z) = \frac{1}{\pi}\frac{\partial}{\partial z}\hat{\Theta}(z), \tag{3.64}$$

where $\hat{n}_s$ is defined by splitting $\hat{n} = \hat{n}_s + \hat{n}_f$ the total density operator into slow ($\omega < \omega_{\text{cut}}$) and and fast ($\omega > \omega_{\text{cut}}$) frequency parts, where $\hbar\omega_{\text{cut}} \sim \mu$ is a (arbitrary) cutoff energy restricting the theory to the low energy limit.
With $\hat{\Pi}$ and $\hat{\Theta}$ the total bosonic field operator can be rewritten as

$$\hat{\Psi}^\dagger(z) \sim [n_0 + \hat{\Pi}(z)]^{1/2} \sum_{m=-\infty}^{+\infty} e^{2mi\hat{\Theta}(z)} e^{-i\hat{\phi}}(z), \tag{3.65}$$

i.e. $\hat{\Pi}$ and $\hat{\Theta}$ describe the density and phase fluctuations of the system, respectively. The symbol $\sim$ means that the field operator is given by the expression on the right up to a prefactor. This prefactor depends on the explicit choice for ω_{cut}.
To obtain the low-energy effective Hamiltonian one inserts the field operator (3.65) into the many-body Hamiltonian (3.4) and keeps only the leading terms, which are quadratic in the gradients of the slowly varying fields $\hat{\Theta}(z)$ and $\hat{\phi}(z)$. Neglecting the (usually weak) longitudinal confinement

leads to [2]

$$\hat{H}_{\text{eff}} = \frac{v_s}{2} \int dz \left[\frac{\pi}{K} \hat{\Pi}^2(z) + \frac{K}{\pi} \left(\frac{\partial}{\partial z} \hat{\phi}(z) \right)^2 \right]. \tag{3.66}$$

Here, all details about the interaction potential are contained in the constants v_s and K, which are known as the "sound velocity" and the "Luttinger parameter", respectively. Consequently, This is one of the main reasons for the versatility of the LL approach, as it describes different physical systems with a unified effective Hamiltonian. v_s and K can usually be calculated numerically, or if possible analytically. If that fails, they can be extracted phenomenologically from experiments.

Cold bosonic gas as Luttinger liquid

In the case of atoms interacting with a delta contact potential (equation 3.8), K and v_s can be calculated analytically for in the weak and strong interaction limits.
For $\gamma \ll 1$ one finds up to second order [38]:

$$v_s = v_F \frac{\sqrt{\gamma}}{\pi} \left(1 - \frac{\sqrt{\gamma}}{2\pi} \right)^{1/2}, \; K = \frac{\pi}{\gamma} \left(1 - \frac{\sqrt{\gamma}}{2\pi} \right)^{-1/2}, \tag{3.67}$$

while for $\gamma \gg 1$

$$v_s = v_F \left(1 - \frac{4}{\gamma} \right), \; K = 1 + \frac{4}{\gamma}. \tag{3.68}$$

Here, $v_F = \hbar \pi n_0 / m$ is the Fermi velocity.
The LL approach is valid only down to finite length scales, due to the high energy cutoff. For the cold atomic gas, the lower length limit for its applicability is given by the healing length $\xi_h \sim 1/n_0\sqrt{\gamma}$ (for $\gamma \gg 1$).

Correlation functions

The Hamiltonian (3.66) can be solved analytically, as it describes nothing but a set of 1d harmonic oscillators. From this, one obtains the mode functions and the eigenenergies of the low energy excitations of the system.
In particular, one can calculate the long-distance off diagonal correlations in the 1d system. For zero temperature, the result is [121]

$$\left\langle \hat{\Psi}^\dagger(z) \hat{\Psi}(0) \right\rangle \sim n_0 \left(\frac{\xi_h}{z} \right)^{1/2K}. \tag{3.69}$$

At finite temperature T, one obtains [38]

$$\left\langle \hat{\Psi}^\dagger(z) \hat{\Psi}(0) \right\rangle_T \sim n_0 \xi_h^{1/2K} \left(\frac{\pi/\xi_T}{\sinh(\pi z/\xi_T)} \right)^{1/2K}, \tag{3.70}$$

where the thermal length ξ_T is given by

$$\xi_T = \frac{\hbar^2}{m \xi_h k_{\text{B}} T} = \frac{\hbar v_s}{k_{\text{B}} T}. \tag{3.71}$$

Equation (3.70) is valid for sufficiently low T so that $\xi_T \gg \xi_h$, or equivalently $T \ll \hbar^2 / k_{\text{B}} m \xi_h^2$. For $z \ll \xi_T$ (3.70) reduces to the zero temperature result (3.69). In the opposite limit $z \gg \xi_T$ the correlation function (3.70) may be approximated as

$$\left\langle \hat{\Psi}^\dagger(z) \hat{\Psi}(0) \right\rangle_T \sim n_0 \left(\frac{\xi_h}{\xi_T} \right)^{1/2K} e^{-\pi z / 2K \xi_T}. \tag{3.72}$$

[2] An extension to the case of an arbitrary trapping potential can be found in [38]

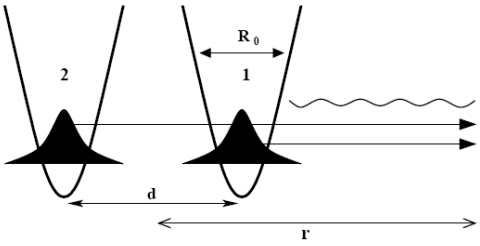

Figure 3.2: Schematic view of the interference experiment for two independent, single mode BEC. Originally the two ensembles of width R_0 are held in two potential mininma separated by a distance d. After the trapping potential is switched off, the BECs expand ballistically and travel a distance r before they overlap and create an interference pattern in the time-of-flight density distribution. Figure taken from [148].

These results reproduce the correlations obtained from the Bogoliubov approach (equation 3.45) and are in agreement with the full calculation [161]. The LL framework is appealing because it reduces the situation to the problem of a set of (coupled) harmonic oscillators, which can be analytically [38]. Many of these existing results can be directly transferred to the case of 1d quasi BECs in atomic gases [226].

3.3 Coherence of two BEC

The macroscopic phase coherence of (3d) BECs was demonstrated by showing interference between atoms coupled out from a single BEC, an idea termed atom-laser [221, 22]. Furthermore, Andrews et al showed that two independent BECs interfere if they overlap [10]. Similar experiments have also been performed with multiple BECs released from optical lattices [104, 120]. These experiments touch on a question raised by P. W. Anderson [6]: Do two superfluids that have never "seen" one another possess a definite relative phase? The interference of two independent BEC will be discussed from a mean-field point of view and in the second quantization formalism in section 3.3.1. A different situation, which will be discussed in section 3.3.2, arises when one considers two BECs produced by coherently splitting a single original condensate. This is done by transforming an initial single minimum trapping into a double well configuration. This system can be viewed as a "matter wave beam splitter", in analogy to photon optics. But in the case of matter waves, the nonlinear atomic interactions play an important role in the evolution of the system, and result in an effect called phase diffusion [6]. This sets fundamental limits on the phase coherence of the coherently split BECs.

3.3.1 Interference of two independent BEC

Figure 3.2 shows the typical setup for an interference experiment of two independent BECs. Two (3d) condensates are held in separated confining potentials, which are then switched off and the BECs expand freely. Once the two clouds overlap, an interference pattern is observed.

Mean-field picture

We consider the situation in the mean-field picture. We describe the two BECs as independent solutions of the GPE for the two trapping potentials

$$\Psi_{1,2}(\mathbf{r}, t = 0) = \phi_{1,2}(\mathbf{r})e^{-i\varphi_{1,2}}. \tag{3.73}$$

In particular, we assume that both wave functions are characterized by single phases $\varphi_{1,2}$. The initial overlap of the two BEC is assumed to be negligible

$$\int d\mathbf{r}\phi_1^*(\mathbf{r})\phi_2(\mathbf{r}) \approx 0. \tag{3.74}$$

The expectation value of the total density after time t reads

$$\langle\rho(\mathbf{r},t)\rangle = |\phi_1(\mathbf{r},t)|^2 + |\phi_2(\mathbf{r},t)|^2 + 2\mathrm{Re}[\mathrm{e}^{\mathrm{i}\triangle\varphi}\phi_1(\mathbf{r},\mathrm{t})\phi_2^*(\mathbf{r},\mathrm{t})], \tag{3.75}$$

where $\triangle\varphi = \varphi_1 - \varphi_2$. The interference pattern is caused by the last term of equation (3.75). As an example, we consider two wave packets initially in Gaussian states centered at points $\pm\mathbf{d}/2$, with initial width $R_0 \ll d$. Then, neglecting any atomic interaction during the expansion, the wave functions at time t can be calculated as

$$\Psi_{1,2}(\mathbf{r},t) = \frac{1}{(\pi R_t^2)^{3/4}} e^{-\frac{(\mathbf{r}\pm\mathbf{d}/2)^2(1+i\hbar t/mR_0^2)}{2R_t^2}}, \tag{3.76}$$

where the width R_t is given by

$$R_t^2 = R_0^2 + \left(\frac{\hbar t}{mR_0}\right). \tag{3.77}$$

Evaluating the last term in (3.75) in the region where the two wave packets overlap yields

$$\mathrm{Re}[\mathrm{e}^{\mathrm{i}\triangle\varphi}\phi_1(\mathbf{r},\mathrm{t})\phi_2^*(\mathbf{r},\mathrm{t})] \propto \cos\left(\frac{\hbar}{\mathrm{m}}\frac{\mathbf{rd}}{\mathrm{R_0^2 R_t^2}}\mathrm{t} + \triangle\varphi\right). \tag{3.78}$$

For sufficiently large t, one can approximate $R_t \approx \hbar t/mR_0$, and obtain oscillations in the density at wave vector $\mathbf{Q} = m\mathbf{d}/\hbar t$, with the positions of the minima and maxima determined by the relative phase $\triangle\varphi$.
This result describes the fringe spacing observed in experiments reasonably well (deviations can be understood by considering the atomic interaction during expansion [284]), but the mean-field theory cannot make a prediction for the relative phase $\triangle\varphi$. Indeed, the whole appearance of interference is based on the ab initio assigning of global phases $\varphi_{1,2}$ to the BEC wave functions. The existence of such a well-defined phase is often explained by assuming a spontaneous symmetry breaking [82, 238] at the moment of condensation. Of all (equally) possible phases the BEC spontaneously "picks" a single one when it forms. This explanation also agrees with the experimental observation that the relative phase $\triangle\varphi$ varies randomly from shot to shot [10]. But the concept of spontaneous symmetry breaking has some fundamental problems in the context of BEC [235] and can be avoided by considering the interference process in second quantization, as we will do in the following.

Second quantization approach

To describe the two initial BECs in second quantization, one defines the creation operators

$$\hat{a}_{1,2}^\dagger = \int \phi_{1,2}(\mathbf{r})\hat{\Psi}^\dagger(\mathbf{r}), \tag{3.79}$$

which create particles in the modes $\phi_{1,2}$ (we again assume that each BEC can be described by a single mode). The bosonic field operator satisfies the usual boson commutation relations

$$\left[\hat{\Psi}(\mathbf{r}'),\hat{\Psi}^\dagger(\mathbf{r})\right] = \delta(\mathbf{r}-\mathbf{r}'),\ \left[\hat{\Psi}(\mathbf{r}'),\hat{\Psi}(\mathbf{r})\right] = \left[\hat{\Psi}^\dagger(\mathbf{r}'),\hat{\Psi}^\dagger(\mathbf{r})\right] = 0, \tag{3.80}$$

and can be written in a density-phase representation

$$\hat{\Psi}^\dagger(\mathbf{r}) = \sqrt{\hat{n}}\exp(-i\hat{\phi}). \tag{3.81}$$

From the commutation rules (3.80) it follows that

$$\left[\hat{n}(\mathbf{r}),\hat{\phi}(\mathbf{r}')\right] = i\delta(\mathbf{r}-\mathbf{r}'), \tag{3.82}$$

implying that an uncertainty relation between the particle number and the phase of a BEC exists.

Number states

We now consider a state

$$|N_1, N_2\rangle = \frac{1}{\sqrt{N_1! N_2!}} (a_1^\dagger)^{N_1} (a_2^\dagger)^{N_2} |0>, \tag{3.83}$$

where the creation operators act N_1 and N_2 times on the vacuum state $|0>$. In such a number state, the particle numbers N_1 and N_2 in each of the two modes is precisely determined. Consequently, the relative phase between the two modes is not well-defined [285].
Neglecting any interaction between the modes, during the free expansion of the BECs the occupation numbers of the two modes do not change, only the envelopes $\phi_{1,2}(\mathbf{r}, t)$ evolve. Consequently, the time evolution of the initial state is completely described by the time dependence of the mode functions $\phi_{1,2}(\mathbf{r}, t)$. Hence, the field operator at time t is obtained, by simply replacing the initial envelopes $\phi_{1,2}(\mathbf{r})$ with $\phi_{1,2}(\mathbf{r}, t)$ in the definition of the creation operators (3.79).
Using the Gaussian wave packets (3.76) and neglecting any atom-atom interactions in the expansion, one gets

$$\phi_{1,2}(\mathbf{r}, t) = u_{1,2}(\mathbf{r}, t) e^{i\mathbf{Q}_{1,2}\mathbf{r}}, \tag{3.84}$$

where $\mathbf{Q}_{1,2} = m(\mathbf{r} \pm \mathbf{d}/2)/\hbar t$, and $u_{1,2}$ are slowly varying real function, which determine the overall density profiles. After sufficiently long expansion time ($R_t \gg d$), the clouds overlap strongly, and we have

$$\int d\mathbf{r} u_1(\mathbf{r}, t) u_2(\mathbf{r}, t) \approx 1, \tag{3.85}$$

i.e. the envelopes of the two wave packets are approximately the same.
What we are interested in, is the amplitude of density oscillations at wave vector $\mathbf{Q} = \mathbf{Q}_1 - \mathbf{Q}_2$. The corresponding operator for this observable is

$$\hat{\rho_Q} = \int d\mathbf{r} \hat{\Psi}^\dagger(\mathbf{r}) \hat{\Psi}(\mathbf{r}) e^{i\mathbf{Q}\mathbf{r}}, \tag{3.86}$$

which is nothing but the Fourier component of the field operator at wave vector $\mathbf{Q}$. The expectation value of this operator for the number state (3.83) is given by

$$\langle N_1, N_2 | \hat{\rho_Q} | N_1, N_2 \rangle = \langle N_1, N_2 | \int d\mathbf{r} \hat{\Psi}^\dagger(\mathbf{r}) \hat{\Psi}(\mathbf{r}) e^{i\mathbf{Q}\mathbf{r}} | N_1, N_2 \rangle . \tag{3.87}$$

The integral over $d\mathbf{r}$ can be performed by using the normalization (3.85) and assuming that the envelopes $u_{1,2}$ vary on scales much larger than the fringe spacing $1/Q$. The Fourier part of the integral removes all contributions with wave vectors other than $\mathbf{Q}$. As final result one finds

$$\langle N_1, N_2 | \hat{\rho_Q} | N_1, N_2 \rangle = \langle N_1, N_2 | a_1^\dagger a_2 | N_1, N_2 \rangle = 0, \tag{3.88}$$

as different number states are orthogonal. This vanishing expectation value seems to suggest that there is no interference for number states. According to the usual interpretation of expectation values in quantum mechanics, $\langle \hat{\rho_Q} \rangle$ gives only the statistical average over many experiments. Indeed, in each particular experiment run, the complex number ρ_Q can have nonzero value. To show this, one has to consider the variance $\langle |\hat{\rho_Q}|^2 \rangle$, which is the density-density correlation function at wave vector $\mathbf{Q}$. This yields

$$\langle |\hat{\rho_Q}|^2 \rangle = \langle N_1, N_2 | a_1^\dagger a_2^\dagger a_1 a_2 + a_1^\dagger a_1 a_2^\dagger a_2 | N_1, N_2 \rangle = N_1 N_2 + N_1 + N_2, \tag{3.89}$$

i.e. there is a density-density correlation of order $N = N_1 + N_2$ at wave vector $\mathbf{Q}$. For higher moments $\langle |\hat{\rho_Q}|^{2n} \rangle$ one finds in the limit of large N_1, N_2

$$< |\hat{\rho_Q}|^{2n} >= (N_1 N_2)^n \left(1 + \mathcal{O}\left(\frac{1}{N_1}\right) + \mathcal{O}\left(\frac{1}{N_2}\right) \right). \tag{3.90}$$

The leading term implies that for large N_1, N_2 the distribution function $|\hat{\rho_Q}|^2$ is strongly peaked at $N_1 N_2$, which in turn means that in each individual experiment there is a high visibility fringe pattern at wave vector **Q**. By showing that any operator of the form $\hat{\rho_Q}^n \hat{\rho_{-Q}}^m$ vanishes for $m \neq n$, one shows that the phases of these patterns are uniformly distributed between 0 and 2π [285]. This uniform distribution is the reason why the expectation value $\langle \hat{\rho_Q} \rangle$ vanishes. In the average over randomly shifted interference patterns, each with high visibility, the modulations cancel out and one obtains a flat profile.
A famous example from astronomy where higher order correlations are used is the Hanbury Brown and Twiss experiment, where second order correlations in signals from two incoherent stellar sources are investigated [28, 29]. Similar experiments have also recently been performed to measure correlations in cold bosonic [273] and fermionic [78] gases.

Phase states

A better physical understanding of the situation can be obtained by introducing another set of many-body states, the so-called phase states [285]

$$|\varphi, N\rangle = \frac{1}{(2^N N!)^{1/2}} (a_1^\dagger e^{i\varphi/2} + a_2^\dagger e^{-i\varphi/2})^N |0\rangle . \tag{3.91}$$

These states have a fixed relative φ between the two modes, consequently the particle numbers N_1 and N_2 are not specified (the total number N is, which is not a contradiction to a well defined *relative* phase). Following the same procedure as for the number state leads to

$$\langle \hat{\rho_Q} \rangle = \langle \varphi, N | \, a_1^\dagger a_2 \, | \varphi, N \rangle = \frac{N}{2} e^{-i\varphi}, \tag{3.92}$$

i.e. one finds interference with a fixed phase φ in each single shot.
The phase states form an (overcomplete) basis set of the many-particle Hilbert space, hence any number state can be written as a superposition of phase states. For example,

$$|N/2, N/2> = \left(\frac{\pi N}{2}\right)^{1/4} \int_0^{2\pi} \frac{d\varphi}{2\pi} |\varphi, N> . \tag{3.93}$$

In the limit of large N the phase states are almost orthogonal. One can then see the measurement of the atomic density distribution as a projection onto a (random) phase state. Hence, in this picture, the random relative phase between two interfering independent BECs is considered to be measurement induced, which removes the necessity of assuming an a priori phase symmetry breaking. [153, 36]
So far the atomic interaction has been neglected completely in this discussion. Recently, new approaches to the treatment of interfering independent BECs have been developed which include this effect [324, 39]. Indeed, these calculations suggest that the observed interference is due to interaction-induced coherence developing during the overlap of the condensates.

3.3.2 Coherent splitting of a BEC

In the last section, phase states were introduced as a tool for explaining the interference of number states. The question arises if one can prepare a system of two BECs in such a phase state, so that they show a fixed relative phase in every single shot interference experiment. The idea to achieve this is to "split" a single BEC in a phase preserving way, in analogy to a beam splitter in optics.
For this we consider a trapping potential dynamically changing from a single minimum to a double well configuration, which separates a single initial condensate into two parts. In the initial system the BEC occupies the single ground state of the single well, while the final system has two (near)

degenerate ground states, one corresponding to each of the two wells. During the deformation the initially well separated ground and first exited state of the single well approach each other until they become degenerate for large splitting. For finite splitting time this process cannot be adiabatic. This makes the treatment of the splitting process somewhat involved and has led to some controversy how it is best described [152, 183, 154].
There is general agreement though on the outcome of the splitting process, which is discussed in most detail both for ideal and interacting atoms in [152]: The division of a single BEC into two parts prepares a phase coherent state, which upon interference will always result in the same relative phase. This result does not require the broken phase symmetry discussed above, i.e. it does not rely on the initial BEC having a global phase. The splitting process itself introduces a fixed relative phase between the two parts of the system.

Phase diffusion

In the case of interacting particles, the coherently split state shows an effect called phase diffusion [6, 182]. The relative phase and relative particle number are conjugate operators (equation 3.82). In the case of coherent splitting, the relative phase is initialized with a narrow distribution, consequently there is an uncertainty in the atom number in each well. The width of the phase distribution expands ballistically under the influence of the interaction term, if the system is left alone after the splitting. As a consequence, for increasing wait time after the splitting, the shot to shot fluctuations of the observed relative phase will increase linearly. One can define a phase diffusion time T_{D} after which the width of the observed width of the phase distribution becomes of the order unity and cannot be distinguished from the uniformly distributed phase of a number state anymore [197]:

$$T_{\mathrm{D}} = \frac{\hbar}{\triangle N \left(\frac{\partial \mu}{\partial N}\right)}. \tag{3.94}$$

Here, $\triangle N$ is the uncertainty in the relative particle number. Assuming the Poissonian width of a coherent state $\triangle N = \sqrt{N}$ and using the TF approximation for the (3d) BECs yields [322, 152]

$$T_{\mathrm{D}} = \frac{5\hbar\sqrt{N}}{2\mu} = \frac{5}{15^{2/5}} \left(\frac{\hbar}{m a_{\mathrm{s}}^2}\right)^{1/5} \frac{N_0^{1/10}}{\omega_{\mathrm{ho}}^{6/5}}, \tag{3.95}$$

where equation (3.29) was used for μ to obtain the second equality. It can be seen that T_{D} depends on the number of atoms N_0 only extremely weakly. Hence, the diffusion time is mostly determined by the trapping frequencies of the confining potential. Tight confinement, as provided by atom chip magnetic traps, reduces the diffusion time. For typical values $N_0 = 10^4$ and $\omega_{\mathrm{ho}} = 2\pi \times 500$ Hz, we have $T_{\mathrm{D}} = 10$ ms.

Dynamic splitting of a BEC

This model turns out to be too simple to describe the phase diffusion of a dynamically split state. The initial phase and number uncertainties of the prepared phase coherent state depend strongly on the details of the splitting process. In general, sufficiently strong coupling during this process is expected to significantly reduce the number fluctuations [183].
We consider a simple model of the splitting process, where the potential barrier is raised over a characteristic time t_s. We neglect any coupling of the internal dynamics (distribution of the particles between the two modes) and the external dynamics (evolution of spatial wave function of the modes), which is reasonable when the raising time of the potential barrier t_s is large compared to $t_{\mathrm{trap}} = 1/\nu_{\mathrm{trap}}$, where ν_{trap} is the trapping frequency in the splitting direction [217]. One then considers the splitting as a two stage process [183, 154]. Initially, the tunnel coupling through the

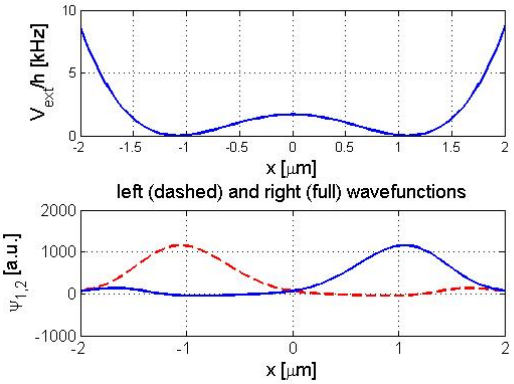

Figure 3.3: Example numerical calculation of the wavefunctions $\psi_{1,2}(\mathbf{r})$. For a given double potential, shown in **(a)**, the first symmetric and antisymmetric GPE solutions are obtained using the split-operator method presented in section 3.1.3. **(b)** Wave functions (mainly) concentrated in the left and right well are constructed by linear combination of the GPE solutions, which are then used for the calculation of E_{C} and E_{J}.

potential barrier is large and the splitting is approximately adiabatic. The system then remains in the ground state of the coupled double well system. During this stage the system can be described by a Josephson Hamiltonian with a time dependent tunneling term

$$H = \frac{E_{\mathrm{C}}}{2} N_r^2 - E_{\mathrm{J}}(t)\cos(\varphi) \approx \frac{E_{\mathrm{C}}}{2} N_r^2 - \frac{E_{\mathrm{J}}(t)}{2}\varphi^2, \tag{3.96}$$

where $N_r = N_1 - N_2$ is the relative atom number in the two wells, which is a conjugate variable to the relative phase $[\varphi, N_r] = i\hbar$. $E_c = d\mu/dN$ is the charging energy due to interactions in each well, and $E_{\mathrm{J}}(t)$ is the time-dependent tunneling energy, which decreases with the raising of the potential barrier. E_{J} can for example be numerically calculated from the overlap of the two mean-field wave packets [291, 263].
The cosine in equation (3.96) can be expanded if E_{J} is not too small, in which case one finds the Hamiltonian of a harmonic oscillator with a characteristic Josephson frequency $\hbar\omega_j = \sqrt{E_{\mathrm{J}} E_{\mathrm{C}}}$. This description holds as long as $\omega_j(t) > 1/t_{\mathrm{s}}$. Once this condition fails, the splitting is no longer adiabatic. The second stage of the process is then approximated as instantaneous [183]. This is equivalent to saying that the final state of the fully split system with $E_{\mathrm{J}} = 0$ is approximated by the ground state of equation (3.96) at the moment t_{ad}, when the adiabaticity condition fails $\omega_j(t_{\mathrm{ad}}) = 1/t_s$. Then one obtains for the fluctuations of the relative atom number $\triangle N_r \sim \sqrt{hN/\mu t_s}$ [183, 31]. The reduction of number fluctuations compared to the square root fluctuations of a coherent state can be expressed in terms of a "squeezing" factor $\xi = \sqrt{N}/\triangle N_r > 1$. Recent observations of phase coherence times at least 10 times longer than predicted by (3.95) [156] seem to be in reasonable agreement with this calculation.

Quantum phase model

It is important to note that phase diffusion is a quantum effect, which is not described in the mean-field picture. The two models discussed above, heuristically add the effect to the classic description. Consequently, for a more accurate discussion of the atom number squeezing during the splitting and the phase diffusion process after the separation, one has to turn to a quantum version of the two modes model [257]. For this we rewrite the two mode model in the second quantization formalism, as we did in section 3.3.1 for the discussion of the interference process.
We again consider a two mode field operator

$$\hat{\Psi}(r,t) = \psi_1(r,t)\hat{a}_1 + \psi_2(r,t)\hat{a}_2, \tag{3.97}$$

where $\psi_{1,2}$ are the time dependent wave function corresponding to the two modes. Inserting this into the second-quantization Hamiltonian (3.4), yields the second quantization version of the Josephson

Hamiltonian [154, 253]

$$\hat{H} = \frac{E_C}{4}(\hat{a}_1^\dagger \hat{a}_1^\dagger \hat{a}_1 \hat{a}_1 + \hat{a}_2^\dagger \hat{a}_2^\dagger \hat{a}_2 \hat{a}_2) - \frac{E_J}{N}(\hat{a}_1^\dagger \hat{a}_2 \hat{a}_2^\dagger \hat{a}_1). \tag{3.98}$$

A standard approach to constructing the mode functions $\psi_{1,2}$, already mentioned above, is to use $\pm$ combinations of the first symmetric and antisymmetric GPE dynamical wave functions in the trapping potential [291, 263]

$$\psi_1(\mathbf{r}) = \frac{1}{\sqrt{2}}(\psi_s + \psi_{as}) \tag{3.99}$$

$$\psi_2(\mathbf{r}) = \frac{1}{\sqrt{2}}(\psi_s - \psi_{as}). \tag{3.100}$$

One main advantage of this construction is the relative ease with which these modes can be (numerically) calculated for a given external potential $V_{ext}(r,t)$, using for example the numerical methods presented in section 3.1.3, as shown in figure 3.3. This approach leads to explicit expressions for the charging energy and the Josephson energy. In particular, in the case of a simple two-mode model, which neglects the effects of interactions in the overlap regions, one finds [291, 253]

$$E_C^{1,2} = 2g \int |\psi_{1,2}(r,t)|^4 dr \tag{3.101}$$

$$E_J = -N \int \left[\frac{\hbar^2}{2m}(\nabla \psi_1^*(r,t) \nabla \psi_2(r,t)) + \psi_1^*(r,t) V_{ext} \psi_2(r,t) \right]. \tag{3.102}$$

The equivalent formulas for an improved two-mode model can be found in [4]. We are now interested in two things: First, we want to find a time t_{split}, i.e. the moment during the splitting process when the coupling between the two BECs vanishes, and the relative phase and the phase dispersion start to evolve freely. Secondly, we want to know the initial phase spread at this time t_{split}, which gives the degree of number-squeezing of the split state. For the calculation of these two quantities it is convenient to work in the phase state basis $|\varphi, N>$ introduced in equations (3.93) and (3.91). The decomposition of a general state of the two mode-system in this basis reads

$$|\psi\rangle = \int_0^{2\pi} \frac{d\varphi}{2\pi} \Psi(\varphi,t) \, |\varphi, N\rangle \, . \tag{3.103}$$

All information of the state is contained in the phase amplitude $\Psi(\varphi,t)$. We can transform the action of any operator on the state $|\psi>$ into a differential equation for $\Psi(\varphi,t)$. In particular, inserting (3.103) into the Josephson Hamiltonian (3.98) leads to the equation

$$i\hbar \frac{\partial \Psi(\varphi,t)}{\partial t} = -\frac{E_C}{2} \frac{\partial^2 \Psi(\varphi,t)}{\partial \varphi^2} - E_J(t) \cos(\varphi) \Psi(\varphi,t), \tag{3.104}$$

which is the quantized equivalent to the classical Josephson Hamiltonian (3.96).
For a given splitting process, i.e. for a known change over time of $V_{ext}(r,t)$ and fixed atom number N, the time dependence of $E_J(t)$ can be calculated numerically with equation (3.102). In turn, the phase distribution $\Psi(\varphi,t)$ can then be calculated by numerically solving equation (3.104), if an initial value $\Psi(\varphi,0)$ is specified. In principle, for the single, unsplit condensate $\Psi(\varphi,0)$ is a delta peak at the (arbitrarily chosen) value $\varphi = 0$. For practical computation it is sufficient to approximate this delta function with a narrow Gaussian distribution with an initial width $\sigma_\varphi(0) \ll 2\pi$. This width changes only slightly as long as the tunnel coupling remains sufficiently large.
A reasonable definition for the moment of splitting t_{split} is the time when $E_J \approx 0$, i.e. when the second term in equation (3.104) becomes negligible. Beyond this time, the phase spread expands

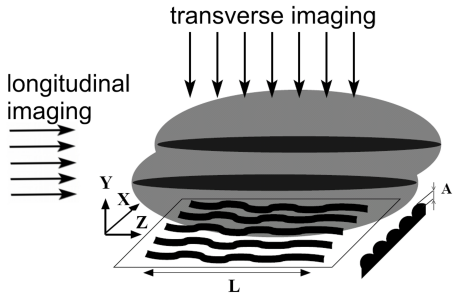

Figure 3.4: Schematic of the interference of two 1d quasi BECs. In contrast to the 3d situation, the 1d quasi BECs do not have a single uniform phase, but instead is described by a fluctuating (time-dependent) phase field. Consequently, in interference experiments the measured relative phase varies along the axis of the system, resulting in local shifts of the observed fringe pattern. This can be imaged directly with an imaging system along the transverse direction. Alternatively, the shifting fringe patterns lead to a reduced contrast and increased phase spread of the integrated pattern when imaged longitudinally. (Picture adapted from A. Imambekov et al [147].)

"ballistically" under the influence of the term proportional to E_C. This is exactly equivalent to the dispersion of a single-particle wave packet in space under the influence of the kinetic energy term in the Schroedinger equation.
In [253] analytic expressions for t_{split} and t_{ad}, the point in time when the adiabaticity of the splitting process breaks down, are calculated for a particular splitting ramp. Specifically, a linear increase of the distance between the potential minima and the height of the (quartic) potential barrier are assumed. In that case, the Josephson energy is found to decay exponentially with time [326], which is a reasonable approximation for many experimental situations.
One important result of [253] is that t_{ad} is always smaller than t_{split}, which means that the tunnel coupling between the two wells cannot be neglected even after the breakdown of adiabaticity, in contrast to the assumption of the simple model presented in the last section [182, 183]. The calculated phase spread $\sigma_\varphi(t_{split})$ depends greatly on the splitting process. The slower the splitting is performed, the longer the system can adiabatically follow the potential change and keep its phase spread minimized. This leads to a quite complex analytical expression for the dephasing time T_D, which is found to always be longer than the simple estimate (3.95).

3.4 Interference of 1d quasi-condensates

In this section, the concepts discussed in the previous two sections, namely quasi-BEC in 1d systems and interference, will be combined. The situation we consider is shown in figure 3.4: similar to the 3d case the starting point are two (quasi) BECs held in a double well potential configuration, from which they are released, so that the matter-wave packets overlap after expansion. The difference to the 3d case is that the quasi BECs cannot be described as single mode (point-like) sources. Instead, the phase along the axis of each system is dominated by fluctuations, as discussed in section 3.2. Consequently, the relative phase between the two systems, measured in interference experiments, also becomes a function of position. This can be directly observed if the system is imaged in transverse direction, as indicated in figure 3.4. Alternatively, by imaging in longitudinal direction, one obtains a single integrated image of the shifting density distribution. The fluctuating relative phase then leads to a reduction of the fringe contrast and an increase of the shot to shot fluctuations of the single phase extracted from the longitudinal images.
Turning this argument around, the interference patterns between two 1d quasi BECs can be used to extract information about the phase fluctuations in each individual system [259, 107, 147, 31]. In the following, we will first discuss how the second quantization formalism of the interference can be extended to 1d systems (section 3.4.1). We then apply this to the cases of independent (section 3.4.2) and coherently split (section 3.4.3) pairs of quasi BECs.

3.4.1 Second quantization approach

The formalism introduced in section 3.3.1 can be transferred to the 1d case with few modifications. First, one has to adapt the field operators for the two condensates.
The field operators now become time-dependent functions of the spatial coordinates to describe the (fluctuating) phase modes. Consequently, in the density correlation function after the expansion, one now has to include the integration over the system length

$$\left\langle \hat{\rho}^\dagger(x_1)\hat{\rho}(x_2)\right\rangle = \delta(x_1-x_2)\int_0^L dz n(z) + \int_0^L dz_1 dz_2 \hat{\Psi}^\dagger(r_1)\hat{\Psi}^\dagger(r_2)\hat{\Psi}(r_1)\hat{\Psi}(r_2). \tag{3.105}$$

Here, the field operator $\hat{\Psi}$ is the one after the expansion time t. The relation to operators before the expansion are done in analogy to equation (3.84). But instead of the single mode operators $\hat{a}_{1,2}$ (eq. 3.79), we now need to introduce a spatial and temporal dependence in the field operators corresponding to each condensate $\hat{a}_{1,2}(z,t)$ to include the phase fluctuations.
The interference pattern arises from the second term in equation (3.105). Neglecting interaction effects during the expansion, one finds again the spacing of the fringe modulations as $s = \hbar t/md$, where t is the expansion time and d is the original distance. In this approach, also any expansion of the system in longitudinal direction during time of flight is neglected. This is usually fulfilled to a very good degree, due to the weak longitudinal confinement.
We again express the Fourier component of the density correlation function at wave vector $Q = md/\hbar t$ (equation 3.86) in terms of the field operators before the expansion, and calculate its variance, which now depends on the integration length L.

$$\left\langle |\hat{\rho}_Q|^2\right\rangle = \int_0^L dz_1 dz_2 \left\langle \hat{a}_1^\dagger(z_1)\hat{a}_2^\dagger(z_2)\hat{a}_1(z_2)\hat{a}_2(z_1)\right\rangle. \tag{3.106}$$

Assuming the same density (and identical particles) in each cloud , this simplifies to

$$\left\langle |\hat{\rho}_Q|^2\right\rangle = \int_0^L dz_1 dz_2 \left\langle \hat{a}^\dagger(z_1)\hat{a}(z_2)\right\rangle, \tag{3.107}$$

where we have dropped the index of the field operator for simplicity.
To understand the physical meaning of this average fringe amplitude, its useful to consider the too limiting cases. First, if the correlation function $\left\langle \hat{a}^\dagger(z)\hat{a}(0)\right\rangle$ decays exponentially with distance with a correlation length much shorter than the system length $\xi \ll L$, one finds $|\rho_Q(L)| \propto \sqrt{L\xi}$, which can be interpreted in the following way: Since the phase in each BEC is coherent only over a length ξ, the system can be considered as a series of L/ξ pairs of interfering independent condensates. The total amplitude $\rho_Q(L)$ is the result of adding L/ξ independent vectors of constant length ξ and random direction, which gives the obtained square root scaling [83].
The opposite limit of is that of two perfect condensates, for which $\left\langle \hat{a}^\dagger(z)\hat{a}(0)\right\rangle$ is constant, in which case we find $|\rho_Q(L)| \propto L$, i.e. the fringe amplitude scales as the system size, as one would expect when the interference patterns are perfectly aligned.
The main idea here is, that if one knows the (phase) correlation properties of the system, a quantitative prediction for the function $\left\langle |\hat{\rho}_Q|^2\right\rangle$ can be made. Or, the other way around, from the measured fringe amplitudes for different L, inference on the phase fluctuations in the system can be made.

3.4.2 Independent sources

We first consider the case of two independent 1d BECs, i.e. the phase fluctuations in both systems are uncorrelated. Equation (3.107) for $\left\langle |\hat{\rho}_Q|^2\right\rangle$ can be used for uniform as well as for trapped condensates. Extending it to non-equal densities in both condensates is also straight-forward,

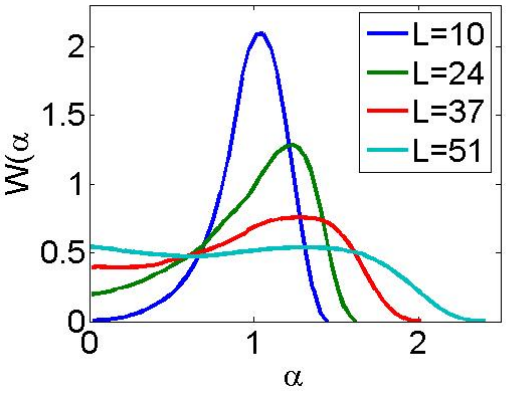

Figure 3.5: Numerically calculated distribution functions $W(\alpha)$ for $K = 46.7$ and $\xi_T = 0.92\,\mu$m and different L. It can be seen that the shape of $W(\alpha)$ changes significantly for different values of $\xi_T K/L$ between the two extremes of a narrow peaked distribution for $\xi_T K/L \gg 1$ and a wide Poissonian for $\xi_T K/L \ll 1$. The Monte Carlo simulations were performed by A. Imambekov.)

using equation (3.106). We focus here on the uniform case with equal densities. Experimentally, that corresponds to restricting the length L to values much smaller than the longitudinal size of the condensates. This scenario is equivalent to using open boundary conditions (OBC), which slightly modifies the results [147], compared to the periodic boundary conditions used in [259, 107].
Using the LL formalism for describing the two condensates, we can use equations (3.69) and (3.70) for the phase correlations in the system. Inserting these expressions into equation (3.107), we obtain for $T = 0$ and $L \gg \xi_h$

$$\left\langle |\hat{\rho}_Q|^2 \right\rangle = C n_{1\mathrm{d}}^2 L^2 \left(\frac{\xi_h}{L}\right)^{1/K}, \tag{3.108}$$

where C is a constant of order unity. The interference fringe amplitude $|\hat{\rho}_Q|$ scales as a non trivial power of the imaging length. In the noninteracting limit ($K \to \infty$), the scaling is linear $|\hat{\rho}_Q| \propto L$, as expected for a fully coherent system. For the Tonks gas ($K = 1$), one finds $|\hat{\rho}_Q| \propto \sqrt{L}$, in agreement with the absence of coherence in the fermion like system.
For finite T, the correlation function is given by equation (3.70), which leads to [107]

$$\left\langle |\hat{\rho}_Q|^2 \right\rangle_T = C_1 n_{1\mathrm{d}}^2 \xi_h L + C_2 n_{1\mathrm{d}}^2 \xi_h^{1/K} L^{2-1/K} f(\xi_T/L, K), \tag{3.109}$$

where C_1 and C_2 are again constants of order unity, and the function $f(\xi_T/L, K)$ is defined as

$$f(x, K) = \int_0^1 \int_0^1 du dv \left(\frac{\pi}{x \sinh(\frac{\pi|u-v|}{x})}\right)^{1/K}. \tag{3.110}$$

Using the expression (3.67) for K, equation (3.109) is a function of only three experimental parameters: the density $n_{1\mathrm{d}}$, the transverse trapping frequency $\omega_\perp$ (which enters through the effective coupling constant $g_{1\mathrm{d}}$), and the temperature T. Assuming $n_{1\mathrm{d}}$ and $\omega_\perp$ can be measured directly, equation (3.109) provides a method for thermometry in 1d systems, which in principle works for arbitrarily low T (in fact we can expect this model to be increasingly accurate for lower T). In a similar way the thermal fluctuations of the relative phase of two coupled 3d BECs have recently been used for measuring the temperature of the system in the experiment presented in [92, 91].

Full distribution functions

As already discussed in the context of interference of two independent single mode BECs, calculating the expectation value of a quantum mechanical operator is equivalent to averaging over many experimental results. The same argument can be applied to the operator $\hat{\rho}_Q$. From shot to shot, the square of the experimentally observed fringe amplitude may vary significantly from (3.109).
To describe the full distribution function of measured fringe amplitudes, one has to consider higher

moments of the operator $\hat{\rho}_Q$. Following the same procedure which led to equation (3.107), we obtain

$$\left\langle |\hat{\rho}_Q|^{2n} \right\rangle = \int_0^L dz_1 ... dz_n dz'_1 ... dz'_n \left| \left\langle \hat{a}^\dagger(z_1) ... \hat{a}^\dagger(z_n) \hat{a}(z'_1) ... \hat{a}(z'_n) \right\rangle \right|^2 . \tag{3.111}$$

The term in the brackets is nothing but the n-th order correlation function. Consequently, this can again be turned around: The measured distribution of the fringe amplitude contains information about all higher order correlation functions.
In the LL framework, the higher moments of the fringe amplitude can be calculated as

$$\left\langle |\hat{\rho}_Q|^{2n} \right\rangle = A_0^{2n} Z_{2n}, \quad A_0 = \sqrt{C n_{1\mathrm{d}} \xi_h^{1/K} L^{2-1/K}}. \tag{3.112}$$

The function Z_{2n} is given by [107]

$$Z_{2n} = \int_0^1 du_1 ... dv_n e^{\frac{1}{K}\left(\sum_{i<j} G(u_i,u_j) + \sum_{i<j} G(v_i,v_j) - \sum_{i,j} G(u_i,v,j)\right)}, \tag{3.113}$$

where the symmetric function $G(x, y) = G(y, x)$ depends on the problem specific boundary conditions [107, 147].
We define the variable $\alpha = |\rho_Q|^2 / \left\langle |\hat{\rho}_Q|^2 \right\rangle$, where ρ_Q is the fringe amplitude of a single measurement and $\left\langle |\hat{\rho}_Q|^2 \right\rangle$ is obtained by averaging over all measurements. We can then express the distribution function of the fringe amplitude $W(\alpha)$ through

$$\frac{Z_{2n}}{Z_2^n} = \int_0^\infty W(\alpha) \alpha^n d\alpha. \tag{3.114}$$

This expression can be inverted to obtain a (rather complex) dependence of $W(\alpha)$ on the functions Z_{2n}, which can be found in [147]. The important aspect is, that $W(\alpha)$ depends only on L, $n_{1\mathrm{d}}$, $\omega_\perp$, and T. To use this method for thermometry, one obtains $W(\alpha)$ for a fixed set $(L, n_{1\mathrm{d}}, \omega_\perp)$ and different T from Monte Carlo simulations as discussed in [147, 148] and optimizes the agreement between experimental data and numerical distribution functions. Example calculations for $K = 46.7$ and various ξ_T/L are shown in figure 3.5.

3.4.3 Coherently split sources

We now consider the case where the two 1d systems are initialized with a fixed relative phase. In analogy to the 3d case, this can be done by splitting a single 1d quasi BEC along the whole longitudinal axis. This process creates two identical "copies" of the phase field pattern at the moment of the splitting.
This phase coherent state is a highly nonequilibrium one for the split condensate system. As soon as the two parts are decoupled the system will start to relax to thermal equilibrium, in which the phase fluctuations of the two parts are completely uncorrelated. Similar to the 3d case, one driving mechanism in this process is the phase diffusion due to particle number uncertainty in each well [182]. But the enhanced phase fluctuations in 1d provide a second, usually dominating, driving force in this decoherence process [19, 31].
The coherence between the two condensates can be quantified with the so called coherence factor [257, 31], which in its complex form reads

$$\Psi_d(t) = \frac{1}{L} \left| \int_0^L dz e^{i \triangle\varphi(z,t)} \right|, \tag{3.115}$$

where $\triangle\varphi(z, t)$ is the relative phase between the two condensates. In the case of $\triangle\varphi(z, t) = const.$ the coherence factor is one. Note that this does not mean that the absolute phase in each of the

two systems is constant, only that the spatial variations of the two phase fields are identical.
The time evolution of the coherence factor has been theoretically studied recently by Burkov [31] et al. based on a path integral approach to the LL description of the phase fluctuations [38]. They find the following result for zero temperature:

$$\Psi_d(t) \propto \exp[-\mu^2 t^2/2N\xi^2] \times \exp[-\mu t/2\pi K\xi^2], \tag{3.116}$$

where ξ is the squeezing factor defined in section 3.3.2. The first of the two exponents comes from the "global" phase diffusion due to atom number uncertainty, while the second one is due to the quantum phase fluctuations present in a uniform 1d system even at $T = 0$. For a finite size system below T_ϕ, i.e. the temperature at which the phase coherence length is equal to the system length, this second term vanishes and one only has the standard phase diffusion process destroying the coherence over time.
The thermal part of the phase fluctuations can only be neglected for times $t < \hbar/k_{\mathrm{B}}T$. To observe a significant effect on the coherence factor due to the quantum fluctuations in this time, $\mu/2\pi K\xi^2 T$ must be large. As expected, quantum effects become more important for small K and T.
For $t > \hbar/k_{\mathrm{B}}T$, the thermal fluctuations have to be included in the calculations. The coherence factor is then dominated by a decay of the form

$$\Psi_d(t) \propto \exp[-(t/t_0)^{2/3}], \tag{3.117}$$

with the time constant $t_0 = 2.61\pi\mu K/T^2$. The important feature of this result is the nonanalytic time dependence, which is a general feature of 1d classical decoherence dynamics. This is due to the fact that in 1d liquids damping at finite T is always nonhydrodynamic [9].
Furthermore, at finite T there is an anharmonic coupling of the two degrees of freedom of the system, namely the relative phase $\triangle\varphi = \varphi_1 - \varphi_2$ and the "center-of-mass" total phase $\Phi = \varphi_1 + \varphi_2$. The problem is treated by considering the (unobservable) total phase of the system as a "thermal bath" for the relative phase modes. In practise, this will result in some heating of the total phase modes, i.e. an increase in the total temperature. Hence, the temperature in equation (8.2) should be considered as the final equilibrium temperature of the system. The strength of the coupling between the different modes is given by the parameter $\gamma = \sqrt{4TK}/\pi\mu$, i.e. it increases with both the temperature and the density (through K), so we expect this effect to be stronger for larger T and $n_{1\mathrm{d}}$.

3.5 Coupled one dimensional systems

In this section we study the case of two (quasi)-condensates in a double well potential with a barrier small enough such that a finite tunnel coupling between the two systems exists. This situation has been extensively studied in the case of single mode 3d condensates. As early as 1986, Javanainen [151] pointed out the similarity of BECs of non-interacting particles in the double well to super-conducting Josephson junctions [158] and liquid helium baths connected by micropores [245]. The inclusion of the interaction induced non-linearity further enhances the richness of the dynamics of the system [291]. In a classical phase description the BEC system (as well as the helium case) is shown to be exactly mappable onto the classical problem of a non-rigid pendulum [263, 212], in contrast to the super-conducting Josephson junctions, which are equivalent to rigid pendulums [13, 201].
The two-mode model predicts a number of different regimes for the interacting BEC Josephson junction, depending on the ratio between the tunneling strength to the interaction energy of atoms in each well [291, 181]. For small interaction energy, one expects Rabi-like single-particle oscillations oscillations between the wells. For large interaction energy the Josephson regime is entered. In this regime, oscillations around equilibrium configuration have a reduced amplitude in atom

number and their frequency depends on the mean field energy. This regime can be subdivided into various classes, depending on the initial conditions of the system [263]. Specifically, for large initial number imbalance an interaction-induced macroscopic self-trapping can occur, which suppresses the tunneling oscillations [223, 291]. Self-trapping and small-amplitude Josephson oscillations in a BEC Josephson junction have recently been observed for the first time in an optical double well potential [1]. After an improvement of the two-modes model [4], there seems to be good quantitative agreement with the experiment [90].
A very brief description of the Josephson regime of the two-mode model was given in section 3.3.2 in the context of coherent splitting of a condensate. For the purpose of this thesis, only the approximative calculation of a (time-dependent) tunneling rate is of importance. Much more detailed reviews of the two-mode theory and the different possible regimes can be found in the theses of M. Albiez [1] and T. Schumm [282].
Here we consider the case of two tunnel-coupled one-dimensional quasi-condensates. In this case, the tunnel coupling easily becomes larger than the longitudinal phase-mode spacing and the two modes model a priori breaks down. Instead we find a situation where two effects act in opposite directions: the longitudinal phase fluctuations in each condensate tend to smear out the relative phase between the two condensates, while the coupling between the condensates energetically favors the case of identical local relative phase [314]. This system has a stable solution of uniform Josephson oscillations over the whole length of the condensate, which will be discussed in section 3.5.1. However, the non linearities introduced by interactions may cause instability of the uniform Josephson mode, causing the uniform Josephson oscillations to decay into modes of non vanishing longitudinal momentum [25]. This nonlinear system is shown to be a realization of the quantum Sine-Gordon model if treated in the Luttinger liquid framework [108, 109]. The Sine-Gordon model predicts a rich variety of possible dynamical modes like solitons and breather-modes [109]. Section 3.5.2 tries to give a brief overview of this complex system. The flexibility of cold atomic systems make the coupled 1d condensates a highly promising candidate for studying this widely used quantum field-theory model.

3.5.1 Equilibrium state

The steady state at finite temperature of two coupled 1d-BECs has been studied by Whitlock and Bouchoule [314]. They calculate the energy spectrum and the mode-functions of the system using the Bogoliubov approach (section 3.1.2).
In particular, they consider two homogeneous 1d-systems coupled by a spatially independent coupling energy J. They find the Bogoliubov modes as plane waves with amplitudes

$$S_k = \sqrt{\frac{\frac{\hbar^2 k^2}{2m} + 2J + 2g_{1\mathrm{d}} n_{1\mathrm{d}}}{\frac{\hbar^2 k^2}{2m} + 2J}}. \tag{3.118}$$

The corresponding eigenenergies are

$$\epsilon_k = \sqrt{\left(\frac{\hbar^2 k^2}{2m} + 2J\right)\left(\frac{\hbar^2 k^2}{2m} + 2J + 2g_{1\mathrm{d}} n_{1\mathrm{d}}\right)}. \tag{3.119}$$

From this, the spatial correlation function of the relative phase $\triangle\varphi(z)$ at finite T can be calculated as

$$\left\langle \triangle\varphi(z)\triangle\varphi(z')\right\rangle = \frac{k_{\mathrm{B}} T}{2 n_{1\mathrm{d}} \hbar}\sqrt{\frac{m}{J}} \exp\left[\frac{-2\sqrt{mJ}|z - z'|}{\hbar}\right], \tag{3.120}$$

which gives the amplitude of the relative thermal phase fluctuations and their correlation length $1/J$. The phase fluctuations are small if

$$k_{\mathrm{B}}T \ll n_{1\mathrm{d}}\hbar\sqrt{\frac{J}{m}}. \tag{3.121}$$

Conversely, for temperatures larger than the energy scale set by the tunnel coupling J, the local fluctuations in each condensate dominate, and the tunnel coupling cannot balance them.
This result can also be stated in dynamical form, by expressing the tunnel coupling as a Josephson like oscillation with frequency

$$\omega_{\mathrm{J}} = \frac{\sqrt{Jg_{1\mathrm{d}}n_{1\mathrm{d}}}}{\hbar}, \tag{3.122}$$

and the phase modes by the frequencies

$$\omega_{\mathrm{k}} = \frac{k\sqrt{g_{1\mathrm{d}}n_{1\mathrm{d}}}}{\sqrt{m}}. \tag{3.123}$$

The evolution of the phase at a single point z after one Josephson oscillation period reads

$$\left\langle [\triangle\varphi(1/\omega_{\mathrm{J}}) - \triangle\varphi(0)]^2 \right\rangle = \frac{k_{\mathrm{B}}T\sqrt{m}}{\hbar n_{1\mathrm{d}}\sqrt{J}}. \tag{3.124}$$

Relative phase fluctuations are small, if this quantity is small, which results in condition (3.121).
The calculation of the time correlation of the relative phase can also be used to obtain a phase randomization time of an initially phase coherently split state, if the tunnel coupling vanishes, which is of interest for the complete splitting discussed in the last section. The result reads

$$t_{\mathrm{dec}} = \frac{2\pi\hbar^2}{k_{\mathrm{B}}T}\sqrt{\frac{n_{1\mathrm{d}}}{mg_{1\mathrm{d}}}}. \tag{3.125}$$

The results (3.118) and (3.119) have been used by I. Lesanovsky to calculate the equilibrium coherence factor (3.115) at finite T of the system:

$$\Psi(T) = \exp\left[-\frac{\sqrt{mg_{1\mathrm{d}}}}{4\pi\hbar\sqrt{n_{1\mathrm{d}}}}F(b)\right] \times \exp\left[-\frac{\sqrt{mg_{1\mathrm{d}}}}{2\pi\hbar\sqrt{n_{1\mathrm{d}}}}S(b)\right], \tag{3.126}$$

where the abbrevation $b = J/g_{1\mathrm{d}}n_{1\mathrm{d}}$ was introduced. The auxiliary function $S(b)$ is given by

$$S(b) = \int \mathrm{d}a \frac{\sqrt{1/(a^2+b)+1}}{e^{\frac{\sqrt{(a^2+b+1)(a^2+b)}}{k_{\mathrm{B}}T}}-1}, \tag{3.127}$$

which is just the integral over the Bogoliubov amplitudes (3.118) weighted by the Boltzmann factor, rewritten with the abbreviations b and $a^2 = \frac{\hbar^2k^2}{2m}$.
Similarly, the function $F(b)$ is given by

$$F(b) = \sqrt{1/(a^2+b)+1} - 1. \tag{3.128}$$

In this form, $S(b)$ and $F(b)$ can be integrated numerically in a straight-forward manner. The two exponentials on the right hand side of equation (3.126) correspond to the quantum and thermal contributions to the coherence factor. For our experiment parameters the quantum term is always close to unity, i.e. the quantum fluctuations lead to no reduction of the coherence factor. Equation (3.126) can be used for a direct extraction of the coupling energy J from our measurements, as will be shown in chapter 8.

3.5.2 Dynamics

The equilibrium solution derived in the last section is unstable against minimal perturbations due to the nonlinearity of the system. Even at zero temperature, smallest deviations from the uniform Josephson mode can lead to excitation of longitudinal modes, resulting in conversion of the tunneling energy into longitudinal momentum. This system has been investigated in the Bogoliubov framework by I. Bouchoule in [25]. A very similar situation, two coupled 1d-ring traps has been studied more recently in [195], where the same instability is found.
Complementary investigations of the system in the Luttinger liquid framework can be found in [108, 109].
In both approaches, the total Hamiltonian of the system is found to be a combination of the quantum Sine-Gordon Hamiltonian [201] and an anharmonic coupling term, which causes the instabilities. To see this, the system is rewritten in relative and "center-of-mass" coordinates, for phase and momentum in the Luttinger framework and phase and density in the Bogoliubov picture. In the latter, these new coordinates are $\varphi_\pm = \varphi_1 \pm \varphi_2$, $n_- = (n_1 - n_2)/2$, and $n_+ + n_0 = (n_1 + n_2)/2$, where $n_0 = n_{1\mathrm{d}}$ is the equilibrium density equal in both systems and $n_{1,2}$ are the densities in each well in the presence of oscillations. The total Hamiltonian then divides into three components [25]

$$H = H_+ + H_- + H_\mathrm{C} \tag{3.129}$$

with the symmetric term

$$H_+ = \int \left(\frac{\hbar^2 n_0}{4m} \left(\frac{\partial \varphi_+}{\partial z} \right)^2 + g_{1\mathrm{d}} n_+^2 \right) \mathrm{d}z, \tag{3.130}$$

the antisymmetric term

$$H_- = \int \left(\frac{\hbar^2 n_0}{4m} \left(\frac{\partial \varphi_-}{\partial z} \right)^2 + g_{1\mathrm{d}} n_-^2 - 2J n_0 (\cos(\varphi_-) - 1) \right) \mathrm{d}z, \tag{3.131}$$

and the coupling term

$$H_\mathrm{C} = -2J \int n_+ (\cos(\varphi_-) - 1) \mathrm{d}z. \tag{3.132}$$

In the Luttinger approach the Hamiltonian has exactly the same form [109]. H_- is the quantum Sine-Gordon Hamiltonian, which occurs in such diverse areas of physics as quantum gravity and low dimensional superconductors [201]. If the coupling term H_C is neglected, the center-of-mass dynamics described by H_+ are fully decoupled and the experimentally observable (local) relative phase and density imbalance follow the dynamics of the Sine-Gordon model [108, 109].
Gritsev et al propose two different experimental approaches for studying the Sine-Gordon dynamics in this system. In [108], the case of coherently split but still coupled 1d condensates is considered. As discussed in sections 3.3.2 and 3.4.3, the splitting produces an initially number squeezed non-equilibrium state with coherence factor $\Psi(t = 0) = 1$. The inclusion of finite tunnel coupling in the decay dynamics of the coherence factor is found to lead to periodic behavior instead of exponential decay. The power spectrum of these oscillations would be a direct measurement of the power spectrum of the quantum Sine-Gordon model.
Alternatively, in [109], the (linear) response of the split system to various artificially introduced deviations from the equilibrium state are investigated. Specifically, time-dependent modulations of the tunnel-coupling J and/or the energy difference $\triangle E_0$ of the ground states of the two wells are considered. Both modulations could be implemented by a periodic variation of the external potential.
In contrast to these papers, Bouchoule studies the system including the coupling term H_C [25],

which results in a modified Sine-Gordon model. The coupling between the symmetric and asymmetric degrees of freedom leads to a damping of the pure Sine-Gordon modes, which limits for example the number of observable oscillations in the coherence factor.
It remains to be seen how important this damping term is and to what extent in general the Sine-Gordon dynamics can be extracted from experiments like ours. First experiments of coherently split, coupled 1d-condensates presented in chapter 8 show none of the signatures predicted in [108]. More detailed investigation of the expected time-scales for our parameters is currently in progress.

4 Experimental setup

The experiments presented in this manuscript are carried out with ultra cold thermal or Bose-Einstein condensed rubidium-87 atoms. In this chapter, the experiment setup used for these experiments, the RbII setup, is described. Section 4.1 gives an overview of the experiment hardware, while in section 4.2 the experimental procedure of BEC production is outlined. Both topics are covered only briefly here. More detailed descriptions of the various experiment components can be found in previous theses [15, 96, 129, 27, 140, 316]. The characterization and optimization of the different steps in the experiment cycle is summarized in [140, 316].

4.1 The RbII setup

The main design goal of the RbII experiment was to create a simple, stable setup for BEC production. To achieve this goal, the setup was reduced in complexity and size compared to the first approach for a BEC experiment in our group, the RbI setup [277, 278, 165, 164]. In the following the main hardware components of the experiment are reviewed one by one.

4.1.1 Vacuum System

One step towards a simplified setup is the use of a single chamber vacuum system, which means that all steps of the experiment cycle take place in the same location, the *experiment area*. For long trapping times of ultra cold atoms, and specifically for the realization of BEC, the experiments have to be performed in ultra-high vacuum (UHV), because collisions with the room-temperature background gas atoms lead to loss and heating of the trapped ensembles. On the other hand, for fast and efficient loading of a magneto-optical trap (MOT) from background vapor, a sufficiently high Rb concentration is required. Since both of these experiment stages take place at the same location, stringent requirements on the vacuum pumps are set. During each experiment cycle the vacuum has to be improved by two orders of magnitude between the loading and magnetic trapping phases within a few seconds.
To achieve this a large volume ion pump is used, which restores pressures in the range of 10^{-11} mbar with the required speed. Additionally, once per week a titanium filament is used to emit a two minute pulse of titanium into the chamber which condenses on the chamber wall and then absorbs impurities in the chamber. This pump combination achieves a base vacuum pressure below 5×10^{-12} mbar, although the pressure increases to 10^{-10} mbar during the rubidium dispensing phase of each experiment cylce.
Figure 4.1 shows the layout of the complete vacuum system. The experiment area is located at the bottom of the setup. The octagonal shape of the experiment chamber with openings on seven sides provides good optical access to the experiment area. The eighth side of the chamber is used for feedthroughs to connect three rubidium dispensers inside the vacuum. At the bottom of the chamber an additional window allows access to the experiment area from below. A detailed description of the chamber design can be found in [129].

4.1.2 Atom chip mounting

The atom chip is located upside down at the top of the experiment area, as shown in figure 4.1a. It is attached to a 30 cm high chip mounting hanging down from the top of the vacuum system.

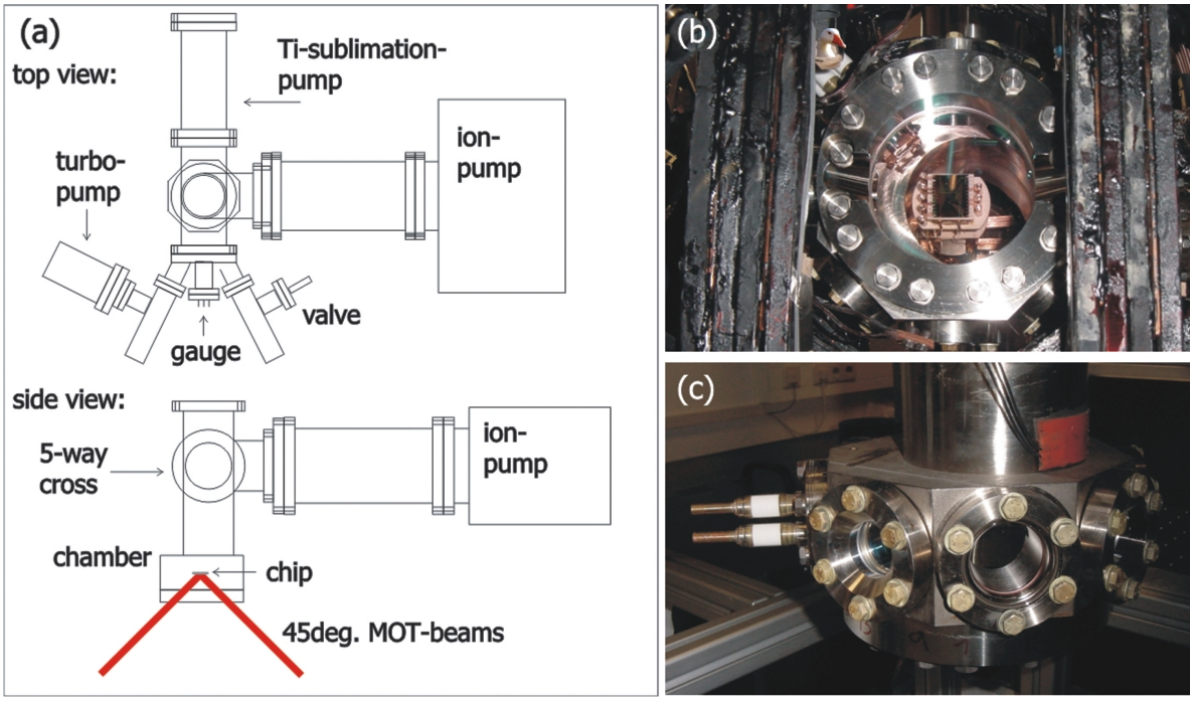

Figure 4.1: Design of the vacuum system. **(a)** Layout of the whole vacuum system from top and side. The experiment chamber is located at the lower end of the system. **(b)** Photograph of the experiment chamber from below. The mounted atom chip inside the chamber can be seen. **(c)** Side view of the experiment chamber after bakeout, showing the octagonal design of the chamber. On the left the current feedthroughs for the Rb dispensers inside the vacuum can be seen.

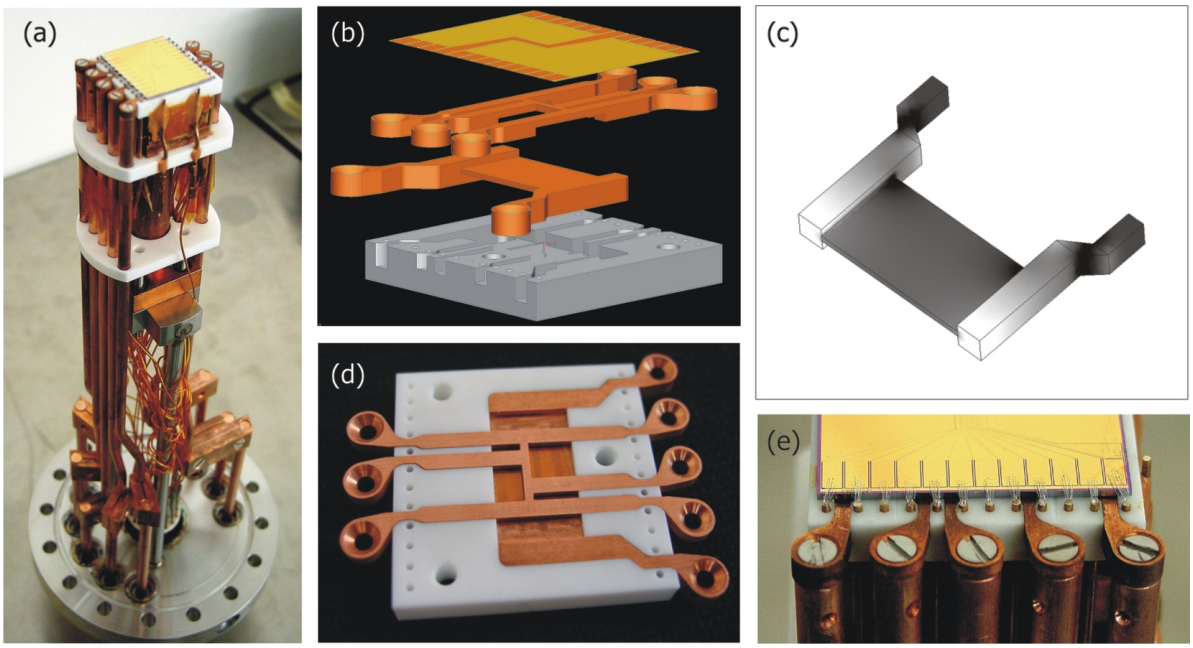

Figure 4.2: Photographs and design drawings of the assembled chip mounting and the integrated macroscopic wire structures. **(a)** The complete mounting before integration into the vacuum. The atom chip can be seen on the top of the mounting. **(b)** Design drawing of the copper wire structures directly underneath the atom chip. **((c)** Simulation of the current density in the broad U-wire structure. **(d)** Photograph of the final macroscopic wire assembly before the mounting of the atom chip. **(e)** Photograph showing the copper connections of the macroscopic wires and the smaller bondings of the atom chip wires to copper pins in the chip mounting.

The vacuum flange closing the top of the chamber is directly integrated into this mounting, with current feedthroughs connected to the chip wires.
A feature specific to the setups of our group is the integration of a set of macroscopic wires into the atom chip mounting [117, 278, 165]. These wires can sustain significantly larger currents than the atom chip wires (up to 100 A), and consequently provide stronger inhomogeneous fields than realizable with the atom chip. In our setup we employ two independent structures:

- A U-shaped structure built from a single copper piece in combination with an external homogeneous field provides a quadrupole like magnetic field centered at a distance of $6 - 8$ mm from the chip surface. The quadratic outer leads (3mm $\times$3mm cross-section) of this U-wire are thicker than the central plate (0.7mm $\times$10mm $\times$18mm) to make the current flow through the central plate more homogeneous (figure 4.2c). This optimized design reduces the deformation of the resulting field from an ideal quadrupole field compared to a simple U-wire over the whole size of the trapping area of MOT [15]. This wire replaces the usual coil pair in anti-Helmholtz configuration for the MOT field, greatly reducing the power consumption and removing any water cooling requirements. The U-wire is currently operated at 60 A, limited by the used power supply (HP 6011A).

- A second H-shaped structure of 1mm thickness with six connections is placed on top of the U-structure, as shown in figure 4.2d. The two wires are isolated from each other by a thin Kapton foil. Depending on which connectors are used either a Z- or U-shaped wire can be realized. The Z-wire can have a central bar of either 4mm or 10mm (8mm can also be realized with an off-center configuration). Normally the central 4mm Z-configuration is used, with a current of also 60 A (power supply HP 6551A), to provide a macroscopic Ioffe-Pritchard magnetic trap for a first stage of evaporative cooling as will be discussed in the next section.

The copper wires are embedded into an isolating glass ceramic (MACOR) block, which provides good thermal conductivity (1.5 $\mathrm{WK^{-1}m^{-1}}$). To ensure maximal thermal contact, both the ceramic block and the wires were machined with error tolerances below 50 μm. The connections from the vacuum feedthrough to the wire structures are solid 5 mm diameter copper rods, which further facilitate an efficient heat transport away from the atom chip.
The MACOR block also holds 12 gold covered pins each on two sides of the atom chip, which are connected to the feedthroughs by isolated copper wires. The electrical connection to the chip wires is realized by bondings between the chip connection pads and the pins (figure 4.2e). Complete design plans for the mounting can be found in [15].

4.1.3 External magnetic fields

Since all required inhomogeneous magnetic fields are provided by the atom chip or the copper wire structures, only homogeneous fields have to be generated outside the vacuum chamber. This is done by pairs of coils in Helmholtz configuration. Three such coil pairs are mounted directly around the experiment chamber, providing an arbitrarily oriented homogeneous magnetic field in the experiment area. The coils are wound (88 windings each) of a massive 2 mm $\times$ 10 mm copper wire, held together by a special epoxy resin with good thermal properties (Stycast 2850). Each pair can create fields of up to 100G [27]. As the power supplies (HP 6651A) cannot switch off the the currents through the coils sufficiently fast, electronic switches are used to achieve turn off times below 100μs. These are specifically designed to take into account the inductivity of the large coils which requires special means of fast energy dissipation (details can be found in [277]).
In addition, the employed power supplies are unipolar, so that the direction of each field can only be inverted by switching the connectors. Since this is impractical during the experiment, smaller

extra coils (100 windings of a 0.5 mm cylindrical wire, power supplies HP 66312A) were added to each coil. These additional coil pairs can create constant fields of up to 10 G in the opposite directions of the original coil fields.
A third set of three coil pairs on a rack surrounding the whole vacuum chamber (side length 60 cm, 100 windings of a 1 mm cylindrical wire, power supplies HP 66312A) is used to permanently cancel stray magnetic fields originating from outside sources, like the earth magnetic field or the electronics in the laboratory, in the experiment area.

4.1.4 Atom chip

The chip used in our experiment was fabricated by S. Groth at the Weizmann Institute of Science, Rehovot, Israel in collaboration with the group of I. Bar-Joseph [111]. It consists of a two-layer gold surface on a silicon substrate, manufactured in a multi-step evaporation process.

Fabrication process

The starting point of chip fabrication is a standard silicon substrate wafer with a thickness of 0.6 mm. Silicon is used because offers good heat conductivity. As silicon tends to leak currents, especially in the presence of light, the substrate is factory covered with a thin (40 nm) isolating layer of SiO_2.
Onto this a 40 nm titanium adhesion layer is evaporated before the final conducting layer is applied. The material of choice for the conducting layer is gold, which offers a low electric resistance and good fabrication properties. The wire structures are defined by $1-10\,\mu$m thick grooves in the titanium and gold layers. To produce these grooves the chip is first covered completely with a layer of image reversal photoresist and is then exposed to ultraviolet light shined through an electron beam patterned mask that blocks the light in the areas of the future grooves. In a standard development procedure the photo resist is removed in the areas where it was exposed to the ultraviolet light, while it is left in place in the areas of the future grooves. After the evaporation of the titanium and gold layers the remaining resist is removed in a chemical bath, leaving the desired free spaces between the gold wires.
The thickness of a single gold layer is limited due to the evaporation process to $< 2.5\,\mu$m. To increase the wire height on our chip, a second gold layer was added by repeating the production process with a second mask. For the top layer a mask was used where all wire widths have been reduced by $2\,\mu$m, to avoid misalignment of the two layers due to misplacement of the second mask on top of the first layer. The use of a different mask also allows to selectively leave out wires onto which a second layer is applied. This makes it possible to increase the height of wide structures, while for the narrow wires 'tower'-like structures with greater height than width can be avoided. It also prevents reduction of the surface quality due to the second layer in areas where it is not needed, like large area ground pads. The thickness of the gold layers is $1.3\,\mu$m (bottom) and $1.8\,\mu$m (top). The increase of the wire height for wide wires increases the maximal possible current through these wires.
On our chip, wire widths range from 1 to $100\,\mu$m, with fabrication errors on the order of 100 nm. The grain size in the evaporated gold layers is $50-100$ nm. The surface quality of the chip is very good, with a reflectivity of $> 95\%$.
The fabrication process is described in great detail in [111], and the electrical and thermal properties of our atom chips are extensively studied in [112].

4.1.5 Chip design

The chip used in the experiments described in this thesis was designed with the goal of observing atom interference in chip-based traps. Hence, a number of wire arrangements suitable for interfer-

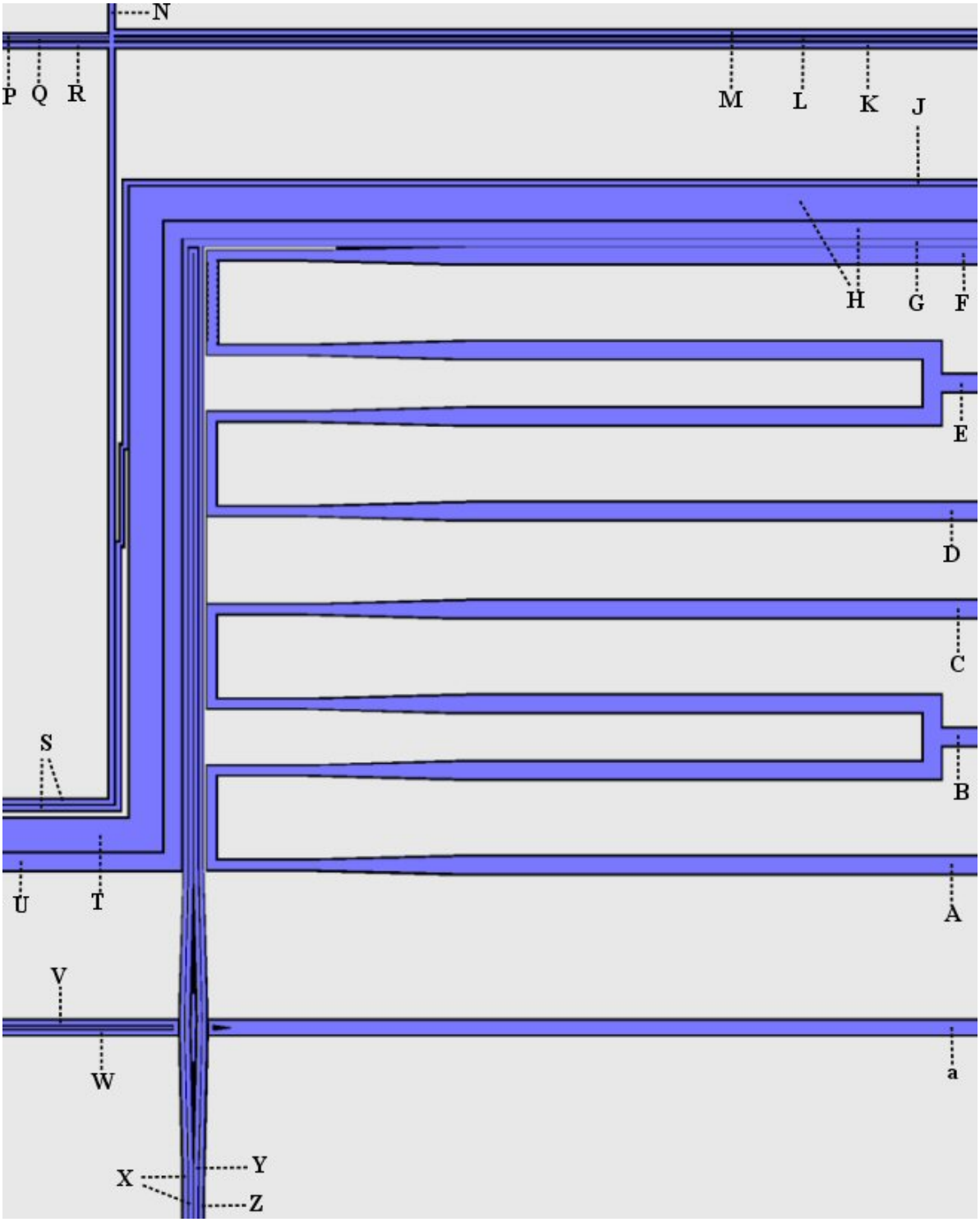

Figure 4.3: Central region (3.1×3.9 mm^2) of the chip design used in this experiment. Outside the field of view the wires broaden towards the 2.2mm wide connection pads. The groves in the gold layer which define the wires are shown in black. The gold wires are shown in blue, while the grey areas are gold parts that are grounded. The letters are used to label the connections and correspond to the labels used in the laboratory. The individual wire parameters are given in the text.

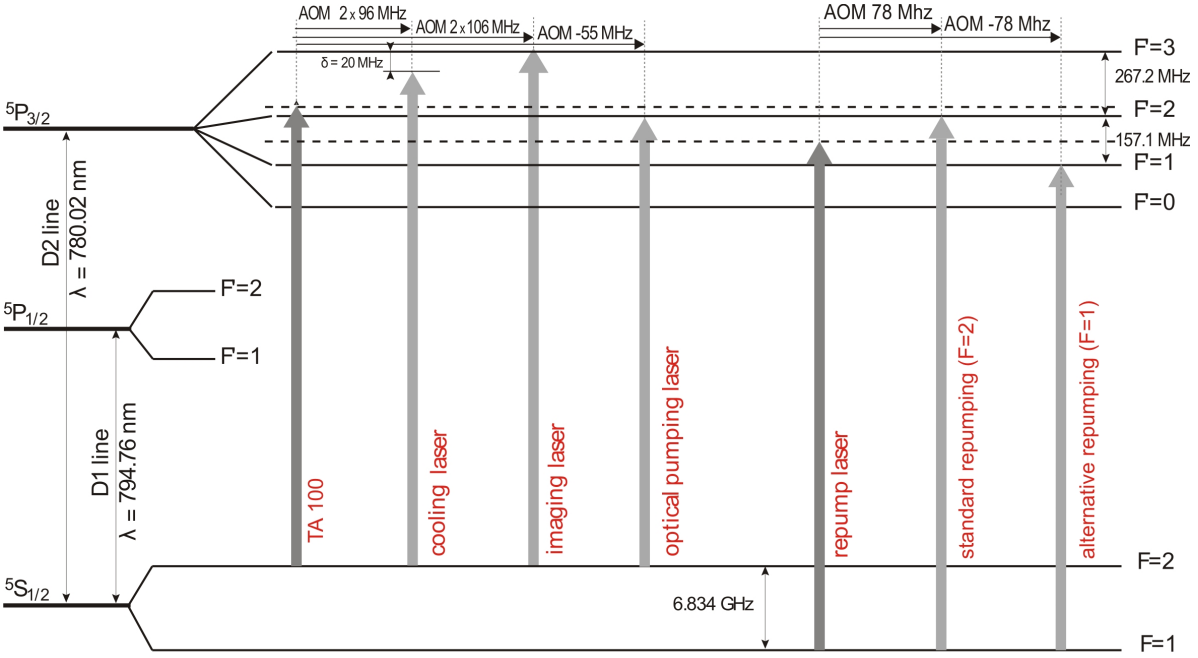

Figure 4.4: Schematic of the hyperfine transitions of the D2 line in ^{87}Rb. The frequencies of the two lasers used in the experiment are indicated by the dark grey arrows. The additional frequencies produced from these two stabilized sources by frequency shifting are shown as light grey arrows. The corresponding AOM frequencies are also given.

ence experiments can be found on the chip.
The whole center region of the chip design containing all relevant parts for the experiments is shown in figure 4.3. The letter designations used in the figure and in the following text correspond to the labels used in the laboratory.
The largest structures on the chip are two Z-shaped wires of 100 μm (T - H) and 50 μm (U - H) width.
Four parallel wires of 10 μm width (X, Y, Z, G) are situated next to the Z-wires. These wires form a four-wire guide, containing a splitting and recombining region consisting of two Y-beam splitters, which functions as an interferometer for guided atoms. There are two structures perpendicular to the four wires at the splitting region, a U-shaped wire (V - W) and a single electrode (a). These can be used to provide a magnetic and/or electric potential to break the symmetry of the two interferometer paths.
The two outer wires of the four-wire guide can be used individually (X - G or Z - G) to form an L-shaped wire. The four U-shaped wires (A, B, C, D, E, F) can be used to provide confining or pushing fields for potentials formed by the four 10 μm wires or the two Z-wires.
There are two more wire structures which form interferometers on the chip. The 10 μm-Z (S - J) next to the 100 μm-Z has a smaller, also Z-shaped, substructure at the center with which a time-dependent interferometer can be realized. Another Z-trap can be realized with the 10 μm wires shown in the top left corner of the image (K, M, P, R). The Z-potential can be split into a double well potential by the central 5 μm-wire (Q - L). The vertical wire (S - N) is intended for loading this trap. The various interferometer schemes for the traps on this chip are detailed in [175].

4.1.6 Laser System

In the experiment, laser light with frequencies corresponding to the various D2-line hyperfine transitions of ^{87}Rb is required, as is shown in figure 4.4. These wavelengths around 780 nm can be conveniently produced by semiconductor diode lasers.

In our setup we use two separate laser systems, one self-built master/slave diode laser pair with an output power of 50 mW and one commercial tapered amplifier system [1] with an output power of 1000 mW.
To ensure the selective driving of specific hyperfine transitions the frequency of the laser light must be accurate to a precision well below the natural line width of the transitions [220]. Thus both lasers are stabilized with spectroscopic locking techniques on an atomic transition, resulting in laser line widths of < 1 MHz. For the TA100 frequency-modulation (FM) spectroscopy is used to lock the laser on the 1-3 crossover spectroscopy line of the $|5S_{\frac{1}{2}}, F = 2\rangle \rightarrow 5P_{\frac{3}{2}}$ transition [96]. The self-built master laser is locked on the 1-2 crossover line of the $|5S_{\frac{1}{2}}, F = 1\rangle \rightarrow |5P_{\frac{3}{2}}\rangle$ transition with saturation spectroscopy [129]. The light from the TA100 is coupled into a polarization-preserving single-mode fiber to provide a higher beam shape quality. Both lasers with their respective spectroscopy systems are mounted on an additionally vibration-isolated breadboard and are placed into a closed wooden box to provide better frequency stability.
In a separate optics area, the two output beams of the lasers are split and then frequency-shifted by acousto-optical modulators (AOMs) to produce the required wavelengths for the experiment. The TA100 beam is split into three parts. Two of these, containing 90% (optical cooling) and 8% (imaging) of the beam power, respectively, are shifted by double-pass AOMs to be (near)-resonant with the $|5S_{\frac{1}{2}}, F = 2\rangle \rightarrow |5P_{\frac{3}{2}}, F = 3\rangle$ transition. The double-pass setup allows a change of the frequency shift without changing the direction of the outgoing beam, so that the detuning from the resonance can be changed during the experiment.
The remaining 2% of the beam power are shifted by a single pass AOM to be resonant with the $|5S_{\frac{1}{2}}, F = 2\rangle \rightarrow |5P_{\frac{3}{2}}, F = 2\rangle$ line. This beam is used for optical pumping of the atoms into the $m_F = 2$ state of the $|5S_{\frac{1}{2}}, F = 2\rangle$ level.
The output beam from the self-built laser system is split into two parts, which are frequency shifted by single-pass AOMs to be resonant with the $|5S_{\frac{1}{2}}, F = 1\rangle \rightarrow |5P_{\frac{3}{2}}, F = 2\rangle$ and the $|5S_{\frac{1}{2}}, F = 1\rangle \rightarrow |5P_{\frac{3}{2}}, F = 1\rangle$ lines, respectively. The first is used as a repumper beam to create a closed two-level system for the magneto-optical trap. The second can be used for an alternative optical pumping scheme to magnetically trap the $m_F = -1$ state of the $|5S_{\frac{1}{2}}, F = 1\rangle$ level.
After the splitting and frequency shifting the different beams are guided to the experiment area. The imaging and optical pumping beams are coupled into single-mode fibers to improve their beam shapes, while the cooling and the repumper beam are sent through telescopes to widen them to diameters of approximately 24 mm before they reach the experiment area. A detailed description of the complete optics system can be found in [316]

4.1.7 Imaging System

In our setup we use three independent imaging systems for atom detection, which allows imaging of the atomic ensembles along all three main axes. Each of these imaging systems consists of a fiber out-coupler aimed into the vacuum chamber and a set of magnifying optics and a CCD camera with high quantum efficiency in the near infrared on the other side of the vacuum chamber, as shown in figure 4.5. The standard imaging technique we employ is absorption imaging [166], which can be performed with each of the imaging systems. Additionally by combining the imaging beam from one system with the imaging optics and camera of another, fluorescence imaging can be used [140]. The two imaging systems parallel to the chip surface are labelled *transverse* and *longitudinal* imaging, respectively (figure 4.5a). The *vertical* imaging is perpendicular to the other two and points onto the chip surface from below the vacuum chamber.
For the transverse imaging a fast frame-transfer 16-bit CCD-camera (Roper Scientific MicroMAX 1024BFT) is used that can take two images of 1024×1024 pixels within 10 ms. This camera has

[1] Toptica, TA100 system

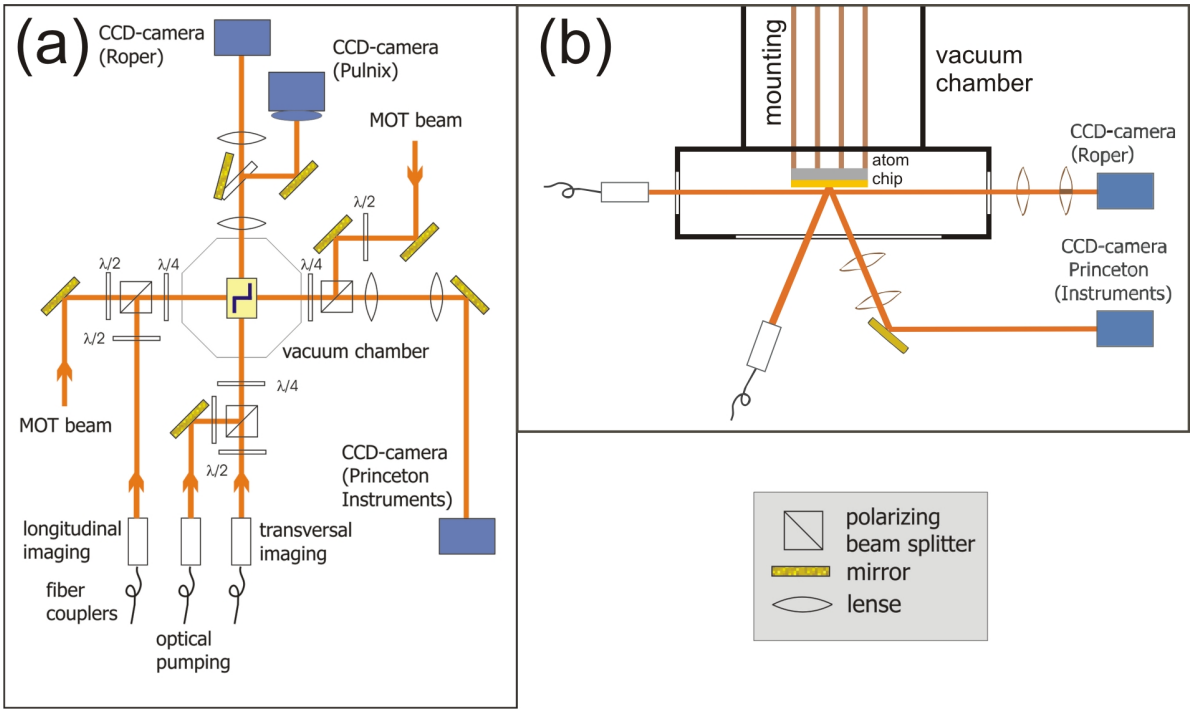

Figure 4.5: Schematic drawings of the three imaging systems in the experiment. **(a)** Horizontal imaging is performed longitudinally and transverse with respect to the elongated atomic samples. The longitudinal imaging light is overlapped with the horizontal MOT-beams using two beam-splitters. For the transverse imaging two cameras can be used, depending on the position of a flip mirror: A high-resolution imaging using a frame-transfer camera or an overview imaging using a standard CCD-camera combined with an objective. **(b)** The vertical system images along the axis perpendicular to the chip surface. The imaging beam is reflected at the chip surface, so that incoming and outgoing beam overlap. The incident angle of the beam is exaggerated in the drawing. In the experiment it is 5° with respect to the chip normal, which is necessary for the outgoing beam to pass the fiber outcoupler.

a quantum efficiency of 70% at 780 nm, the pixel size is $13 \times 13\,\mu\text{m}^2$. In front of the camera two lenses function as an objective to focus and magnify the image. The lenses currently used have focal lengths of 100 mm and 400 mm respectively. The measured magnification factor is 3.88 ± 0.02. To allow precise focussing the lenses are mounted on a motorized translation stage with a positioning accuracy of $2.5\,\mu\text{m}$ to guarantee optimal focussing on the atom cloud. The resolution of this imaging system has been measured by imaging test gratings with varying spacings before integration into the experiment. The obtained value is $3.3\,\mu\text{m}$.

The transverse imaging can be switched to an additional low-resolution 8-bit CCD camera (Pulnix TM6AS) by a flip mirror that can be moved between the two lenses. The first lens combined with a 50 mm camera objective focussed on infinity results in a demagnification factor of 3. We use this camera for overview images during the early stages of the experiment when the atom cloud is too large to be imaged with the high-resolution camera.

For the longitudinal imaging a 1340×400 pixel 16-bit CCD camera (Roper Scientific NTE/CCD-1340/400) is used. A pixel size of $20 \times 20\,\mu\text{m}^2$ combined with a magnification factor of 8 provided by two lenses (150 mm and 1200 mm focal length) in front of the camera gives as area per pixel $2.5 \times 2.5\,\mu\text{m}^2$. The diffraction limit of the resolution of this system is $5.7\,\mu\text{m}$. This imaging system was not tested independently outside the experiment. We determined its resolution by comparing images of small atom clouds from both images, and find a reduced value of $9 \pm 0.3\,\mu\text{m}$. We attribute this to astigmatisms introduced by additional optical elements in the imaging beam path.

For the vertical imaging only a low-resolution 8-bit Pulnix TM6AS is used at the moment. The two imaging lenses have focal lengths of 140 mm and 700 mm, resulting in a magnification factor

of 5. The vertical imaging beam is pointed at the chip surface from which it is reflected into the camera. A small angle of $\sim 5^\circ$ is necessary for the reflected beam to pass the fiber out-coupler (figure 4.5b). Due to the non-reflecting groves on the chip the wire structure is imprinted onto the imaging beam, reducing the quality of the images. Hence we use the vertical imaging mainly to survey the position of the atom cloud in relation to the chip structure during chip trap experiments instead of for quantitative analysis.

4.1.8 Experimental control

The experiment is controlled by a combination of an external signal processing system (Adwin-Pro-System) and a control software running on a standard personal computer. The Adwin-Box has its own processor and calculates signal values based on the parameters passed to it by the control computer at the start of each experiment cycle. This separation of the user input from the actual signal generating processor greatly reduces the technical noise and facilitates high update frequencies of the output signals. Also, the addition of other hardware and software components to the experiment control is guaranteed not to lead to compatibility problems with the stand-alone Adwin system.
The Adwin system currently has 32 digital output channels, 24 analog (16bit) output channels, and 8 analog input channels. Because of its modular structure both additional channels and extra processor and memory units can be added in the future if necessary. At the moment the system allows a time resolution for all 64 channels of $20\,\mu$s, a better update frequency is possible if less channels are used.
The Matlab-based user interface allows the graphical programming of the digital and analog output channels. The modular programming facilitates the integration of other components into the control system, for example GPIB based hardware. The user interface and the Adwin system are described in detail in [27].
The control computer is integrated into a local network with the camera computers and a data-processing computer. This network provides permanent synchronization of the camera data with the experimental control. A Matlab program running on the data-processing computer converts the raw image data from the various cameras to a standard tiff format, and labels the files with correct date and experiment cycle count obtained from the control computer. Additionally the complete set of control parameters for each run is saved together with the image files. This greatly simplifies the analysis of large data sets and reduces the amount of extra documentation required.

4.2 Experiment cycle

The experiment is run in cyclic operation, with a single cycle lasting $40 - 45$ seconds. Table 4.1 shows the different phases that make up one run. The experiment starts with a magneto-optical trap (MOT) to capture and cool atoms to $\sim 100\,\mu$K. The atoms are then further cooled by an optical molasses and transferred to the desired spin-state for purely magnetic trapping by optical pumping. Next follows a phase of radio frequency-induced evaporative cooling in a magnetic trap created by the copper H-wire structure inside the vacuum chamber, until temperatures below $10\,\mu$K are reached. At this point, the atoms are transferred to magnetic traps created by atom chip wires and a second stage of evaporative cooling is carried out. Finally the actual experiments in the desired chip trap are performed. Each cycle ends with the imaging of the atomic ensemble.

4.2.1 Magneto-Optical Trap

A magneto-optical trap (MOT) is the standard starting point for experiments with ultra-cold atoms. It provides a highly efficient and robust trapping mechanism that can capture and cool

Step	Duration	Temperature	Number of atoms
MOT	$20-28$s	200μK	3×10^8
Optical molasses	10ms	$\leq 50\mu$K	3×10^8
Optical pumping	300μs	$\leq 50\mu$K	3×10^8
Copper-Z trap	10s	$1-10\mu$K	10^5-10^6
Transfer to chip trap	100ms -1s	$\leq 10\mu$K	10^5-10^6
Chip trap	$0-8$s	100nK -10μK	10^3-10^6
Imaging	$0-30$ms		

Table 4.1: Operational sequence of a typical experiment run. Also listed are typical final temperatures and numbers of atoms for each step.

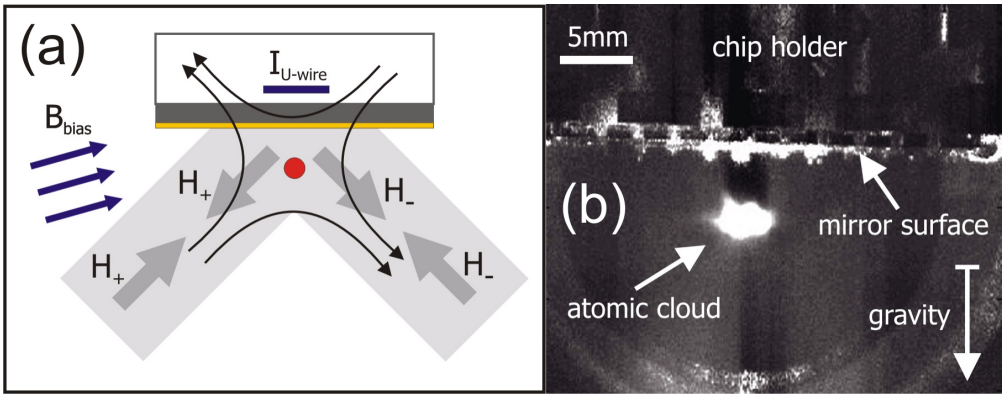

Figure 4.6: The reflection MOT allows magneto-optical trapping close to the chip surface. **(a)** Configuration of laser beams and magnetic quadrupole field for the mirror-MOT setup. The reflected beams form beam pairs of opposite helicity with the incoming beams. The pair of horizontal beams travels perpendicular to the image plane. The magnetic field is provided by a current in the U-wire in the chip mounting combined with an external bias field. The optimal quadrupole field is achieved for a bias field with an inclination of 13° in respect to the chip surface. **(b)** Photograph of the actual U-MOT in the experiment. The atom cloud trapped close to the chip surface can be seen in the center of the image.

room temperature atoms to μK temperatures.
The velocity dependence of the radiation pressure of a laser beam is used to slow and thus cool atoms. A beam red-detuned from a resonance frequency results in a net momentum transfer to the atom in the direction of the beam, causing a friction force on the atom. Combining such beams from all six directions causes an overall slowing of the atom.
The spatial trapping of the atoms is achieved by adding a magnetic quadrupole field. Due to the Zeeman-effect the absorption rate of the atom becomes sensitive to the polarization of the laser beams. When the helicity of the beams is matched correctly to the magnetic field the radiation force acting on the atom always points toward the trap center, confining the atoms.
Detailed explanations can be found in standard textbooks, for example [220, 246].

The U-MOT

We use a modification of the standard six-beam MOT setup that is adapted to the specific setup of atom chip experiments, where the chip mounting blocks the optical access to the trapping area from one direction. In this case, only four are beams are directed into the vacuum chamber, two counter-propagating ones parallel to the chip and two hitting the chip under 45 degrees, as shown in figure 4.6, with the chip-surface acting as a mirror for these beams. Because the helicity of the beams is inverted by the reflection, the incoming and reflected beams form two perpendicular

pairs of beams with correct polarization in the region where all beams overlap. Together with the horizontal beam pair the standard six-beam configuration is restored in this area. This *Mirror-MOT* setup is used in many atom-chip experiment [266, 84].
Because the helicity of the two 45° beams must be opposite in this configuration, the magnetic quadrupole field must be oriented such that the symmetry axes coincidence with the 45° beams. This tilted quadrupole field is provided by the U-shaped copper-structure underneath the chip combined with a homogeneous bias field. The optimization of the U-wire and the large diameter of the MOT beams allow for a large capture range and short loading times.

Laser cooling

For the MOT to work the transition used for cooling the atoms must form a closed two-level system. In our case the $|5S_{\frac{1}{2}}, F = 2\rangle \rightarrow |5P_{\frac{3}{2}}, F = 3\rangle$ transition is used. Because the $|5P_{\frac{3}{2}}, F = 2 >$ state lies only 267 MHz lower than the $F = 3$ level there is a finite probability that atoms are excited to this level from which they can decay to both the $|5S_{\frac{1}{2}}, F = 1\rangle$ and $|5S_{\frac{1}{2}}, F = 2\rangle$ level. Atoms in the $F = 1$ state are not excited by the cooling light and therefore are lost from the cooling cycle. To prevent this the repumper laser is added to the MOT by overlapping its two beams with the 45° cooling beams. It is running on the $|5S_{\frac{1}{2}}, F = 1\rangle \rightarrow |5P_{\frac{3}{2}}, F = 2\rangle$ transition and permanently pumps the atoms decaying into the wrong ground state back into the excited state. This effectively creates the required closed two-level system.

MOT-Loading

The U-MOT is loaded directly from the background pressure in the vacuum chamber. The Rb atoms are emitted into the chamber by three dispensers which can be heated by running a current through them. By changing this current, the amount of Rb in the chamber during the MOT-loading can be changed. Higher background pressure means faster loading and greater total size of the MOT, but also a degradation of the vacuum. This in turn reduces the lifetime of the magnetic traps later in the experiment, because collisions between trapped atoms and the hot background gas become more likely.
Therefore a balance has to be found between fast MOT-loading and long magnetic trap lifetime. Another factor limiting the loading speed is the Rb dissipation rate into the chamber. The used dispensers were tested to withstand a continuous current of 27 A (since we use three dispensers connected in parallel the current through each dispenser is 9 A). To avoid the risk of a burn through the dispenser temperature during pulsed operation should not exceed the value reached during this continuous operation. By using a larger current (32.5 A) during the beginning of the loading phase heats the dispensers to the maximal temperature in a short time. After this temperature is reached the current is reduced to 27 A to maintain a constant temperature until the dispensers are switched off. Typical observed loading rates are 3×10^7/s once the dispensers are heated. After a total dispenser time of 28 s, the number of atoms in the MOT saturates at 3×10^8. In most cases, we reduce the loading time to 20 s, resulting in a MOT size of 1×10^8 atoms, because this leads to sufficiently large BECs for our experiments and increases the number of cycles per given time.
During the last five seconds of the MOT loading the dispenser are turned off while the MOT continues to load from the background pressure. This is done to ensure optimal vacuum conditions for the magnetic trapping phase. The dispensers are water cooled to decrease the time required for cooling.
The intensity of the MOT beams is reduced during the final five seconds to avoid atom loss due to light induced collisions which start to play a role for the atom densities achieved at the end of the MOT phase.

In the final 100 ms of the loading-phase the MOT bias field is ramped up to compress the atom cloud and move it closer to the chip surface. The other two homogeneous fields can be used to displace the trap in the plane perpendicular to the chip surface to cancel imbalances in the MOT beams, if necessary. To facilitate an effective transfer the MOT should sit directly above the center of the magnetic trap into which the atoms are loaded.

4.2.2 Optical Molasses

After the MOT phase all magnetic trapping fields are switched off for a duration of 10 ms, while the cooling light is detuned to about 70 MHz below resonance. This stronger detuning results in further cooling of the atoms. Although the atoms are no longer spatially trapped, the diffusion of the atoms is small because of the already low temperature. Even small outside magnetic field would disturb the atoms and cause an acceleration of the cloud along the field direction. Hence the compensation fields can be calibrated by observing the movement of the molasses.
After this extra cooling step the temperature of the atom cloud is $\sim 40\,\mu$K and densities of 10^{10} cm^{-3} are achieved.

4.2.3 Optical Pumping

After the optical molasses the atoms are distributed equally over the five magnetic sublevels of the $F = 2$ ground-state. To transfer all atoms to the $m_F = 2$ state, which is the maximally spin stretched state for the $F = 2$ level, a small bias field is turned on to provide a quantization axis and a 300 μs optical pumping pulse of σ^+-polarized light resonant to the $|5S_{\frac{1}{2}}, F = 2\rangle \rightarrow |5P_{\frac{3}{2}}, F = 2\rangle$ transition is sent through the chamber along this axis. Because of the circular polarization we have $\Delta m = +1$ for the excitation, while for the spontaneous decay back to the ground state all possible transitions are equally probable ($\Delta m = -1, 0, +1$). Over time this results in an accumulation of the atoms in the $m_F = 2$ ground state, which is a "dark"-state for σ^+-light. To prevent the loss of atoms decaying into the $|5S_{\frac{1}{2}}, F = 1\rangle$ state the repumper must be left on during this phase.
Very small intensities of 20 μW are sufficient to achieve complete polarization of the atom cloud. Higher intensities actually can have the negative effect of pushing the atom cloud into the beam direction, reducing the loading efficiency into the magnetic trap.

Pumping into the $|F = 1, m_F = -1>$ state

Alternatively, the atoms can be prepared in the $F = 1$ ground state. Since $g_1 = -1/2$, only the $m_F = -1$ state is a low-field seeker. To populate this state, the atoms first have to reach the $F = 1$ level, which is achieved by turning off the repumper laser before the molasses phase ends. We found a good time for this switch off to be 1 ms before the molasses phase ends. The cooling transition then no longer is closed off, and atoms accumulate in the $F = 1$ state. They are then optically pumped into the $m_F = -1$ state by a σ^--polarized beam resonant to the $|5S_{\frac{1}{2}}, F = 1\rangle \rightarrow |5P_{\frac{3}{2}}, F = 1\rangle$ transition. For this, the fiber on the optical pumping outcoupler has to be changed.
The magnetic trapping steps of the experiment cycle are unchanged if the $|F = 1, m_F = -1\rangle$ state is used. The reduction of the steepness of the magnetic traps by a factor two compared to $|F = 2, m_F = 2\rangle$ is very noticeable in the efficiency of the evaporative cooling, making successful condensation more difficult.
To detect the atoms with the normal imaging beam, the atoms have to be illuminated with the repumper laser during the imaging. The repumping is very efficient, so that turning the laser on for 2 ms is sufficient.

4.2.4 Magnetic Copper-Z Trap

At this stage the atoms are sufficiently cold so that they can be trapped by a purely magnetic trap. Instead of transferring the atoms directly to a chip-based trap, as is done in many other atom chip experiments [240, 124], we use an intermediate step. The initial magnetic trap for all our experiments is generated by the copper Z-structure underneath the chip. Together with a homogeneous field parallel to the wire plane, it creates a Ioffe-Pritchard type [85]. The homogeneous field can be decomposed into two components, one perpendicular to the central part of the Z-wire, and one parallel to it, which we label *bias* and *anti-Ioffe* field, respectively.
Due to its larger size and the much larger possible currents, both the effective capture area and the trap depth of the copper Z-trap are larger than what can be achieved with the chip traps. This allows a nearly complete transfer of the optical molasses to the magnetic trap. Only after a first evaporative cooling stage in the copper Z-trap, the atoms are transferred into an atom chip based trap.

Trap Loading

To guarantee an efficient transfer from the optical molasses to the magnetic trap, two factors have to be considered. Firstly, the center of the trap should overlap with the molasses center as precisely as possible. Secondly the initial steepness of the magnetic trap should match the temperature and extension of the atom cloud, i.e.

$$\omega_i = \sqrt{\frac{k_B T}{m r_i^2}} \tag{4.1}$$

where r_i is the extension of the molasses in the ith dimension. If the trap is too steep, the atoms will be heated during the transfer. If it is too shallow, the atoms can expand non-adiabatically which results in reduced phase-space density. This synchronizing of the magnetic trap and the optical molasses is known as *mode-matching* [166].
In our case the Cu-Z trap can not be made to exactly match the molasses shape, which is determined by the U-MOT potential, so that (4.1) can not be fulfilled for all three dimensions. The standard approach we choose is to use a trap with too steep transverse confinement (ω_x and ω_z larger than suggested by equation 4.1), because only then a sufficient longitudinal confinement is guaranteed. For this trap we use a current of 60 A in the Cu-Z, a bias field of 38 G, and a anti-Ioffe field of 20 G. With this trap we achieve the highest transfer efficiency of nearly 100%.
The steeper confinement both compresses and heats the atoms, typical temperatures are $\sim 350\,\mu$K after 50 ms magnetic trapping. Because of the higher density in the magnetic trap the phase space density stays roughly constant ($\phi = n\lambda_{dB}^3 \approx 10^{-7}$). This means that the transfer to the magnetic trap is almost adiabatic (for good mode matching).
The second aspect of the mode-matching is the overlapping of the optical molasses with the center of the magnetic trap. Since the parameters for the magnetic trap are determined by the matching of the trap shapes, the position of the magnetic trap center is fixed. The position of the optical molasses, on the other hand, can be changed by adjusting the magnetic fields during the final compression stage of the MOT. A displaced molasses in respect to the magnetic trap will lead to oscillations in the magnetic trap, which heats the atoms.

First evaporative cooling stage

After the initial transfer into the copper Z-trap, the bias and the anti-Ioffe field are ramped up to 45 G and 28 G within 1 s. This results in a magnetic trap with frequencies $\omega_x \approx \omega_y \approx 2\pi \times 400$ Hz and $\omega_z \approx 2\pi \times 40$ Hz. The minimum field strength at the center is 1 G. In this trap, the atoms are held for another 9 s.

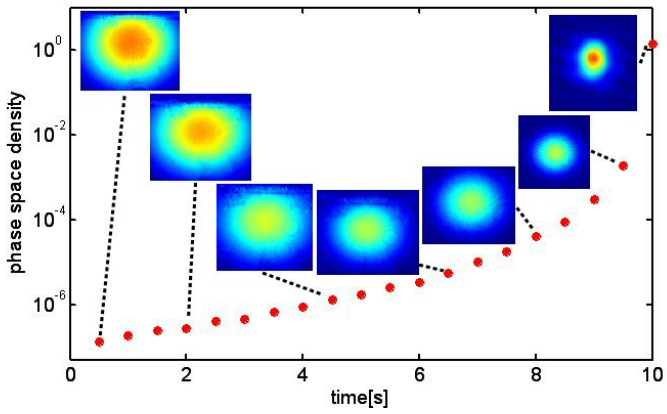

Figure 4.7: Increase of phase space density during the evaporative cooling in the Copper-Z trap. In contrast to the normal operation discussed in the text, here the final frequency of the rf cooling sweep was lowered to observe BEC in the Copper-Z trap. It proved to be much easier to transfer thermal atoms to the chip traps and only condense at the very end of the preparation cycle, as discussed in the main text.

During the total 10 s in the copper Z-trap a first stage of forced evaporative cooling is applied. A sinusoidal AC current (function generator: Agilent 33220A 20MHz Function/Arbitrary Waveform Generator) is coupled into the copper U-wire via a self-built bias-T to provide the required rf field. Analytical models of the evaporation process predict the most efficient cooling for exponential reduction of the radio frequency [246, 205, 58], but in practise linear frequency ramps work sufficiently well. We use a two-step linear sweep, which starts at 20 MHz. The frequency is then ramped down to 5 MHz in 5 s, followed by a second 5 s ramp from 5 MHz to $1-1.5$ MHz. The final temperature of the atoms is then $10-15\,\mu$K. In figure 4.7 the increase of phase space density during the cooling is shown. Note, that in this series of measurements the final cooling frequency was lowered to achieve BEC in the Copper-Z trap [140].

4.2.5 Transfer to atom chip traps

After the first rf-cooling phase in the Cu-Z trap the atoms are transferred to traps generated by one or more chip wires. Which wires are used depends on the actual experiments that are to be performed. The specific traps used will be described when these experiments are discussed in the next chapters

The transfer to a chip trap always follows the same scheme: After the end of the rf sweep in the copper Z, the current(s) in the chip wire(s) are ramped up to their final value for the desired trapping potential within 100 ms, while the copper-Z current and the homogeneous fields remain unchanged. In the next 100 ms the copper-Z current is ramped to zero, while the homogeneous fields are changed to values, such that the center of the resulting chip trap roughly coincides with the center of the original copper-Z trap. Then nothing is changed for 100 ms, after which the homogeneous fields are ramped up in another 100 ms ramp to the required values for the actual chip trap we want to work with. The total transfer to the atom chip takes 400 ms.

We found this scheme to be applicable to all chip traps we have loaded so far. The two stage approach of first transferring into and then compressing the chip trap reduces the atom loss and heating during the transfer. Care has to be taken during the whole process to avoid small or zero field strength at the trap minimum, so that Majorana losses are prevented. The transfer to different chip traps is described in detail in [140].

4.2.6 Chip experiments

Once the atoms are loaded into an initial chip trap, usually a second stage of rf cooling follows. From there on the remaining steps depend on the actual experiment. For the experiments discussed in this manuscript, almost exclusively the single wire Z-trap based on the $100\,\mu$m wide Z-shaped chip wire (T-H) is used, which will be discussed in detail in the next chapter.

Typical experiment durations in the chip traps are 1−5 s. In general the duration of the experiments is limited by the heating of the chip wires. Usually we monitor the resistance of the used wires during the experiments. We choose the upper values for the currents and the experiment duration in such a way that we observe no temperature-induced resistance change larger than 1% during an experiment run to avoid the risk of permanently damaging the chip structures.
The chip currents are provided by custom built controlled current power supplies with a maximum current of 2 A (accuracy $\sim$ 0.1 mA). Fast electronic switches allow turn-off times on the order of 10 μs.

4.2.7 Imaging of the Atom Distribution

The final step of each experiment cycle is the imaging of the atom distribution. The standard imaging technique we employ is absorption imaging, in which the attenuation of a laser beam passing through the atom cloud is measured [166].
To obtain an absorption image a pulse of resonant laser light is send through the experiment area onto the imaging optics and is imaged with the CCD camera. Depending on the distribution of atoms in the beam path the beam profile will be altered because an amount of light proportional to the number of atoms will be scattered. After the atoms have dispersed from the imaging area an image of a second pulse is taken, to obtain the unattenuated beam profile. This serves as a reference and accounts for inhomogeneities in the profile. A third image is taken when all laser light is switched off to measure stray light falling onto the camera.
From these three images the final image is calculated by the following pixel-wise operation:

$$I_{absorp} = 1 - \frac{I_{withatoms} - I_{background}}{I_{withoutatoms} - I_{background}}. \tag{4.2}$$

From this image, the column density of the atom ensemble, i.e. the density distribution integrated along the imaging axis (chosen to be z-axis here), can be obtained:

$$\tilde{n}(x,y) = \int \mathrm{d}z n((r)) = -\frac{1}{\sigma_{abs}} \log(I_{absorp}(x,y)), \tag{4.3}$$

where σ_{abs} is the effective absorption cross section of the atoms (which depends on the used polarization) [66].
From absorption images taken *in situ*, while the magnetic trapping fields are on, the actual atom distribution in the magnetic trap can be obtained. The spatially dependent detuning of the imaging beam due to the trapping field has to be taken into account. Because of the high densities of the trapped atoms the atom cloud is usually *optically dense*, meaning that the imaging light is fully absorbed in the area around the trap center. This prevents a calculation of the number of atoms in the cloud because densities above a certain saturation value can not be differentiated. To avoid this problem the frequency of the imaging beam can be shifted away from resonance (*off-resonance imaging* to lower the amount of absorbed light.
An alternative is to use a *time-of-flight* (ToF) method. For this the atom distribution is imaged a certain time after the magnetic trapping fields have been switched off. In this duration the atoms expand ballistically in all directions and fall down because of gravity. When the ToF is chosen long enough to ensure no optical dense areas the number of atoms can be calculated from the total amount of absorbed light [166]. Here also no modification of the images due to magnetic fields occurs. From the speed of the expansion also the temperature of the atom ensemble can be calculated.

5 Implementation of radio-frequency potentials on an atom chip

Atom chips are ideally suited for the experimental realization of the rf dressed state potentials discussed in chapter 2. Rf (near) fields with large amplitudes can be created by oscillating currents of relatively low amplitude in the chip wires. Additionally, the precise control and the strong field gradients of chip traps traps allow to fully exploit the spatial dependence of both the detuning and the Rabi frequency of the rf potentials. In turn, the integration of oscillating fields on atom chips further enhances the flexibility of these devices, as this and the next chapters will show.
In this chapter we present the atom chip wire setup we use for the implementation of rf potentials in our experiment (section 5.1). A combination of three main current-carrying wires and external magnetic fields is used to create a field configuration corresponding to a standard Ioffe-Pritchard trap (compare section 2.1.4) and two independent, (approximately) linear rf fields of same frequency [193, 142].
In section 5.2 we will use the RWA formalism derived in section 2.3.2 and approximative descriptions of the involved fields to calculate simple analytic formulas for the resulting rf potentials of this three-wire trap [193, 186]. We find that besides the obvious parameters, the amplitude and frequency of the rf fields, the shape of these potentials is mainly determined by the phase shift between the two rf fields. In particular, we discuss in detail the two special cases of linearly and circularly polarized total rf field, which result in a double well and a ring like potential configuration, respectively. We also show that in the general case of arbitrary phase shift, the dependence of the rf potentials on the hyperfine g-factor of the trapped atoms can be used to realize state-dependent potentials.
In section 5.3 we improve the potential calculation by considering realistic magnetic wire fields. Using the method presented in section 2.2.3 for calculating the wire magnetic fields present in the experiment, a full three-dimensional (numeric) calculation of the rf potentials is carried out. We find a particularly strong deviation from the analytic formulas in the case of the ring potential. In contrast, we show that in the case of the double well, the spatial dependence of the wire fields can be constructively used to counter potential imbalances introduced by gravity.
A further improvement in precision is obtained when the non-RWA contributions to the rf potentials are included, which is done in section 5.4. We find that noticeable deviations from the RWA calculations should indeed occur for the upper range of typical experimental parameters [141]. In particular, we find that in the case of the double well, the height of the potential barrier can be significantly altered by the non-RWA effects. From these results we can estimate validity ranges for the numerically less time-intensive RWA calculations. An experimental verification of the non-RWA effects by means of a spectroscopic measurement will be discussed in chapter 6.
The observation of the different realizable potential configurations of the three-wire trap in the experiment is presented in section 5.6. The scheme for loading atoms into the rf dressed state potentials is discussed. We demonstrate the freely tunable orientation of the double well potential for the case of linearly polarized total rf field and show how a state-dependent double well can be realized with elliptical rf field polarization [142].
Some of the results presented in the next chapters were obtained with a slightly different wire configuration employing only a single rf field. This configuration is only very briefly discussed in section 7.1, a much more detailed discussion can be found in the thesis of T. Schumm [282]. The field configuration of this two-wire trap can be seen as a special case of the three-wire trap with

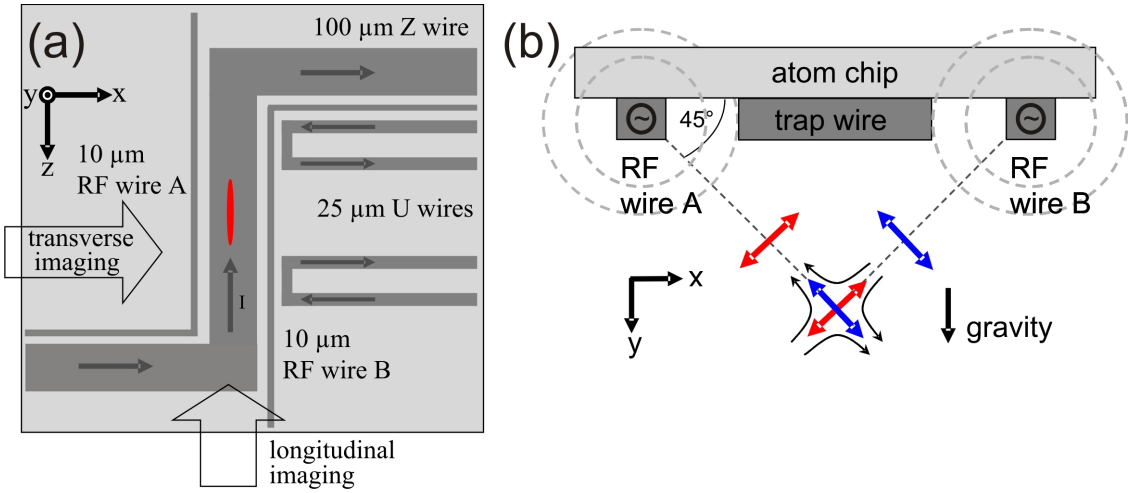

Figure 5.1: Layout of the three-wire RF trap. **(a)** Top view. A central Z-shaped wire provides the inhomogeneous part of the static magnetic field. In combination with a homogeneous bias field an elongated harmonic trap is formed. The aspect ratio of the trap can be modified by the U-shaped wires on the side. The rf field is created by two independent L-shaped wires, one on each side of the Z-trap. The directions of the two horizontal imaging systems is indicated. The wires are not drawn to scale here. **(b)** Side view from the longitudinal direction. The transverse quadrupole field component of the static trap is shown. It can be seen that its main axes are under 45° to the chip surface. The two rf wires create fields that coincide with these axes in the vincinity of the static trap minimum.

linearly polarized rf field, in particular the analytical results derived in this chapter can be directly transferred to the two-wire case.

5.1 Three-wire rf trap layout

We use wire configuration consisting of three main wires to implement the rf potentials. The schematic wire layout of this three-wire trap is shown in figure 5.1a. The letters used in the following to label the different wires correspond to the notation of figure 4.3 and the labels used in the laboratory.

The central 100 μm wide Z-shaped wire (T-H) is used to form a static Ioffe-Pritchard trap (section 2.2.2). For the trap minimum to be located directly below the Z-wire, a bias field parallel to the chip surface is required. Two L-shaped wires, one on each side of the Z-wire, function as rf sources, the (S-N) wire on the left side, and the (X-G) wire on the right side. The width of both of these wires is 10 μm. Since these two wires do not share any connections, independent AC currents can be applied to them. The center to center distance of the (S-N) wire to the Z-wire is 125 μm, for the (X-G) wire it is 115 μm. This asymmetric distance of the two rf wires can be compensated in the experiment by accordingly adjusting the ratio of the AC currents.

Two U-shaped wires of width 25 μm (B-C and E-F) on the right side of the three-wire configuration can be used to modify the longitudinal confinement of the Z-wire trap (almost) independently of the transverse confinement and the distance between trap center and chip surface. This allows a modification of the static trap aspect ratio without changing the transverse field configuration of the rf trap.

In figure 5.1b the resulting field configuration in the x-y plane is schematically shown. The main axes of the transverse quadrupole field underlying the Z-trap are tilted by 45° in respect to the chip surface. The two rf wires create circular magnetic field, which can be approximated as being linear over the area of the static trap center. If the static trap is placed at a surface distance equal to the distance between rf wires and Z-wire, the two rf fields are perpendicular in the vicinity of the static trap minimum. The asymmetry in the rf wire distances is not shown in this scheme, since

it can be compensated by scaling the AC currents, to provide rf fields with identical amplitude at the trap center.

5.2 Analytical calculation of the rf potential

We will start the calculation of the rf potential produced with the three wire setup by considering idealized fields, which approximate the real wire fields in the area around the static trap center. We will also restrict the calculation to the transverse plane, and only consider the (much smaller) effect of the rf field on the longitudinal component of the potential later. For these idealized fields the rf potentials can be calculated analytically, allowing for a systematic discussion of the resulting trap geometries. In the next section we will see, that consideration of realistic wire magnetic fields will quantitatively change the rf potentials, but not qualitatively alter the trap geometries compared to the idealized calculation.
As discussed in section 2.2.2, the magnetic field of a Z-trap in the x-y plane can be approximated in the vicinity of its minimum by

$$\mathbf{B}_{\mathrm{S}}(\mathbf{r}) = G\rho\left[\cos\phi\mathbf{e}_x - \sin\phi\mathbf{e}_y\right] + B_{\mathrm{I}}\mathbf{e}_z, \tag{5.1}$$

i.e. by a quadrupole field with gradient G in the plane perpendicular to the central part of the Z-wire and a constant Ioffe field with amplitude B_{I} parallel to it. $\rho = \sqrt{x^2+y^2}$ and $\phi = \arctan\frac{y}{x}$ are polar coordinates.
The rf field we write as the superposition of two perpendicular, linear fields

$$\left[B_{\mathrm{A}}\mathbf{e}_x + B_{\mathrm{B}}e^{i\delta}\mathbf{e}_y\right]e^{\omega_{\mathrm{rf}}t} = \mathbf{B}_{\mathrm{rf}}e^{\omega_{\mathrm{rf}}t}. \tag{5.2}$$

Here, δ is the phase shift that can be introduced between the two components of the rf field. With the fields (5.1) and (5.2) we can calculate the rf potentials, as discussed in chapter 2. First, the static field term is diagonalized by the unitary transformation (2.3)

$$U_{\mathrm{S}}(\mathbf{r}) = \exp\left[-iF_{\mathrm{z}}\phi(\mathbf{r})\right]\exp\left[-iF_{\mathrm{y}}\beta(\mathbf{r})\right] \tag{5.3}$$

with $\cos\beta = \frac{B_{\mathrm{I}}}{|\mathbf{B}_{\mathrm{S}}(\mathbf{r})|}$ and $\sin\beta = -\frac{G\rho}{|\mathbf{B}_{\mathrm{S}}(\mathbf{r})|}$ and $|\mathbf{B}_{\mathrm{S}}(\mathbf{r})| = \sqrt{G^2\rho^2 + B_{\mathrm{I}}^2}$.
The corresponding rotation matrices which are applied to the magnetic fields read

$$R_y\left[\beta\right]R_z\left[\phi\right] = \begin{pmatrix} \frac{B_I}{\sqrt{B_I^2+G^2\rho^2}} & 0 & -\frac{G\rho}{\sqrt{B_I^2+G^2\rho^2}} \\ 0 & 1 & 0 \\ \frac{G\rho}{\sqrt{B_I^2+G^2\rho^2}} & 0 & \frac{B_I}{\sqrt{B_I^2+G^2\rho^2}} \end{pmatrix}\begin{pmatrix} \cos\phi & -\sin\phi & 0 \\ \sin\phi & \cos\phi & 0 \\ 0 & 0 & 1 \end{pmatrix}. \tag{5.4}$$

To reach a Hamiltonian of the form (2.33) we remove the F_y component of the oscillating field by another rotation around the (new) z-axis, with the rotation angle λ being given by

$$\lambda = \arctan\left(\frac{\tilde{B}_{\mathrm{rf,x}}}{\tilde{B}_{\mathrm{rf,y}}}\right), \tag{5.5}$$

where $\tilde{B}_{\mathrm{rf,x}}$ and $\tilde{B}_{\mathrm{rf,y}}$ are the x- and y-components of the rf field after the first rotation $\tilde{\mathbf{B}}_{\mathrm{rf}} = R_y\left[\beta\right]R_z\left[\phi\right]\mathbf{B}_{\mathrm{rf}}$, respectively. After this rotation, the rf field has the form

$$R_z\left[\lambda\right]R_y\left[\beta\right]R_z\left[\phi\right]\mathbf{B}_{\mathrm{rf}} = \begin{pmatrix} B_{\mathrm{rf}\perp} \\ 0 \\ B_{\mathrm{rf}\parallel} \end{pmatrix}, \tag{5.6}$$

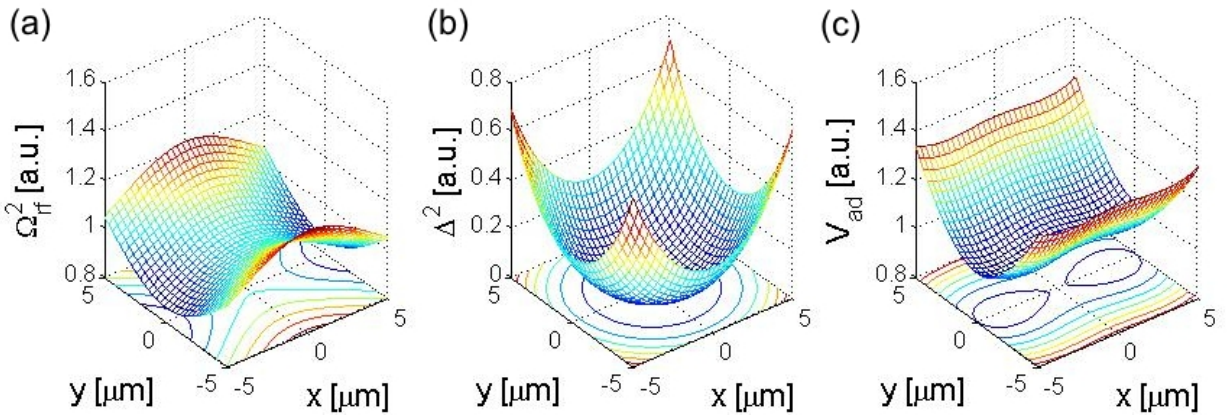

Figure 5.2: Formation of the double well potential in the case of linear polarized rf field. **(a)** The complete angular dependence of the adiabatic potential is contained in the Rabi frequency Ω. This term always has two minima, which are located at $\pm(\alpha, \alpha+\pi)$, depending on $\delta = 0$ or $\delta = \pi$. **(b)** The detuning Δ is a function of ρ only. For $\mu_B B_I > \hbar\omega_{rf}$ it has a single minimum at the origin, as shown here. If $\mu_B B_I < \hbar\omega_{rf}$, the detuning vanishes on a circle of radius $\rho = \frac{\sqrt{(\hbar\omega_{rf})^2 - B_I^2}}{G}$ and has a local maximum at $\rho = 0$. **(c)** The resulting adiabatic potential has the same angular dependence as the Rabi frequency, resulting in the formation of a double well potential. If the detuning has its minimum at the origin ($\Delta_0 > 0$), the rf field amplitude must be larger than a critical field strength B_C, to form a double well. If the field amplitude is too small, the two minima coincide at $\rho = 0$. For $\Delta_0 < 0$ there always is a double well.

which x-component can now be inserted into equation (2.46) to obtain the (RWA) adiabatic rf potential. This leads, after some calculation, to

$$V_{ad} = \tilde{m}_F g_F \mu_B \sqrt{\Delta(\mathbf{r})^2 + \Omega(\mathbf{r})^2}, \tag{5.7}$$

with the detuning and the Rabi frequency

$$\Delta(\mathbf{r}) = |\mathbf{B}_S(\mathbf{r})| - \frac{\hbar\omega_{rf}}{|g_F \mu_B|} \tag{5.8}$$

$$\frac{8\,|\mathbf{B}_S(\mathbf{r})|^2\,\Omega^2(\mathbf{r})}{B_A^2 + B_B^2} = 2B_I\,[B_I + |\mathbf{B}_S(\mathbf{r})|\sin(2\alpha)\sin\gamma] \tag{5.9}$$

$$+G^2\rho^2\,[1 - \cos(2\alpha)\cos(2\phi) \tag{5.10}$$

$$+\sin(2\alpha)\sin(2\phi)\cos\gamma]\,.$$

Here, $\tan(\alpha) = \frac{B_B}{B_A}$, and $\gamma = -\frac{g_F}{|g_F|}\delta$ is the effective phase shift which depends on the sign of the g-factor g_F.
In the following, we will consider two special cases for the phase shift δ. First, we treat the case $\delta = 0, \pi$, i.e. the two field components being in phase, or shifted exactly by half an oscillation period. In either situation, the resulting total field oscillates along a single line, or in other words it is *linearly polarized*. The rf potential resulting in this case will be discussed in section 5.2.1.
For phase shifts $\delta = \pi/2, 3\pi/2$, the total rf field is *eliptically polarized*. A special case of elliptic polarization is *circular polarization*, which is given here if $B_A = B_B$. This case will be discussed in section 5.2.2.

5.2.1 Linear polarization: double well

If $\delta = 0, \pi$, the Rabi frequency (5.9) simplifies to

$$\Omega^2(\mathbf{r}) = \frac{B_A^2 + B_B^2}{8\,|\mathbf{B}_S(\mathbf{r})|^2} \times \left[2B_I^2 + G^2\rho^2 f(\phi)\right], \tag{5.11}$$

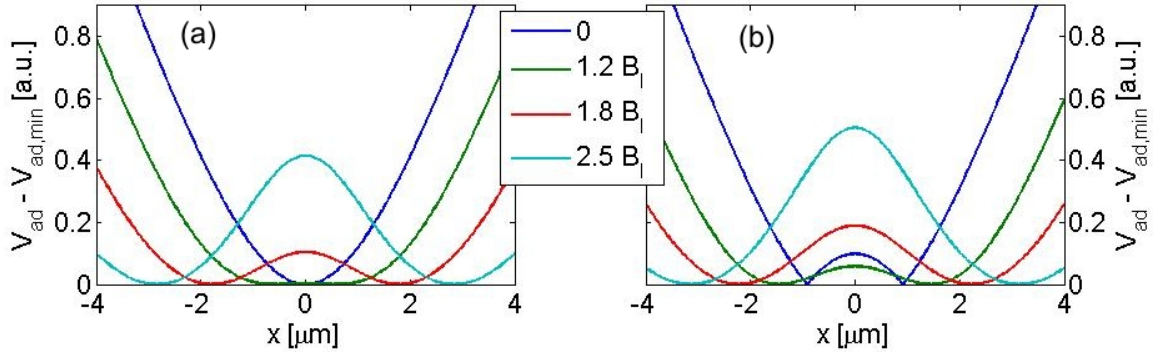

Figure 5.3: Double well potentials for different detunings and rf field amplitudes **(a)** Rf potentials for different rf field amplitudes for $\frac{\Delta_0}{\mu_B B_I} = 0.2$. The rf field amplitude is expressed in units of the Ioffe field strength B_I. For rf field amplitudes smaller than B_C the potential only has only a single minimum, while for for larger amplitudes, a double well is established. The potential bottom of the individual curves has been substracted. **(b)** Rf potentials for $\frac{\Delta_0}{\mu_B B_I} = -0.2$. In this case, the potential always is a double well, even for arbitrarily small rf fields (the rf amplitude 0 case should be understood here as infinitesimally small value).

with

$$f(\phi) = 1 - \cos(2\alpha)\cos(2\phi) \pm \sin(2\alpha)\sin(2\phi). \tag{5.12}$$

Here, the sign of the third term is positive (negative) for $\delta = 0$ ($\delta = \pi$). In figure 5.2 the detuning and the Rabi frequency are plotted independently. Since $|\mathbf{B}_S(\mathbf{r})| = \sqrt{G^2\rho^2 + B_I^2}$ is rotationally symmetric, the detuning (5.8) is not a function of ϕ (figure 5.2b). Consequently, the complete angular dependence of the adiabatic potential is contained in $f(\phi)$ (figure 5.2c). This function has two minima ϕ_1, ϕ_2 in the interval $[0, 2\pi]$, at $\alpha, \alpha + \pi$ for $\delta = 0$ and at $-\alpha, -\alpha + \pi$ for $\delta = \pi$. Comparing this result with the orientation of the magnetic field vectors shows that the minima are located on the axis where the rf field and the quadrupole field are parallel.
Along this axis, the adiabatic potential in the area where $\rho \ll B_I/G$ can be approximated by

$$V_{DW}(\rho, \phi_{1,2}) = \tilde{m}_F g_F \mu_B \sqrt{\frac{G^4}{B_I^2}\left(\frac{\rho^2 - \rho_0^2}{2}\right)^2 + B_0^2}, \tag{5.13}$$

with the position of the potential minimum (for $|\mathbf{B}_{rf}| \geq B_C$)

$$\rho_0 = \frac{1}{\sqrt{2}G}\sqrt{|\mathbf{B}_{rf}|^2 - B_C^2}, \tag{5.14}$$

and the field amplitude at the minimum

$$B_0 = \frac{|\mathbf{B}_{rf}|}{4B_I}\sqrt{4B_I^2 + B_C^2 - 2G^2\rho_0^2} \approx \frac{|\mathbf{B}_{rf}|}{2}\sqrt{1 + \frac{\hbar\Delta_0}{|g_F|\mu_B B_I}} \tag{5.15}$$

In order to arrive at the last term we have exploited $G\rho_0 \ll B_I$. Furthermore, we introduced the critical field strength

$$B_C^2 = 2B_I\frac{\hbar\Delta_0}{|g_F|\mu_B} \tag{5.16}$$

and the detuning at the origin

$$\hbar\Delta_0 = |g_F|\mu_B B_I - \hbar\omega. \tag{5.17}$$

For $\Delta_0 > 0$, there are two possible cases. If $|\mathbf{B}_{rf}| \leq B_C$, (5.13) has a minimum at $\rho = 0$. The rf field only deforms the original static potential from its harmonic shape. When $|\mathbf{B}_{rf}|$ becomes larger

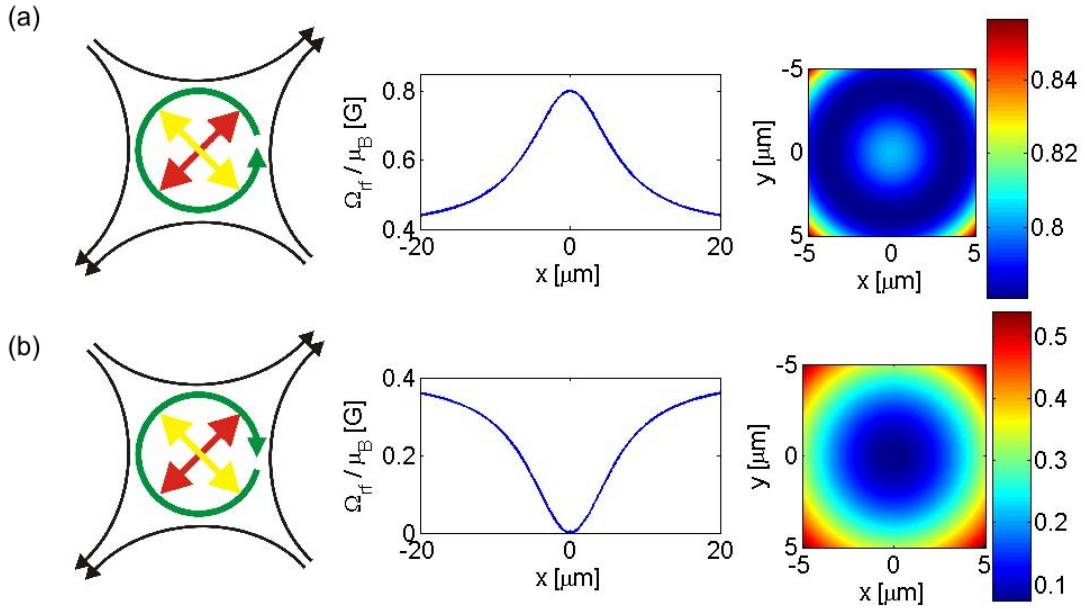

Figure 5.4: Rf potentials for circular polarization of the rf field in the case of $|g_F| = 1$, $\tilde{m}_F = 2$, and $\Delta_0 < 0$. **(a)** For a phase shift $\delta = \pi/2$, the polarization of the rf field is left-handed (left image). The Rabi frequency then is maximal at the original trap center (center image). This results in a ring shaped adiabatic rf potential if the rf field amplitude is larger than a critical value (right image, showing V_{ad}/μ_B in units of Gauss). **(b)** For right-handed circular polarization $\delta = 3\pi/2$, the Rabi frequency has a minimum at the origin. The resulting potential always has only a single minimum, regardless of the rf field amplitude.

then the critical field strength B_C, the position of the potential minimum moves away from the origin and a double well is formed, as shown in figure 5.3a.
If the frequency of the rf field is larger than the static field Lamor frequency at the trap center, i.e. if $\Delta_0 < 0$, B_C^2 is negative. In that case, the rf potential always has a minimum at $\rho_0 > 0$, which again means a double well is formed (figure 5.3b).
In summary, for a linearly polarized rf field the resulting potential is either a deformation of the original static potential with the same minimum position or a double well potential. The orientation of the double well is determined by the rf field direction, the minima lie on the line where rf field and static quadrupole field are parallel.

5.2.2 Circular polarization: ring potential

We now consider the case of a circularly polarized rf field, which is given if $\delta = \pi/2, 3\pi/2$. The second requirement is $B_A = B_B$, which means $\alpha = \pi/4$. Entering these angles into (5.9), leads to

$$\begin{aligned}\Omega^2(\mathbf{r}) &= \frac{|\mathbf{B}_{rf}|^2}{8\,|\mathbf{B}_S(\mathbf{r})|^2}\left[2B_I\left[B_I \pm |\mathbf{B}_S(\mathbf{r})|\right] + G^2\rho^2\right] \\ &= \frac{|\mathbf{B}_{rf}|^2}{8\,|\mathbf{B}_S(\mathbf{r})|^2}\left[|\mathbf{B}_S(\mathbf{r})|^2 \pm 2B_I\,|\mathbf{B}_S(\mathbf{r})| + B_I^2\right] \\ &= \frac{|\mathbf{B}_{rf}|^2}{8\,|\mathbf{B}_S(\mathbf{r})|^2}\left(|\mathbf{B}_S(\mathbf{r})| \pm B_I\right)^2. \end{aligned} \tag{5.18}$$

The $\pm$ sign depends on the effective phase shift $\gamma = -\frac{g_F}{|g_F|}\delta$, which can take four values. For $\gamma = \pi/2, -3\pi/2$ the sign is positive, for $\gamma = -\pi/2, 3\pi/2$ it is negative. As a consequence, the

resulting potential is determined not only by the helicity of the rf field, but also by the sign of the g-factor g_F of the trapped atoms.
The Rabi frequency (5.18) is a function of ρ only, hence the effective adiabatic potential is rotationally symmetric (since Δ also does not depend on ϕ). In the "minus" case, the Rabi frequency vanishes at the origin and then grows monotonically towards the constant value $|\mathbf{B}_{rf}|/\sqrt{8}$. For the "plus" sign, it has a maximum at $\rho = 0$ and then converges towards the same value for large ρ.
The total adiabatic potential reads

$$V_{ad} = \tilde{m}_F g_F \mu_B \sqrt{\left[|\mathbf{B}_S(\mathbf{r})| - \frac{\hbar\omega_{rf}}{|g_F|\mu_B}\right]^2 + \frac{|\mathbf{B}_{rf}|^2}{8\,|\mathbf{B}_S(\mathbf{r})|^2}\,(|\mathbf{B}_S(\mathbf{r})| \pm B_I)^2}. \tag{5.19}$$

Assuming $\rho \ll B_I/G$ the extrema of this function formally lie at radial positions

$$\rho_0 = \frac{1}{2G}\sqrt{|\mathbf{B}_{rf}|^2\,[1+\sin(\gamma)] - 2B_C^2}, \tag{5.20}$$

with B_C^2 as defined in (5.16). For $\Delta_0 < 0$ (equation 5.17), i.e. for a radio frequency larger than the frequency spacing between static m_F levels at the trap center, B_C^2 is negative, and there always is a minimum at $\rho_0 > 0$, independent of γ. In this case, the resulting potential is ring-shaped for any $|\mathbf{B}_{rf}|$. Changing the helicity of the rf field then only shifts the position of minimum, i.e. changes the diameter of the ring (it also affects the potential bottom of course).
If $\Delta_0 > 0$, a more interesting situation arises. For $\sin(\gamma) = -1$, the potential always has a single minimum at $\rho = 0$ (formally ρ_0 becomes purely imaginary), independent of the rf field amplitude. In the case of $\sin(\gamma) = 1$, on the other hand, the radial minimum moves away from the origin, once $|\mathbf{B}_{rf}|^2 > B_C^2$. This means, that for $\Delta_0 > 0$, the helicity of the rf field plays a fundamental role in the formation of the adiabatic potential. One handedness leaves the static potential unchanged, while the other can deform it into a ring trap, with the sign of the g-factor deciding which handedness results in which potential. This dependence on the helicity is shown in figure 5.4 for the case $|g_F| = 1$.

5.2.3 Arbitrary polarization: state-dependent potentials

The dependence of the adiabatic potential on the sign of the g-factor of the trapped atoms, as discussed above for the special case of circularly polarized rf field, is a general feature of the system for arbitrary polarization. It only vanishes in the case of linear polarization, where the potentials are identical for both signs of g_F.
This can be used for internal state-dependent manipulation of atoms. For this, two hyperfine states $|1\rangle$ and $|2\rangle$ with $g_{F,|1\rangle} = -g_{F,|2\rangle}$, but with identical magnetic moment $\mu = m_F g_F \mu_B$ are required. In the case of ^{87}Rb, the $|F = 1, m_F = -1\rangle$ and the $|F = 2, m_F = 1\rangle$ states fulfill this requirement, since $g_1 = -1/2$ and $g_2 = 1/2$. In a static magnetic field, these states experience the same energy shift. For this reason, these states are used in Rb atom clocks, where the (microwave) frequency of this transition is used as a time reference [306], and are hence known as *Rb clock states*. More specifically, in a magnetic trap, both states will see identical confining potentials.
If such a magnetic trap containing atoms of both species is now modified by an rf field of polarization $\delta \neq 0, \pi$, the resulting potentials will differ. In the example considered in the last section, the potential of one species can be deformed from a single minimum to a ring trap by adiabatically ramping up the rf field amplitude. The potential seen by the other species is unaffected by the rf field, leading to a spatial separation of atoms in different states.
Another example is shown in figure 5.5. Here, an elliptically polarized rf field is used to create a double well potential for one species, while the second species sees a (deformed) single minimum potential. Depending on the parameters chosen, the spatial overlap between the two species can be controlled. Such a setup could be used for example for studying the effects of inter-species

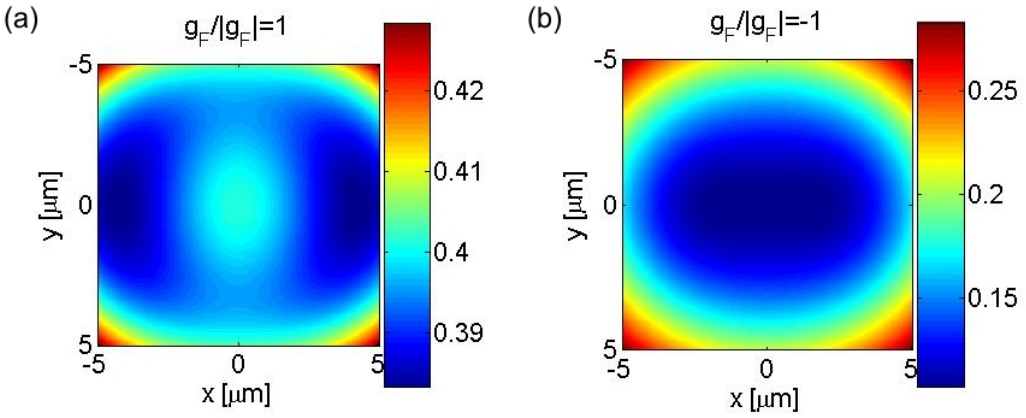

Figure 5.5: State dependence of the rf potentials for elliptically polarized rf field. **(a)** Adiabatic potential $V_{\mathrm{ad}}/\mu_{\mathrm{B}}$ in units of Gauss for $g_{\mathrm{F}} = 1/2$,$\tilde{m}_{\mathrm{F}} = 1$ for a phase shift of $\delta = \pi/2$ (parameters $\nu_{\mathrm{rf}} = 650$ kHz, $G = 0.15$ G/μm, $B_{\mathrm{I}} = 1$ G, $B_{\mathrm{A}} = 1$ G, $B_{\mathrm{B}} = 0.6$ G). Atoms in this hyperfine state experience a slightly deformed double well potential. **(b)** Resulting potential for the same parameters seen by atoms in a hyperfine state with $g_{\mathrm{F}} = -1/2$,$\tilde{m}_{\mathrm{F}} = -1$. The underlying static confinement is elongated in one direction by the rf field, but no potential barrier exists in the center.

collisions on the coherence properties of a coherently split BEC. The experimental realization of such a potential and the demonstration of its state-dependence will be described in section 5.6.4.

5.3 RWA rf potential for realistic wire fields

The model magnetic fields used in the last section allowed a detailed qualitative discussion of the resulting rf potentials and yielded first order quantitative formulas. For a more accurate calculation of the rf potentials the actual wire magnetic fields produced by the configuration used in the experiment have to be considered . These wire fields can be calculated following the scheme discussed in 2.2.3. The current flow in the wire geometry shown in figure 5.1 is approximated by rectangular "current blocks", for which the magnetic field is given by equation (2.31). The three dimensional rf potential is then obtained by entering these magnetic fields in Hamiltonian (2.37) and numerically performing the unitary transformations as discussed in the last section.
The result of this calculation for a typical parameter set is visualized in figure 5.6. Here, a phase shift of $\delta = \pi$ was used, resulting in a double well potential. The highly anisotropic trap shape can be seen. Also, the transverse potential changes asymmetrically along the z-direction.
In general, the consideration of realistic fields leads to deviations from the idealized analytical formulas derived in the last section, as could be expected. The overall shape of the resulting potentials remains unchanged, though. A double well or a ring shaped potential is still obtained for (approximately) linear and circular polarization. In the following, we will discuss which properties of the realistic fields are most important for the deviations and how good the approximate results of the last section are in practise. We will first focus again on the potential in a single transverse plane at the longitudinal minimum position z_0. Next, in section 5.3.2 the longitudinal behavior of the potential will be discussed.

5.3.1 Realistic rf potential in the transverse plane

We define the transverse plane as the one perpendicular to the longitudinal axis of the static Z-trap. As discussed in section 2.2.2, this plane is slightly titled with respect to the (x, y) plane by an angle β which is determined mainly by the length of the central bar of the Z-wire and the trap distance

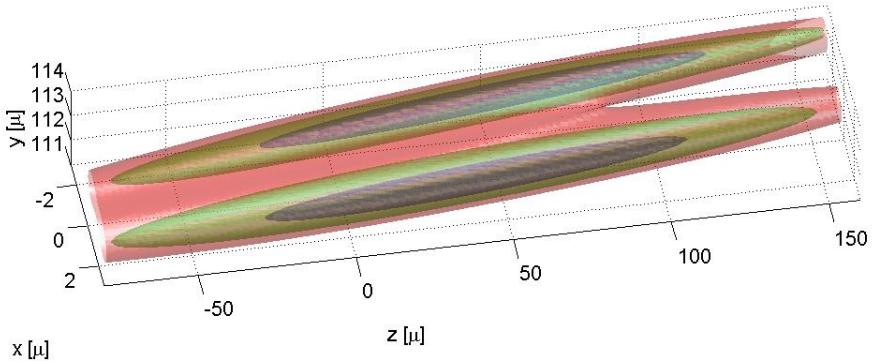

Figure 5.6: 3d visualization of the rf potential of the three-wire trap for $g_F = 1/2$, $\tilde{m}_F = 2$ calculated with realistic wire magnetic fields. The complete, three dimensional wire configuration, consisting of the Z-trap wire, two L-shaped rf wires, and two additional U-wires is included. Shown are the equipotential surfaces for $V_{ad}/h = 2, 5, 8$ kHz (blue, green,red). The origin of the coordinate system is located at the central point of the Z-wire, which also is the middle point of the atom chip. The chip surface lies in the (x, z) plane.
Parameters are $I_Z = 1.5$ A, $\mathbf{B}_{bias} = (25, 0, 0.6)$ G, $I_U = 0.5$A, $I_{rf,A} = 40$ mA, $I_{rf,A} = 29$ mA, $\delta = \pi$, $\nu_{rf} = 650$ kHz. The resulting rf potential is a double well, slightly rotated in the (x, y) plane. The potential is also tilted in the (x, z) plane with respect to the Z-wire, which is due to slightly rotated main trap axis of the static Z-trap. Furthermore, it can be seen that the transverse confinement and the barrier height are functions of the z-coordinate.

to the chip. For our experiment parameters the numeric potential calculation yields $\beta \approx 0.5°$, so that the asymmetry in the rf field setup introduced by this rotation has (nearly) no effect. We still include the transformation of the coordinate system onto the main axes of the Z-trap by a rotation of angle β around the y-axis, to better isolate other effect contributing to potential asymmetries in the following considerations.
All relevant fields in the transverse plane in an area around the trap minimum for typical experiment parameters are shown in figure 5.7. Three important deviations from the idealized fields considered in the last section can be identified: the rf fields and the Ioffe field have gradients in their absolute field strength, due to the distance dependence of the wire fields (figure 5.7a,b,e). Thirdly, for growing distance from the center point the two rf fields are no longer exactly perpendicular to each other (figure 5.7c). The importance of each one for the obtained rf potentials can be tested by artificially removing this deviation in the calculation.
The result of this procedure is that the inhomogeneity in the field amplitude of the rf fields leads to the main modification of the rf potentials, followed by the inhomogeneity of the Ioffe field strength. The deviation from perpendicular orientation only causes very small effects and can be neglected, if the rf trap is placed near the center point of perfect orthogonality, which lies at a distance of $d = 107.5\,\mu$m from the chip surface. For displacements larger than $r \approx 10\,\mu$m this effect can become dominant.
The modification of the rf potential effected by the realistic wire fields depend on the particular potential considered. Below we discuss the special cases of linear and circular polarization.

Linear polarization: Horizontal double well

In the case of the double well oriented parallel to the chip, the real wire effects play no significant role in the transverse direction. The formulas derived in the last section and listed in [193] describe the potential with good precision.

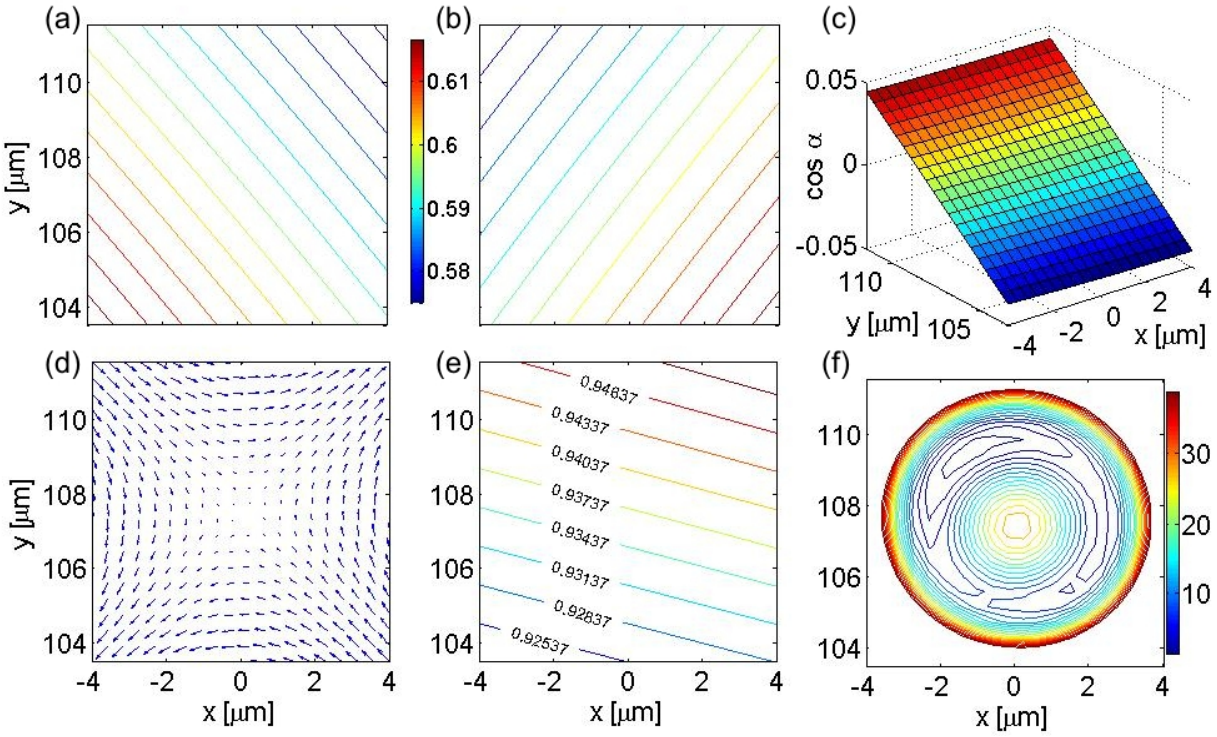

Figure 5.7: Analysis of the realistic wire field effects in the transverse direction of the three wire rf trap. **(a)** and **(b)** Contour plots of the absolute value of the magnetic fields produced by the two rf wires in a $8 \times 8\,\mu\mathrm{m}^2$ area around the trap minimum for identical wire currents $I_{\mathrm{rf}} = 50$ mA in Gauss. The gradient in the field amplitude is due to the increasing distance from the field generating wires. Over the considered area there is a change of 5% in the field amplitude. Also the absolute values for each wire field differ slightly due to the distance difference of the two wires to the trap center. **(c)** Surface plot showing the angle α between the two rf fields as a function of position. The deviation from perpendicular fields in the considered area is up to 0.05rad$\approx 3°$. The deviation increased more strongly in the vertical than in the horizontal direction, which is a consequence of the rectangular shape of the rf wires. **(d)** Vector plot of the transverse component of the total static field, which is well described by a rotationally symmetric quadrupole field. A slight rotation of the main axes is caused by the asymmetric field of the U-wires. **(e)** Contour plot of the longitudinal component of the static field in units Gauss. Again a growing field strength toward the chip surface can be seen. The difference over the observed area is $\approx 2\%$ for a typical Ioffe field strength of 1G. Also the field lines are tilted with respect to the chip, due to the finite length of the outer bars of the Z-wire and the asymmetric contribution from the U-wires. **(f)** Contour plot of the resulting rf potential V_{ad}/h for phase shift $\delta = \pi/2$ in units kHz. The potential has a ring-like shape, but the realistic wire fields result in asymmetries in the potential. The ring has a pronounced minimum at the side opposite from the chip surface, caused mainly by the inhomogeneous rf fields. The inhomogeneous Ioffe field also contributes. The horizontal asymmetry is due to the different rf wire distances, but can be removed by adjusting the rf currents. The inhomogeneity of the ring potential is in practise further increased by gravity, which is not included here.

Linear polarization: Vertical double well

For the rotated double well, and most significantly for the vertical double well, aligned perpendicular to the chip surface, the inhomogeneous rf fields result in an imbalancing of the potential. While the well separation remains nearly unchanged, the potential bottoms at both minima are modified. Here, two effects play a role: For distances near the $d = 107.5\,\mu$m at which the two rf fields are perpendicular, the inhomogeneity in the field amplitudes dominates, resulting in a larger Rabi frequency at the potential well closer to the chip surface. Away from this center point the deviation of the angle between the two rf fields from 90° becomes the dominating effect, resulting in a reduction of the effective rf field amplitude, reducing the Rabi frequency for the well further away from the center point.
We have used this to balance the vertical double well against gravity. Since the atom chip in our experiment is oriented perpendicular to the direction of gravity, a potential gradient mg is added to the vertical double well, where m is the mass of the atoms and g is the acceleration of gravity (for ^{87}Rb this gradient is $G_\mathrm{g} = 2.1389$ kHz/μm).
This effect can be canceled by moving the rf trap closer to the chip surface, which can be understood as follows. Around the center point, the rf field strength gradient actually enhances the imbalance caused by gravity. At the well closer to the surface the rf field amplitude is larger, resulting in a larger Rabi frequency and a more strongly lifted potential bottom compared to the well further away.
While this gradient increases in strength closer to the chip surface (due to shrinking distance to the rf wires), the shrinking angle between the rf fields compensates this effect. The closer one goes towards the chip the smaller the angle between the rf fields will become, tending to zero directly at the chip surface. For a phase shift of $\delta = 0$ the vertical components of the rf fields always compensate each other, so that for smaller distances to the chip the effective field amplitude of the combined (horizontally oriented) rf field will get smaller.
Consequently, when the rf trap is moved closer to the chip surface, at some point the Rabi frequency at the well further away from the chip will be larger, and this well will be lifted more, compensating gravity. The exact position of the balance point, where the wire field imbalance cancels gravity, depends on the well separation. For typically used separations of $s = 3...6\,\mu$m and standard experiment parameters it lies at a distance $d \approx 80\,\mu$m from the surface.

Circular polarization

While the field inhomogeneities could be constructively exploited in the double well case, this is not true for the ring potential. Circular polarization can only be (approximately) realized around the center point, which is fixed by the wire distances on the atom chip. Gravity only enhances the effect of the field amplitude gradients, resulting in the ring potential having a minimum on the side away from the chip. The potential difference on the ring becomes > 10 kHz for ring diameters $d = 2\,\mu$m, which is an order of magnitude larger than the transverse ground state trap frequencies in the ring (for our wire setup).

5.3.2 Longitudinal modification of the rf potential

So far we have only considered the transverse rf potential at the longitudinal minimum position. In many cases, due to the extreme anisotropy of the static trap, it is a reasonable approximation to neglect the z-dependence of the fields and assume the rf potential to be the same transversally over the length of the area occupied by trapped atoms. This essentially means that the rf potential is decoupled from the (weak) longitudinal confinement provided by the static fields.
For a precise quantitative calculation, the full three dimensional field setup has to be considered, including the field inhomogeneities due to the finite length of the chip wires and the additional U-

wires as well as the spatial variation of the Ioffe field. Consequently all parameters characterizing the transverse potential, for example the minima positions and the potential bottom, become functions of the z-coordinate.

Double well balancing and barrier height

This is of importance for the double well potential, where it complicates the balancing of the two minima. The potential imbalance now has to be considered (and minimized) along the whole length of the system. While it can be made zero at any specific z, it cannot be made to vanish completely over the whole system length. This means that the relative phase evolution between BECs in the two wells will be a function of the z-coordinate, leading to an additional phase diffusion mechanism. For optimized balancing, this effect is negligibly small compared to the dominating phase diffusion mechanism, the one-dimensional thermal phase fluctuations (chapter 8), though. This means, that for all experiments regarding independent BECs neglecting the longitudinal dependence of the potential is justified.
This may no longer be true if tunneling between the wells becomes important. Since the tunneling rate depends exponentially on the potential barrier, its z-dependence may lead to a noticeable variation of the tunnel current along the longitudinal axis. In the analysis of coupled 1d BECs in chapter 8, we avoid this problem by considering only the center part of the total system, over which the longitudinal trapping potential may then be neglected. A full treatment including a spatially dependent tunneling rate has not yet been developed.

Longitudinal confinement in the rf potential

Another important parameter affected by the longitudinally changing rf potential is the longitudinal confinement. In the static Z-trap this confinement is provided by the (approximately harmonic) inhomogeneity in the Ioffe field. Since the Ioffe field affects both the (local) detuning and Rabi frequency, this inhomogeneity will map into the rf potential. In particular, for negative detuning at the static trap minimum ($\Delta_0 < 0$), this leads to a flattening of the potential in the longitudinal direction. While this inhomogeneous lifting of the trap bottom due to the rf field is extremely small in absolute numbers, its relative change of the longitudinal confinement can be quite large, as this confinement is extremely weak already initially. For typical experimental parameters, the longitudinal trap frequency changes by up to a factor two from the initial static trap to the rf trap. This is of importance for the coherent splitting of a BEC in the rf potential, as it makes the excitation of longitudinal modes very likely for typical splitting speeds. In most cases, this is not a problem, since the longitudinal dynamics are slow compared to the transverse splitting so that they can be safely neglected. This is no longer the case if the long time phase evolution between two coherently split BEC is investigated, as will be discussed in chapter 7.

5.4 Beyond-RWA rf potential

As final step in calculating the rf potential of the three wire setup, we will now consider the contribution of the beyond-RWA terms to the total potential. As discussed in section 2.3.3, these terms become important, when the Rabi frequency Ω or the detuning Δ (locally) become comparable to the energy splitting V_{mag} between the bare levels.
For the Rabi frequency, this most likely occurs near the static trap center in the three wire setup. There, the static field is mainly given by the Ioffe field, with the transverse field completely vanishing directly at the center. At the same time, the rf fields are (almost) perpendicular to the Ioffe field, so that in this region, the full rf field strength contributes to the rf potential. From equation (5.9) it follows, that for $G\rho \ll B_{\mathrm{I}}$ the Rabi frequency is approximately given by $\Omega \approx B_{\mathrm{rf}}/2$, where

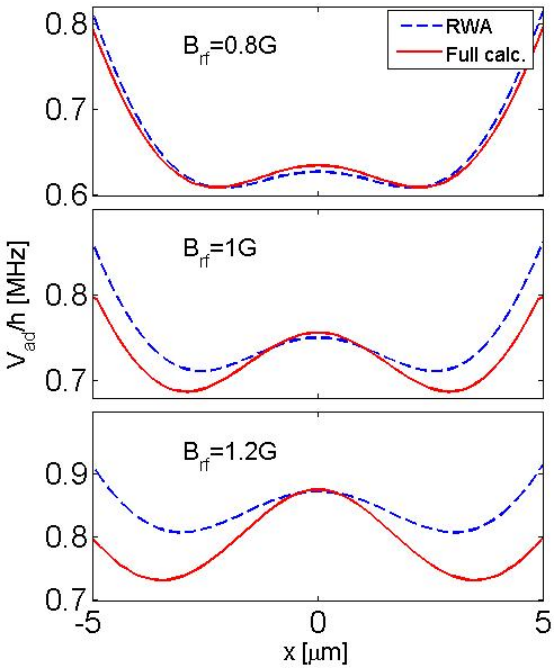

Figure 5.8: Comparison of the RWA and the beyond RWA rf potential of the three wire trap for various rf field amplitudes and $B_{\mathrm{I}} = 1$ G and $\Delta_0 = 1.1$ (other parameters are $I_{\mathrm{Z}} = 1.5$ A, $B_{\mathrm{bias,x}} = 25$ G, $I_{\mathrm{U}} = 0.7$ A, $\delta = \pi$, $g_{\mathrm{F}} = 1/2$, $\tilde{m}_t extF = 2$). The deviation between the two calculations increases for growing rf field amplitude (value given is the amplitude at the static trap center). Specifically, the RWA calculation leads to a significant underestimation of the central potential maximum height for large rf fields.

B_{rf} is the absolute value of the total rf field. Since the energy level distance near the trap center is proportional to B_{I}, it follows that $\Omega \approx V_{\mathrm{mag}}$, when $B_{\mathrm{rf}} \approx 2B_I$. Typically, the Ioffe field strength in our experiments is $B_{\mathrm{I}} \approx 1$G, while the rf field amplitude at the trap center reaches values of up to 1.5G. Consequently, while for our parameters the Rabi frequency never becomes equal to the energy splitting, we can expect significant contributions from the beyond RWA effects for the larger field amplitudes used in the experiment.

The second RWA condition, requiring the detuning to be small compared to the resonance frequency, is well fulfilled around the trap center, if $\frac{\hbar\omega_{\mathrm{rf}}}{|g_{\mathrm{F}}\mu_{\mathrm{B}}|} \approx B_{\mathrm{I}}$, but is violated further out from the center even for rf on resonance at the static trap minimum. Since $|\mathbf{B}_{\mathrm{S}}(\mathbf{r})|$ grows rapidly for increasing ρ (in the transverse direction), the radio frequency term in the detuning $\Delta = |\mathbf{B}_{\mathrm{S}}(\mathbf{r})| - \frac{\hbar\omega_{\mathrm{rf}}}{|g_{\mathrm{F}}\mu_{\mathrm{B}}|}$ becomes negligible for large ρ and Δ/V_{mag} converges against the magnetic level energy spacing, which is given by the static field amplitude. For typical Ioffe field $B_{\mathrm{I}} \approx 1$G, transverse gradient $G = 0.2\mathrm{G}/\mu\mathrm{m}$, and radio frequency on resonance at the trap center ($\Delta_0 = 0$), we already have $\Delta \approx V_{\mathrm{mag}}/5$ for $\rho = 4\mu$m. We expect beyond-RWA effects due to large detuning to become significant approximately for $\rho \geq 3$.

In figure 5.8 the RWA and the beyond RWA rf potentials are compared for fixed radio frequency ($\Delta_0 = 1.1$) and increasing rf field amplitudes, which is the typical situation in most of our experiments, as will be described below. In this configuration, the minima distance is controlled solely by the rf field amplitude. As expected the significance of the beyond RWA effects grows with increasing rf field amplitude. It can be seen that they result in a (small) reduction in the minima separation, and an increase in the central maximum height. Although only the field amplitude is changed, the breakdown of the RWA is due to violation of both validity conditions, as the minima position is pushed into the region where the large detuning becomes significant. Both effects, large Rabi frequency at the center and large detuning away from the center, contribute to the modifications of the potential, and it is not possible to separate these effects in this configuration.

5.5 Summary of the potential calculation

In the last sections, different approaches for calculating the rf potential of the three wire trap with increasing precision were presented. While all discussed method give qualitatively similar results, the quantitative differences can be large depending on the experimental parameters. For the most general and accurate result both the full three dimensional chip wire layout and the beyond RWA effects have to be taken into account. That this method indeed leads to a precise reproduction of the rf potentials present in the experiment is verified by a spectroscopic analysis, which will be presented in the next chapter.
On the other hand, for many practical situations, the beyond RWA and/or the real wire layout effects on the three dimensional potential can be safely neglected. For fast online calculation of the rf potentials in the laboratory a two dimensional RWA calculation, including the real cross section of the wires but neglecting the longitudinal confinement, turned out to be the best compromise. The wire field inhomogeneities in the transverse plane have to be considered, as they lead to significant modifications of the rf potentials. For example this calculation method is accurate enough to find balancing positions for tilted double wells with reasonable precision, the fine tuning can then be done experimentally.
The importance of the beyond RWA corrections greatly depends on the experimental parameters used. For the typical experimental configuration with a Ioffe field of $B_{\mathrm{I}} = 1$ G and a minimal detuning of $\Delta_0 > 1.05$ (corresponding to $\nu_{\mathrm{rf}} < 650$kHz) the RWA result agrees well with the full calculation for minima separations up to 5μm, which makes it generally applicable for many of the experiments discussed in the following chapters, since usually smaller separations are used. Additionally, the error in the determination of the splitting distance if the beyond RWA terms are neglected, is small in any case, while the barrier height is underestimated. Hence the tunneling rate is overestimated, when the RWA result is used. The beyond RWA corrections for the barrier height only lead to a further reduction in the tunnel coupling, and consequently can be neglected for experiments where negligibly small tunnel coupling is desired.
In summary, while in principle the rf potential can always be calculated with the full 3d beyond RWA method, in practise the choice of the potential calculation method should be based on a balance between the desired accuracy and the required computation time, which easily becomes unacceptably large ($>$ 1 hour) for the full calculation.

5.6 Experimental results

So far only the final resulting rf potentials of the three wire trap for different parameter sets have been discussed. In this section, the experimental scheme for loading atoms into these potentials will be presented. Then, the results of first demonstration experiments of the rf potentials generated by the three wire trap are shown. One of these is the rotation of the double well potential around the longitudinal trap axis, another is the state-dependence of the potential for elliptically polarized rf field.

5.6.1 Adiabatic loading of the rf potentials

Starting point for all the rf potential experiments in the three wire trap, is the static single wire created by the $100\,\mu$m wide Z-wire (T-H) and external bias fields. Ultra cold thermal atoms ($T \approx 10\,\mu$K) are loaded into this trap from the macroscopic Copper-Z trap, following the scheme described in section 4.2.5.
The initial parameters of the chip trap are $B_{bias,x} = 20$ G and $I_{\mathrm{Z}} = 2$ A, while $B_{bias,z}$ is set so that the field strength at the minimum position is $B_0 = 1$ G. This value is measured by finding the final evaporation cooling frequency for which atoms all atoms are removed from the trap. A minimum

field strength of 1 G corresponds to a frequency of 700 kHz. The resulting trap frequencies for these parameters are $\omega_\perp = 2\pi \times 915$ Hz and $\omega_z = 2\pi \times 10$ Hz, the minimum is located 190μm from the chip surface.
The atoms are held in this position for 1.5 s, while an evaporative cooling ramp from 3 to 0.9 MHz reduces the temperature to $\sim 3\,\mu$K. After this cooling stage, the trap minimum is moved closer to the chip to its final position for the rf trap by linearly changing the bias field and the wire current in 100 ms. During the same time, the current I_U in the two U-wires (B-C and E-F) is ramped up to 0.7 A. This two-step approach for transferring the atoms to the desired static trap with an intermediate cooling phase is necessary to avoid atoms with sufficient temperature to spill over the potential barriers along the longitudinal direction provided by the U-wires. Performing this first cooling stage at a larger surface distance than the final trap position is a matter of convenience only. The 2 A, 20 G Z-trap serves as a standard reference point for atom number and temperature after the first rf chip trap cooling phase, which provides a fast check if the initial experiment stages work well [234].
The final static trap position and confinement depend on the specific rf potential to be realized and the experiment to be performed in it. At the distance $d = 108\,\mu$m the magnetic fields created by the two rf-wires (S-N and X-G) are perpendicular, making this a standard distance for the static trap, realized by setting $I_Z = 1.5$ A and $B_{bias,x} = 26$ G, which results in trap frequencies $\omega_\perp = 2\pi \times 1.6$ kHz and $\omega_z = 2\pi \times 13$ Hz (due to the U-wires). Moving the static trap away from this position is used for balancing tilted double wells or changing the effective total rf field as discussed in the previous sections. Specific parameters are given when these experiments are discussed. The transverse confinement can be increased (lowered) without changing the trap position by simultaneously increasing (decreasing) the wire current and the bias field strength. The longitudinal confinement can be lowered (almost) independently of the other trap characteristics by reducing the current in the U-wires.
After the transfer to the final position, a last rf cooling stage consisting of a linear frequency ramp of duration 500 ms starting at 1.2 MHz reduces the temperature of the atomic ensemble to the desired value, usually below the critical temperature T_C. The field strength at the minimum is set to 0.9...1G, which corresponds to resonance frequencies between energy levels at the trap center of 650...700kHz. Final values of the rf ramp usually lie 5...100kHz above this resonance frequency, depending on the desired temperature and/or condensed atom number. Pure BECs (no detectable thermal background) in this trap contain up to 10^5 atoms, although usually we intentionally work with lower numbers, in the range of 2000 to 40000 atoms.

Adiabatic transfer into the rf potential

Once the desired temperature is reached, the atoms are transferred into the rf potential. This is done by continuously deforming the static energy levels denoted by m_F into the dressed energy levels $\tilde{m}_F$. For this, AC currents with frequency ν_{rf} are ramped up in the two rf wires, while the static trapping fields remain unchanged. We start with atoms in the $m_F = 2$ state and transfer them into the $\tilde{m}_F = 2$ level. To ensure a loss free transfer, ν_{rf} is always set to a value smaller than the minimal energy splitting of the stating levels, i.e. with positive minimal detuning $\Delta_0 > 0$. At the start of the AC current ramp, when the rf field amplitudes are small, the energy distance between dressed levels is given solely by the detuning, and a large enough separation is required to suppress Landau-Zener tunneling from the $\tilde{m}_F = 2$ level to other dressed states (section 2.3.2). From equation (2.13) it follows, that for $\Delta_0 \geq 10$ kHz the tunneling rate is practically zero, and the transfer is loss free. Experimentally, we have used minimal detunings in the range of 20...150 kHz, with the most common value being 50 kHz. The role of this initial detuning in the case of coherent splitting of a BEC will be discussed in chapter 7.
The final current values of this initial amplitude ramp range from 30...100 mA in each of the rf

wires, depending on the desired rf potential. The ramping speed is limited by the adiabaticity condition: the potential change has to be small to the effective Lamor frequency of the atoms in the trap (equation 2.45). Since the minimal Lamor frequency during the transfer is on the order 10 kHz, ramp durations of the order 10 ms fully ensure the adiabaticity of the transfer. In the experiments, we have used ramp durations in the range 3 to 50 ms, with most common values being 15...20 ms. Longer ramp durations are of course possible, as there is no fundamental upper limit.
In most cases, we use a single linear current ramp for simplicity. Alternatively, we have employed ramps with two or more linear steps. The calculation of the rf potential shows that for currents below 20 mA, the original static potential is not significantly changed (for typical minimal detunings of 50 kHz), so that this first stage of the ramp can be done very fast ($<$ 1ms), followed then by a slower ramping to the final current values.
For many experiments, the transfer consists only of this ramping up of the AC currents with a fixed frequency (below resonance). Alternatively, after the desired AC currents are established, in a second ramp, the detuning is changed. Once the rf field amplitudes are sufficiently large, the minimal detuning can also become negative, since the Rabi frequency alone ensures a large enough level distance to prevent atom loss. The detuning can be changed either by modifying the AC current frequency ν_{rf} or the Ioffe field B_{I}. This way, we have employed detunings of up to 3 MHz creating double well potentials with a well separation of 80μm [282]. Its important to note, that for this situation the violation of the RWA detuning condition is extreme.

5.6.2 The radio frequency sources

The AC currents are generated independently by two phase locked frequency generators (Stanford Research Systems SRS345). The amplitude of the rf outputs is voltage controlled via analog input channels of the generators by the experiment control computer. The maximal peak-to-peak voltage the SRS345 can generate is 10 V, but it turned out that for large amplitudes the sinusoidal signal becomes quite distorted. Consequently, we set the maximum amplitude of the generators to the small value of 0.2 V and use stand alone fixed gain (24 dB) amplifiers (MiniCircuits ZHL-3a-BNC), operated with low-noise power supplies (Voltcraft PPS 3003), to amplify the output signals.
The spectral characteristics of the SRS345 are very good, the linewidth of the output signal is below 1 Hz, and the higher order sideband frequency suppression is < -60 dB. Additionally, for experiments with fixed radio frequency 600 kHz a self-built bandpass filter was used, with cut off frequencies at 500 and 800 kHz.
To avoid unnecessary zero amplitude output noise from the generators during the BEC production and for fast switching of the rf fields, TTL controlled rf switches (MiniCircuits ZYSWA-2-50DR) were used, which provide a suppression of -42 dB. The rf signals are coupled into the chip wires via a ground free 1:1 isolation transformer (MiniCircuits T1-1T), decoupling the frequency generator ground from the chip ground.
To determine the actual AC current from the applied rf voltage the AC resistance of the chip wires has to be known. Although the circuit consists mainly of straight wires, there is a significant frequency-dependent impedance contribution to the resistance. Both wires were characterized in the frequency range of 400 kHz to 4 MHz with a network analyzer. For the purely ohmic resistance we found $R[\Omega] = 1.212 \times 10^{-6} f^2 + 0.014 f + 5.819$ for the (S-N) wire and $R[\Omega] = 1.155 \times 10^{-6} f^2 + 0.016 f + 6.273$ for the (X-G) wire where $[f]$ =kHz. The impedance increases approximately linearly from 11.6Ω (11.9Ω) at 400 kHz to 87.8Ω (89.1Ω) at 4 MHz for the (S-N) ((X-G)) wire, resulting in a significant resistance increase compared to the DC case, resulting in increased heating of the wires. To avoid damage to the wires, we decided on maximum AC currents of 100 mA (compared to 400 mA for the DC case), limiting the rf field amplitudes to 2 G at the standard trap position $d = 110\mu$m above the central Z-wire.

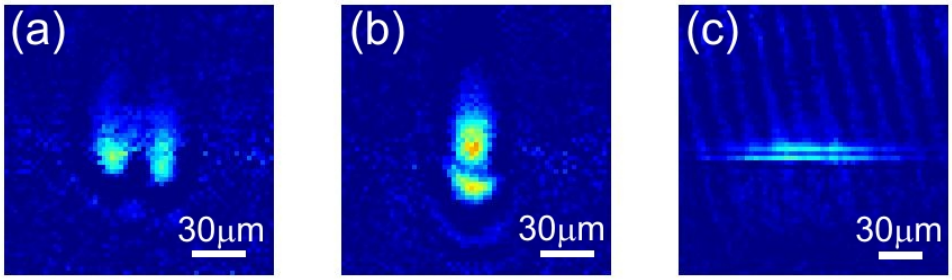

Figure 5.9: In situ images of atoms in the rf double well. **(a) and (b)** Atomic ensembles in the horizontal and vertical double well with large splitting distance imaged with the longitudinal imaging. From this point of view only the small extension of the atom cloud in the transverse direction is visible. That the micrometer sized objects look significantly bigger in the image is due to the finite focal depth and the bad resolution of the imaging system. **(c)** In situ image of atoms in the vertical double well for a splitting distance of 6μm obtained with the transverse imaging system, which enables the observation of the splitting along the complete longitudinal system size.

5.6.3 Linear polarization: rotating double Well

The main feature of the three wire setup, from our current perspective, is the flexible double well potential that can be realized with it. This configuration is the basic building block of the coherent manipulation experiments described in chapter 7 and the study of one-dimensional quasi-condensates by interference discussed in chapter 8. The double well is (most conveniently) realized by setting the phase shift to $\delta = 0, \pi$. Below, we will first discuss the direct observation of the resulting horizontal or vertical double wells. Then we will discuss the experimental observation of the rotation of the double well for changing relative rf field amplitudes.

Large splitting: resolved double well

The successful loading of atoms into the double well potential can be directly observed if the well separation is sufficiently large, so that the division of the trapped atomic ensemble into two distinct clouds can be resolved. The minimal splitting distance, for which this is possible, depends on the used imaging system. While the longitudinal imaging can only resolve the double well for minima separations larger than $15\,\mu$m, the better spatial resolution of the transverse imaging makes resolving splitting separations down to $5\,\mu$m possible.
In either case, the double well distance is too large to be realized by just increasing the rf field amplitude at fixed (positive) minimal detuning. Achieving splitting distances of 15μm or more is only possible by implementing a frequency ramp after the initial rf amplitude ramp, such that the minimal detuning becomes negative, as discussed in the last section. Compared to the large distance splitting scheme reported in [282], there is a technical complication in the three-wire case. Changing the output frequency of the SRS345 generators externally while they are operated in phase lock mode is not possible, hence with the current hardware the frequency ramp could not be implemented when two generators were used. This problem can be bypassed by connecting both rf wires in series to a single SRS345, which can execute a single, TTL triggered (pre-programmed) linear ramp if it is not phase locked. Depending on the order of the connections, this realizes either $\delta = 0$ (X-G-S-N) or $\delta = \pi$ (X-G-N-S). Images of atoms in the large distance double well realized in this was are shown in figure 5.9a,b for either phase shift.
Figure 5.9c shows a medium distance ($6\,\mu$m) vertical double well, imaged with the transverse imaging system. The vertical orientation of the double well allows the observation of the splitting over the whole longitudinal extend of the atom cloud, which opens new options for the study of one-dimensional phase fluctuations as discussed in chapter 8. The splitting shown in this picture is

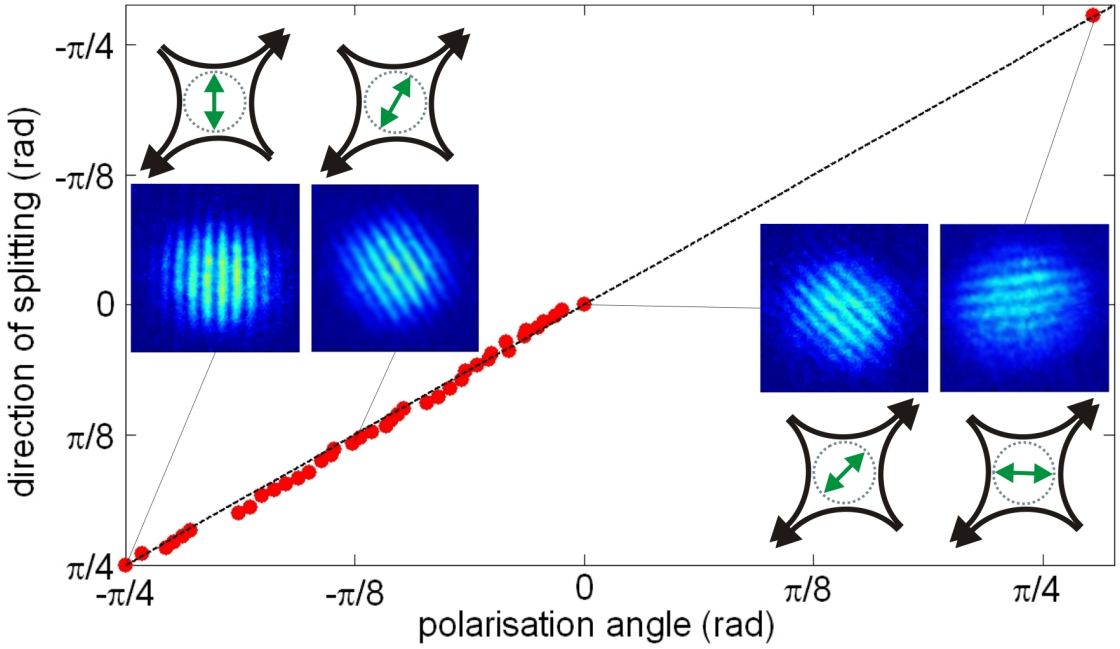

Figure 5.10: Orientation of the double well potential as a function of the plane of polarization in the case of a linearly polarized RF field (angles are measured with respect to the x-axis). The double well orientation is inferred from interference patterns. The observed fringes are always perpendicular to the double well axis. Coherent splitting is possible in all directions.

realized by lowering the Ioffe field after the rf amplitude. This alternative to ramping the frequency has the advantage that it can be done with both currently used frequency generators in operation. Furthermore, the modification of the Ioffe field is an alternative option for controlling for example the double well distance without changing the rf fields. Based on the numerical calculations this may be a good way to change the double well while keeping it well balanced. Another possible application is the readout of the number of atoms in each well with the transverse imaging after (tunneling) experiments in small distance double wells, for which a precise determination of the relative atom number in each well is required [1, 92].

Small splitting: interference fringes

For double well distances below 5 μm the splitting of the atom cloud cannot be resolved directly. Instead, we can infer the double well potental by observing interference patterns in time-of-flight (ToF) between the matter-wave packets released from the two wells. The interference patterns and the information they contain will be discuss in detail in chapter 7. Here, we only use the fact that the observed interference fringes are always perpendicular to the double well axis, which enables us to extract the orientation of the double well from these images. In principle, the splitting distance can also be deduced from the fringe spacing, but this is complicated by the atom-atom interaction during the expansion [284].

From equation (5.11) it follows, that the splitting direction of the double well depends on the orientation α of the plane of polarization of the linear total rf field, which is determined by the ratio of the rf field strengths $B_\mathrm{B}/B_\mathrm{A}$. The double well always forms in the direction along which the transverse quadrupole field is parallel to the total rf field. The experimental observation of this rotation of the double well is shown in figure 5.10. Here, α is varied while the total rf field amplitude B_rf is held constant, resulting in a fixed fringe spacing. As expected, the double well orientation changes linearly with α.

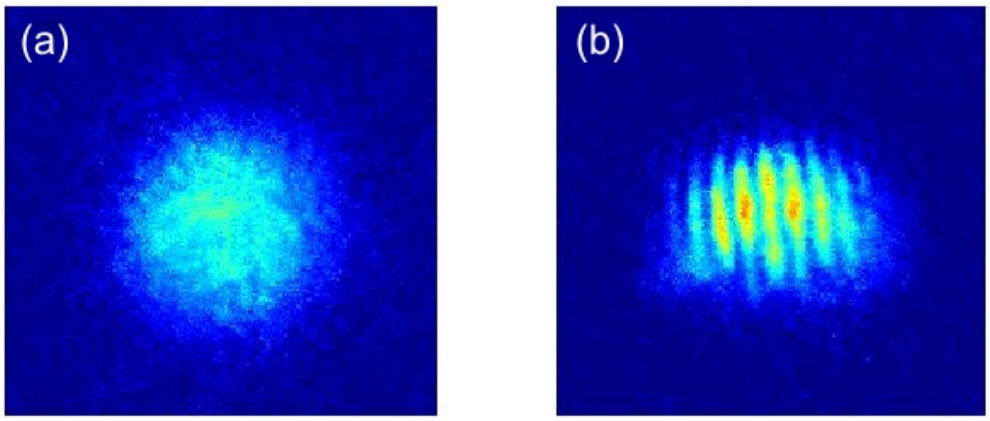

Figure 5.11: Experimental test of the state dependence of the rf potentials for elliptically polarized rf field. ToF images of BECs released from rf potentials with identical parameters except for the handedness of the (elliptically polarized) rf field. **(a)** For a phase shift of $\delta = \pi/2$ the rf field has no visible effect on the static potential. **(b)** For $\delta = 3\pi/2$ the rf potential is a double well, leading to the observation of an interference pattern in the ToF image.

To cover the complete range of $\pi/2$ of possible splitting directions, both phase shifts $\delta = 0, \pi$ have to be used, since each one can cover only half of the circle. Note, that it is the vertical rf polarization that results in the horizontal double well, while the horizontal polarization leads to a vertical splitting direction. This is due to the 45° tilt of the main axes of the quadrupole field with respect to the coordinate system (and the chip surface).
The potential imbalance introduced by gravity can be compensated by exploiting the inhomogeneity of the chip wire rf fields as described in section 5.3.1. The precise balancing point for each α has to be found experimentally, but during the rotation from horizontal to vertical double well, the surface distance changes roughly linearly from $110\,\mu$ to $80\,\mu$m.
The ability of rotating the double well opens up interesting possibilities for experiments. The main feature exploited for the experiments discussed in this thesis is the fact that the vertical splitting, and the resulting horizontal interference patterns, can be observed with both imaging systems. An interesting future experiment could be the rotation of a BEC on a circular path, by applying a periodic modulation to the RF amplitudes. This rotation is always centered perfectly on the minimum of the static trapping potential. For small rf amplitudes $B_{\mathrm{rf}} < B_{\mathrm{C}}$ (single minimum potential), this could be used to stir a single BEC with the goal of vortex creation [208].

5.6.4 Elliptical polarization: State dependent double well

To demonstrate the state-dependence of the rf potentials, we have investigated the effect on the potential configuration for ^{87}Rb atoms in the $|F = 2, \tilde{m}_{\mathrm{F}} = 2 >$ state, if the handedness of circularly or more generally elliptically polarized fields is inverted.
In figure 5.11 the effect of this inversion of the phase shift from $\delta = \pi/2$ to $\delta = 3pi/2$ is shown for the specific case of rf field parameters $I_{\mathrm{A}}/I_{\mathrm{B}} = 1.66$, $\nu_{rf} = 600$ kHz, and a standard static trap at $d = 110\mu$m ($B_{\mathrm{bias,x}} = 25$ G, $I_{\mathrm{Z}} = 1.5$ A, $I_{\mathrm{U}} = 0.7$ A, $B_I = 0.92$ G). According to the calculations in section 5.2.3, we expect a (slightly deformed) double well for the $\delta = 3\pi/2$ case and (almost) no effect on the static potential if $\delta = \pi/2$. Indeed, the ToF images of BECs released from these rf potentials agree with this prediction. The atomic expansion observed for $\delta = \pi/2$ (figure 5.6.4a) shows no difference compared to the expansion from the static trap, while in the $\delta = 3\pi/2$ case an (horizontally elongated) interference pattern is obtained.

To fully exploit the state-dependence of the rf potentials, loading of atoms in two different states with identical magnetic moment but different g-factor into the initial static trap is required. Experimentally feasible in our case is the use of the Rb clock states, i.e. different hyperfine states with inverted g-factor, as discussed in section 5.2.3. For this, the initial static trap has to be loaded with atoms in the $|F = 1, m_F = -1 >$ state, of which a fraction can then be transferred into the $|F = 2, m_F = 1 >$ by a two-photon microwave transition [302]. So far, we have only realized the very first step of this procedure, the loading of (thermal) atoms in the $|F = 1, m_F = -1 >$ state into the static chip trap (section 4.2.3). Bose condensation of atoms in this state and the application of an (external) microwave field are near future goals for the experiment (see outlook). Such a setup would enable for example the study of inter-spinstate collisions on the coherence properties of BECs via interference measurements.
Generally, application of state-dependent rf potentials could be of interest in the context of spinor mixtures or even multiple species experiments in optical traps. For example the spatial overlap of different species in the same trap could be modified, which means the ratio of atoms of different species in the overlap region could be precisely controlled and modified during the experiment.

5.6.5 Circular polarization: ring potential

As discussed in section 5.3.1 the realization of the ring potential greatly hindered by the wire field inhomogeneities. With our current setup, it does not seem to be possible to achieve a sufficient potential bottom flatness around the whole circumference of the ring to load a connected BEC into it. Displacing the trap in any direction does not help. While a better balance along one direction may be achieved this way, one has to pay for this with asymmetries in the perpendicular direction. Specifically moving the trap center closer to the chip introduces a potential barrier in the horizontal direction (one approaches the elliptical configuration discussed in the last section).
In figure 5.12 the deformed ring potential for typical parameters (given in the figure caption) is shown, together with the corresponding ToF image of an atom cloud expanding from this potential. A two-dimensional GPE calculation of the many body ground state of the potential and the subsequent simulation of the expansion after the potential is switched off is in reasonable agreement with the experimental observations.
While this problem could not be overcome in our current setup, there are various ideas for future experiments. Tilting the whole experiment setup by 90° would remove the gravity gradient, but the wire effect would remain (and is dominant anyway). A possible solution is to use a compensating electric field gradient, which could be created by charging the Z-wire. For our wire dimensions a static charge of 80 V needs to be applied, while the rest of the chip must be grounded. Such a charge on a single chip wire would lead to electric field strength at the chip surface of order 10 MV/m, which would risk a break through current, either through the vacuum, or more likely the chip substrate [171]. A saver approach is to use additional rf wires on or underneath the atom chip to compensate the field inhomogeneities. An atom chip incorporating such wires is currently being designed and will be used in future experiments [308, 99].

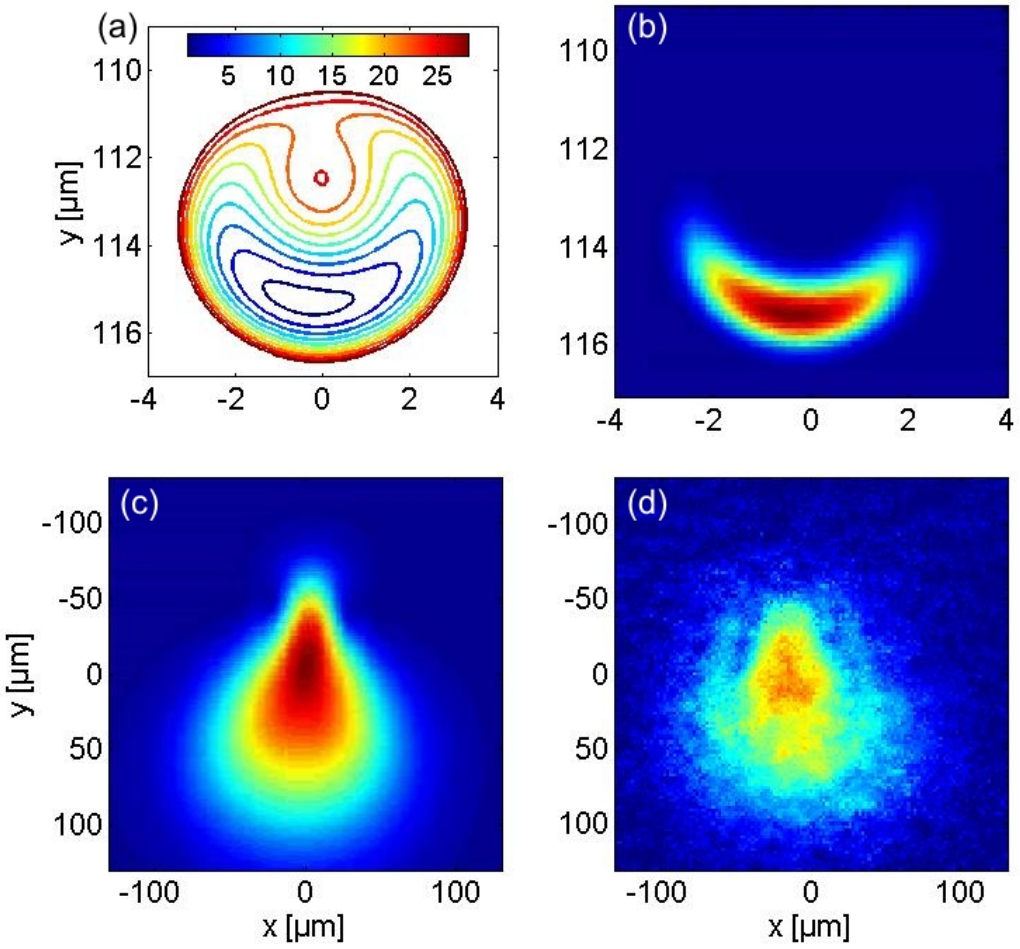

Figure 5.12: Analysis of the expansion of a BEC from the deformed ring potential **(a)** Transverse cut through the ring-shaped rf potential V_{ad}/h including gravity for parameters $I_{\mathrm{A}} = I_{\mathrm{B}} = 50$ma, $\nu_{rf} = 600$ kHz, $B_{\mathrm{bias,x}} = 25$ G, $I_{\mathrm{Z}} = 1.5$ A, $I_{\mathrm{U}} = 0.7$ A, $B_I = 0.92$ G in units kHz. **(b)** Solution of the 2d GPE for the potential shown in (a) for $N_{\mathrm{atoms}} = 10^4$. **(c)** GPE simulation of the ToF expansion starting with the wave function shown in (b). **(d)** Absorption image observed in the experiment. There is good qualitative agreement between experiment and simulation.

6 Spectroscopy of radio-frequency potentials

Spectroscopic measurements of atomic level structures are a standard technique widely used in all areas of atomic physics. In the context of (ultra) cold atoms, for example spectroscopy of atomic hyperfine transitions is the basic building block of atomic fountain clocks [163, 323, 122]. Another example of vast importance is rf spectroscopy of trapped atoms [213], which is the basis of evaporative cooling in magnetic traps [135].
The common methods used in the spectroscopy of bare atoms can also be applied to dressed atoms. Indeed, the spectroscopic study of atoms in vapor cells and atomic beams in strong oscillating fields has been extensively pursued in the 1960s and 1970s [127, 128, 243], and played an important role in the development of the quantum mechanical picture of dressed states [289, 46].
In this chapter we present spectroscopic measurements of the level structure of ultra cold rf dressed atoms trapped in the three-wire trap introduced in the last chapter [141]. We measure the energy difference between dressed states by irradiating the atoms with an additional weak rf "tickling" field [127, 2]. If this field is resonant with the dressed state level spacing, transitions to untrapped states are induced. This results in trap loss, which is the signature for a resonance.
For a spectroscopy field much weaker than the dressing field this situation can be treated in time-dependent perturbation theory within the dressed state framework, this calculation is presented in section (6.1). Similar to the case of bare atoms, we find that transitions rules resulting from angular momentum conservation limit the number of allowed transitions between dressed hyperfine states [127, 141]. Experimental results of the spectroscopy of dressed BECs are presented in section (6.2). These measurements provide a precise characterization of the rf adiabatic potentials realized in the experiment. We use this for calibrating the actual rf field amplitude present in the experiment, which are hard not measurable in a precise manner directly.
The non-RWA effects in the rf dressing can be seen in the spectroscopy results as Bloch-Siegert like shifts of the resonance lines [20]. This shows that ultra cold rf dressed atoms trapped on an atom chip may be a suitable system for the study of beyond-RWA effects [310, 184].
The perturbation theory approach is of course only valid for two rf fields of highly different amplitude. At the end of this chapter (section 6.3), we briefly discuss the situation that aries if this condition is violated, i.e. if two (or more) rf fields of different frequency but comparable amplitude are applied. The multi frequency dressing can be considered in different theoretical frameworks, and is a promising extension of the rf adiabatic potentials. It may lead to the realization of various highly interesting potential configurations like two counter-propagating ring traps [79, 196] or flexible multi-well magnetic traps similar to optical standing wave traps [50].

6.1 Calculation of the allowed transitions

The dressed state picture presented in section 2.3.1 offers a convenient method for calculating the transitions induced by the weak spectroscopy field, using time-dependent perturbation theory. It is easiest to work in the basis formed by the bare states $\{|m_{\mathrm{F}}, N\rangle\}$. From the matrix diagonalizations discussed in 2.3.2 and 2.3.3, we already have the dressed states composition in terms of this bare state basis.
We now write the perturbation operator of the spectroscopy field as $\mathbf{B}_{\mathrm{spec}}(\mathbf{r}) \cdot \mathbf{F}$, and construct its matrix representation in the bare state basis. This operator only acts on the magnetic quantum number, i.e. it only couples bare states within the same κ-manifold. Consequently its matrix

representation in the bare state basis sorted into these manifolds, breaks up into repeating blocks of the standard $2F + 1$ dimensional spin operator matrix. More specifically, the F_z matrix is a diagonal matrix with repeating blocks of entries running from $-F$ to F. On the other hand, the F_x and F_y matrices only have entries in the two off-diagonals corresponding to $\triangle m_\mathrm{F} = \pm 1$ and $\triangle N = 0$. Since $F_y = iF_x$, these two components lead to the same allowed transitions, consequently as long as we are only interested in the transition rules, it is sufficient to include only one of them, i.e. F_x in the calculation. Alternatively, this can be seen as another rotation of the coordinate system which ensures that the component of the tickling field perpendicular to the static field points in the x-direction everywhere. This only has to be specifically taken into account if the determination of the exact orientation of the tickling field is desired, which is usually not the case for our experiments.
With the thus constructed perturbation matrix, we can now calculate the transition matrix elements

$$\left\langle \tilde{m}'_\mathrm{F}(\kappa') \right| \mathbf{B}_\mathrm{spec}(\mathbf{r}) \cdot \mathbf{F} \left| \tilde{m}_\mathrm{F}(\kappa) \right\rangle \tag{6.1}$$

to determine the allowed transitions. This calculation is carried out numerically, which will be done explicitly for specific adiabatic potentials in the next section. Here, we only discuss general aspects valid for all situations.
The first observation from this calculation is that for any dressing field strength achievable in our setup non-vanishing elements only occur if $|\tilde{m}'_\mathrm{F} - \tilde{m}_\mathrm{F}| = 0, 1$. While this may seem obvious from the construction of the perturbation operator on first sight, one has to remember that the dressed states are superpositions of all involved bare states. This suggests that non-vanishing transition matrix elements can in principle exist between all dressed states. Still, a selection rule similar to the case of RF-transitions between undressed states is found. This is not generally true for dressed state systems, a typical example of extra transitions appearing in the dressed system is the Mollow triplet observed in the spontaneous decay in an optically dressed two-level system [225]. Also, this transition rule breaks down for very large dressing field ($\Omega \gg \omega_0$), since then the effective magnetic quantum numbers $\tilde{m}_\mathrm{F}$ and the sorting of the dressed states into κ-manifolds become meaningless (see section 2.3.3).
Furthermore, we observe that for weak dressing field, only transitions with $|\kappa' - \kappa| = 0, 1$ occur, resulting in a total of three allowed transitions. This is due to the fact that in the case of weak dressing the dressed states only contain (significant) contributions from bare states of a single κ-manifold and that the spectroscopy operator does not act on the photon quantum number of the bare states.
Here it is important to note, that if the RWA is applied in the calculation of the dressed states, this result holds for any dressing field strength, i.e. there are always only three allowed transitions predicted. This is again due to the fact that within the RWA only couplings within one manifold are considered, which the spectroscopy operator cannot break up. In contrast, the full numerical calculation predicts higher order transitions to occur in the case of large dressing fields, when bare states with different κ contribute significantly to each dressed state. This leads to a chain of allowed transition frequencies given by $\nu_\mathrm{trans} = n\nu_\mathrm{rf} \pm \triangle V$, where $n = 0, 1, 2, ...$ and $\triangle V$ is the energy difference between dressed states within one κ-manifold. The appearance of these additional higher order transitions in the spectroscopy can thus be used as an indicator for the break down of the RWA calculation.
The transition rates for the allowed transitions can be obtained by entering the transition matrix elements into Fermi´s golden rule, considering that we are dealing with magnetic transitions. The calculated rates strongly depend on the parameters of the static and the dressing field. For increasing RF coupling, the higher order transitions become stronger. Additionally, the maximum transition rate is no longer located at $n = 0$ but at higher n. We will consider this in more detail for specific situations in the next section, where experimental results are discussed.

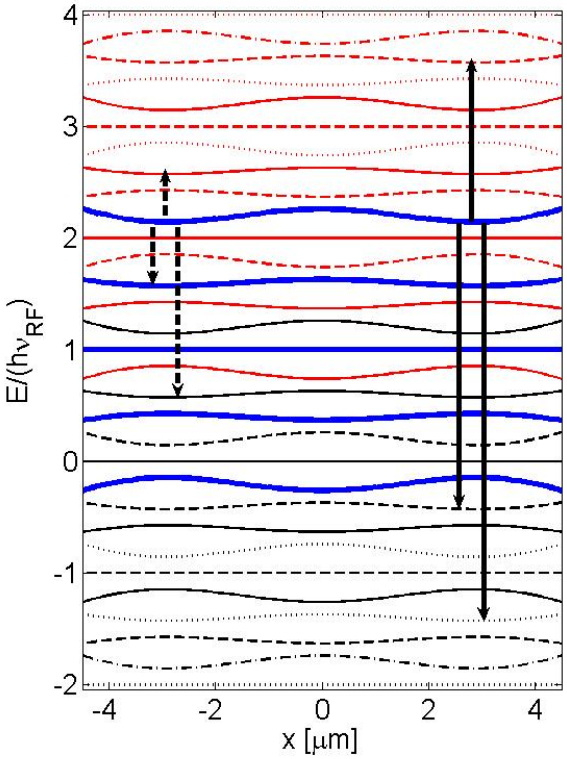

Figure 6.1: Spectroscopy on atoms trapped in the double well potential. The atoms are initially confined in the potential minima of the energetically highest branch ($\tilde{m}_\mathrm{F} = 2$) of the $\kappa = 0$ manifold, which levels are shown in blue (we consider only a single photon state of the classical rf field here, as discussed in section 2.3.3). Also shown are all other dressed levels lying in an energy range of $\pm 2h\nu_{rf}$ around this manifold, the color and line style differentiates between different manifolds. A coupling strength is chosen for which the different manifolds completely overlap. The observable transitions induced by the tickling field are those with $|\triangle\tilde{m}_\mathrm{F}| = 1$, as they lead to atom loss through a cascade of transitions to untrapped states. Within the RWA calculation, and for weak dressing in the full calculation, this leads to three observable transitions, shown by the dashed arrows ($|\kappa' - \kappa| = 0, 1$). For strong dressing the full calculation including the non-RWA terms predicts the appearance of additional transitions at larger frequencies, indicated by the solid arrows. Here, the situation for a symmetric double well is shown, where atoms are equally removed from both wells. In the case of an asymmetric double well, each of the indicated transitions leads to two measured frequencies (if the asymmetry is larger than the frequency resolution).

6.2 Rf spectroscopy in the three-wire rf trap

The rf spectroscopy technique was used to characterize the adiabatic potential of the three-wire rf trap introduced in the last chapter. The experimental procedure used for performing the spectroscopy is as follows: After adiabatically transferring a BEC or a thermal cloud from the static trap into the RF potential, the weak spectroscopy field is switched on for a time t_spec at frequency ν_spec, while all other parameters are held constant. This field is generated by an AC current of 0.1 mA applied to the macroscopic Copper-U wire in the chip mounting (the same wire is used for applying the rf field used for evaporative cooling in the static trap). After the spectroscopy time we switch off all fields and measure the number of atoms by taking a time-of-flight absorption image of the released cloud. Between experiment cycles we vary ν_spec and search for frequencies at which we observe atom loss.

In the last section we calculated transition rates for fixed dressed states, neglecting any spatial dependence. To understand the frequencies of the transitions observed in the experiments, we have to take into account that the spectroscopy is performed on atoms trapped in spatially inhomogeneous adiabatic potentials. In this situation the frequencies of the allowed transitions also become functions of space.

On the other hand, the area of the potential that can be probed spectroscopically is limited to the potential minimum locations where the atoms are actually confined. Consequently, for each allowed transition we can expect to measure one resonance frequency for each occupied minimum. For example, in the case of the double well, an asymmetry in the potential will lead to two different resonance frequencies for each allowed transition, corresponding to induced transitions from either well, respectively (see figure 6.1).

In practise this means, that although the spectroscopy method only yields information about the level distance at potential minima (occupied with atoms), for the theoretical prediction of the observed resonance frequencies the full adiabatic potential has to be calculated. To compare the

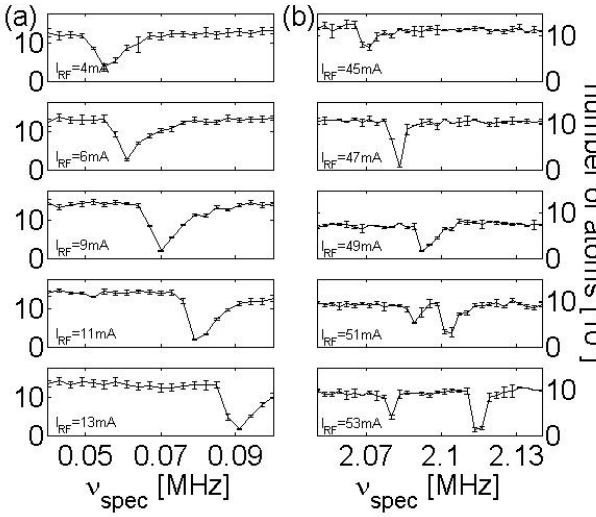

Figure 6.2: (a) Frequency scans for increasing RF dressing current I_{RF} in the range corresponding to the lowest lying transition. The signature of a transition is the loss of atoms from the trap. Each data point is the average of the observed atom number of $5-10$ experiments with identical parameters, reducing the signal noise due to shot-to-shot fluctuations of the atom number. The slightly asymmetric shape of the observed atom loss signal is caused to the finite size and temperature of the probed BECs. The position of the resonance shifts to higher frequency with the RF current, as expected. **(b)** Similar scans of the frequency range corresponding to the crossing of the $3\times\omega_{\mathrm{RF}}/(2\pi)+\Omega$ and the $4\times\omega_{\mathrm{RF}}/(2\pi)-\Omega$ non-RWA transitions at large RF currents. It can be seen that for the same spectroscopy time $t_{\mathrm{spec}}=100$ ms and tickling field amplitude the lower transition rates of these resonances result in weaker atom loss. Specifically, the $4\times\omega_{\mathrm{RF}}/(2\pi)-\Omega$ only becomes discernible for sufficiently large dressing fields.

measured spectral lines to calculated transition rates, also the (relative) number of atoms in each potential minimum has to be known, as from the measured total atom number after the spectroscopy we cannot distinguish between small (global) transition rates and parts of the atom cloud being shifted out of resonance due to multiple potential minima.

6.2.1 Observed resonances

Figure (6.2) shows typical examples of measured resonances lines. Each plot shows a single spectroscopy scan over a certain frequency range for a fixed set of parameters of the rf potential. Between plots a single parameter of the potential was changed to investigate the resulting change on the resonance position. In the examples shown here this parameter was the AC current in the rf wires. For simplicity, in these scans the same current was used in both wires $I_{\mathrm{rf}}=I_{\mathrm{A}}=I_{\mathrm{B}}$. Both sets of scans were performed in the usual trap configuration using positive minimal detuning $\Delta_0=50$ kHz, and with a spectroscopy time $t_{\mathrm{spec}}=100$ ms.
The scans in figure (6.2a) show the lowest lying resonance ($|\kappa'-\kappa|=0$), i.e. the transition within the same manifold. Hence, the position of the spectroscopy line directly corresponds to the energy difference $\triangle V_{\mathrm{ad},0}$ at the potential minimum of the dressed states within each manifold. For small rf field amplitude the Rabi frequency Ω vanishes, and $\triangle V_{\mathrm{ad},0}$ should converge towards Δ_0 (equation 2.46), which we observe in this set of scans.
Figure (6.2b) shows a set of scans in the frequency range where we expect to find the $3\nu_{\mathrm{rf}}+\triangle V$ and the $4\nu_{\mathrm{rf}}-\triangle V$ non-RWA transitions. More specifically, the AC current values cover the range around where $\triangle V=1/2\nu_{\mathrm{rf}}$, i.e. where we expect that the two resonances cross each other. For the lowest AC currents, we only observe a single resonance, which moves towards increasing frequency with increasing rf amplitude. Only for the two largest AC currents, the second resonance appears. As expected both resonances are equally distant from the frequency $\nu_{\mathrm{cross}}=3.5\nu_{\mathrm{rf}}$, where we expect the crossing.
From the scans it can be seen that the lowest order transition result in a much more pronounced spectral line than the higher order transitions. Indeed, for the investigated parameter set of the adiabatic potential the $4\nu_{\mathrm{rf}}-\triangle V$ transition is so weak, that it is not resolved for $I_{\mathrm{rf}}<50$ mA at all for the used tickling field strength and spectroscopy duration. The relative strength of the resonances is in good agreement with the numerical calculations presented in the last chapter. An absolute measurement could be used to determine the field strength and the orientation of the tickling field.
For the calibration of the dressing field, which we are primarily interested in, the position of the

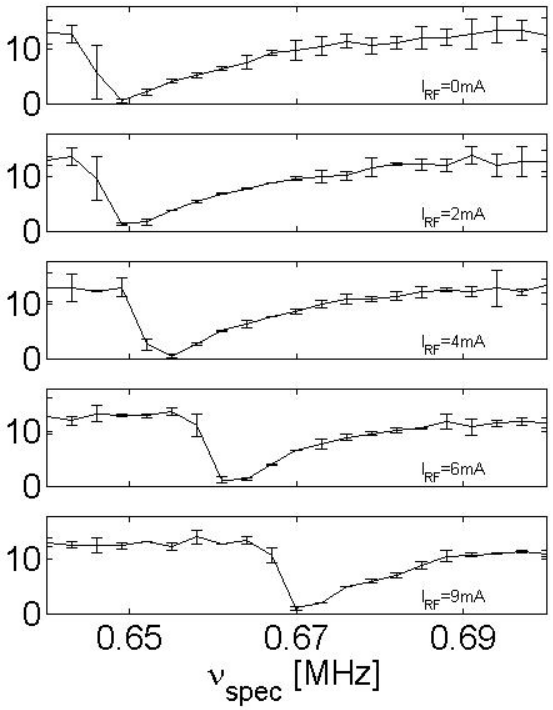

Figure 6.3: Rf spectroscopy with thermal atoms. The finite size and temperature of the probed atomic cloud leads to an asymmetric broadening of the spectral lines. For frequencies above the resonance frequency at the potential minimum, there is a resonance condition $\nu_{spec} = \triangle V$ at some distance from the trap center. The fraction of the atoms with sufficient energy to reach this position is removed from the trap, which is the principle of forced evaporative cooling.

resonances suffices, as will be shown in the next section. Of course, the accuracy of this position determination also depends on the strength of the observed spectral line. For strong resonances, there is a "saturation" effect, i.e. all atoms are removed over a range of frequencies around the actual resonance frequency, if the spectroscopy time is chosen too long or the tickling field amplitude is too large. On the other hand, the weak resonances may be too narrow to be resolved with the used frequency resolution or too shallow to be discernible from shot-to-shot fluctuations of the atom number. The latter effect can be greatly reduced by averaging over multiple frequency scans, while the first can be solved by reducing the step size of the frequency scan (which on the other hand increases the experiment duration).
Additionally, the finite temperature and extension of the atomic cloud lead to an asymmetric broadening of the observed spectroscopy lines, since (partial) atom loss is induced over a finite frequency range above the resonance frequency corresponding to the minimum energy separation. This effect can be seen in figure (6.3). Here, the spectroscopy was performed with thermal atoms instead of a BEC, leading to a strong enhancement of this effect. For frequencies above the minimum position resonance part of the atomic cloud is already removed. This effect can be reduced by lowering the temperature of the atomic sample as much as possible before performing the spectroscopy. Another correction that has to be included in the exact determination of the minimum resonance is due to the gravitational sag of the atoms in the potential, which causes a slight shift of the observed frequencies.

Evaporative cooling in rf potentials

The partial removal of (the hottest) atoms by the spectroscopy field is essentially the same as the radio-frequency induced forced evaporation commonly used in static traps [57], only that here transitions between (rf)-dressed levels are induced, compared to the magnetic levels in the static case. In the spectroscopy measurements with thermal clouds we observe a reduction of the sample temperature in conjunction with the partial removal of atoms.
To convert the spectroscopy into a cooling technique, the only change required is that instead

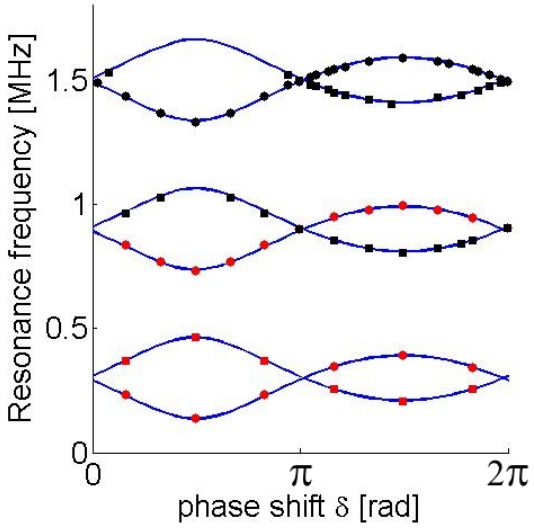

Figure 6.4: Rf resonances for varying phase shift δ. The plot shows the results of multiple spectroscopy scans, where in between scans the phase shift δ was incrementally changed. Each data point shows a resonance where atom loss is observed. The red points correspond to RWA transitions, while the black ones are non-RWA transitions ($n > 1$). The circles are $n\nu_{\mathrm{rf}} + \triangle V$ transitions, while the boxes are $n\nu_{\mathrm{rf}} - \triangle V$ transitions. The strength of the resonances also changes with δ. The $2\nu_{\mathrm{rf}} - \triangle V$ and $3\nu_{\mathrm{rf}} - \triangle V$ transitions are too weak to be resolved near $\delta = \pi/2$, where the rf coupling is weakest. Consequently the non-RWA transitions are much less pronounced. The error bars are smaller than the markers for all shown data points. The solid lines are fits using the beyond-RWA model for calculating the transitions. The only free parameters are the rf wire currents. From these fits these currents, and the resulting rf amplitudes can be precisely calibrated.

of holding ν_{spec} constant, it is reduced over time, starting at a value well above the minimum resonance frequency. Variation of the ramp shape and duration show that efficient cooling can be achieved with a single linear ramp. We observe a decrease in the cooling efficiency in the double well potential, which can be compensated by increasing the ramp duration to $800 - 1000$ ms, compared to $200 - 500$ ms in the single well static trap, for the final evaporation from $\sim 3\,\mu$K to degeneracy. We attribute this to the reduced collision rate due to the smaller density in each of the potential wells.

The main difference compared to evaporation in the static trap is that there are now multiple resonance frequencies which can be used for cooling. We have tested both the RWA ($n = 0, 1$) and the first non-RWA transitions ($n = 2, 3$) (for the strong dressing field case) for cooling and found no significant difference in the efficiency.

More interesting is the existence of sufficiently separated resonance frequencies for different potential minima. We have used this to prepare two independent BECs with different atom numbers in each well of an asymmetric double well potential. For this, thermal atoms were loaded into the tilted double well, followed by a linear evaporation ramp of ν_{spec}, resulting in a (small) number imbalance, as the evaporation frequency comes closer to the minimum resonance frequency on one side. The resulting number imbalance could be observed by an increased reduction of the interference contrast (see sections 3.3 and 7.2.1). For this approach to be useful as a reliable scheme for producing number imbalances, the potential bottom of each well has to be extremely accurate, though.

6.2.2 Phase shift scans

The rf spectroscopy enables us to precisely calibrate the rf potentials created in the experiment, by measuring the resonance positions for different trap parameters and comparing to the expected transition frequencies obtained from the numeric potential calculations.

Of the parameters affecting the rf potential, the amplitude of the rf field is the one known with least precision. While the peak to peak voltage output of the frequency sources can be measured with an impedance matched volt meter, this does not reproduce the actual AC voltage applied to the chip wire, since there is an (uncompensated) mismatch between the generator, which expects a load with an impedance of 50 Ohm, and the frequency and amplitude dependent impedance of the total AC wire, which includes also the BNC cables and copper rods leading to the actual chip wire. While we have measured the impedance of the complete current carrying structure inside the vacuum (section 5.6.2), we cannot determine the AC peak to peak voltage actually applied over

the chip wires, which means that the AC current I_{rf} is not directly known.
The rf spectroscopy scans can be used to extract the rf field amplitudes, from which the AC currents can be calculated using the three-dimensional wire field formulas presented in section 2.2.3 and the (precisely known) position of the atoms relative to the wires. With this, the functional dependence of the actual AC current in the chip wires I_{rf} on the peak to peak voltage provided by the frequency generators can be established (for a fixed frequency).
Usually it is convenient to vary only a single trap parameter between the spectroscopy scans, while all others are held constant. In figure (6.4) an example of such a scan is shown, where the varied parameter is the phase shift δ between the two rf currents. For the shown data set, the other parameters were $B_{\mathrm{I}} = 0.92$ G, $\nu_{\mathrm{rf}} = 600$ kHz, $I_{\mathrm{Z}} = 1.5$A, $B_{\mathrm{bias,x}} = 25$G, and $I_{\mathrm{U}} = 0.7$A. The (constant) AC currents I_{A} and I_{B} are determined by fitting the observed resonances with a model calculation of the transition frequency based on the numeric rf potential and the three-dimensional chip wire layout.
In this scan, we observe the occurrence of the higher order spectroscopy lines predicted by the beyond-RWA calculation (black data points in figure 6.4), which is a clear indication that the RWA fails for this parameter set and the full numeric potential model has to be used. It can be seen that the number of observed resonances depends on δ. It is important to note here, that the higher order resonances grow continuously in strength with increasing rf field amplitude and detuning, but we only measure them with statistical certainty once they pass a certain threshold, which is determined by the tickling field strength, the spectroscopy time and the atom number detection noise. Since the tickling field and the spectroscopy time are constant over the whole scan, the higher order resonances only "appear", once they are sufficiently strong.
The correlation of the occurrence of the non-RWA transition with the rf coupling strength can be nicely seen. For a phase shift of $\delta = \pi/2$, where we expect the effect of the dressing field to be weak (for the $|F = 2, \tilde{m}_{\mathrm{F}} = 2 >$ state), no non-RWA transitions are observed at all. In contrast, around $\delta = 3\pi/2$ the effect of the dressing field is largest (largest $\triangle V$), and we observe the strongest resonance lines.
In the complete curve the sinusoidal dependence of the Rabi frequency on the phase shift can be seen (equation 5.2). One reason for the visible asymmetry is the inhomogeneity of the wire fields, which lead to deviations from the analytic formula, as discussed in section (5.3.1). Another effect is due to the different positions in space of the potential minimum (minima) for different δ, which results in the effective detuning Δ experienced by the atoms also being a function of the phase shift. More specifically, during a full cycle of δ from 0 to 2π the potential changes from an imbalanced vertical double well ($\delta = 0$) to a single well located at the original trap center ($\delta = \pi/2$) to a horizontal double well ($\delta = \pi$) to a distorted ring ($\delta = 3\pi/2$). Especially for the ring potential and the vertical double well the distribution of the atoms in the rf potential is important for the interpretation of the measured resonance lines. This was included in the calculations by numerically propagating a wave packet in the time dependent potential during the transfer into the rf trap to determine the density distribution in the final spectroscopically probed potential.
The plotted lines in figure (6.4) are the resulting fits, using the model described above. The only free parameters are the AC currents in the rf wires. We find extremely good agreement with the measured data, which enables us to calibrate these currents to a precision $\triangle I_{\mathrm{rf}} < 1$ mA.

6.2.3 Rf field amplitude scan

The AC current calibration discussed in the last section allows us to measure the dependence of the resonance frequencies on the rf field amplitude, which is shown in figure (6.5), where the transition frequencies are plotted as a function of the AC currents. The other (constant) parameters of the spectroscopically probed RF potential are $B_{\mathrm{I}} = 0.92$ G, $\nu_{\mathrm{rf}} = 600$ kHz, $I_{\mathrm{Z}} = 1.5$A, $B_{\mathrm{bias,x}} = 25$G, and $I_{\mathrm{U}} = 0.7$A. The phase shift of the two rf currents is set to $\delta = \pi$, resulting in a horizontal

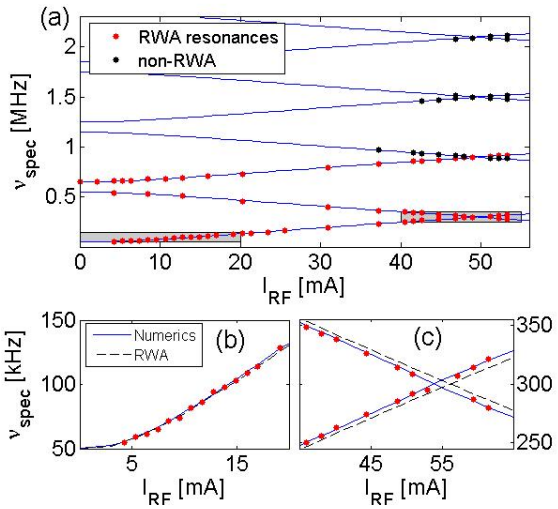

Figure 6.5: (a) Observed resonances between 0...2.2 MHz for $I_{\mathrm{RF}} = 0...60$ mA. The numerically calculated transition frequencies are shown as blue lines. It can be seen that for low I_{RF} only three transitions are observable (red points). For higher rf currents additional resonances appear (blue squares). The error bars are smaller than the markers for all shown data points. **(b)** Zoom ins into the two grey-shaded regions of plot (a). Both the numerically calculated transition frequencies (solid line) as well as those obtained from the RWA calculations are plotted (dashed line). For low RF amplitudes the RWA is in good agreement with the full calculation and both agree well with our measurements (left). At higher rf amplitude the non-RWA terms lead to a shift of the resonances (right).

double well. For simplicity, only a single rf current $I_{\mathrm{rf}} = I_{\mathrm{A}} = I_{\mathrm{B}}$ is used. This leads to a small imbalance in the double well potential due to the asymmetric rf wire distance, which has to be included in the calculations of the resonance frequencies.

Direct observation of the non-RWA effects

In this scan the break down of the RWA with increasing rf field amplitude can be directly seen. Firstly, we observe the occurrence of the higher order spectroscopy lines predicted by the beyond-RWA calculation for sufficiently large rf currents (black data points in figure 6.5a). The quantity of the observed resonances increases with the rf amplitude, as we expect from our calculations. Again, it is important to note, that the higher order resonances grow continuously in strength with increasing rf field amplitude, and that the sudden "appearance" of the resonances is due to the measurement precision, determined mainly by the tickling field strength and the spectroscopy time.

Secondly, we observe a Bloch-Siegert shift of the transition frequencies for large dressing fields [20, 310], which can be seen in figure (6.5c). For weak dressing, the non-RWA terms are small and the RWA calculation of the transition frequencies is identical to the full calculation. The measured frequencies are in good agreement with these calculations (6.5b).

For larger dressing field amplitudes, we observe an increasing deviation from the RWA calculations (6.5c), which is also in excellent agreement with the full calculation. For the strongest coupling realized in this measurement set ($I_{\mathrm{rf}} = 58$ mA), this shift is on the order of 10 kHz, which is one order of magnitude larger than the precision of the spectroscopic measurement. We verify that this effect is indeed a beyond-RWA effect and cannot be ascribed to an uncertainty of our experiment parameters. To this end we independently fit the RWA model to the data, using the field amplitudes as free parameters. This model fails to reproduce the shift of the resonance crossing while at the same time yielding good agreement with the observed resonances for small RF currents.

Note that although the plot shown in figure (6.5a) with the shifted crossing of two resonances looks similar to typical plots describing the Bloch-Siegert effect, we actually plot something different than what is usually shown. In most cases the dependence of two (or more) dressed states on the frequency of the dressing field is plotted in the vicinity of a crossing of these levels, showing that due to the non-RWA terms, this crossing is shifted towards lower frequency. In our case, the plot shows the energy difference (in frequency units) of the dressed states as a function of the dressing field amplitude. It is also important to note, that although only the amplitude of the dressing field is modified externally, the effective detuning experienced by the atoms trapped in the rf potential also changes, due to the change in position of the trap minima in the inhomogeneous static field.

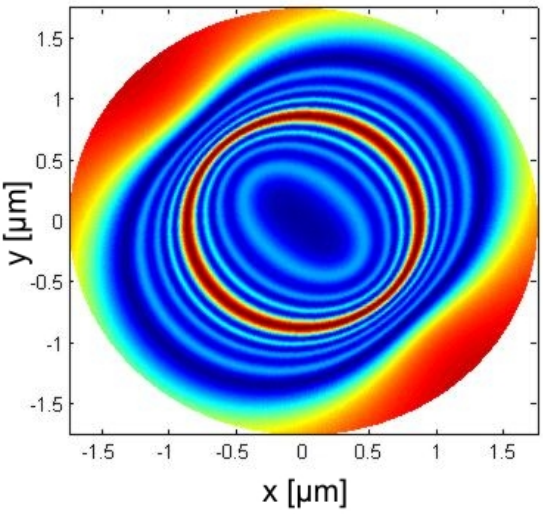

Figure 6.6: Example Floquet calculation of the rf potential of our three-wire structure if the applied AC currents are superpositions of eleven different oscillations with evenly spaced frequencies. Instead of the double well, a much more complex multi-well structure results. A number of interesting potential configurations, like ring arrays, are possible in this configuration. (Calculation by I. Lesanovsky)

This leads to the fact that for increasing rf currents actually both validity conditions of the RWA, $\Omega \ll \omega_0$ and $\Delta \ll \omega_0$ are violated simultaneously. In that sense, the plot shows a more generalized Bloch-Siegert effect than the usually shown level shift due to large Δ.
Finally, it has to be emphasized that we measure only the shift on the energy difference at the minima position between two dressed states due to the non-RWA terms. The absolute deviation between RWA and full calculation for individual dressed states is larger and is a function of space (see figure 5.8).
Typical AC currents for the experiments described in the next chapters are $30 - 50$ mA, which according to the spectroscopy results is the range where the non-RWA terms start to become important. How significant they are in practise depends greatly on the specific experiments, though. In the case of the double well, for the case of positive minimum detuning, which we always use, the main change is an increase in the potential barrier height. Consequently, for experiments where a negligible tunneling rate is desired, the RWA calculation is sufficient most of the time, since it sets only overestimates the tunneling rate compared to the non-RWA calculation.

6.3 Multi-frequency rf potentials

In the experiments presented in this chapter the weak spectroscopy field could be safely treated as a perturbation acting on the fixed dressed states realized by the strong rf field. Naturally, the question aries what happens when the spectroscopy rf field becomes comparable in strength to the dressing field, and one faces the situation of two (or more) strong rf fields with different frequencies acting on the trapped atoms.
A very specific case is considered in [50]: If the differences of the frequencies of the multiple rf fields are large compared to the associated Rabi frequencies, each frequency can be treated separately within the RWA, with only minor corrections from neighboring frequencies. Instead of a double well, such a multi-frequency rf setup combined with a standard Ioffe-Pritchard trap would create a multi-well configuration, where the distance between wells is controlled by the frequency spacing or the static field gradient. The calculation seems somewhat artificial, because the separated RWA treatment breaks down, as soon as the different wells approach each other, which is of course the interesting case.
An interesting application of multi-frequency rf fields for a highly specific field geometry is discussed in [79]. Here a combination of a permanent magnet static trap and rf fields is proposed to realize two ring traps next to each other. A second rf field with slightly different frequency is suggested

to induce a counter-rotation in the two rings. This calculation also stays within the RWA.
In principle, the full system can be treated straight-forwardly in the dressed state picture. Additional field energy and coupling terms have to be included in the Hamiltonian (2.33) and the bare state basis is extended by an additional quantum number describing the rf photons of each field, $|m_{\mathrm{F}}, N_1, N_2, ...\rangle$. The non-RWA calculation then can be carried out as discussed in section (2.3.3) by diagonalizing the resulting matrix. It is easy to see that this quickly becomes highly impractical. Especially in the case of large rf field amplitudes, i.e. for large coupling, the number of required basis states grows very fast. In the context of rf spectroscopy of dressed atoms in room temperature gas cells, a calculation along those lines for homogeneous static and rf fields of two frequencies has already been carried out in 1971 [2].
A much more manageable approach is given by Floquet theory in the case of (arbitrarily many) equally spaced frequencies. This theory has first been developed by Shirley in 1965 as an alternative to the dressed state approach [289] and has since then found wide-spread applications in many areas of physics. In more general form, it presents a solution scheme for a much more general class of periodic Hamiltonians.
Figure (6.6) shows a first example Floquet calculation for our three-wire trap and the case of eleven different frequencies carried out by I. Lesanovsky. It can be seen that the resulting potential resembles a multi-well structure as proposed by [50], but that the full calculation results in a more complex geometry.
The implementation of multiple rf frequencies in the experiment seems realistic. The design of a versatile, multi-frequency rf source is a near future goal. Alternatively, frequencies from multiple generators can be easily mixed with standard rf components. Of course, questions like adiabaticity and stability of the traps arise, but is seems likely that stable trapping is possible. The possible applications seem very versatile, from multiple minimum traps to complex time-dependent modulations of simpler traps.
The idea of multiple frequencies is further extended to a different regime in [196]. Here, the concept of time-orbiting-potential (TOP) static traps [247, 5] is applied to rf-dressed traps. In TOP traps the atoms are confined to an effective potential which is the time-average of a modulated potential. This averaging is possible if the modulation is fast compared to the trap frequencies and slow compared to the Larmor frequency of the trapped atoms. The idea proposed in [196] is to apply a similar (slow) modulation to the dressed potential, resulting in a *time-averaged adiabatic potential* (TAAP). For the time-averaging of the rf dressed potentials to be valid, the modulation only has to be small compared to the Rabi frequency. As can be seen in this chapter, this is not a strong restriction compared to the standard TOP traps as the Rabi frequency can be made comparable to the Larmor frequency by sufficiently strong rf dressing. The TAAP offers a large variety of complex potentials, and it will be highly interesting to see if this trapping method is experimentally realizable.

7 Coherent splitting of a Bose-Einstein condensate

The potential calculations presented in chapter 5 showed that the rf adiabatic potentials can be used for the deformation of single minimum into a double well potential. Dynamically splitting a single condensate into a two parts confined in the double well is analogous to a beam splitter in optics and hence forms a basic element of a matter wave interferometer, as discussed in section 3.3.2.
However, it has been shown to be extremely challenging to maintain the phase coherence throughout the splitting process in various experimental approaches [10, 288]. The first successful phase preserving splitting of a condensate has been achieved in 2004, using optical potentials based on focussed red detuned laser beams. The relative phase has been read out in interference experiments using the entire clouds [287] as well as using small amounts of optically extracted atoms [272]. Coherent dynamics in a double well with adjustable barrier height have been observed in a combined optical potential based on focussed lasers and standing waves [1, 90].
The integration of a coherent matter wave beam splitter on an atom chip has been a long standing goal. Microchip interferometers seem to be extremely well suited for the study of decoherence effects due to coupling to the environment [332], which could be introduced in a "controlled" way by changing the distance of the interferometer to the chip surface [134, 133]. Another motivation stems from the fact that simple and robust atom-chip beam splitters and interferometers may constitute the building blocks for quantum information processing on the atom chip [33, 32, 44]. Finally, a technological application of chip-based atom interferometers could be inertial sensors on a microscale [162].
For all of these applications it is imperative that the deterministic coherent quantum evolution of the matter waves is not perturbed by the splitting process itself. Although several atom-chip beam-splitter configurations have been proposed and experimentally demonstrated [35, 232, 177, 144, 288], none of them has fulfilled this crucial requirement.
In this chapter, we discuss the realization of a matter wave beam splitter based on rf adiabatic potentials. In section 7.1 we review the potential configuration and the technical implementation of the rf beam splitter. In section 7.2 we study the evolution of the relative phase during the splitting and show that the rf beam splitter experimentally realizes, for the first time, coherent spatial splitting and subsequent stable interference of matter waves on an atom chip [284, 142]. The phase dynamics of the split system after the splitting process is investigated in section 7.3. We show that longitudinal fluctuations of the phase in the two elongated 3d condensates in the double well potential are the main cause of decoherence in the system. In turn, we show how the interferometer scheme can be used to study these phase fluctuations.
The ability to evaporatively cool atoms in the rf dressed double well potential allows us to prepare independent and phase-coherent condensates in exactly the same potential configuration [142]. The comparison of the resulting interference patterns is presented in section 7.4. We also show first results of experiments studying the (re-)combination of two BECs in the trap.
Finally, in section 7.5 we investigate what differentiates the rf beam splitter from static magnetic field implementations by comparing it to the commonly used two-wire static field beam splitter [62, 35, 138, 126, 293, 144, 288, 74]. We argue that the differences between the two approaches illustrate general advantages of the rf dressed state potentials over (quasi)-static magnetic traps.

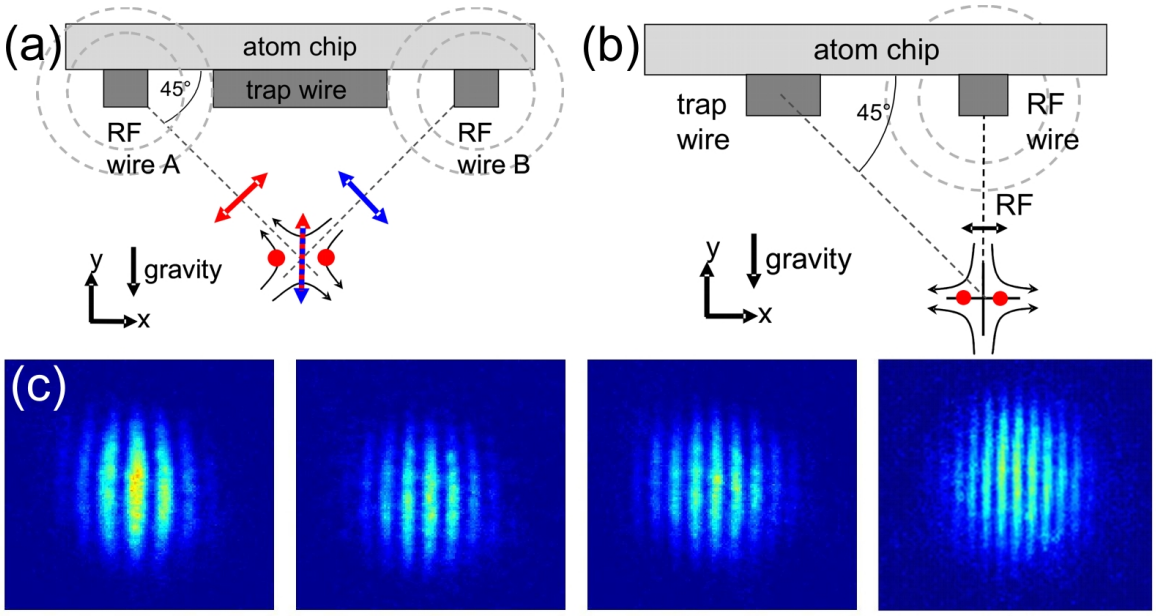

Figure 7.1: **(a)** Schematic of the three-wire configuration for the horizontal double well. The phase shift between the two rf fields is chosen such that the total rf field is vertically polarized, which results in the indicated horizontal double well. **(b)** Some of the results in this chapter have been obtained with the two-wire trap configuration. Here the rf field is produced by a single wire. To realize the correct orientation of the rf field with respect to the static quadrupole, the static trap center is rotated directly underneath the rf wire. This trap position is critical for the realization of a balanced horizontal double well, making the two-wire trap more prone to misalignment errors than the three-wire trap. **(c)** Example interference patterns for condensates released from the three wire trap. The fringe spacing (and consequently the total number of fringes) is roughly inversely proportional to the original double well separation.

7.1 RF potential configuration and splitting procedure

The procedure of loading a BEC into the adiabatic potentials was discussed in section 5.6.1. The splitting of a single BEC into two parts is realized by transforming the static single minimum trap into the rf double well configuration. In particular, we focus here on the horizontal double well, which for the three-wire trap is realized by setting the phase shift between the two AC currents to $\delta = \pi$ (section 5.2.1) and using equal current amplitudes [1], as shown in figure 7.1a.
The splitting is realized by ramping up the AC currents at a fixed frequency ω_{rf} smaller than the Larmor frequency ω_{Larmor} at the minimum of the static trap ($\Delta_0 > 0$, compare equation 5.17). We consider a BEC as "split" in two halves, once the potential barrier between the two parts is sufficiently high such that tunnel coupling between the two wells can be neglected. Typical durations for the amplitude ramps are 10...50 ms.
Following the theoretical considerations of section 3.3, we expect to see a matter-wave interference effect when the two separated parts are recombined. This recombination is achieved by employing the scheme shown in figure 3.2: the double well potential is switched off and the atoms are allowed to expand freely. The interference effect is then visible as a modulation in the atomic density in time-of-flight pictures. For the horizontal double well configuration, the resulting interference

[1] Note that the current implementation of the three-wire trap has a small asymmetry due to different distances of the rf wires, which is compensated by adequately scaling the two rf currents. If we talk of "equal" amplitudes we assume that this scaling has been included. The actual values of the currents used in the experiment are not identical of course.

fringes are perpendicular to the atom chip, hence they can only be imaged in one (the longitudinal) of the horizontal directions. In the transverse direction the imaging integrates over the modulation and only the usual, unmodulated density profile is visible. Indeed, we added the longitudinal imaging specifically for the observation of these interference patterns.
Examples images of interference patterns taken with the longitudinal imaging are shown in figure 7.1c. It can be seen that for different double well distances (increasing from left to right in the figure), the fringe spacing decreases accordingly, roughly following the prediction for non-interacting particles derived in section 3.3.1. A more careful analysis of the fringe spacings we measure shows significant deviations from this simple model [284, 282], which can be attributed to atomic interactions affecting the wave packets shape in the double well and during the first phase of expansion[270]. This effect becomes increasingly important for small trap separations and not entirely split condensates. A detailed study of this effect based on numerical simulation of the expansion can be found in [282].
Parts of the results presented in the next section have been obtained with a two-wire rf potential configuration instead of the three-wire trap discussed in this manuscript. The two-wire trap is shown in figure 7.1b, the underlying field configuration, static Ioffe-Pritchard trap plus linear rf field, is the same as for the three-wire trap. The two-wire trap was the first rf trap we used in our experiment and the one in which we originally demonstrated coherent splitting of a BEC, as will be shown in the next section. A detailed characterization of this trap and description of early experiments can be found in [282]. The three-wire setup offers some distinct advantages, such as free choice of the orientation of the double well potential and circularly polarized rf fields, as discussed in the last chapter. In regard to coherent splitting of a BEC, the three-wire trap has the advantage that its inherent symmetry makes the balancing of the double well easier.

7.2 Phase coherence of split BEC

Based on the arguments presented in section (3.3), observing an interference pattern in every single run of the experiment does not suffice for proving phase coherence between two BEC. Instead, we have to verify that the two halves have the same, fixed phase relation in many runs of the experiment with identical splitting parameters [36].
We first discuss how the relevant information is extracted from the interference images (section 7.2.1), and list a few aspects of circular statistics, which play a role in the analysis of the obtained data sets of relative phases (section 7.2.2). We then present experimental results showing the phase coherence directly after the splitting (section 7.2.3) and the phase evolution in the final part of the splitting process (section 7.2.4).

7.2.1 Measuring phase and contrast

The relative phase between the two BECs can be directly seen in each imaged interference pattern as a spatial shift of the minima positions in relation to the maximum position of the density profile (equation 3.75). To extract this relative phase, as well as the contrast and fringe spacing, from a single image, we use two different procedures, which are both shown for an example image in figure 7.2.
We obtain a single line density by integrating the absorption image in y-direction (parallel to the interference stripes). Usually, only a limited number of pixel rows at the center of the density distribution is used, as indicated in figure 7.2a. The resulting line profile is fitted with a modulated Gaussian function of the form

$$f_{\text{fit}}(x) = Ae^{-\frac{(x-p_0)^2}{2\sigma^2}} \left(1 + C\cos\left(2\pi\frac{x-p_0}{s} + \triangle\phi\right)\right), \tag{7.1}$$

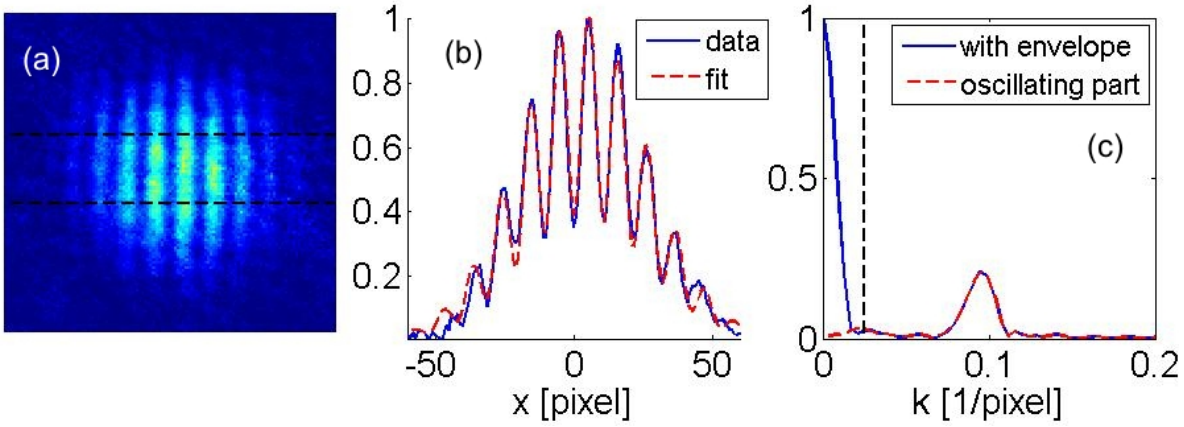

Figure 7.2: Illustration of the data analysis process. **(a)** A single line profile of the fringe pattern is obtained by summing up the central slices of the interference pattern image in vertical direction. **(b)** The resulting profile is fitted with a modulated Gaussian function. The amplitude of the modulation gives the contrast while its displacement with respect to the Gaussian envelope yields the relative phase between the two interfering condensates. **(c)** The same information can be extracted from a fast fourier transform of the fringe profile. Here the absolute value of the fourier function is shown, which has a peak at the wavenumber corresponding to the fringe spacing. The contrast is proportional to the amplitude of this peak, while the phase is given by the angle of the complex fourier coefficient. The FFT method is significantly faster than the fitting of the spatial pattern and is as accurate for sufficiently many (≥ 5) fringes in the pattern.

where A, σ, and p_0 are the amplitude, width and center position of the Gaussian envelope, respectively. From the cosine part, we get the contrast C, with values between 0 and 1, the relative phase $\triangle\phi$, and the fringe spacing s (the distance between interference minima) (figure 7.2b).
Alternatively, these three quantities of interest can also be extracted from the FFT of the line density (figure 7.2c). The spectrum of the interference pattern, show a broad peak at small wavenumbers corresponding to the Gaussian envelope, and a second peak at the wavenumber corresponding to the fringe spacing due to the interference pattern. The absolute value of the unnormalized FFT profile at this position is the fringe amplitude ρ_Q, defined in equation (3.86), while $\triangle\phi$ is the phase of the corresponding (complex) fourier coefficient. The fringe amplitude ρ_Q and the contrast C are identical except for normalization with the total particle number in the integration area. The FFT method works with comparable accuracy as the fitting for sufficient number of fringes (≥ 5), its advantage is highly increased processing speed. Also, for comparison with the theory presented in section 3.4, we are interested in the fringe amplitude ρ_Q, which is directly obtained from the FFT method.

7.2.2 Circular statistics

The relative phase $\triangle\phi$ is a circular variable, i.e. it has a periodicity of 2π. This can cause some ambiguity in the definition of the mean value and variance of sets of relative phases. In particular, when these sets are spread over a significant fraction of the interval $[0, 2\pi]$, fitting a normal distribution is problematic, as its tails can extend over the boundaries of the interval.
It is convenient to transfer circular data onto the unit circle. For a given set ϕ_k of N measured phases, one calculates the phasor

$$R = re^{i\bar{\phi}} = \frac{1}{N}\sum_{k=1}^{N} e^{i\triangle\phi_k}. \tag{7.2}$$

Here, $\bar{\phi}$ is called the mean phase, while r is known as the mean resultant length [83]. r, which can take values between 0 and 1, is a measure for the concentration of the data set. $r = 1$ implies that all data points are coincident. However, $r = 0$ does not imply a uniform distribution of the phases. For example a set of phases alternating between 0 and π has $r = 0$. In that sense, defining $\bar{\phi}$ as the mean phase of the set is only sensible if the data is unimodal.
To get a measure of the dispersion of a unimodal data set around its mean value $\bar{\phi}$, it can be fitted with a wrapped normal distribution (WND)

$$f_{\mathrm{W}}(\phi) = \frac{1}{\sqrt{2\pi}\sigma} \sum_{k=-\infty}^{\infty} e^{-\frac{1}{2}\frac{(\phi-\bar{\phi}+2\pi k)^2}{\sigma^2}}, \tag{7.3}$$

which is a 2π-periodic version of the standard linear normal distribution [83], or in other words a Gaussian "wrapped" around the unit circle. The width σ of the WND is related to the mean resultant length by

$$\sigma = \sqrt{-2\ln(r)}. \tag{7.4}$$

For data sets with a small spread ($\sigma \ll 2\pi$), the circular nature of the phase plays no role, and the WND is identical to the linear normal distribution.
An alternative, and often simpler, method for testing the unimodality of a data set, which works well also for small N, is the Rayleigh test [83]. For a finite number N of data points the mean resultant length r is also finite even for uniformly distributed phases. The Rayleigh test compares the mean resultant length r of a given data set with the distribution of mean resultant lengths for random data sets of the same size. A good approximative form of the Rayleigh test is given by

$$P = \exp[\sqrt{(1 + 4N + 4N^2(1 - r^2))} - (1 + 2N)]. \tag{7.5}$$

The randomness P is the probability that a uniformly distributed data set produces a mean resultant length larger than r. Uncorrelated data sets have an expected value of randomness $P \approx 0.5$, while unimodal data sets with narrow width have a small randomness value. For example ten data points drawn from a distribution with variance $\pi/5$ have a randomness value of $P \approx 10^{-4}$. If a series of phase measurements has a randomness value of 0.01 (0.1), the relative phase is non-random with a probability of 99% (90%) [83].

7.2.3 Observed phase distribution

To test for phase coherence between the two halves of the BEC split by the rf potential, we repeat the experiment a large number of times with identical parameters and check whether the measured relative phase shows a statistically significant deviation from a random distribution, using the statistical methods introduced above.
Figure 7.3 shows histograms of the measured relative phases for 40 repetitions of the experiment for two different splitting distances ($d = 3.4\,\mu$m and $3.8\,\mu$m) in the two-wire trap. We clearly find a non-random distribution in both cases. For the smaller splitting, a (linear) Gaussian fit to the data gives a width of the distribution of $\sigma = 13°$, while for the larger splitting we obtain $\sigma = 28°$. We also see that the mean value of the second sample has shifted
In both cases, the potential barrier between the well is sufficiently high to prevent any residual tunnel coupling on the timescale of the experiment, hence the two BEC are truly "split". For the number of atoms used in these experiments and the used trap parameters, the adiabacity and the two mode tunneling model, fails at $d \approx 3.3\,\mu$m (compare section 3.3.2).
The increased phase spread for the larger splitting can be understood as follows. The durations of both splitting ramps are the same, but for the larger splitting the end value of the AC current is increased. Consequently, the rate at which the current grows is larger in that case, and the (fixed) current corresponding to $d \approx 3.2\,\mu$m, where we assume the decoupling of the wells to happen, is

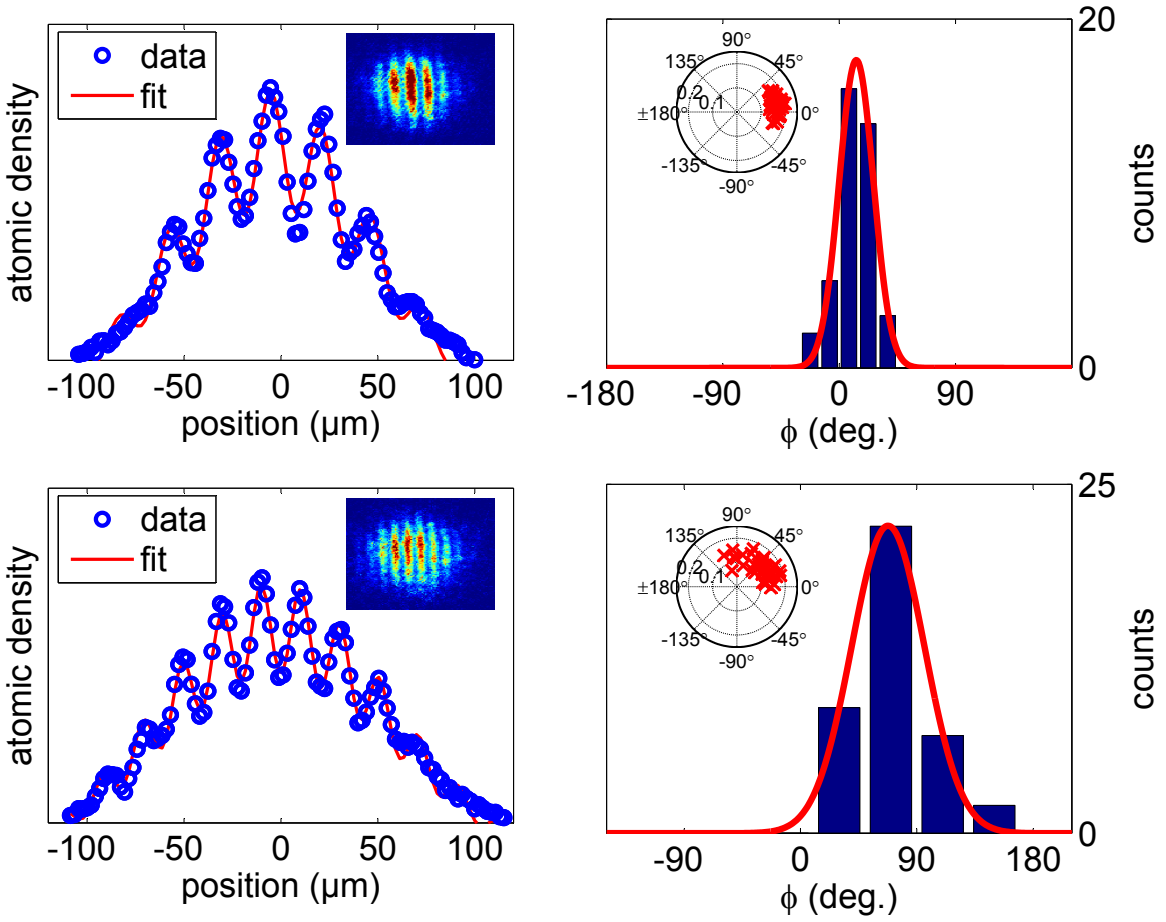

Figure 7.3: The relative phase of the two halves of the BEC is measured in 40 experiments with rf current amplitudes corresponding to 3.4 μm (top) and 3.8 μm (bottom) double well separation, each. Larger initial distance of the BECs results in smaller fringe spacing, as can be seen in the line density plots on the left. The relative phase is extracted from the interference patterns by fitting equation (7.1) to density profiles. The obtained phase sets are shown as histograms on the right. A non-random distribution can clearly be seen. From Gaussian fits, we determine the widths of the distributions as $\sigma = 13°$ (top) and $\sigma = 28°$ (bottom) for the smaller and larger splitting, respectively.

reached earlier. Note that although we use a linear AC current ramp, the barrier in the transverse potential only appears towards the end of this ramp. The time during which the two condensates are held in the trap but are not coupled anymore is usually restricted to the final $\sim$ 2ms of the splitting process. For the parameters of the considered experiments we find a change of the free evolution time from $t \approx 0.2$ ms for the small splitting to $t \approx 0.8$ ms for the second data set. In this time we expect the phases to evolve, and the phase spread to increase. We will analyze this process in more detail in section 7.2.4. A similar result obtained with the three-wire setup, is shown in figure 7.4. Again, the repeated measurement of the relative phase shows a narrow spread. The Gaussian fit yields $\sigma = 10°$. From numerical calculations of the two mode tunneling rate for the measured atom number ($N = 2 \times 10^4$) and the calculated rf potential, we estimate that the two condensates were released ~ 0.3 ms after the coupling between the two wells vanished.
We attribute the small reduction in the initial width of the phase distribution compared to the early results obtained with the two-wire setup to reduction of noise in the rf electronics. One mayor noise source could be identified in the power supplies of the rf switches used for shutting of the rf currents, which accordingly were replaced with better, i.e. less noisier, supplies (compare

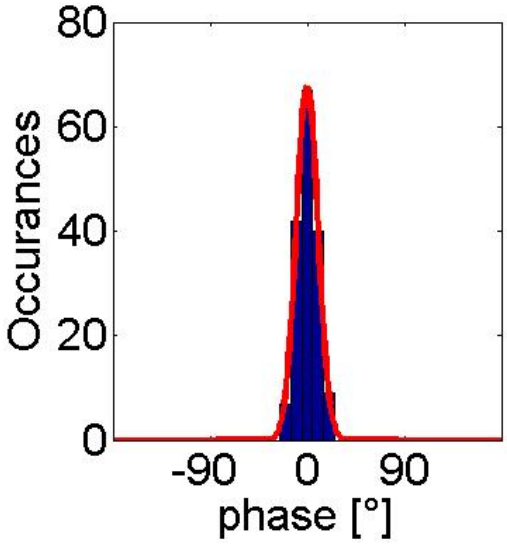

Figure 7.4: Histogram of measured relative phase of the two BEC parts ~ 0.3 ms after complete separation in the three-wire trap. The width of the distribution is $\sigma = 10°$. We attribute the slight improvement compared to the early data obtained with the two-wire setup to the slower splitting ramp and/or reduced noise in the electronics coupling the frequency generators to the chip wires.

section 5.6.2).

7.2.4 Phase evolution during the splitting

We have monitored the evolution of the relative phase and the behavior of the phase spread for the final part of the splitting ramp after the complete separation of the two wells, as is shown in figure 7.5 for data obtained in the two-wire trap.
We observe a deterministic evolution of the mean relative phase, due to (small) energy imbalances between the two wells. The speed of this evolution can be modified, and its sign can be reversed, by slightly changing the double well parameters (in the case of figure 7.5 the DC current in the static trap wire was changed). The observed phase evolutions are in very good agreement with quadratic fits, which can be understood as follows. After the separation we expect the relative phase to evolve as

$$\triangle\phi = \frac{t}{\hbar}\triangle E = \frac{t}{\hbar}(E_1 - E_2), \tag{7.6}$$

where $E_{1,2}$ are the energies of the many-particles states (including interactions) in the left and right well. If we assume that the energy difference itself grows (approximately) linearly with time, i.e. $\triangle E = ct$, the time evolution of the relative phase becomes quadratic

$$\triangle\phi = \frac{ct^2}{\hbar}, \tag{7.7}$$

in accordance with the measurement. We find exactly the same behavior during the splitting in the three-wire trap, which is shown in figure 7.6. From the quadratic fit, we can calculate the rate at which the imbalance increases as $c \approx 50$ Hz/ms, which in turn yields a final imbalance for this example of $c \times 2.2$ ms ≈ 110 Hz. Note that this imbalance is smaller than the transverse ground state in the double well and the chemical potential by approximately a factor 30 and 60, respectively. The imbalance is caused by a small asymmetry of the double well, leading to a (small) lifting of the degeneracy of the two separated single particle ground states. This in turn causes a small difference in the (mean) atom number in each well, leading to different many-particle ground state energies. Its important to note that this exact determination of the mean relative phase and its deterministic evolution are not in contradiction to the phase-atom number uncertainty relation and the consequential phase diffusion. This effect manifests itself in the shot to shot fluctuation of the relative phase, not in the mean value, which in turn remains well defined as long as the

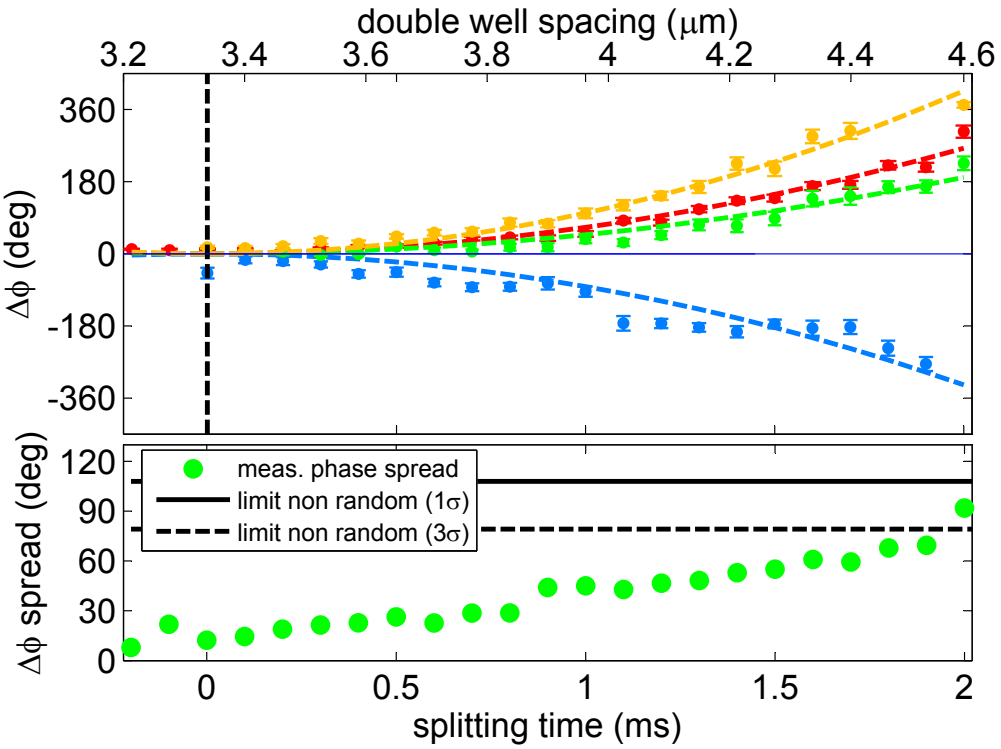

Figure 7.5: **(Top)** Time evolution of the mean relative phase during the splitting process. The vertical dashed line indicates the time/well separation where the two wells completely decouple. From this moment on the relative phase starts to evolve freely. The phase evolution can be modified by slightly changing the trap parameters, deliberately introducing a double well imbalance (different imbalances are distinguished by color). The error bars indicate the statistical variance of the mean of the measured relative phase. The dashed colored lines are quadratic fits to the data, which indicate a linear increase of the imbalance over time (see main text). **(Bottom)** Width of the relative phase distribution throughout the splitting. The data points correspond to the green curve in the upper plot. The solid (dashed) line indicates the level, below which the measured phase distribution can be distinguished from a random phase by one (three) sigma.

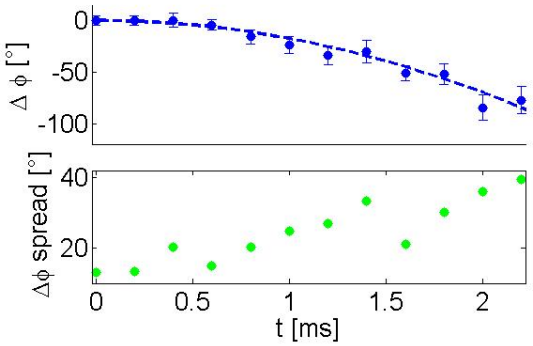

Figure 7.6: Same plots as in figure 7.5 for a data set measured in the three-wire trap. The top plot shows the (quadratic) evolution of the mean relative phase over time, which is caused by the increasing energy imbalance during the splitting. The bottom plot shows the (roughly) linear increase of the width of the phase distribution.

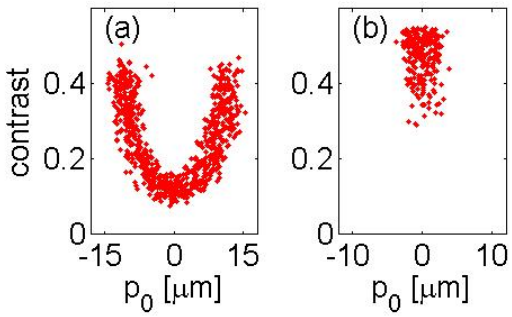

Figure 7.7: Reduction of unwanted condensate excitations during the splitting process. (a) For $\Delta_0 = 200$ kHz and a total ramp duration of 20 ms we observe strong fluctuations of the contrast in the interference patterns of BECs released 0.5 ms after the end of the rf splitting ramp. These fluctuations are strongly correlated with fluctuations of the center position of the total density distribution. This fluctuation dominates any deterministic evolution of the contrast after the splitting. Similarly phase and phase spread evolution are strongly modified. (b) The problem can be strongly reduced by working at smaller minimal detuning $\Delta_0 = 50$ kHz, which results in a more linear increase of the splitting distance and avoids a strong initial "kick" in the separation process.

phase spread is not too large. In the bottom plots of figures 7.5 and 7.6 the width of the phase distributions corresponding to two of the plotted mean phase evolutions are shown. In both cases we find a (roughly) linear increase of the distribution widths over time, which corresponds to a constant diffusion rate. In principle, one would expect to see an increase in the diffusion rate with increasing transverse confinement during the continuing splitting ramp, according to equation (3.95). Using the final transverse trapping frequency, we can get a rough lower bound for the diffusion time for the respective parameters of the two experiments. For the two-wire trap corresponding to the data set in figure 7.5 we have $\omega_\perp = 2\pi \times 2$ kHz, $\omega_z = 2\pi \times 30$ Hz, and $N_{1,2} \approx 2 \times 10^4$. The parameters of the three-wire trap are $\omega_\perp = 2\pi \times 2.5$ kHz, $\omega_z = 2\pi \times 10$ Hz, and $N_{1,2} \approx 2 \times 10^4$. From equation (3.95) we get $T_D \approx 10$ ms for both traps. Expressing this as a diffusion rate gives $R \approx \pi/10$ rad/ms $\approx 20°$/ms. Remember that this is a lower bound because it neglects any number squeezing due to interactions during the tunnel-coupled part of the splitting process (compare section 3.3.2).
The values obtained from the experimental data are $R_{\mathrm{exp}} \approx 30°$/ms and $R_{\mathrm{exp}} \approx 20°$/ms for the two-wire and three-wire traps, respectively. The reduction of the diffusion rate in the three-wire trap is most likely due to reduced technical noise.
In general, our values are (slightly) smaller than the lower bound on the (3d) phase diffusion rate, and show no dependence on the splitting speed, as we would expect according to the arguments presented in section 3.4.3. We attribute this to longitudinal phase fluctuations in the elongated BECs [252]. Even in the 1d-3d crossover regime, into which these experiments fall, they are quite pronounced at typical temperatures on the order of $\sim$ 200 nK and our trap parameters [94]. Indeed, we observe them at any stage of the splitting process as random density modulations in transverse time-of-flight images [65]. The observation of phase coherence times of nearly 200 ms in a very similar experiment [156] seems to be in contradiction with this conclusion, though. A possible explanation for the absence of phase fluctuations could be an extremely low temperature $T \ll T_\phi \approx 70$nK in the investigated system.
We obtain further indication that the phase fluctuations play a dominant role even in the elongated 3d case by observing the system for hold times in the double well potential of up to 200 ms, as will be discussed in the next section. Experiments demonstrating the dominant role of phase fluctuations in the 1d-regime will be presented in the next chapter.

7.3 Evolution of the system after the splitting

To study the time evolution of the split system beyond the duration of the splitting ramp, the two BEC have to be held in the double well configuration after the initial rf amplitude ramp. In addition to some practical issues regarding the external control of the single frequency generator in the original configuration, we observed that the dynamics of the system after the splitting was

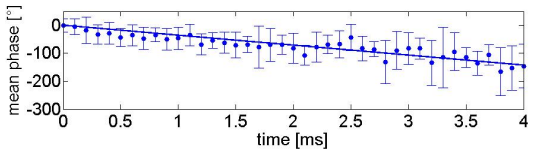

Figure 7.8: Evolution of the mean relative phase after the splitting process. The time $t = 0$ corresponds to the end of the splitting ramp. The phase starts to evolve about 1.5ms earlier, and has been set to zero for $t = 0$. For the first milliseconds the relative phase grows linearly, as one would expect for a system with a small energy imbalance between the two wells. This imbalance can be calculated from the slope of the phase evolution as $\triangle\mu \approx 90$ Hz. The error bars are the standard deviation obtained in averaging 7-9 individual measurements per time t.

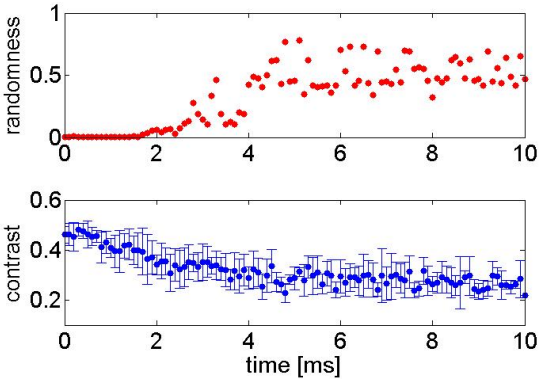

Figure 7.9: (a) Calculated randomness of the observed relative phase over a time of 10 ms after the splitting. The data during the first 4 ms corresponds to the mean relative phase shown in figure 7.8. The growing of the phase spread over time translates into an increased randomness. After $\sim$ 4 ms, the randomness becomes equal to that of totally uncorrelated data. (b) Measured average contrast over time for the same data set. In correspondence with the increasing randomness, we observe a continuous decrease of the average contrast in the first 4 ms, which then becomes constant at a finite value.

clearly dominated by breathing mode excitations and collective oscillations of the two BECs, which destroyed any deterministic phase evolution directly after the ending of the amplitude ramp [282]. For example, these oscillations showed up as a pronounced correlation between contrast and center position of the observed interference patterns (figure 7.7a), dominating any other effect in the time evolution of the contrast. The main reason for these excitations was the rather abrupt start and stop of the condensate motion during the splitting process.

To solve this problem, the splitting ramp was adjusted to make both the beginning of the splitting as well as the stopping of the relative motion of the two condensates at the end of the process smoother. One step to achieve this was to introduce a two step rf amplitude ramp, with a fast (3 ms) ramp up slightly below the critical rf field amplitude B_C (equation 5.16), followed by a slower (17...47 ms) increase to the final amplitude value.

An alternative improvement was found to be the use of smaller minimal detuning Δ_0, which has two consequences: For fixed ramping time the effective duration of the splitting ramp is increased, as the critical field amplitude B_C is reached earlier during the ramp. Additionally, the increase of the minima separation becomes smoother, as can be seen from equation (5.14). For large B_C (large Δ_0), the well separation shows a steep increase once B_C) is reached due to the square root dependence. For small detunings this initial rise becomes less steep, changing to linear in the limiting case of $\Delta_0 = 0$.

On the other hand, working too close at the resonance frequency turned out to be also problematic, as the interference depends more critically on the actual phase of the rf field at the moment of switching off for small detuning [186]. The best compromise between simple splitting, avoidance of condensate excitations and measured average interference contrast directly after the splitting was found at $\Delta_0 \approx 50$ kHz.

7.3.1 Short time: linear phase evolution

The improving of the splitting process as described above enables us to observe the split system for times beyond the splitting ramp duration. Figure 7.8 shows the now measurable evolution of the relative phase directly after the end of the splitting ramp.

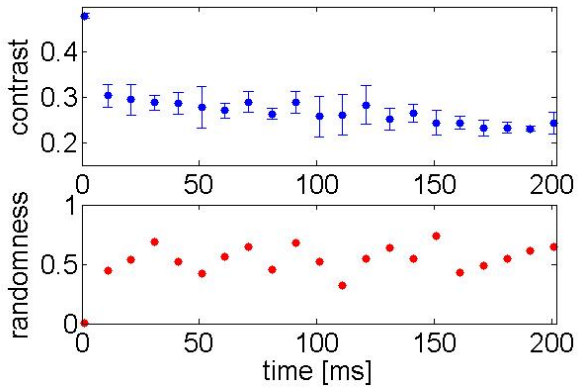

Figure 7.10: Contrast evolution for long hold times. **(a)** After an initial reduction of the contrast during the phase randomization in the first few milliseconds, we observe a much slower decrease over long times. The two condensates can be seen as independent sources, once the correlation of the phase fluctuation patterns imprinted by the splitting is washed out. The change of contrast then is due only to the slowly increasing temperature of the system. **(b)** The calculated randomness of the relative phases corresponding to the data used in (a) shows that the condensates indeed can be seen as independent after the initial fast phase randomization.

We see a linear increase of the relative phase, as we would expect for two uncoupled condensate with a (small) energy imbalance. This energy imbalance between the many particle ground states in the left and right well can be directly obtained from the slope of the linear phase evolution

$$\triangle\mu = \hbar\frac{\triangle\phi}{t}, \tag{7.8}$$

yielding an imbalance of ~ 90 Hz between the two wells for the example shown in figure 7.8.
The linear phase evolution is accompanied by a growing phase spread. For the number of measurements (7-9) per time t in this data set the randomness, as defined in equation (7.5), is better suited to characterize the phase spread than the standard deviation of a normal distribution fit. Figure 7.10a shows the obtained randomness for a measurement of the evolution of the system over 10 ms after the splitting. The data points for the first 4 ms correspond to the mean phase values shown in 7.8.
The growing phase spread leads to an increase of the randomness, which becomes comparable to the expected value for totally uncorrelated data roughly after these 4 ms. Including the free evolution time during the splitting process, the total phase randomization time is ~ 5.5 ms, which again is shorter than the minimal phase diffusion estimate of $t_{\mathrm{D}} = 7.6$ ms (parameters for this data set: $\omega_\perp = 2\pi \times 3.5$ kHz, $\omega_{\mathrm{z}} = 2\pi \times 15$ Hz, $N_0 = 2 \times 10^4$ atoms).
An argument for the longitudinal phase fluctuations to be the main cause for the phase randomization is the observed behavior of the average interference contrast. The loss of phase memory is accompanied by a continuous reduction of the average contrast, as shown in figure 7.10b. The contrast then remains constant at a finite level with relatively small fluctuations, even for times where the relative phase is totally random.
This observation is in agreement with the argument given in section 3.4.2: the contrast reduction suggests a loss of local relative phase relations, showing that $\phi_{1,2}$ cannot be treated as constant over the whole system length. In contrast to this, a randomization of the global phases of each condensate would not lead to a contrast reduction, while alternatively a destructive process such as heating cannot explain the leveling off of the observed contrast.
We can use equations (8.2) and (3.125) to estimate a decoherence time due to the phase fluctuations. Note that both formulas are derived for true 1d systems, while the experiments fall into the 1d-3d crossover regime. Still, it is reasonable to use these formulas to get an idea of the expected dephasing time due to the phase fluctuations. For the parameters given above, we find $t_{\mathrm{dec}} \approx 5$ ms, which agrees surprisingly well with the observed phase randomization time.

7.3.2 Long time: random phase and finite contrast

The time evolution of the interference contrast can be further studied for longer holding times of the two BECs in the double well potential. In figure 7.10 the measured average contrast and the

phase randomness for 10 individual measurements each are shown for times up to 200 ms after the splitting. The experiment parameters are the same as given in the last section.
The relative phase again fully randomizes within the first few milliseconds, so that no information can be gained from this quantity at long times. On the other hand, we observe a non-vanishing contrast for the full duration of the measurement. Following the fast decrease from initially 0.5 to 0.3 during the phase randomization, the contrast then slowly decreases over the full time period to ~ 0.23.
This finite contrast can be understood along the lines of the argument given in section 3.4.2: Once the two condensates have lost any relative phase memory, they can be considered as two independent (phase-fluctuating) sources. Imaging the interference pattern between these two sources along the longitudinal axis of the system is equivalent to integrating over a chain of interfering pairs of single-mode BECs, with the number of these condensates being given by the temperature-dependent phase correlation length [259]. With equation (3.55) we can estimate the phase coherence temperature $T_\phi \approx 15$ nK for the parameters of this experiment. The temperature $T = 170$ nK of the BECs at $t = 0$ is obtained from the thermal wings in transverse images. Consequently, we can consider the two quasi-BECs as a chain of $T/T_\phi \approx 11$ phase coherent condensates, which should result in a contrast reduction to $1/\sqrt{11} \approx 0.3$. Here it is important to note, that there are various factors reducing the maximum contrast measured in the experiment, like for example finite resolution and focal depth of the imaging system. Instead of assuming an initial contrast of 1, it seems reasonable to consider the average contrast directly after the splitting as "full" contrast. This value is not available in this measurement, as the point $t = 0$ in figure 7.10 is roughly 1.5 ms after the moment of splitting, but we know it from other measurements to be roughly 0.6 for these parameters. Hence, we observe a contrast reduction of roughly 50% during the phase randomization, which is in reasonable agreement, on the level of this consideration, with the 70% we estimated from the theoretical temperature dependence of the phase coherence length in the quasi-condensates.
The slow decrease of the average contrast over time visible in figure 7.10 is in agreement with the above argument and can be attributed to heating of the BECS. The temperature of the BECs at $t = 200$ ms obtained from transverse images is $T = 220$ nK. From this temperature increase we would expect a contrast decrease of $\sqrt{170/220} \approx 0.85$, i.e. a final measured contrast of ~ 0.25, which fits quite well to the measured value.

Contrast statistics

The dependence of the interference contrast on temperature suggests that in turn the contrast reduction due to the phase fluctuations can be used as a thermometer. A similar method has been successfully applied recently to the thermal fluctuations of the relative phase of two coupled 3d condensates [92, 91].
The obvious problem in our case is that the measured contrast strongly depends on a number of other parameters besides the temperature. Hence, any calibration of the average contrast with temperature obtained for example from the standard time-of-flight method would only be valid for a single specific combination of parameters, making this approach highly impractical.
This problem can be circumvented by looking at the full distribution of the measured contrasts at fixed T, as discussed in section 3.4.2. In that case the absolute value of the contrast is unimportant and any technical factors reducing this absolute value are inconsequential. Figure 7.11 shows histograms of the quantity $\alpha = \frac{C^2}{<C^2>}$ for different hold times after the splitting ($t = 20, 70, 120, 170$ ms from a to d), where $0 < C < 1$ is the measured contrast as defined by equation (7.1). Note that for a given system length the contrast C and the fringe amplitude A are proportional. Hence, the contrast and the fringe amplitude can be used interchangeably in the calculation of α.
The effect of increasing temperature with longer hold time can be seen in the change of the shape of the distribution functions. For the shortest hold time (lowest temperature), we observe a peaked

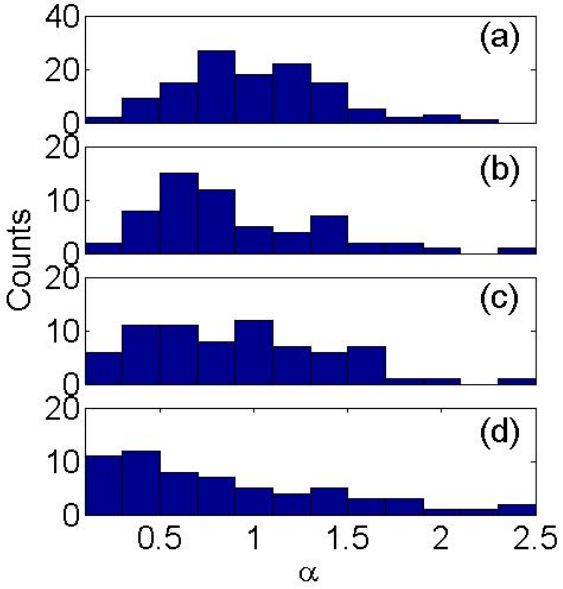

Figure 7.11: Histograms of the normalized, squared contrast $\alpha = \frac{C^2}{<C^2>}$) for different hold times in the double well potential after the initial splitting ($t = 20, 70, 120, 170$ ms from **(a)** to **(d)**). The change of the shape of the distribution functions can be attributed to heating of the system over time. The observed transition from the peaked distribution in **(a)** to a broad Poissonian distribution in **(d)** is in good agreement with theory.

distribution centered at $\alpha = 1$, which then changes over time to a broad Poissonian distribution with maximum near $\alpha = 0$. This is exactly the behavior we expect according to the discussion of section 3.4.2. From the fact that we observe an already quite broad distribution at $t = 20$ ms, we can conclude that the initial temperature of the system was well above T_ϕ in this measurement.
A quantitative analysis of this data is currently in progress. Numerical calculations of the distribution functions for our experiment parameters for comparison with our measurements are being carried out by A. Imambekov. At the moment there are two complications in the analysis of this data set and others obtained with the longitudinal imaging. The most important one is the fact that the longitudinal imaging limits us to a single length L, namely the total system length $L_{\max}$, since the longitudinal imaging automatically integrates over the whole condensate length. Under this condition the inhomogeneity of the 1d-density due to the longitudinal confinement cannot be neglected, which the theory currently does [107, 147]. Another aspect is that the data set shown in figure 7.11 corresponds to condensates in the 1d-3d crossover regime ($\mu \approx \hbar\omega_\perp$, $T > \hbar\omega_\perp$) instead of being truly one-dimensional. The contrast statistics theory is currently being extended to the case of trapped 1d-gases by A. Imambekov and V. Gritsev. It will be interesting to see if this improves the agreement with our measurements. We can then hope to characterize how strongly the transition from true 1d to elongated 3d changes the contrasts statistics.
More advanced analysis of data obtained with the transverse imaging will be presented in the next chapter.

7.4 Coherent splitting vs. independent BECs

In the last section we showed that due to the thermal phase fluctuations any phase relation between two coherently split quasi-condensates is quickly lost. We argued that the two BECs can then be viewed as independent sources in the sense introduced in section 3.3.1.
As already discussed in section 6.2.1, we can also evaporatively cool ensembles of atoms directly in the rf adiabatic potentials by applying a frequency scan with another, weak rf field slightly above a frequency corresponding to an allowed transition between different dressed states. This enables us to produce two independent BECs in exactly the same double well potential as reached by slowly deforming a single trap.
These two different approaches are illustrated in figure 7.12. The final situation is similar in both cases, two separated BECs in a double well potential. In particular, the density distributions in

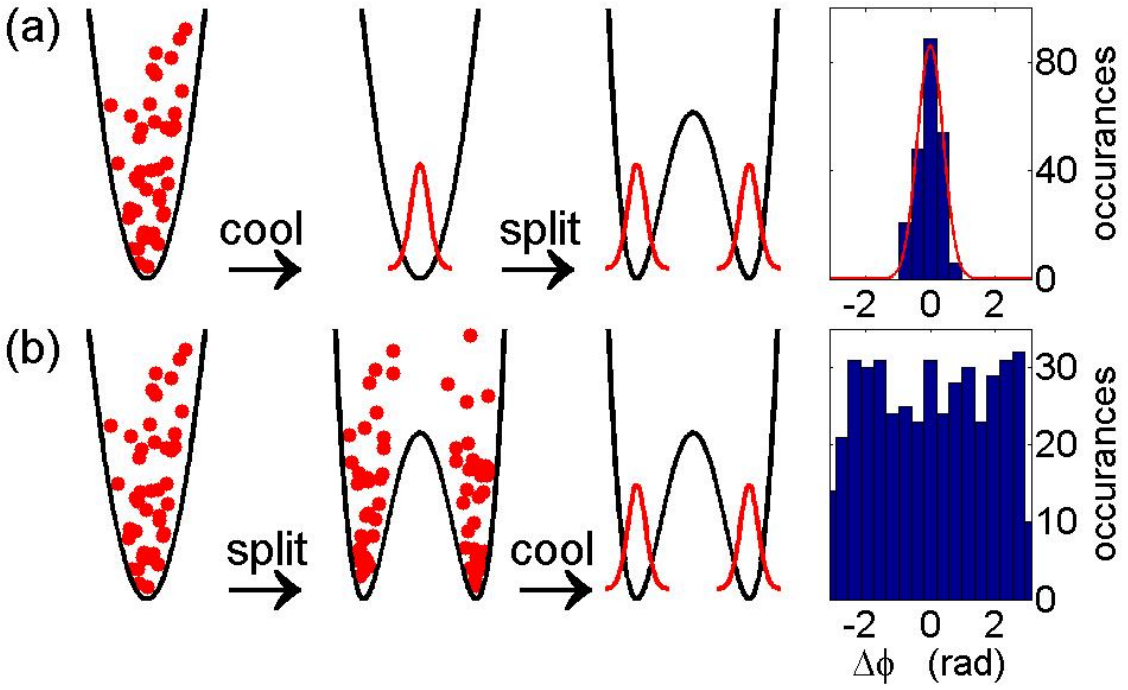

Figure 7.12: Comparison of independent and coherently split BECs. **(a)** The standard coherent splitting scheme starts with a BEC in the single well, which is then deformed to a double well. We observe a narrow phase distribution for many repetitions of an interference experiment between these two matter waves, showing that there is a deterministic phase evolution during the splitting, as discussed in the previous sections. **(b)** To produce two independent BECs, the double well is formed while the atomic sample is thermal. Condensation is then achieved by evaporative cooling in the dressed state potential. The observed relative phase between the two BECs is completely random, as expected for two independent matter waves.

either situation are identical. But the wave functions describing the two many-particle states are highly different, as has been discussed in section 3.3. The coherently split BECs are best described by phase coherent states, while the independent BECs correspond to number states.
The relative phases we measure in the experiment are in agreement with this assumption. As already discussed in the last sections, in the case of the split BECs, we find a reproducible relative phase from shot to shot (figure 7.12a). For this specific experiment, we observe a gaussian distribution with $\sigma = 22.7$ rad. The slightly broader phase spread than for example in figure 7.4 stems from the fact that a large splitting was used, increasing the duration between the decoupling oft the two wells and the release from the trap. In this time the phase distribution already broadens slightly (see figures 7.5 and 7.6).
This large splitting ($d = 6.3\,\mu$m) is used to realize a large potential barrier between the two wells to ensure that the ensembles in the two wells are truly separated long before condensation sets in. We calculate the height of the barrier for the used parameters as $U/k_{\mathrm{B}} \approx 7\ \mu$K, which is large compared to the condensation temperature $T_C \approx 0.4\ \mu$K.
In the case of the independently created BECs we also observe an interference pattern in every single shot, but the relative phase varies completely randomly between experiments (figure 7.12b), as expected for two totally uncorrelated condensates [36, 307].
While this experiment confirms the standard picture of the difference between independent and coherently split BECs in exactly the same potential for first time, it cannot prove or disprove newer theories which attribute the interference pattern to atom interactions [324, 39]. To study these proposals, one would have to tune the scattering length close to zero with a Feshbach resonance, for which an optical trap is better suited than an atom chip trap.

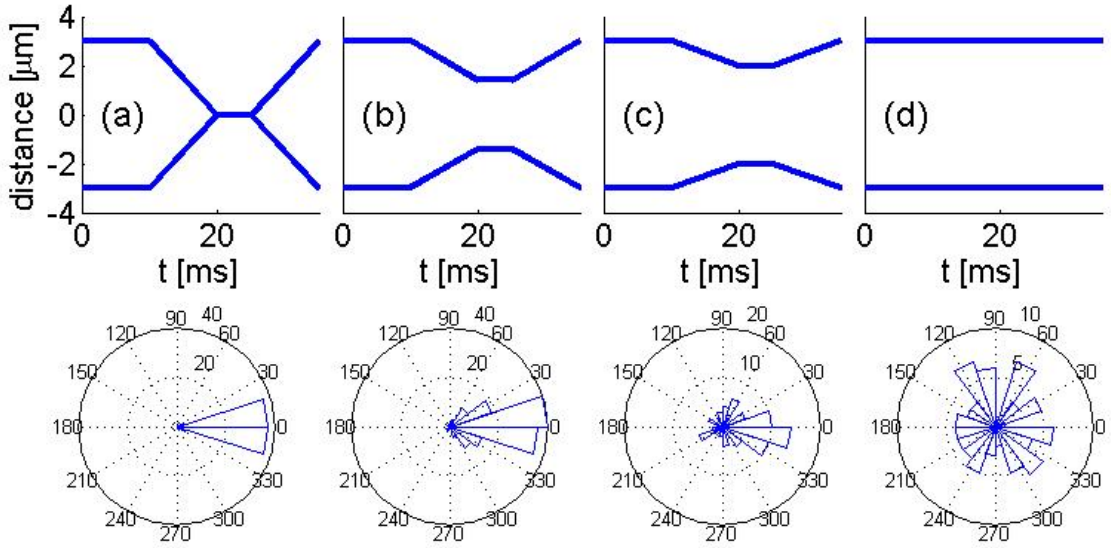

Figure 7.13: Combination of two initially independent quasi-BECs. Two BECs are produced by evaporative cooling in a double well with sufficiently large well separation and potential to ensure the two parts are completely uncorrelated. The separation between the wells is then reduced by decreasing the rf field amplitude, to different minimal values (increasing from **(a)** to **(d)**). After 5 ms hold time at this minimal value, the original large double well separation is restored and the relative phase between the two clouds is read out in the standard way from the resulting interference patterns. **(a)** For the complete removal of the barrier, we observe a narrow phase spread, comparable to the results of coherently split BECs. Within the 5 ms combination time the two BECs apparently completely adjust their phases. We observe no (measurable) heating in contrast to [155]. **(b)** and **(c)** If the condensates are not completely combined, we still observe a narrowing of the phase spread, which can only be due to particle exchange between the two parts through tunneling. **(d)** The control experiment, where the potential is not changed, shows a completely random phase distribution, as expected.

The distributions of the measured contrasts in the case of the independent BECs behave similar to those measured for long hold times ($(t \geq 10$ ms). Indeed, for the same temperatures and densities we reproduce within experimental and statistical errors the distribution functions shown in figure 7.11. This confirms the conjecture that the phase fluctuations in each of the condensate destroy any coherence between the two BECs within a few milliseconds. In particular, we conclude from this that the theoretical framework for the interference of uncorrelated quasi-condensates presented in section 3.4.2 [259, 107, 147, 148] can be safely applied to coherently split systems for times long compared to the phase randomization time.

7.4.1 Combination of two BEC

The ability to produce phase coherent and independent BECs in the same trap opens up the possibility for a number of experiments. While this may be of somewhat limited interest in the 1d-case, where complete loss of any correlation within the first few milliseconds happens automatically, the situation is different for (single mode) 3d condensates. Here, the full loss of any relation between the phases of the two condensates may take quite long. Also there is no obvious way to discern between a phase coherent state with a phase spread comparable to 2π and a number state. In both cases, one observes a (within the experimental limits) perfect interference contrast with a apparently random phase in each experimental run. The possibility of directly creating truly uncorrelated ensembles close to each other by evaporative cooling may be of interest for example in studies of the build up of the macroscopic phase of each individual BEC [169, 269].
Another interesting question is what happens when two uncorrelated (quasi)-condensates are com-

bined by removing the barrier between them. The (re-)combination of two phase-coherent condensates has been studied in the context of guided matter wave interferometers mainly for ideal particles [126, 7]. In the 3d case, the inclusion of interaction effects shows that the recombination process is much more sensitive to atomic interactions than the splitting process since merging clouds with opposite phase involves excited modes of the recombined potential and can lead to exponential growth of unstable modes [293]. One would expect that a similar effect is also be present in 1d quasi-condensates.
The in-trap recombination of two coherently split 3d condensates has recently been studied experimentally [155], and indeed a strong phase-dependent heating has been found. We have performed a similar experiment with independently created (quasi)-condensates: After the creation of the two BECs and a waiting time of 10 ms, the amplitude of the rf field providing the splitting is ramped down within another 10 ms, reducing the potential barrier between the two wells. After a "contact time" of 5 ms, the rf field is ramped up to its original, large value within 10 ms, before the atoms are released and the relative phase is read out from the interference pattern.
The results of this experiment for various approaching distances are shown in figure 7.13. If the two BECs are completely combined for 5 ms and then taken apart again, we find a narrow phase distribution (circular standard deviation $\sigma_c = 13°$), comparable to what we obtain for the same splitting of a single original condensate (figure 7.13a). This suggests that during the combination the phase modes of the two BECs completely merge to those of a single (quasi)-condensate. Unlike the results in [155], we observe no (measurable) heating of the system during the recombination. One might suspect that the multi-mode nature of the quasi-condensates plays an important role here. In the report of a previous experiment merging two single mode BECs with highly unequal atom numbers and no phase relation, there is also no mention of heating [40]. In a more recent experiment, it was observed that the combination of three independent BECs led to vortex formation [274].
We also observe a clearly non-random phase spread if the two wells are not completely merged, but remain separated by a finite potential barrier larger than the chemical potential of the condensates at all times. For the data shown in figure 7.13b we find $\sigma_c = 36°$ and calculate a barrier height of $V_0/h \approx 5$ kHz and a well separation of $d \approx 2.6\,\mu$m during the 2 ms when the barrier is minimal. The chemical potentials of the two condensates we calculate as $\mu/h \approx 2.5$kHz. This suggests that a phase matching occurs through the tunnel coupling between the two wells. For the minimal distance $d = 4.2\,\mu$m (figure 7.13c), we find a larger, but still non random phase spread of $\sigma_c = 80°$. The minimal potential barrier height here is $V_0/h \approx 15$ kHz. For comparison, in figure 7.13d the measured phases for the same total hold time and no reduction of the well separation are shown. Here we find a uniform phase distribution, as expected.
This experiment has to be seen as an early test of the possibility of (re)-combining condensates in the rf double well, but they already show that interesting effects occur, which warrant further experimental study and theoretical considerations.

7.5 Comparison between rf and (quasi)-static field beam splitter

The interferometer scheme based on rf adiabatic potentials presents the first successful realization of an all-magnetic phase coherent matter-wave beam splitter [283, 142]. This success can be traced to various fundamental advantages of rf potentials compared to purely static magnetic traps. Some of these aspects have already been discussed in a general way in section 2.3.2. Here we consider how these general concepts apply to the specific case of the rf beam splitter as presented in this chapter, by comparing it with the widely discussed two-wire static field beam splitter [62, 35, 138, 126, 293, 144, 288, 74]. The original design goal of our atom chip and of our experiment was to realize a (guided) matter wave interferometer based on modified versions of this two-wire scheme ([7, 96, 175, 140] and section 4.1.5). The discussion in this section shows that the rf beam splitter

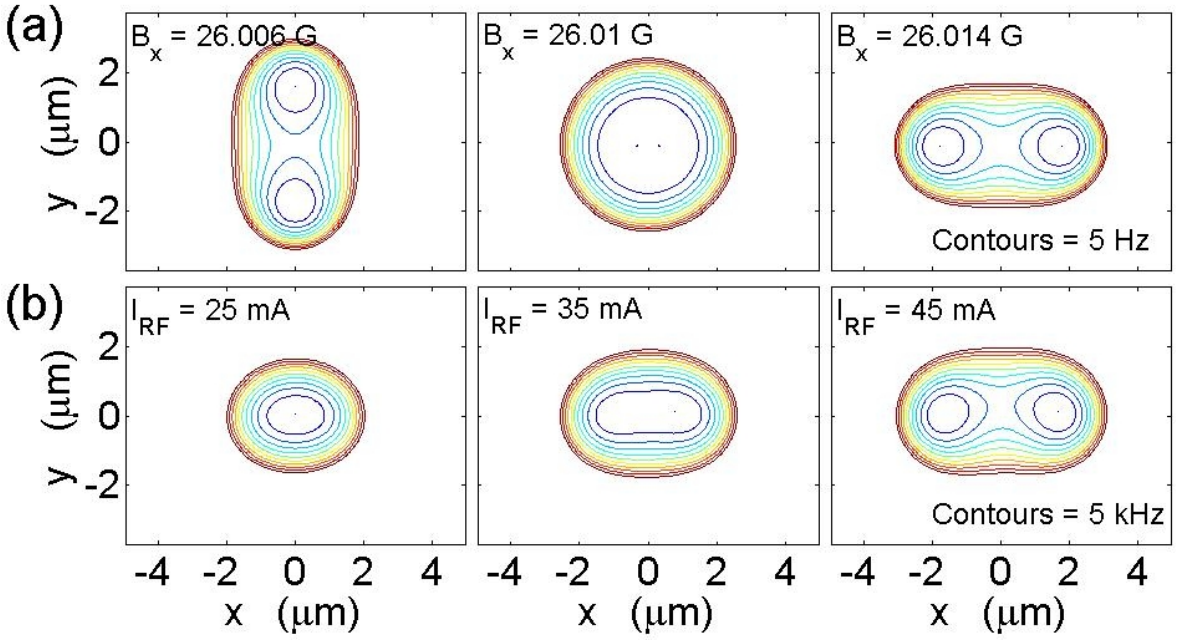

Figure 7.14: Comparing double well potentials created with static fields and rf dressing based on the same structure size and distance to the chip. **(a)** Static two-wire beam splitter: The splitting commences from two incoming guides evolving into two outgoing guides, through a region with a hexapol confinement. Equipotential lines are drawn at steps of 5 Hz. **(b)** Double well created by RF dressing a single Ioffe trap. The splitting smoothly transforms a single trap to a double well. The transverse confinement stays nearly constant and harmonic. At the splitting point one finds a x^4 confinement in the direction of the splitting. Equipotential lines are drawn at steps of 5 kHz.

overcomes a number of problems in the (quasi)-static field implementation, which were encountered by us and other groups [126, 175, 144, 74, 288].

7.5.1 One-to-two splitting

One fundamental advantages of the rf beam splitter can be seen in a difference in the topology of the splitting compared to the two wire case (figure 7.14). In the rf configuration a smooth transition from a true single well to a double-well can be achieved by varying any of the parameters ω_{rf}, B_{rf}, or B_{I}. In contrast, in the static case one encounters a transition from two vertically to two horizontally split minima, if the strength of a homogeneous bias field is modulated [138]. Consequently, in the vicinity of the splitting region this leads to unwanted tunneling processes into the second vertical (loss) channel just before the intended splitting sets in [293]. This poses a severe obstacle for establishing an adiabatic process.
The existence of this loss channel is a unavoidable consequence of Maxwell's equations which put constrains on the design of static magnetic potentials [321, 167]. In particular, a simple complex analysis argument shows that for wire traps, the number of minima in the field configuration is always equal to the number of wires [59]: In the plane perpendicular to the wires, the total magnetic field of the wire trap (plus external bias field) can be written as a complex polynomial of Nth order, where N is the number of wires. From the fundamental theorem of algebra it then follows that there are N field minima. This number can effectively be reduced by merging multiple minima at one position, which is exactly the idea behind the two wire beam splitter. But this merging always results in an unwanted reduction of confinement around the minimum position, as will be discussed in the next section. A more detailed discussion of this complex analysis approach to wire traps and its implications atom chip traps can be found in [96].

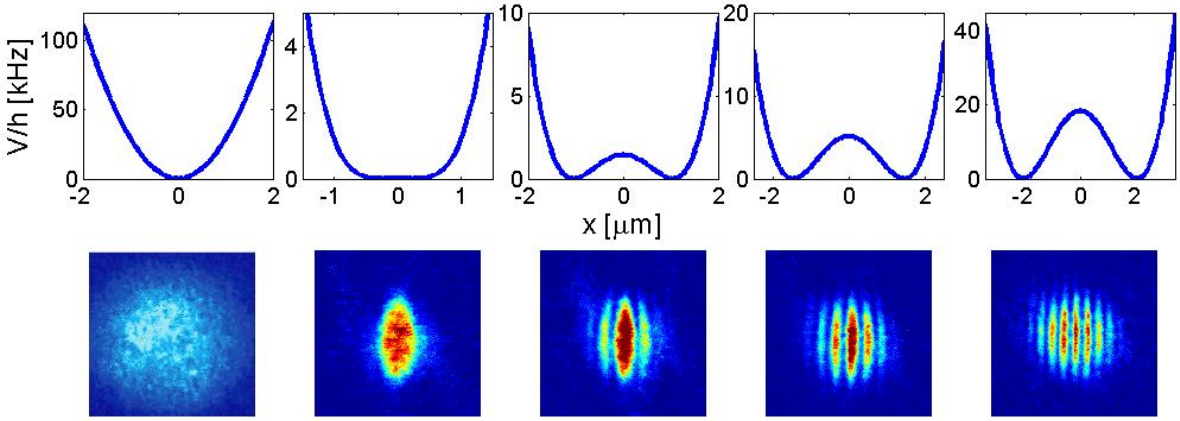

Figure 7.15: Change of the shape of the potential in the splitting direction from the initial single well trap to the double well. The bottom row shows corresponding ToF images of condensates released from the potentials shown in the top row. The initial deformation of the harmonic potential to an x^4 shape results in a single vertical stripe in ToF. For a potential barrier $V_0 \leq \mu$ we observe a broade central fringe with smaller additional fringes appearing on the sides. This is in agreement with numerical GPE simulations of the expansion process. The broadening of the central fringe disappears once $V_0 > \mu$, i.e. when the condensate halves are spatially separated. We then observe an equidistant fringe spacing. The constant confinement in the transverse direction perpendicular to the double well can be seen in the unchanged vertical expansion width of the condensates.

The rf beam splitter does not face this limitation, as the dressed atoms are not trapped at minima positions of the total applied magnetic field, but instead at the minima position of the (virtual) effective field B_{eff} introduced in section 2.3.2. This effective field does not to satisfy Maxwell's equations since it is no true magnetic field, which manifests itself here in the non-conservation of the number of field minima during the splitting process (figure 7.14b).

7.5.2 Tight confinement and structure size

The second main difference between the two splitting methods has already implicitly been stated in the last section. In the case of static fields, the splitting process relies on the merging of two potential minima, which results in a hexapol order minimum with significantly reduced confinement in both transverse directions compared to the quadrupole based Ioffe traps at the start and the end of the splitting sequence [74].
In contrast, for the rf potential the confinement in the splitting direction relaxes only slightly and is basically constant in the orthogonal direction. This can be directly seen from the ToF images in figure 7.15, which show that the expansion in the direction orthogonal to the splitting is unchanged during the splitting process.
The difference of confinement in the splitting direction for the two methods can be quantified by directly comparing the resulting potentials for the two cases for similarly sized wire structures. Figure 7.14 shows the numerically calculated potentials of our three-wire rf trap and a two-wire static configuration realized at the same atom-chip distance (100 μm) and with field parameters ($B_{\text{bias}} = 30$ G, $B_{\text{Ioffe}} = 1$ G) similar to those used in our experiments. It can be seen, that for the same splitting distances the confinement is approximately a factor 1000 stronger in the rf case.
For a more general comparison of the confinement in the splitting direction for the two methods we model the resulting potentials with a simple generic polynomial potential of the form

$$V_{\text{DW}} = bx^2 + dx^4. \tag{7.9}$$

If $b > 0$ there is only one minimum, for $b < 0$ a double well is formed. The confinement during the splitting process depends only on d, the coefficient of the x^4 term. Using equation (5.11) for the rf beam splitter and the expression given by Estève et al in [74] for the two wire configuration as analytical descriptions of the potentials, we find d_{rf} and $d_{2\mathrm{w}}$ by Taylor expansion. In particular, for the ratio of d_{rf} and $d_{2\mathrm{w}}$ we obtain the expression

$$\frac{d_{\mathrm{rf}}}{d_{2\mathrm{w}}} \approx \left(\frac{B_{\mathrm{bias}}}{B_{\mathrm{I}}}\right)^2, \tag{7.10}$$

which is always much larger than unity. In particular, for $B_{\mathrm{bias}} = 30$ G and $B_{\mathrm{Ioffe}} = 1$ G, we reproduce the numerical results discussed above. The essence of equation (7.10) is that the achievable potential modulation at a given distance to the chip is always about a factor 1000 larger in the rf potential case than in the static field configuration.
Another way of expressing this advantage of tighter confinement in the case of rf potentials is to look at the scaling of the confinements as a function of the distance D of the splitting region to the atom chip. In static implementation of the double-well this distance is fixed by the distance $2D$ of the wires on the chip [74]. Provided that the wire current I and B_{I} are equal for both setups and assuming for simplicity $\triangle = 0$ the trap frequencies and the height of the barrier between the wells obey

$$\frac{\omega_{\mathrm{T,RF}}}{\omega_{\mathrm{T,static}}} \propto \frac{D}{\rho_0}\sqrt{\frac{B_{\mathrm{RF}}}{B_{\mathrm{I}}}} \quad , \quad \frac{h_{\mathrm{T,RF}}}{h_{\mathrm{T,static}}} \propto D^2\frac{G^2}{B_0 B_I}. \tag{7.11}$$

The essence of these expressions is their scaling with respect to the parameter D. To realize a confinement comparable to the rf case with the static implementation the atom-surface distance and the wire dimensions on the chip have to be similar to the splitting distance, i.e. a few micrometers. In contrast, the rf trap can realize potential modulations on the micron scale with much larger structures and thus farther away from the chip surface. This is an extremely important advantage, as hereby potential corrugations induced by surface roughness [87, 172, 179, 180, 157, 73, 176, 283, 318, 317] and coherence-destroying surface interactions [134, 281, 133] are strongly inhibited. The stronger increase of the potential barrier in the rf case is advantageous as it permits a true spatial separation of trapped atom clouds even for small splitting distances.
A final difference is found in the sensitivity of the splitting process to technical noise, which can also been seen in figure 7.14. The parameter characterizing the two wire splitting (the external bias field B_{bias}) has to be controlled to a precision of 10^{-5} for a controlled splitting, which presents a severe technical challenge [74, 282]. In contrast for rf potentials the control parameter (the rf field amplitude) changes by a factor two during the splitting and only has to be stabilized on a milli-Ampere level. This also makes the rf beam splitter much less sensitive to outside influences like stray magnetic fields, which can totally modify the splitting in the static case.

8 Interference of one-dimensional condensates

In the last chapter, we showed that the phase dynamics in our rf double well are dominated by thermal phase fluctuations in the highly elongated condensates. Turning this argument around, the rf interferometer provides an ideally suited setup for investigating the quasi-BEC phase dynamics. Phase fluctuations have been observed in the 1d-3d crossover regime in macroscopic magnetic traps indirectly either in the form of density modulations in time-of-flight images [65, 132] or in momentum space via Bragg spectroscopy [268, 95, 146] (compare section 3.2.3). Interferometry is a natural way of studying this phenomenon as it provides a direct measurement of the fluctuating phase in the quasi-BEC. This approach was first demonstrated in [131] where an interferometer based on two consecutive Bragg pulses is realized. From the observed interference signal second-order density correlation functions can be extracted which in turn can be related to the phase coherence length in the system.

The rf double well offers a few distinct advantages over this method. The main one is that the split system consisting of two quasi-BECs can be held in the trap after the splitting, i.e. we can study the time evolution of the phase fluctuations. Secondly, the transverse splitting and subsequent interference allows a spatially resolved direct measurement of the local relative phase between two quasi-condensates, while the relative longitudinal shifting of two parts of the BEC in [131] only gives access to the overall phase coherence length.

A third advantage is the flexibility of the initial state in which the system is prepared. The phase coherent rf splitting creates two identical copies of a single quasi-condensate, while alternatively two completely uncorrelated BECs can be created by direct condensation in the double well potential. The latter corresponds to the equilibrium state of the split system, while the phase coherent splitting results in a highly non-equilibrium state. This gives access to time resolved study of the non-equilibrium phase dynamics in the system. The only previous investigation of non-equilibrium quasi-condensates is reported in [290], where a condensate focusing technique was used to study shock cooled BECs with non-equilibrium density distributions. In that case the phase fluctuations are not collective modes of the system, but instead are due to the true nucleation of the total system into individual condensates. In particular, they play no important role in the observed time-of-flight distributions.

Beyond these differences to previous experiments studying phase fluctuations, the rf double well provides access to a wholly new system, i.e. two 1d systems coupled by a finite tunneling rate. As has been discussed in section 3.5 the counteracting of the local phase fluctuations in each condensate and the phase-maintaining tunneling leads to rich non-linear dynamics in the system [25, 108].

In this chapter, results of experiments along the above discussed lines are presented. Previous experiments, which are summarized in the thesis by S. Wildermuth, demonstrated that sufficiently large trap aspect ratios for the realization of a single weakly interacting Bose gas in the true 1d regime ($\mu, T < \hbar\omega_\perp$) can be achieved in our setup [316, 318]. In section 8.1 the combination of 1d confinement with the rf double well setup is discussed. In particular the advantages of using the vertical double well orientation realizable with the three-wire trap in regard to the study of the phase fluctuations are elucidated.

In section 8.2 experiments studying the phase dynamics after coherent splitting are presented. For the case of uncoupled systems, we observe the decay behavior predicted by the theory presented in section 3.4.3. First experiments in the tunnel coupled regime are also described. Here, we find a fast decay towards an equilibrium state with reduced phase fluctuations compared to the uncoupled

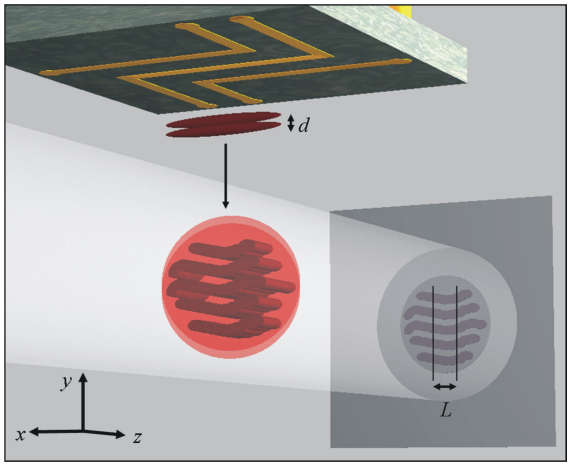

Figure 8.1: Schematic of the experiment configuration for the study of the longitudinal phase fluctuations. The advantage of vertical splitting can be seen: the resulting horizontal interference pattern can be imaged with both horizontal imaging systems. In particular, in the transverse imaging the mapping of phase fluctuations into locally changing spatial phase of the interference pattern can be directly observed.

case. Tunneling rates deduced from the data (compare section 3.5.1) are in reasonable quantitative agreement with the observed decay time and two-mode-model calculations.
In the final section 8.3 the equilibrium state of the uncoupled system is studied. Our results are compared to the theoretical predictions for the contrast statistics (compare section 3.4.2). The expected temperature dependence of the average contrast as a function of the system length and the change of shape of the full distribution functions are confirmed by our data. On the other hand, we also find deviations from the theory, which can be attributed to the density fluctuations in the time-of-flight images and atomic shot noise effects. The inclusion of these effects will hopefully make the contrast statistics measurement a quantitative thermometry tool.

8.1 Direct observation of phase fluctuations in the vertical double well

The effect of longitudinal phase fluctuations in the split system on the observed interference pattern has been schematically shown in figure 3.4: The fluctuating (time-dependent) phase along the long axis of each individual quasi-BEC results in a spatially varying relative phase. Imaged along the transverse direction, this effect should be observable as local shifts of the observed fringe pattern.
In the case of the horizontal double well discussed in the last chapter, transverse imaging is prevented by the atom chip blocking the optical access. The vertical imaging system (section 4.1.7) is not suited for studying interference patterns in time-of-flight, as its focal plane is located on the surface of the atom chip. Additionally the beam reflection would always result in a mirror image overlapping with the original image.
These problems can be circumvented by using the vertical double well configuration realizable with the three-wire setup (compare section 5.2.1). The interference pattern can then be observed in both horizontal imaging systems installed in our setup. In particular, the high resolution transverse imaging can be used to observe the longitudinally varying relative phase, as illustrated in figure 8.1.

8.1.1 Vertical double well

The vertical double well is realized by setting the phase shift between the AC currents in the rf wires to $\delta = 0$. The resulting total rf field is horizontally polarized in the area directly underneath the static trap Z-wire (figure 8.2a). This is true for any distance to the chip, as the vertical components (which increase closer to the chip) always compensate each other. But due to the circular nature of the wire magnetic fields, the effective amplitude of the horizontal total rf field becomes a function of the chip distance. As discussed in section 5.3.1 and demonstrated in section 5.6.3, the resulting imbalance in the vertical rf double well can be used to counter the effect of gravity, which now also

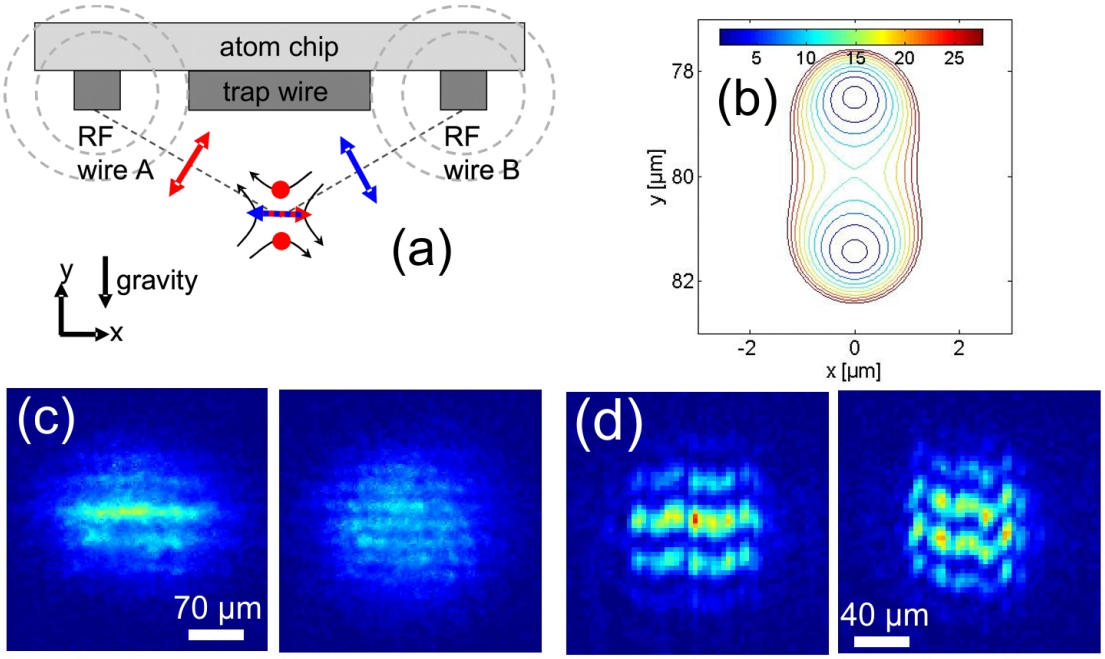

Figure 8.2: **(a)** Field configuration for the vertical splitting. The center of the static quadrupole field is brought closer to the chip surface. As a consequence the two rf fields are no longer perpendicular at the static trap minimum. For a phase shift of $\delta = 0$, the vertical components of the rf fields still cancel each other at all times, resulting in a horizontally polarized total rf field with reduced amplitude. In particular, this effective amplitude is now a function of y, along the central (vertical) axis of the double well. **(b)** This spatial dependence of the rf field amplitude counters the imbalance introduced by gravity. For typical well separations $2r_0 = 2...5\,\mu$m the balance point is found at chip distances $d \approx 80\,\mu$m for $B_{\rm bias} = 25$ G. **(c)** Images of the resulting fringe patterns taken with the longitudinal imaging for two different well separations. In these images the effect of the phase fluctuations is observable as a reduction of the contrast. **(d)** Images taken with the transverse imaging for similar double well parameters as in (c). Here, the spatial dependence of the relative phase along the longitudinal direction can be directly seen as local shifts of the interference pattern. The visible longitudinal density modulations are also caused by the phase fluctuations. To reduce this effect, a shorter time-of flight (10 ms) compared to the longitudinal images (16 ms) is used. The fringe pattern can be resolved for shorter expansion times, due to better optical resolution of the transverse imaging.

affects the effective potential.

For any specific well separation and barrier height, a set of parameters can be found which results in a symmetric double well. We usually keep the external bias field constant at $B_{\rm bias} = 25$ G, and vary the DC $I_{\rm Z}$ and AC currents $I_{\rm rf}$ to find the balance position (the Ioffe field $\mu_{\rm B}B_{\rm I}/h = 650$ kHz and the radio frequency $\nu_{\rm rf} = 600$ kHz are always kept constant). For these parameters, the symmetric double well is found at chip distances of $d \approx 70...90\,\mu$m, depending on the specific double well distance one aims for. In figure 8.2b a contour plot of the balanced vertical double well for a well separation of $2r_0 = 3.5\,\mu$m is shown, the trap center then lies at $d = 80\,\mu$m and the currents are $I_{\rm Z} = 1.12$ A, $I_{\rm rf} = 38$ mA.

The stability of this balancing against technical fluctuations of the involved parameters is reasonably good. We find the deviations from the balance values of the parameters which result in an imbalance of $\triangle E/h = 100$ Hz as $\triangle B_{\rm bias} \approx 0.1$ G, $\triangle I_{\rm Z} \approx 3$ mA, and $\triangle I_{\rm rf} \approx 2$ mA. We estimate the experimental stability and reproducibility of all three parameters to be at least better by a factor 0.5.

8.1.2 Balanced splitting

From the above calculations we can conclude that we can create a stable and reproducible static double well in the vertical configuration, in which we can produce equally sized BECs by evaporative cooling in the double well. The situation becomes more involved when the dynamic splitting of the single trap is considered. For a fixed static field (constant I_Z and B_{bias}), the imbalance of the double well changes during the splitting. To ensure the symmetry of the double well throughout the process, one has to change for example the static current I_Z in addition to the AC currents. This in turn results in a vertical shift of the trap center during the splitting, which is prone to inducing unwanted oscillations in the system.
In practice, we avoid such more complex balancing approaches. Instead, we aim for parameters resulting in a balanced double well roughly at the time when the tunneling between the wells breaks down, which ensures condensates with (reasonably) equal densities in each well. The imbalance of the final potential after the full splitting only results in a faster linear evolution of the (global) relative phase. Since we are interested in local effects induced by the phase fluctuations this global behavior is of no consequence.
In the actual experiment, we start with the calculated parameters for balanced splitting and then optimize the process experimentally, by searching for the settings resulting in the maximal (local) contrast in transversally imaged interference patterns. The maximal contrast of course occurs when the number of atoms in each well is equal. In figure 8.2c,d interference patterns of dynamically split condensates in the vertical double well are shown. As already discussed, in the longitudinal images the contrast is strongly reduced due to the spatially varying relative phase. Consequently, this is not a good measure for the atom number balance.
On the other hand, in the transverse images, the local contrast, i.e. the contrast in each individual vertical pixel slice, depends only on this balance. Note that this statement is wrong if the phase correlation lengths is much smaller than the optical resolution, i.e. when the relative phase changes significantly over the length of one pixel. Then the same effect as in the longitudinal imaging occurs in each pixel in the transverse imaging: averaging over multiple shifted patterns results in a random reduction of the local contrast. This is not what we find, though. The contrast along the images is (roughly) constant, hence it makes sense to use it as a measure of the balance during the splitting.

8.1.3 One-dimensionality of the confinement

To check wether it is realistic to reach the effective 1d-regime in this trap configuration, we have to measure the trap frequencies characterizing the potential. Because of the difference by three orders of magnitude between the transverse and longitudinal frequencies, we employ two different techniques for determining each.
The transverse frequency we measure by parametric heating of trapped condensates [93]. A small AC modulation is added to the wire current I_Z and the atom loss/heating is measured as a function of the frequency of this modulation. From the resulting loss curve we obtain ν_t with an accuracy of ± 10 Hz [140].
The (small) longitudinal frequency can be obtained from the frequency of center of mass and breathing mode oscillations of BECs in the trap. Center of mass modes can be excited by momentarily replacing the trap center, which is done for this configuration by a stepwise increase/decrease of the current I_U in one of the U-wires. The breathing mode oscillations are excited by instantly reducing the longitudinal confinement slightly, which is done by simultaneously changing the current I_U in both wires. Both the center-of-mass and the breathing mode oscillations can then be nicely observed in changes of the longitudinal width in time-of-flight images of BECs released after varying hold time [218].
For the single static trap underlying the vertical double well, we find for the parameters given in

the last section: $\nu_{t,0} = 3.8...4.0$ kHz, depending on the exact height which is used for the specific desired double well distance, and $\nu_{z,0} = 5$ Hz, which in turn is controlled (almost) independently of $\nu_{t,0}$ by the U-wire currents. From equation (3.57) it follows, that this trap is effectively 1d for atom numbers smaller than $N_{1d} \approx 10^4$. Additionally, $k_B T < h\nu_{t,0}$ is fulfilled for $T < 200$ nK.
The trap frequencies of each minimum in the double configuration can be measured with the same techniques. It is important to note that the two transverse frequencies can be quite different in this case. While ν_y stays constant throughout the splitting, the confinement in the splitting direction is first relaxed, and then, for large splitting, increased compared to the static trap value.
For the determination of the longitudinal frequency, the splitting process itself can be used to induce the breathing mode oscillations. As discussed in section 5.3.2 the longitudinal confinement is slightly relaxed during the splitting due to the spatial dependence of the minimal detuning. Consequently, it is extremely easy to induce oscillations simply by splitting the system much faster than $1/\nu_z$.
We find good agreement between the numerical potential calculations and trap frequency measurements for different double well configurations. Consequently, we rely on the calculations for determining the trap frequencies in cases where no direct measurement has been performed. In general, the trap frequencies in the double well case are $\nu_y = \nu_{t,0}$, $\nu_x \approx 1...5$ kHz, and $\nu_z \approx 1...5$ Hz, depending on the exact parameters. The relaxation of ν_x for small to moderate splitting distances is more than compensated by the reduced longitudinal confinement in regard to the condition $\mu < h\nu_x$. If additionally $k_B T < h\nu_x$ is fulfilled, has to be checked for each individual situation.
Another important aspect is that the total number of atoms is now distributed over two potential minima, resulting in an actual line density reduced by a factor two in each well. This pushes the system deeper into the 1d regime, without increasing the difficulty of detecting low atom numbers. Essentially the same is done in the realization of the Tonks gas in optical traps, where the total number of atoms are distributed into 1000 individual 1d potential tubes, and the Tonks gas is then inferred from the (averaging) total absorption signal [241].
From these considerations, we can conclude that reaching $\mu < h\nu_{x,y}$ in the vertical double well is (relatively) easy. With the transverse imaging the lower limit of delectability for the atom number is $N \approx 1000$ for time-of flight $t_{tof} \geq 8$ ms, which is required to resolve the interference signal in the expanding cloud. The experiments presented in the following are carried out with $N = 2...10 \times 10^3$ atoms, which provides good absorption signals and sufficiently low chemical potential.
To fulfill the condition $k_B T < h\nu_x$, temperatures $T = 50...200$ nK have to be reached. In the static trap, we observe the onset of condensation at $T_C \approx 400$ nK for $N \approx 10^4$ atoms, which means to reach the true 1d regime, we have to work well below T_C. Measuring the temperature from the time-of-flight expansion of the thermal background works reliably down to $T \approx 80$ nK for typical atom numbers and if the profile is obtained by averaging over multiple images to increase the signal-to-noise ratio. An alternative is to look at the insitu thermal distributions, which has the advantage that even very weak thermal wings can be detected [140, 301]. On the other hand, the correct differentiation between thermal and condensate fraction insitu can be quite difficult. For the lowest temperatures we produce we do not reliably detect any thermal background either insitu or in time-of-flight, which makes measuring T with these standard methods impossible. But from the last reliably determined T, we can estimate that we have $k_B T < h\nu_t$ for most configurations.

8.2 Non-equilibrium: coherence decay

In this section we present the study of the time-evolution of the system if it is initially prepared in a phase-coherent state. Starting point of the experiments is a single 1d quasi-condensate, which is split into two parts, as discussed in the last section. Directly after the splitting, the relative phase between the two condensates is zero over the whole length of the system, i.e. the splitting creates two identical copies of the phase fluctuation pattern at the moment of the splitting.

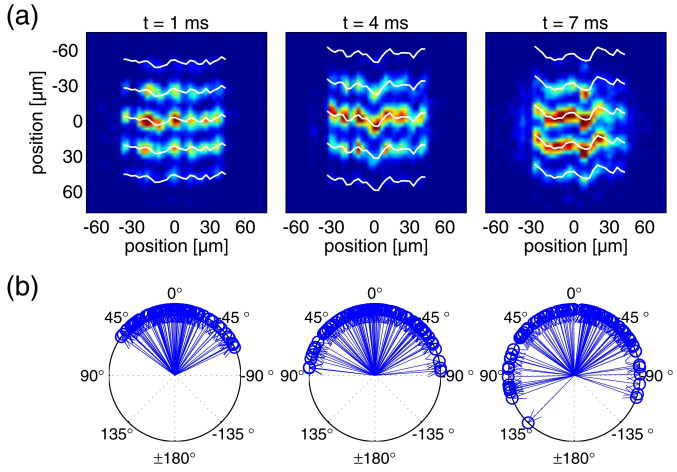

Figure 8.3: Decay of the phase coherence between two uncoupled 1d-condensates. The top row shows example interference patterns for **(a)** $t = 1$ ms **(b)** $t = 4$ ms **(c)** $t = 7$ ms after the decoupling of the two systems. The decoherence decay can be qualitatively seen in the increase of wiggles in the fringe pattern. This effect is quantified by extracting the local relative phase from the position of the fringe minima in each single vertical pixel slice. For each image a phase vector with 25 local phases $\triangle\varphi(z_j, t)$ is extracted. For the quantitative analysis the central slices in the range $L < 1/2L_{\mathrm{tot}}$ are used. The bottom row shows corresponding polar plots of these phases from 5 images per hold time each. Over time an increase in the phase spread can be observed. The phase distributions have been corrected to a mean value of 0. We are not interested in the absolute value of the local phase, only in the phase spread in each image.

This phase coherent state is a highly non-equilibrium one of the split system, which will accordingly relax to equilibrium over time, which is given by totally uncorrelated phase fluctuations in each condensate. Consequently, the relaxation results in a randomization of the local relative phase $\triangle\varphi(z, t)$. To study the dynamics of this relaxation process, the two BECs are held in the double well for a varying time t before they are released and the interference pattern is imaged. Figure 8.3 shows example images for holding times $t = 1, 4, 7$ ms for a pair of uncoupled condensates. From a single image we extract a vector of the local relative phases $\triangle\varphi(z_j, t)$ along the system by individually analyzing the fringe pattern in each vertical pixel slice.
The relaxation towards equilibrium results in an increasing spread of the phases in each such vector, which is quantified for a single image by the coherence factor

$$\Psi_d(t) = 1/N|\sum_j = 1^N e^{i\triangle\varphi(z_j,t)}|, \tag{8.1}$$

where N is the number of considered pixel slices. We include in the analysis only the central slices in the range $L < 1/2L_{\mathrm{tot}}$, where $L_{\mathrm{tot}} \approx 80...100\,\mu$m is the total length of the 1d condensates. In this central region it is reasonable to consider the line density as constant, i.e. as independent of the longitudinal confinement: $n_{1\mathrm{d}} = \mu g_{1\mathrm{d}}$.
Theoretical predictions for the (time evolution of the) coherence factor for coupled and uncoupled condensates at finite temperature have been presented in sections 3.5.1 and 3.4.3, respectively. In the following we present experimental results first for the uncoupled and then for the coupled case, and compare our measurements to these theories.

8.2.1 Uncoupled 1d systems

To produce a pair of two uncoupled 1d systems after the splitting, we introduce a sufficiently high and wide potential barrier such that any tunnel coupling can be neglected. This is verified by numerical two-mode model calculation of the tunnel coupling. The calculation is reduced to a single dimension (the x-direction) by writing the spatial part of the total wave function as a product of a Gaussian in y-direction (corresponding to the single particle harmonic oscillator ground state), a constant contribution with density $n_{1\mathrm{d}}$ in z-direction (neglecting the weak longitudinal confinement, which is justified in the central condensate region), and an unknown function $\Phi(x)$ describing the condensate profile in the double well direction. This leads to a 1d GPE with effective coupling constant $g_{\mathrm{eff}} = g * n_{1\mathrm{d}}/a_{\mathrm{y}}$, where a_{y} is the oscillator ground state width in y-direction.

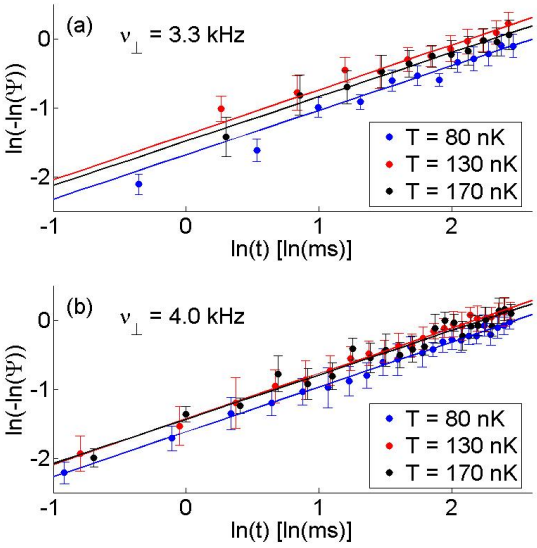

Figure 8.4: Double ln plots of the measured coherence factors over time. As discussed in the text, plotted this way, we expect a linear dependency with a slope 2/3, according to the theoretical prediction. The shown six data sets correspond to different combinations of T,n_{1d}, and transverse confinement $\nu_\perp = 3.3(4.0)$ kHz in **(a)**(**(b)**). All parameters are listed in table 8.1. The initial temperatures have been obtained from fitting the thermal wings of the longitudinal density profile, as discussed in the last section. The solid lines are linear regression fits. The obtained best fit slopes are 0.67 ± 0.06, 0.65 ± 0.07,0.66 ± 0.04 for the data sets in **(a)** (ascending in T), and 0.65 ± 0.03, 0.66 ± 0.03, 0.64 ± 0.06 for **(b)**. All six results are in very good agreement with the theoretical prediction.

Wave functions corresponding to the left $\Phi_L(x)$ and right well $\Phi_R(x)$ can then be constructed in the usual way from the $\pm$ combinations of the symmetric and antisymmetric lowest states of this 1d GPE and the tunnel coupling and the charging energy are calculated in the improved two-mode-model as defined in [4]. The tunnel coupling is negligible if the corresponding tunneling oscillation period is much larger than the experiment time $t \sim 10$ ms.
Using the two-mode model to calculate the tunneling rate between the multi-mode 1d quasi-condensates is justified, because the density profiles of the BECs are identical to those of single mode condensate (if the density modulations are neglected as usual).
As discussed in section 3.4.3, for the temperatures in our experiments $T \approx 100$ nK, we expect the phase dynamics to be dominated by thermal phase fluctuations. The corresponding theoretical prediction for the time evolution of the coherence factor is given by the decay law 8.2. After taking the natural logarithm twice, this equation becomes

$$\ln(-\ln(\Psi_d(t))) \propto \frac{2}{3}\ln(t) + \text{const.} \tag{8.2}$$

In words, if we plot the double natural logarithm of the measured coherence factor as a function of the logarithmic time, we expect to find a linear dependency with slope 2/3. Such plots for six different measurement series of $\Psi(t)$ are shown in figure 8.4. Each data set corresponds to a different combination of initial temperature T, line density n_{1d} and transverse confinement $\nu_\perp$. The solid lines in the plots are linear fits to the data. The exact values of the fitted slopes are given in the figure caption. For all data sets the results of the fits are in very good agreement with the theoretical prediction of 2/3 for the slope. This means we indeed observe the non-trivial time-dependence of the thermal phase decoherence in the system predicted by Burkov et al in the Luttinger liquid framework [31]. We believe this to be the first experimental test (and verification) of a prediction based on the Luttinger liquid description of weakly interacting 1d Bose gases.

Decay times

With the theoretical prediction for the general behavior of the decay law confirmed, we can extract the decay time t_0 by fitting exponential functions to the data with the additional exponent 2/3 fixed. Here, a few things have to be taken into account. The time $t = 0$, when the tunnel coupling vanishes and the two condensates start to evolve independently, is (slightly) different for each data set. The main difference exists between the two different transverse confinements. Larger $\nu_\perp$ is achieved by ramping up the rf field amplitude more and increasing the splitting distance, which also

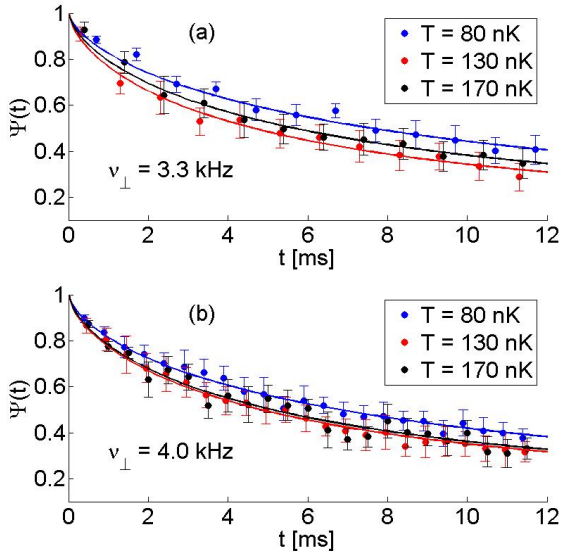

Figure 8.5: Decay of the coherence factor for uncoupled condensates. The shown data sets are the same as in figure 8.4, plotted here with linear axes. The solid lines are exponential fits to the data of the form $\propto e^{-(t/t_0)^{2/3}}$, from which the time constant t_0 is extracted. The results are gathered in table 8.1.

$T_{\mathrm{in}}[nK]$	$n_{1\mathrm{d}}$ [$\mu\mathrm{m}^{-1}$]	$\omega_\perp/2\pi$ [kHz]	t_0 [ms]	T_{f} [nK]
80(30)	20(3)	3.3(0.01)	9.0(0.8)	76(10)
130(25)	35(4)	3.3(0.01)	5.5(0.3)	145(13)
170(20)	50(5)	3.3(0.01)	6.4(0.5)	186(15)
80(30)	20(2)	4.0(0.01)	8.1(0.3)	85(10)
130(25)	35(4)	4.0(0.01)	5.9(0.2)	153(13)
170(20)	50(5)	4.0(0.01)	6.1(0.4)	194(17)

Table 8.1: Table of the experimental parameters and the derived results for the data sets shown in figures 8.4 and 8.5.

results in a larger potential barrier. Since the splitting is always in the same total time, the barrier for which tunneling breaks down is reached earlier for larger splitting (see also section 7.2.3).
A second, smaller modification of the tunnel coupling comes from the different densities $n_{1\mathrm{d}}$ for the different data sets. As discussed above, the density directly affects the tunnel coupling by changing the transverse shape of the mode functions in each well. The moment of the decoupling of the two systems can be estimated by numerically calculating the time dependent tunnel coupling during the splitting using the (simple) two-mode model as discussed above. We use the time when $2\pi/\omega_{\mathrm{J}}$ becomes larger than the total experiment time as an estimate of the starting time $t = 0$ of the independent evolution of the two systems. To cross-check this estimate, one can observe the change of shape of the time-of-flight patterns of condensates during the splitting process [270, 283].
Another aspect that has to be considered is that the coherence factor does not converge to zero, but towards a finite value for a finite length L of the considered area. On the one hand, this is due to the finite value of the temperature-dependent phase-coherence length (equation 3.55 and the following paragraph), which may be larger than a single pixel width [251]. Additionally, the average coherence factor of a finite number of phases is non-zero, even if these phases are totally random (section 7.2.2). This results in an additional offset of the equilibrium coherence factor, which can be determined from the number of data points used in the calculation of Ψ [83].
Taking these aspects into account, we obtain the time constants listed in table 8.1. The calculated decay constant is given by $t_0 = 2.61\pi\mu K/T_{\mathrm{f}}^2$ (section 3.4.3). With $\mu = g_{1\mathrm{d}}n_{1\mathrm{d}}$ and $K = \pi/\sqrt{\gamma}$, t_0 depends only on the experimental parameters T_{f}, $n_{1\mathrm{d}}$, and $\nu_\perp$. Here T_{f} is the final equilibrium temperature of the system after the splitting. Since we can precisely measure/calculate $\nu_\perp$ and obtain $n_{1\mathrm{d}}$ directly from the observed density profiles with good accuracy, we can use the measured

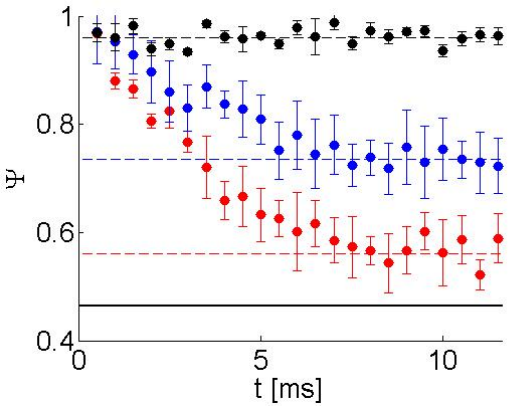

Figure 8.6: Time evolution of the coherence factor for coupled condensates. The three data sets correspond to different potential barriers $V_0 = 1.5, 3.0, 4.6$ kHz and minima separations $d_0 = 1.6, 1.8, 1.9\,\mu$m for the black, blue, and red data sets respectively. After an initial decay of the coherence factor we observe a levelling off at constant, non-random values, which depends on the tunnel coupling. (for the smallest barrier, the decay from $\Psi(0) = 1$ to $\Psi_{\rm eq} \approx 0.95$ is not resolved). The time required for the reaching of this equilibrium value grows with increasing potential barrier. The solid black line shows the Rayleigh test 99%-confidence value for the non-randomness of Ψ. All curves stay clearly above this value.

.

t_0 to calculate $T_{\rm f}$. The results are listed in table 8.1, as well as the initial temperatures of the data sets, which we denote as $T_{\rm in}$ from now on to avoid confusion.
Comparing the different $T_{\rm f}$ and $T_{\rm in}$, we find that the temperatures before the splitting, measured from the thermal profiles, agree with the final equilibrium value estimated from the decay time within the error ranges. We seem to observe a tendency that $T_{\rm f} - T_{\rm in}$ becomes slightly larger for increasing initial one temperature, i.e. that there is some heating during the splitting. This would be in qualitative agreement with the theoretical calculation [31], which predicts the heating during the splitting to increase with both initial temperature and Luttinger parameter K (see section 3.4.3). The measurement accuracy of the time-of-flight temperature extraction is not precise enough to confirm this trend, though.
In general, the agreement between the two methods within the error bounds suggests that the theoretical temperature dependence of the decay time t_0 is correct, which further confirms the validity of the Luttinger liquid approach by Burkov et al [31]. For a confirmation of the heating during the splitting a more accurate, independent temperature measurement is required. An interesting option would be the determination of T with the contrast statistics method (sections 3.4.2, 7.3.2, and 8.3) for sufficiently long t after the splitting, so that the two systems can be considered as uncorrelated, but short enough so that other heating effects can be neglected.

8.2.2 Coupled 1d systems

We observe a change in the time evolution of the coherence factor when the barrier between the two wells is lowered, as can be seen in figure 8.6. After an initial decrease of $\Psi(t)$, we observe a levelling off of the decay at a finite, clearly non-random, value, which depends on the potential barrier. We attribute this to a sufficiently large tunnel coupling between the two 1d systems to (partly) counter the phase fluctuations. This behavior of the coupled system is in agreement with the theoretical prediction for the equilibrium state presented in section 3.5.1.
With (3.126) and independent measurements of T and $n_{\rm 1d}$, we can estimate the tunnel coupling J directly from the equilibrium coherence factors. The experimental parameters and the calculated $b = \frac{J}{g_{\rm 1d} n_{\rm 1d}}$ for the three data sets shown in figure 8.6 are listed in table 8.2. We find that for all data sets, the tunnel coupling is (much) smaller than the charging energy, which means we are in the Josephson tunneling regime [291, 314]. From the calculated J we obtain the corresponding Josephson frequencies (equation 3.122), which are listed in the center columns of table 8.2.
We can compare these frequencies to results of the two-mode tunneling model using numerical calculations for the actual transverse double well potential and the resulting spatial wave functions in the two wells. We use here the improved two-mode model presented in [4]. The minima separations, barrier heights, and the resulting two-mode model Josephson frequencies are listed in the

Ψ_{eq}	$n_{1\mathrm{d}}$ [$\mu\mathrm{m}^{-1}$]	T [nK]	$\frac{J}{g_{1\mathrm{d}}n_{1\mathrm{d}}}$	ω_{J} [Hz]	V_0 [kHz]	d_0 [μm]	$\omega_{\mathrm{J,2M}}$ [Hz]
0.95(0.03)	30(3)	100(20)	0.2(0.1)	2700(1000)	1.5(0.3)	1.6(0.05)	4200(500)
0.73(0.03)	30(3)	100(20)	0.006(0.002)	470(150)	3.0(0.3)	1.8(0.05)	750(150)
0.56(0.03)	35(4)	115(25)	0.001(0.001)	150(120)	4.6(0.3)	1.9(0.05)	400(100)

Table 8.2: Table of the experimental parameters and derived results for the data sets shown in figure 8.6. The given errors for the Josephson frequency calculated from the coherence factors stem from the uncertainties of the measured quantities Ψ_{eq}, $n_{1\mathrm{d}}$, and$T$. The errors in the potential calculation and the resulting two-mode-model Josephson frequency come from estimated uncertainties in $n_{1\mathrm{d}}$ and the experimental parameters influencing the rf potential. In both cases it has to be remarked that the general accuracy of the employed models is most likely less precise than these errors.

right side columns of table 8.2. We find that the Josephson frequencies obtained from the experimental results and those from the two-mode model agree at least within a factor 2. The two-mode results are always larger, which may indicate a reduction of the measured Ψ_{eq} due to other effects, for example technical noise slightly scrambling the local relative phases.

We can also compare the Josephson frequencies to the observed time required for the coherence factor to reach its equilibrium. It seems likely that this time scale is set by the tunneling rate (for constant T and $n_{1\mathrm{d}}$). For the data in figure 8.6 the decay time is < 10 ms, with an indication that it grows with decreasing coupling. Comparing this to the calculated ω_{J}, we find that a balanced equilibrium situation is reached roughly in the time of a single Josephson oscillation or even less, which seems to be too fast to be realistic. This suggests that both the Josephson frequencies calculated from the coherence factor and from the two-mode model underestimate the actual tunneling in the experiment.
On the other hand, one has to keep in mind that both models used for calculating ω_{J} include quite strong simplifications of the actual system. The neglecting of the longitudinal confinement is probably the most drastic one, in practise, $n_{1\mathrm{d}}$ changes by 10% over the considered length. Another aspect is that especially for the smallest barrier height, the confinement in the double well direction is relaxed, so that the conditions for one-dimensionality are not strictly fulfilled. This should not matter too much, as the phase fluctuations are expected to not change significantly in the 1d-3d crossover regime [252, 248]. We note though, that other experiments investigating phase fluctuations in the cross-over regime also found considerable deviations from the theoretical predictions [65, 132]. In general, the applicability of the two-mode model to the situation is debatable.
Also, the uncertainty in experimental parameters translates into large uncertainties especially for the numerical calculations of ω_{J}. The strong transverse confinement results in an increased sensitivity of the barrier height to the rf field amplitude. Realizing a barrier with a stability of $\triangle V_0 < 1$ kHz is at the very limit of realistic error estimates. For the calculation based on the measured equilibrium coherence factor, one can imagine technical noise resulting in an additional reduction of Ψ_{eq}, which translates into an underestimation of ω_{J}.
Considering all these aspects, the agreement of the two theories and the experimental observations within an order of magnitude have to be considered a success for now. These results give a clear sign that studying coupled 1d-systems is possible in the rf-potential double well. The main limitation for the current setup are probably the wire dimensions of the three-wire trap, which make reaching strong transverse confinement together with small potential barrier difficult. The new atom chip currently being integrated in the experiment (see outlook chapter 9) will make the simultaneous achievement of 1d confinement in each well and large tunnel coupling much easier.

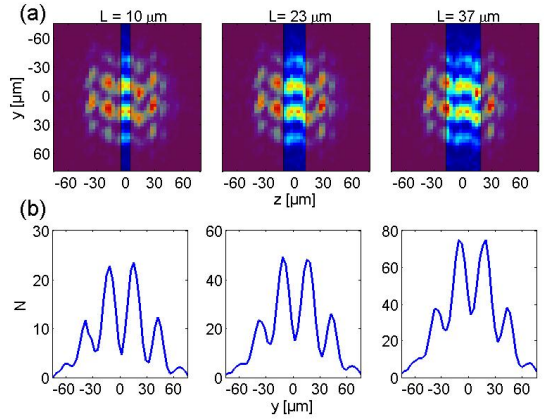

Figure 8.7: Illustration of the data analysis for the contrast statistics. **(a)** From a single image slices with increasing length L around the center of the cloud are cut out. **(b)** One-dimensional fringe profiles are then obtained by integrating these slices in the longitudinal direction, from which contrast (or fringe amplitude) are extracted as discussed in section 7.2.1. The shifting of the patterns from pixel to pixel leads to a decreasing total contrast as a function of L.

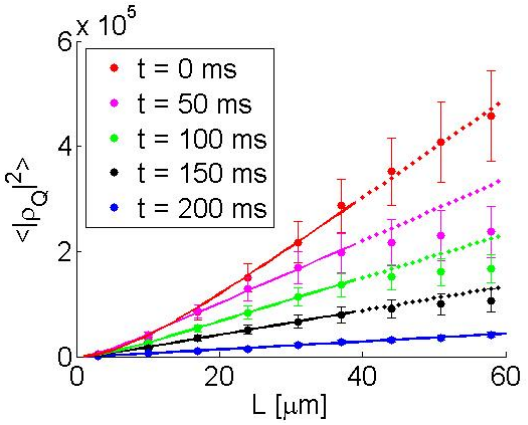

Figure 8.8: Average squared fringe amplitudes $< |\rho_Q|^2 >$ as function of the integration length L for different holding times t before the release from the trap. We observe a decrease of the total fringe amplitudes for increasing t (increasing T), as expected. The plotted curves are fits to the data performed as described in the main text. The solid part of the lines indicate which data points are included in the fitting. The error bars show the standard deviation for the underlying distribution, not the estimated error of the mean value.

8.3 Equilibrium: contrast thermometry

In this section we investigate the statistics of the local interference contrast for the equilibrium state of the system, i.e. two condensates with uncorrelated fluctuations. The basic idea of the analysis has already been discussed in sections 3.4.2 and 7.3.2: The local fluctuations of the relative phase lead to a reduction of the total contrast as a function of the considered system length. The transverse imaging now allows us to extract the contrast (or the fringe amplitude) for varying lengths L as shown in figure 8.7. Starting from the trap center, a single vertical fringe profile for each length L is obtained by integrating over increasingly more pixels. The decreasing contrast for increasing length can be seen in figure 8.7b. The same analysis method has recently been used to study the Berezinskii-Kosterlitz-Thouless crossover in a 2d gas [119].
In the following we will first analyze the behavior of the mean fringe amplitude as a function of L, and then discuss the full distribution functions of the measured contrasts.

8.3.1 Contrast Averages

The fringe amplitude ρ_Q is extracted from the fourier transform of each fringe profile as discussed in section 7.2.1. Unlike the contrast, ρ_Q is not normalized to unity, i.e. it grows with the total number of atoms in the integration area. Following the arguments of section 3.4.1, the rate of this increase depends on the phase coherence length in each of the two interfering condensates (and hence on the temperature of the system).
To investigate this temperature dependence, we perform the following experiment. Two uncorrelated BECs are produced by rf cooling in the vertical double well. After the evaporation stage, the system is held for a varying time t before the atoms are released and the interference pattern is recorded. During the hold time in the trap the system is heated, which we expect to see in the

behavior of ρ_Q over L.
Figure 8.8 shows the measured mean square fringe amplitudes $< |\rho_Q|^2 >$ for the different times. Each data point is the average of 40 individual measurements. The first observation is that we indeed find a gradual decrease of the absolute values for longer t (higher T), as expected. For a more quantitative analysis, we fit equation (3.109) to the data.
Here, we encounter a problem: We consider the absolute value of the fringe amplitude (contrast). The theory assumes a maximal local contrast everywhere, while the experimental values are affected by technical issues like e.g. finite imaging resolution. Consequently the theory overestimates the values of $< |\rho_Q|^2 >$ which we measure. A solution to this problem is to calibrate $< |\rho_Q|^2 >$ for a known temperature and to include the absolute reduction of the experimental fringe amplitude in the pre-factors C_1 and C_2 of equation (3.109). For this to make sense, the contrast reduction has to be independent of T. This should be true for reductions due to the imaging, but it is of course not correct for temperature ranges over which the thermal background changes considerably.
For the hold times $t = 150, 200$ ms we can extract the temperature directly from the longitudinal thermal wings in the time-of-flight images as $T = 130, 145$ nK. Using these temperatures, the line density $n_{1\mathrm{d}} = 30\,\mu\mathrm{m}^{-1}$, and the Luttinger parameter $K = 32$, the only unknowns in equation (3.109) are the "constants" C_1 and C_2, which we find by fitting the two data sets. Independent fits yield $C_1 = 0.15$, $C_2 = 0.24$ for $T = 145$ nK, and $C_1 = 0.18$, $C_2 = 0.22$ for $T = 130$ nK. This similarity suggests that the overall reduction of the fringe amplitude is indeed similar for both curves.
For the shorter hold times, we now in turn keep $C_1 = 0.16$ and $C_2 = 0.23$ fixed and use only the temperature T as free fit parameter. The resulting curves are plotted in figure 8.8. The resulting temperatures we obtain are $T = 40, 75, 105$ nK for $t = 0, 50, 100$ ms.
A number of things have to be stated here. First, the calculated temperatures seem to indicate a temperature dependent heating rate, which increases for lower T. This is in principle what one would expect, as the heat capacity of the system must decrease with T. On the other hand this effect may be caused by the too simple assumption that the absolute contrast reduction is temperature independent. For the lowest T we find $k_\mathrm{B}T \approx 1.1 \times \mu$, which seems not totally unrealistic for a final rf evaporation frequency ~ 3 kHz over the trap minimum. But since we have no alternative method of verifying this result, we cannot judge how accurate it is.
Another interesting observation is the deviation of the measurements from the theoretical curves for large L. The simplest explanation here would be the inhomogeneous line density due to the longitudinal confinement, but this modification is not large enough to explain the observed fringe amplitude reduction. Also, this effect seems to be of varying strength for different holding times.
Discussion of our results with the developers of the used theory [107, 147] is currently in progress and hopefully refinements of the theory will answer some of the open questions. At the moment, it seems save to conclude only that a temperature dependence of $< |\rho_Q|^2 >$ over L can clearly be seen in our data. For a reliable quantitative thermometry method both improvements of the theory and more experimental data are required. One necessary extension of the theory, the inclusion of atomic shot noise, will become apparent when we look at the contrast distributions, which is done in the following section.

8.3.2 Full contrast distributions

A suggestion how to circumvent the problem of dealing with absolute values for the contrast or fringe amplitude has already been published in [147] and discussed in section 3.4.2. Instead of considering the mean fringe amplitude, we can look at the distribution $W(\alpha)$ of the normalized contrasts $\alpha = |\rho_Q|^2 / < |\hat{\rho}_Q|^2 >$, which should remove systematic errors.
Figure 8.9 shows the measured normalized distribution functions for different L for a set of 170 measurements with parameters $n_{1\mathrm{d}} = 60\,\mu\mathrm{m}^{-1}$ and $\nu_\perp = 3.0$ kHz, which gives $K = 47$. We

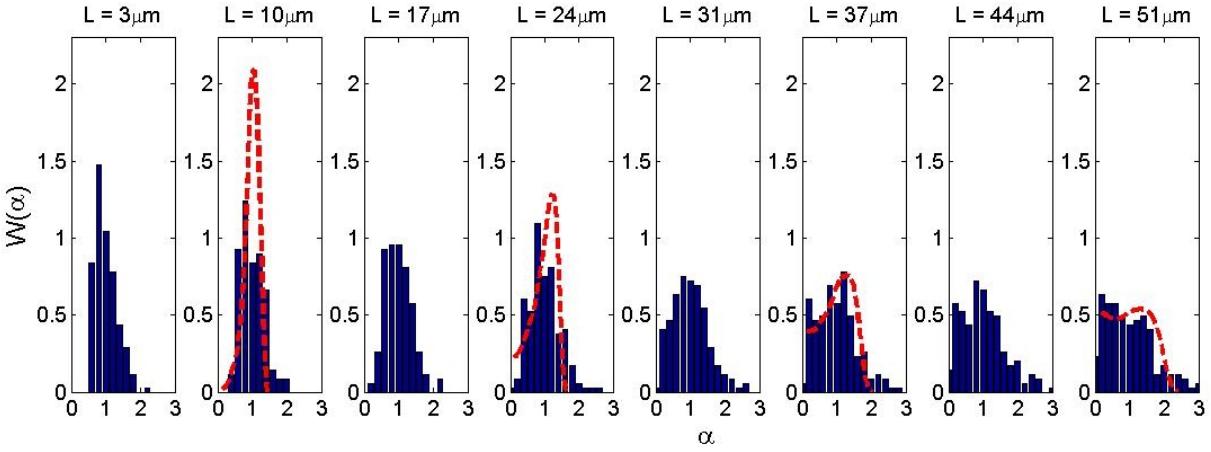

Figure 8.9: Histograms of the measured normalized contrasts for different L. Each distributions is also normalized to unit area. The change from peaked distributions for small L to flat Poissonian distribution with maximum at zero for large L, predicted by the Luttinger liquid theory presented in section 3.4.2, can be seen. The red curves are numerical calculations of the distributions provided by A. Imambekov, which confirm the expected change of the overall shape of the distributions. The increasing quantitative deviation for smaller L is discussed in the main text.

indeed observe the change of the shape of $W(\alpha)$ from a peaked distribution to a broad Poissonian distribution for increasing L, as calculated from the theoretical model [147].
The dashed red lines in figure 8.9 are numerically calculated distribution functions for the above parameters and $T = 50$ nK, carried out by A. Imambekov. The temperature $T = 50$ nK is chosen for the calculation because it is the result obtained from the mean value fitting method discussed above for this data set. We find reasonable agreement between the data and the calculations for $L = 24, 37, 51\,\mu$m, but we find a clear deviation for $L = 10\,\mu$m. In particular, the measured distribution is broader than calculated, which results in a much lower maximum value. Also the experimental data seems to be skewed towards larger values, while the theory predicts a skewing towards smaller values. In general, we observe more shots with large α as expected from the calculations for all L.
There are two main candidates for explaining these deviations at the moment: density fluctuations in the images and atomic shot noise. First, we observe random density modulations in the time-of-flight images, which develop from the phase fluctuations during the expansion of the released system [65]. We try to minimize this effect by reducing the time-of-flight, but this is limited by the requirement that there is enough transverse expansion so that we can resolve the fringe patterns. In the data used here the time-of-flight was 12 ms, and we observe quite strong density modulations (average variation of 10% from the expected smooth profile in each pixel). These random fluctuations cancel quite efficiently when one considers average values as discussed in the last section. This is of course not true when we look at distributions of individual measurements, where no averaging takes place. Consequently it seems likely that this effect has to be taken into account in the theory, as it probably cannot be reduced (much) further experimentally.
Secondly, we are probably observing here not only the evolution of distributions due to the phase fluctuations, but a crossover from the regime when the full distributions $W(\alpha)$ are dominated by shot noise to the regime when the decay of correlation functions is the main mechanism. An estimate of the importance of shot noise effects is obtained as follows. The relative width due to decay of correlation functions in the limit $T = 0$ and $K \gg 1$ equals $\sim 1.34/K$ [148], while the contribution from shot noise scales as $2/\sqrt{N_0}$ [258], where N_0 is the total atom number in both wells. Thus if temperature were equal to zero, the crossover to the shot noise dominated regime happens at $N_0 \approx 4000$.
For the data set shown in figure 8.9 this corresponds to $L \approx 40\,\mu$m. Consequently shot noise should

play an important role in the regime where the contrast distributions are expected to be narrow ($L < 30\,\mu$m). The effect of shot noise becomes more important with smaller L, where deviations between theory and experiment are largest. Additional confirmation for this conjecture comes from the fact that for $L = 3\,\mu$m and $L = 10\,\mu$m the measured distributions are skewed in the wrong direction compared to prediction of [147]. However, this is exactly what is expected for shot noise (compare e.g. figure 6 in [148]).

Unfortunately there is no theory at this point which can combine both shot noise and long range fluctuations to give the full distributions. A. Imambekov and V. Gritsev are currently working on calculating the dispersion (the second moment of the distribution) with both effects taken into account. If and how the density fluctuations in the images can be taken into account is also being discussed. While these effects significantly complicate the extraction of a temperature from the data, the study of the interplay between two fundamental noise effects, shot noise and phase fluctuations, presents a highly interesting topic in itself.

9 Conclusion and outlook

9.1 Summary

This thesis describes experiments on the coherent manipulation of BECs on an atom chip. A new trapping and manipulation technique, rf-induced adiabatic potentials, was experimentally implemented and theoretically studied in detail. The idea of using rf dressing to modify static magnetic traps was first proposed by Zobay and Garraway in 2001 [330, 331]. Our work over the last two years, both experimentally and theoretically, has greatly extended this concept beyond their original considerations and previous experimental implementations [48, 49].
Starting point of this development was the important realization by M. Andersson in our group that the vector nature of the coupling significantly alters the rf potentials, from which he correctly deduced the possibility of realizing a double well potential with the combination of a Ioffe-Pritchard trap and a linear rf field. Based on these initial considerations, we have extended the theory to arbitrary field configurations including multiple phase shifted rf fields (of same frequency) [193, 186]. These treatments reveal the full flexibility of the rf potentials, key examples are the possibility for state-dependent manipulation in purely magnetic traps and the ability to create traps with non-trivial topologies like the ring potential.
We have implemented these new concepts experimentally in the form of the three-wire trap presented in this thesis. The use of a two-component rf field enabled the demonstration of the state-dependency of the rf potentials and their increased flexibility over static magnetic traps in regard to trapping geometries and dynamic potential modulation in the form of the rotating double well and the (deformed) ring potential. [142]. We demonstrated evaporative cooling and direct condensation in the dressed state potentials and verified that the trap lifetimes are identical to comparable (same surface distance, density, temperature) static traps.
The last step in the improved understanding of the rf potentials is the full calculation beyond the RWA presented in this manuscript. We experimentally observed the predicted beyond-RWA effects and found them to be in very good quantitative agreement with the calculations [141]. The spectroscopy method and the numerical tools for calculations using realistic wire magnetic fields developed during this thesis provide an exact knowledge of the realized potentials in our experiment.
Using the rf potential technique we have demonstrated for the first time the coherent splitting of BECs on an atom chip [284, 282]. Our all-magnetic, fully integrated rf beam splitter provides an extremely simple and robust implementation of an atom-interferometer, which exploits all the advantages of the rf potentials (circumvention of the Earnshaw theorem, potential modulation on the micron-scale with large structures and surfaces distances, stability against technical noise) and overcomes the problems encountered by previous chip-based schemes relying on (quasi)-static magnetic or electric fields [293, 74].
In particular, the inherent symmetry of the three-wire configuration and the wide range of tunability it provides for the longitudinal and transverse confinement as well as the potential barrier and the double well separation make this setup extremely versatile and ideally suited for technical applications of microchip interferometers [162] as well as for fundamental studies of condensates in dynamic double well potentials [291]. The realization and thorough characterization of the three-wire dynamic double well have been the main topics of this thesis work over the last year [142]. The splitting process and the subsequent evolution of the split system have been studied in de-

tail. Deterministic evolution of the macroscopic relative phase could be observed during (quadratic phase evolution) and after the splitting (linear phase evolution), and the speed and direction of this evolution could be controlled by (im)balancing the double well potential. The study of the long time evolution (≤ 500 ms) unerringly identified the enhanced longitudinal phase fluctuations in the elongated double well trap as the cause of the observed fast randomization of the global relative phase. The measured timescale of this process (~ 5 ms) is in good agreement with theoretical estimates [314, 282].
Based on this observation, we focussed for the final part of this thesis on the study of the phase fluctuations in weakly interacting Bose gases in the 1d and 1d-3d crossover regimes. We demonstrated phase coherent splitting and independent creation of true 1d quasi-condensates ($\mu, T < \hbar\omega_\perp$) in the three-wire rf trap. In particular, the combination of the vertically oriented double well with high resolution transverse imaging of the interference pattern provides direct access to the local (relative) phase between the two quasi-condensates, and turns out to be a powerful new tool for the investigation of the phase fluctuations.
The ability to coherently split and then hold 1d quasi-condensates gives access to non-equilibrium dynamics in the system. The resultant decay of the phase-coherent state into the uncorrelated equilibrium state could be studied in a time-resolved manner. For the uncoupled system we found the non-analytic time behavior predicted by the theoretical treatment of the system based on the Luttinger liquid approach [31]. First experiments in the tunnel coupled regime found the reduction of phase fluctuations in the equilibrium state due to the phase-stabilizing exchange of particles between the two systems [314]. Tunnel energies extracted from the equilibrium coherence factor agree with two-mode-model calculations within an order of magnitude. The resulting Josephson frequencies qualitatively explain the observed timescale of the decay process to equilibrium.
The complementary interferometric study of uncorrelated quasi-BECs directly produced in the double well potential shows good qualitative agreement with the calculated system length and temperature dependence of the contrast distribution [259, 107, 147], but observed deviations of the full distributions especially for short integration lengths L suggest that additional effects like atomic shot noise have to be included [258]. This extension of the theory is currently in progress and it seems reasonable to hope that the contrast statistics can be develop into a quantitative thermometry method similar to the recent successful phase noise thermometry in 3d [92, 91].

9.2 Conclusion and Outlook

The experiments performed in our group over the last two years and summarized in this thesis establish the rf induced adiabatic potentials as a new and highly versatile tool for the micro-manipulation of neutral atoms. The advantages of this technique can be fully exploited on atom chips, where large amplitude rf fields can be created by oscillating currents of relatively low amplitude in the chip wires, and precise controlled field geometries with strong field gradients for both the rf and static magnetic fields can be realized.
Since our successful experimental implementation a growing number of groups has used rf potentials in their experiments. The single rf field double well configuration has been adapted by others both on atom chips [156, 155] and in macroscopic magnetic traps [313]. The state-dependency of the rf potentials has been used for a species-selective splitting of a Bose-Fermi-mixture on an atom chip [76]. Rf potentials also proved to be a key improvement in the coherent diffraction of a BEC from a magnetic grating on an atom chip [114, 115].
Beyond these experimental successes a variety of proposals for new trap configurations have been published. These include magnetic lattices based on multi-frequency rf fields [50], dynamically controlled toroidal and ring-shaped magnetic traps [79], and high-field seeker magnetic traps [198]. A macroscopic rf potential ring trap is discussed in [229], in [3] the same authors theoretically study evaporative cooling in rf dressed traps in detail. A further extension of the rf potential concept are

the time-averaged adiabatic potentials proposed in [196].
These successful experiments and novel proposals focus on the key advantages of rf potentials demonstrated in our experiment, i.e. the coherent, state (or species)-dependent micro-manipulation of neutral atoms and the realization of non-trivial trapping potentials which overcome the limitations of purely static magnetic traps. Beyond these aspects one can think of completely new directions for future experiments, for example the formation of rf induced Feshbach resonances in atom chip traps [224]. It seems save to conclude that the usage of rf potentials in experiments will keep increasing and that this technique will be at the basis of interesting future results.
The (near) future plans of our experiment include two mayor goals: the continued study of (coupled) 1d systems, and the coherent manipulation of few or hopefully single atoms in the rf potentials. Towards these ends the experiment is currently being rebuild, after the groups move from Heidelberg to Vienna, with two main (and probably many small) improvements: a new atom chip and a new (single) atom detection scheme.
Center piece of the new setup is an atom chip specifically designed for the improved realization of both true 1d and 3d rf double wells. This chip has two independent wire layers, separated by a thin (100 nm) isolation layer [111]. The top layer contains two sets of three straight wires for the implementation of the three-wire rf trap configuration presented in chapter 5. The smaller set consists of three parallel 10 μm wide wires with center-to-center distance of 15 μm, while the larger sets wire dimension are 80 μm and 10 μm for the central and the rf wires, respectively, with a center-to-center distance of 55 μm. The bottom layer contains various wires perpendicular to the six top layer wires to provide longitudinal confinement for the three-wire traps. In particular, the center area of the chip has been separately e-beam written to realize sub-micron sized (700 nm width) wire structures [111]. The complete separation of longitudinal and transverse confinement generating wires will greatly increase the flexibility of the rf traps and will hopefully allow arbitrary tuning of the trap dimensionality.
The second major upgrade is the integration of a new imaging system into the setup, designed for the spatially resolved detection of single atoms. A high-gain CCD camera is mounted underneath the vacuum chamber to collect the fluorescence light of atoms passing through a light sheet created by two asymmetrically broadened, counter-propagating laser beams parallel to the chip surface. First external tests of this system show promising results [271].
These two upgrades will greatly facilitate the continued study of 1d systems. The new imaging system will make further reduction of the atom number possible to go deeper into the 1d-regime. If the achievement and detection of a Tonks gas with this new setup is possible remains to be seen, but this will be one of the main goals in the coming experiments. At the same time the realization of coupled 1d systems in the weakly interacting regime should be much easier with the smaller three-wire setup, which can provide stronger confinement at smaller splitting and potential barrier than the old configuration. The most interesting question here seems to be if and how the Sine-Gordon model predictions for the dynamics in the coupled system can be observed experimentally. In the uncoupled case, the contrast statistics can be further explored, especially the interplay of atomic shot noise and phase fluctuations.
Complementary to the 1d studies, the new chip layout allows the realization of tight longitudinal confinement provided by the e-beam wires in the center of the chip. With these, a rf double well in the 3d regime should definitely be possible, hopefully also the achievement of zero-dimensional ($\mu < \hbar\omega_{\mathrm{x,y,z}}$) potential wells. Combined with the single atom imaging this setup has all the required ingredients for realizing a single (or few) atom(s) collisional phase gate based on the rf double well [33]. In the near future, external microwave fields for preparation of atoms in the ^{87}Rb clock states will be used, but the integration of microwave field generating structures on the atom chip is also being pursued [171]. In general, the combination of microwave and rf fields for state-dependent dynamic potentials is highly promising. This experiment configuration seems to be a very good candidate for finally realizing a quantum gate on an atom chip [44].

Beyond these "short-term" plans for the experiment, there seems to be a wide range of topics to pursue, from the already mentioned study of surface induced decoherence to the possibility of changing atomic properties like the scattering length by rf dressing. Personally, I believe the multi-frequency rf potentials to be highly interesting. Already the "simple" case of a standard static quadrupole field and evenly spaced rf frequencies offers a very flexible "micro-lattice". While well separation and lattice depth may be equally freely tunable in a standard optical lattice, the rf realization has the distinct advantage that the number of wells is exactly known, since it is equal to the number of rf frequencies. Loading a small (and precisely known) number of wells is extremely challenging in optical lattices, while in the case of the rf micro-lattice one can easily imagine something like ten occupied wells. One could for example thing of multi-particle entanglement along the lines of the collisional quantum gate array scheme demonstrated in the Bloch group [211] for exactly known particle number in this configuration, using the state-dependency of the rf potentials.
It seems highly likely that more complex multi-frequency rf field configurations will offer even more interesting potential shapes and dynamic modulations. There definitely seems to be a lot of "playing around" left to do with these basic ideas and I look forward to results from this experiment (and maybe others) in the next years.

A List of publications

In the framework of this PhD thesis and the preceding diploma thesis the following articles have been published:

- S. Hofferberth, B. Fischer, T. Schumm, J. Schmiedmayer, and I. Lesanovsky, Radio-requency-dressed atoms beyond the rotating wave approximation, *quant-ph/0611240*, accepted for publication in Phys. Rev. A
- S. Hofferberth, I. Lesanovsky, B. Fischer, J. Verdu, and J. Schmiedmayer, Radio-frequency dressed state potentials for neutral atoms, *Nature Physics*, **2**, 710 - 716 (2006)
- I. Lesanovsky, S.Hofferberth, J.Schmiedmayer, and P. Schmelcher, Manipulation of ultracold atoms in dressed adiabatic radio frequency potential, *Phys. Rev. A* **74** 033619 (2006)
- S. Wildermuth, S. Hofferberth, I. Lesanovsky, S. Groth, I. Bar-Joseph, P. Krüger, and J. Schmiedmayer, Sensing electric and magnetic fields with Bose-Einstein Condensates, *Applied Physics Letters* **88**, 264103 (2006)
- I. Lesanovsky, T. Schumm, S. Hofferberth, L. M. Andersson, P. Krüger, and J. Schmiedmayer, Adiabatic radio frequency potentials for the coherent manipulation of matter waves, *Phys. Rev. A* **73**, 033619 (2006)
- T. Schumm, P. Krüger, S. Hofferberth, I. Lesanovsky, S. Wildermuth, S.Groth, I. Bar-Joseph, L. M. Andersson, J. Schmiedmayer, A Double Well Interferometer on an Atom Chip, *Quantum Information Processing***5**, 537 - 558
- T. Schumm, S. Hofferberth, L. M. Andersson, S. Wildermuth, S. Groth, I. Bar-Joseph, J. Schmiedmayer, and P. Krüger, Matter-wave interferometry in a double well on an atom chip. *Nature Physics* **1**, 57 (2005).
- B. Zhang, C. Henkel, E. Haller, S. Wildermuth, S. Hofferberth, P. Krüger, and J. Schmiedmayer, Relevance of sub-surface chip layers for the lifetime of magnetically trapped atoms. *Euro. Phys. J. D* **35**, 97 (2005).
- S. Wildermuth, S. Hofferberth, I. Lesanovsky, E. Haller, L. M. Andersson, S. Groth, I. Bar-Joseph, P. Krüger, and J. Schmiedmayer, Microscopic magnetic-field imaging. *Nature* **435**, 440 (2005).
- P, Krüger, S. Wildermuth, S. Hofferberth, L. M. Andersson, S. Groth, I. Bar-Joseph, and J. Schmiedmayer, Cold Atoms close to surfaces: Measuring magnetic field roughness and disorder potentials, *Journal of Physics Conference Series* **19**, 56 (2005)
- P. Krüger, S. Hofferberth, E. Haller, S. Wildermuth, L. M. Andersson, D. Gallego Garcia, S. Aigner, S. Groth, I. Bar-Joseph, and J. Schmiedmayer, Ultracold atoms on atom chips: Manipulation at the μm distance scale, *AIP Conference Proceedings*, **770**, Issue 1, 144 (2005)
- P. Krüger, L. M. Andersson, S. Wildermuth, S. Hofferberth, E. Haller, S. Aigner, S. Groth, I. Bar-Joseph, and J. Schmiedmayer, Disorder potentials near lithographically fabricated atom chips. *arXiv:cond-mat/0504686* (2004).

Currently two manuscripts are being prepared: The first manuscript discusses the results regarding the coherence decay in coherently split coupled and uncoupled 1d-condensates presented in section 8.2. The second manuscript, covering the results regarding the interference contrast statistics presented in section 8.3 and the extension of the relevant theory, is being prepared in collaboration with A. Imambekov, V. Gritsev, and E. Demler.

B Danksagung

Die letzten vier Jahre waren füer mich spannend, lehrreich, und haben insbesondere unglaublich viel Spass gemacht. Dazu haben eine Vielzahl von Leuten beigetragen.
Vielen Dank an

- Jörg, dafür dass er mich vier Jahre lang an diesem Experiment arbeiten lies, für die lockere und freie Atmosphäre in der Arbeitsgruppe, und dafür dass er mir vermittelt hat, was physikalische Intuition ist
- Tischer (Chancentod), für die theoretische Unterstützung über die Jahre, die Gestaltung des Musikprogramms im Büro und die spannendsten Autorennen aller Zeiten
- Peter Kröger, für den Spass während abendlicher Laborsitzungen, dafür dass er mich immer wieder motiviert und meinen Zugang zur Physik entscheidend geprägt hat, und natürlich für alle noch so absurden Spiele und Spielereien
- Stephan (Mack!) Muth, für das Aufbauen des besten Experiments der Welt, für alles praktische Wissen, das er mir vermittelt hat, und für die Weisheit, das am Ende doch nur ordentliches Schnattern weiterhilft
- Thorsten, für entenartige Fähigkeiten im Labor, für die moralische Unterstützung während des Schreibens, Pension Schumm in Wien, und dafür, dass er der einzige Mensch auf dieser Welt sein wird, der diese endlose Arbeit von vorne bis hinten gelesen hat!
- Albrecht, für ultimate frisbee, alle Diskussionen und Streitgespräche (ich hatte immer einen Mordsspass dabei), und dafür, dass ich ihn so oft zur Mensa fahren durfte
- Daniel Kollego und Frau Willig, ich hoffe sie haben zueinander gefunden!
- Alle, die sich am Kauf, der Instandhaltung und der fleissigen Nutzung des Tischkickers beteiligt haben
- Florian, Alex, Bernd und Ulli die sich als starke nächste Generation erwiesen haben
- Alle Mitgliedern der Quantenoptikgruppe in Heidelberg und nun in Wien
  - insbesondere an jene, mit denen ich direkt zusammen gearbeitet habe: Bettina, Christian, Elmar, Jörg, José, Leonardo, Mauritz, Sönke, Stephanie
  - und natürlich an alle anderen, die mit Rat und Tat geholfen haben oder bei denen wir wichtiges Equipment klauen konnten: Doc Schneider, Björn (2:0), Dennis and Marco (das Laser-Duo), Christoph, Martin, Simon
- meine Eltern, für fast 30 Jahre Unterstützung und Rückhalt, und an meinen Bruder, den Meistertrainer
- Nadine, fürs immer da sein während der gesamten Zeit (und insbesondere für das jahrelange Ertragen von unglaublich schlechten Physiker-Witzen...)

MACK

Bibliography

[1] M. Albiez, R. Gati, J. Fölling, S. Hunsmann, M. Cristiani, and M. K. Oberthaler. Direct observation of tunneling and nonlinear self-trapping in a single bosonic josephson junction. *Phys. Rev. Lett.*, 95:010402, 2005.

[2] M. Allegrini and E. Arimondo. Radiofrequency transitions in a dressed atom. *J. Phys. B: At. Mol. Phys.*, 4:1008–1012, 1971.

[3] C. L. Garrido Alzar, H. Perrin, B. M. Garraway, and V. Lorent. Evaporative cooling in a radio-frequency trap. *Phys. Rev. A*, 74:053413, 2006.

[4] D. Ananikian and T. Bergeman. The gross-pitaevskii equation for bose particles in a double well potential: Two mode models and beyond. *Phys. Rev. A*, 73:013604, 2006.

[5] M. H. Anderson, J. R. Ensher, M. R. Matthews, C. E. Wieman, and E. A. Cornell. Observation of bose-einstein condensation in a dilute atomic vapor. *Science*, 269:198, 1995.

[6] P. W. Anderson. The lesson of quantum theory. pages 23–34. Elsevier, Amsterdam, 1986.

[7] E. Andersson, T. Calarco, R. Folman, M. Andersson, B. Hessmo, and J. Schmiedmayer. Multi mode interferometer for guided matter waves. *Phys. Rev. Lett.*, 88:100401, 2002.

[8] M. Andersson. *Quantum Dynamics of Molecular Systems and Guided Matter Waves.* PhD thesis, University of Uppsala, Sweden, 2001.

[9] A. F. Andreev. The hydrodynamics of two-dimensional and one-dimensional fluids. *Sov. Phys. JETP*, 51:1038, 1980.

[10] M. R. Andrews, C. G. Townsend, H.-J. Miesner, D. S. Durfee, D. M. Kurn, and W. Ketterle. Observation of interference between two bose condensates. *Science*, 275:637–641, 1997.

[11] S. Aubin, M. H. T. Extavour, S. Myrskog, L. J. LeBlanc, J. Esteve, S. Singh, P. Scrutton, D. McKay, R. McKenzie, I. D. Leroux, A. Stummer, and J. H. Thywissen. Trapping fermionic ^{40}k and bosonic ^{87}rb on a chip. *J. Low Temp. Phys.*, 140:377–396, 2005.

[12] S. Aubin, S. Myrskog, M. H. T. Extavour, L. J. LeBlanc, D. McKay, A. Stummer, and J. H. Thywissen. Rapid sympathetic cooling to fermi degeneracy on a chip. *Nature Phys.*, 2:384 – 387, 2006.

[13] A. Barone and G. Paterno. *Physics and Applications of the Josephson Effect.* Wiley, New York, 1982.

[14] M. Bartenstein, A. Altmeyer, S. Riedl, S. Jochim, C. Chin, J. Hecker Denschlag, and R. Grimm. Crossover from a molecular Bose-Einstein condensate to a degenerate Fermi gas. *Phys. Rev. Lett.*, 92:120401, 2004.

[15] C. Becker. Eine neuartige magneto-optische falle für atomchip-experimente. Master's thesis, University of Heidelberg, 2002.

[16] T. Bergeman, G. Erez, and H. Metcalf. Magnetostatic trapping fields for neutral atoms. *Phys. Rev. A*, 35:1535, 1987.

[17] P. R. Berman. *Cavity Quantum Electrodynamics*. Academic Press, 1994.

[18] D. J. Bishop and J. D. Reppy. Study of the superfluid transition in two-dimensional 4he films. *Phys. Rev. Lett.*, 40:1727, 1978.

[19] R. Bistritzer and E. Altman. Intrinsic dephasing in one dimensional ultracold atom interferometers. arXiv:cond-mat/0609047, 2006.

[20] F. Bloch and A. Siegert. Magnetic resonance for nonrotating fields. *Phys. Rev.*, 57:522, 1940.

[21] I. Bloch. Ultracold quantum gases in optical lattices. *Nature Physics*, 1:23–30, 2005.

[22] I. Bloch, T. W. Hänsch, and T. Esslinger. An atom laser with a cw output coupler. *Phys. Rev. Lett.*, 82:3008, 1999.

[23] N. N. Bogoliubov. On the theory of superfluidity. *J. Phys. (USSR)*, 11:23, 1947.

[24] S. N. Bose. Plancks gesetz und lichtquantenhypothese. *Z. Phys.*, 26:178, 1924.

[25] I. Bouchoule. Modulational instabilities in josephson oscillations of elongated coupled condensates. *Eur. Phys. J. D*, 32:171, 2005.

[26] C. C. Bradley, C. A. Sackett, J. J. Tollet, and R. G. Hulet. Evidence of bose-einstein condensation in an atomic gas with attractive interactions. *Phys. Rev. Lett.*, 75:1687, 1995.

[27] M. Brajdic. *Entwicklung einer Computersteuerung und ihre Anwendung in einem Experiment zur vereinfachten Bose-Einstein Kondensation in einer Oberflächenfalle*. Diploma thesis, University of Heidelberg, 2003.

[28] R. Hanbury Brown and R. Q. Twiss. A new type of interferometer for use in radio astronomy. *Phil. Mag.*, 45:663, 1954.

[29] R. Hanbury Brown and R. Q. Twiss. Correlation between photons in two coherent beams of light. *Nature*, 177:27, 1956.

[30] K. Brugger, P. Krüger, X. Lou, S. Wildermuth, H. Gimpel, M. W. Klein, S. Groth, R. Folman, I. Bar-Joseph, and J. Schmiedmayer. Two wire guides and traps with vertical bias field on atom chips. *Phys. Rev. A*, 72:023607, 2005.

[31] A. A. Burkov, M. D. Lukin, and E. Demler. Decoherence dynamics in low-dimensional cold atoms interferometers. cond-mat/0701058, 2007.

[32] T. Calarco, H.-J. Briegel, D. Jaksch, J. I. Cirac, and P. Zoller. Quantum computing with trapped particles in microscopic potentials. *Fortschritte der Physik*, 48:945, 2000.

[33] T. Calarco, E. A. Hinds, D. Jaksch, J. Schmiedmayer, J. I. Cirac, and P. Zoller. Quantum gates with neutral atoms: Controlling collisional interactions in time-dependent traps. *Phys. Rev. A*, 61:022304, 2000.

[34] T. Campey, C.J. Vale, M. J. Davis, N. R. Heckenberg, H. Rubinsztein-Dunlop, S. Kraft, C. Zimmermann, and J. Fortágh. Atom counting in ultra-cold gases using photoionisation and atom counting. *Phys. Rev. A*, 74:043612, 2006.

[35] D. Cassettari, B. Hessmo, R. Folman, T. Maier, and J. Schmiedmayer. Beam splitter for guided atoms. *Phys. Rev. Lett.*, 85:5483–5487, 2000.

[36] Y. Castin and J. Dalibard. Relative phase of two bose-einstein condensates. *Phys. Rev. A*, 55:4330–4337, 1997.

[37] Yvan Castin. Bose-einstein condensates in atomic gases: Simple theoretical results. In R. Kaiser, C. Westbrook, and F. David, editors, *Coherent atomic matter waves*. EDP Sciences and Springer-Verlag, 2001.

[38] M. A. Cazalilla. Bosonizing one-dimensional cold atomic gases. *J. Phys. B.: At. Mol. Opt. Phys.*, 37:S1, 2004.

[39] L. S. Cederbaum, A. I. Streltsov, Y. B. Band, and O. E. Alon. Interferences in the density of two bose-einstein condensates consisting of identical or different atoms. *Phys. Rev. Lett.*, 98:110405, 2007.

[40] A. P. Chikkatur, Y. Shin, A. E. Leanhardt, D. Kielpinski, E. Tsikata, T. L. Gustavson, D. E. Pritchard, and W. Ketterle. A continuous source of bose-einstein condensed atoms. *Science*, 296:2193, 2002.

[41] C. Chin, M. Bartenstein, A. Altmeyer, S. Riedl, S. Jochim, J. Hecker Denschlag, and R. Grimm. Observation of the pairing gap in a strongly interacting fermi gas. *Science*, 305:1128 – 1130, 2004.

[42] M. L. Chiofalo, S. Succi, and M. P. Tosi. Ground state of trapped interacting bose-einstein condensates by an explicit imaginary-time algorithm. *Phys. Rev. E*, 62:7438 – 7444, 2000.

[43] S. Chu. The manipulation of neutral particles. *Rev. Mod. Phys.*, 70:685, 1998.

[44] M. A. Cirone, A. Negretti, T. Calarco, P. Krüger, and J. Schmiedmayer. A simple quantum gate with atom chips. *Eur. Phys. J. D*, 35:165 – 171, 2005.

[45] C Cohen-Tannoudj, J Dupont-Roc, and C Fabre. A quantum calculation of the higher order terms in the bloch- siegert shift. *J. Phys. B: At. Mol. Opt. Phys.*, 6:L214, 1973.

[46] C. Cohen-Tannoudji, J. Dupont-Roc, and G. Grynberg. *Atom-Photon Interactions*. Wiley, New York, 1992.

[47] C. N. Cohen-Tannoudji. Manipulating atoms with photons. *Rev. Mod. Phys.*, 70:707, 1998.

[48] Y. Colombe, E. Knyazchyan, O. Morizot, B. Mercier, V. Lorent, and H. Perrin. Ultracold atoms confined in rf-induced two-dimensional trapping potentials. *Europhys. Lett.*, 67:593–599, 2004.

[49] Y. Colombe, B. Mercier, H. Perrin, and V. Lorent. Loading a dressed zeeman trap with cold atoms. *J. Phys. IV France*, 116:247–252, 2004.

[50] Ph. W. Courteille, B. Deh, J. Fortagh, A. Günther, S. Kraft, C. Marzok, S. Slama, and C. Zimmermann. Highly versatile atomic micro traps generated by multifrequency magnetic field modulation. *J. Phys. B: At. Mol. Opt. Phys.*, 39:1055–1064, 2006.

[51] F. Dalfovo, S. Giorgini, M. Guilleumas, L. P. Pitaevskii, and S. Stringari. Collective and single-particle excitations of a trapped bose gas. *Phys. Rev. A*, 56:3840–3845, 1997.

[52] F. Dalfovo, S. Giorgini, L. P. Pitaevskii, and S. Stringari. Theory of bose–einstein condensation in trapped gases. *Rev. Mod. Phys.*, 71:463, 1999.

[53] F. Dalfovo, C. Minniti, S. Stringari, and L. Pitaevskii. Nonlinear dynamics of a bose condensed gas. *Physics Letters A*, 227:259, 1997.

[54] J. Dalibard and C. Cohen-Tannoudji. Dressed-atom approach to atomic motion in laser light: the dipole force revisited. *J.O.S.A.*, B 2:1707, 1985.

[55] J. H. Davies. *The Physics of Low-dimensional Semiconductors.* University Press, Cambridge, 1998.

[56] K. B. Davis, M.-O. Mewes, M. R. Andrews, N. J. van Druten, D. S. Durfee, D. M. Kurn, and W. Ketterle. Bose einstein condensation in a gas of sodium atoms. *Phys. Rev. Lett.*, 75:3969, 1995.

[57] K. B. Davis, M.-O. Mewes, M. A. Ioffe, M. R. Andrews, and W. Ketterle. Evaporative cooling of sodium atoms. *Phys. Rev. Lett.*, 74:5202, 1995.

[58] K.B. Davis, M.-O. Mewes, and W. Ketterle. An analytical model for evaporative cooling of atoms. *Appl. Phys. B*, 60:155, 1995.

[59] T. J. Davis. 2d magnetic traps for ultra-cold atoms: A simple theory using complex numbers. *Eur. Phys. J. D*, 18:27, 2002.

[60] N. H. Dekker, C. S. Lee, V. Lorent, J. H. Thywissen, S. P. Smith, M. Drndić, R. M. Westervelt, and M. Prentiss. Guiding neutral atoms on a chip. *Phys. Rev. Lett.*, 84:1124, 2000.

[61] J. Denschlag, D. Cassettari, A. Chenet, S. Schneider, and J. Schmiedmayer. A neutral atom and a wire: Towards mesoscopic atom optics. *Appl. Phys. B*, 69:291–301, 1999.

[62] J. Denschlag, D. Cassettari, and J. Schmiedmayer. Guiding neutral atoms with a wire. *Phys. Rev. Lett.*, 82:2014, 1999.

[63] J. Denschlag and J. Schmiedmayer. Scattering a neutral atom from a charged wire. *Europhys. Lett.*, 38:405, 1997.

[64] J. Denschlag, G. Umshaus, and J. Schmiedmayer. Probing a singular potential with cold atoms a neutral atom and a charged wire. *Phys. Rev. Lett.*, 81:737, 1998.

[65] S. Dettmer, D. Hellweg, P. Ryytty, J. J. Arlt, K. Stengstock, D. S. Petrov, G. V. Shlyapnikov, H. Kreutzmann, L. Santos, and M. Lewenstein. Observation of phase fluctuations in elongated bose-einstein condensates. *Phys. Rev. Lett.*, 87:160406, 2001.

[66] K. Dieckmann. *Bose-Einstein Condensation with High Atom Number in a Deep Magnetic Trap.* PhD thesis, University of Amsterdam, 2001.

[67] S. Du, M. B. Squires, Y. Imai, L. Czaia, R.A. Saravanan, V. Brigh, J. Reichel, T. W. Hänsch, and D. Z. Anderson. Atom-chip bose-einstein condensation in a portable vacuum cell. *Phys. Rev. A*, 70:053606, 2004.

[68] V. Dunjko, V. Laurent, and M. Olshanii. Bosons in cigar-shaped traps: Thomas-fermi regime, tonks-girardeau regime, and in between. *Phys. Rev. Lett.*, 86:5413, 2001.

[69] S. Earnshaw. On the nature of the molecular forces which regulate the constitution of the luminiferous ether. *Trans. Camb. Phil. Soc.*, 7:97, 1842.

[70] A. Einstein. Quantentheorie des einatomigen idealen gases. *Sitzungsber. Preuss. Akad. Wiss.*, Bericht 22:261–267, 1924.

[71] A. Einstein. Quantentheorie des einatomigen idealen gases. ii. *Sitzungsber. Preuss. Akad. Wiss.*, Bericht 1:3–14, 1925.

[72] U. Ernst, A. Marte, F. Schreck, J. Schuster, and G. Rempe. Bose-einstein condensation in a pure ioffe-pritchard field configuration. *Europhys. Lett.*, 41:1–6, 1998.

[73] J. Estève, C. Aussibal, T. Schumm, C. Figl, D. Mailly, I. Bouchoule, C. I. Westbrook, and A. Aspect1. Role of wire imperfections in micromagnetic traps for atoms. *Phys. Rev. A*, 70:043629, 2004.

[74] J. Esteve, T. Schumm, J.-B. Trebbia, I. Bouchoule, A. Aspect, and C. I. Westbrook. Realizing a stable magnetic double-well potential on an atom chip. *Eur. Phys. J. D*, 35:141–146, 2005.

[75] J. Esteve, J.-B. Trebbia, T. Schumm, A. Aspect, C. I. Westbrook, and I. Bouchoule. Observations of density fluctuations in an elongated bose gas: ideal gas and quasi-condensate regimes. *Phys. Rev. Lett.*, 96:130403, 2005.

[76] M. H. T. Extavour, L. J. LeBlanc, T. Schumm, B. Cieslak, S. Myrskog, A. Stummer, S. Aubin, and J. H. Thywissen. Dual-species quantum degeneracy of potassium-40 and rubidium-87 on an atom chip. In *Proceedings of the 20th International Conference on Atomic Physics*, 2007.

[77] M. Feit, J. Fleck Jr, and A. Steiger. Solution of the schrödinger equation by a spectral method. *J. Comput. Phys.*, 47:412, 1982.

[78] Free fermion antibunching in a degenerate atomic Fermi gas released from an optical lattice. T. rom and th. best and d. van oosten and u. schneider and s. fölling and b. paredes and i. bloch. *Nature*, 444:733 – 736, 2006.

[79] T. Fernholz, R. Gerritsma, P. Krüger, and R. J. C. Spreeuw. Dynamically controlled toroidal and ring-shaped magnetic traps. *physics/0512017*, 2005.

[80] H. A. Feshbach. A unified theory of nuclear reactions. *Annals of Physics*, 19:287, 1962.

[81] A. L. Fetter. Ground state and excited states of a confined condensed bose gas. *Phys. Rev. A*, 53:4245, 1996.

[82] A. L. Fetter and J. D. Walecka. *Quantum Theory of Many-Particle Systems.* McGraw-Hill, New York, 1971.

[83] N.I. Fisher. *Statistical analysis of circular data.* Cambridge University Press, 1993.

[84] R. Folman, P. Krüger, D. Cassettari, B. Hessmo, T. Maier, and J. Schmiedmayer. Controlling cold atoms using nanofabricated surfaces: Atom chips. *Phys. Rev. Lett.*, 84:4749, 2000.

[85] R. Folman, P. Krüger, J. Schmiedmayer, J. Denschlag, and C. Henkel. Microscopic atom optics: from wires to an atom chip. *Adv. At. Mol. Opt. Phys.*, 48:263–356, 2002.

[86] J. Fortagh, A. Grossmann, C. Zimmermann, and T. W. Hänsch. Miniaturized wire trap for neutral atoms. *Phys. Rev. Lett*, 81:5310, 1998.

[87] J. Fortágh, H. Ott, S. Kraft, A. Günther, and C. Zimmermann. Surface effects in magnetic microtraps. *Phys. Rev. A*, 66:041604(R), 2002.

[88] J. Fortagh and C. Zimmermann. Magnetic microtraps for ultracold atoms. *Rev. Mod. Phys.*, 79:235, 2007.

[89] D. Gallego Garcia. Dipolfallen in atomchip-experimenten. *diploma thesis, University of Heidelberg*, 2005.

[90] R. Gati, M. Albiez, J. Fölling, B. Hemmerling, and M.K. Oberthaler. Realization of a single josephson junction for bose-einstein condensates. *Appl. Phys. B*, 82:207, 2006.

[91] R. Gati, J. Esteve, B. Hemmerling, T.B. Ottenstein, J. Appmeier, A. Weller, and M. K. Oberthaler. A primary noise thermometer for ultracold bose gases. *N. J. Phys.*, 8:189, 2006.

[92] R. Gati, B. Hemmerling, J. Fölling, M. Albiez, and M. K. Oberthaler. Noise thermometry with two weakly coupled bose-einstein condensates. *Phys. Rev. Lett.*, 96:130404, 2006.

[93] M. E. Gehm, K. M. O'Hara, T. A. Savard, and J. E. Thomas. Dynamics of noise-induced heating in atom traps. *Phys. Rev. A*, 58:3914, 1998.

[94] F. Gerbier. Quasi-1d bose-einstein condensates in the dimensional crossover regime. *Europhys. Lett.*, 66:771, 2004.

[95] F. Gerbier, J. H. Thywissen, S. Richard, M. Hubgart, P. Bouyer, and A. Aspect. Momentum distribution and correlation function of quasicondensates in elongated traps. *Phys. Rev. A*, 67:051602, 2003.

[96] H. Gimpel. *Magnetische Oberflächenfallen für Atom-Interferometer*. Diploma thesis, University of Heidelberg, 2002.

[97] S. Giorgini, L. P. Pitaevskii, and S. Stringari. Condensate fraction and critical temperature of a trapped interacting bose gas. *Phys. Rev. A*, 54:R4633–R4636, 1996.

[98] M. Girardeau. Relationship between systems of impenetrable bosons and fermions in one dimension. *J. Math. Ph.*, 1:516, 1960.

[99] Martin Goebel. *to be published 2008*. PhD thesis, University of Vienna, 2008.

[100] A. Görlitz, J. M. Vogels, A. E. Leanhardt, C. Raman, T. L. Gustavson, J. R. Abo-Shaeer, A. P. Chikkatur, S. Gupta, S. Inouye, T. P. Rosenband, and W. Ketterle. Realization of bose-einstein condensates in lower dimensions. *Phys. Rev. Lett.*, 87:130402, 2001.

[101] Y. V. Gott, M. S. Ioffe, and V. G. Tel'kovskii. *Nucl. Fusion Supplement*, 3:1045, 1962.

[102] S. Gov, S. Shtrikman, and H. Thomas. Magnetic trapping of neutral particles: Classical and quantum-mechanical study of a ioffe-pritchard type trap. *J. Appl. Phys.*, 87:3989–3998, 2000.

[103] M. Greiner, I. Bloch, O. Mandel, T. W. Hänsch, and T. Esslinger. Exploring phase coherence in a 2d lattice of bose-einstein condensates. *Phys. Rev. Lett.*, 87:160405, 2001.

[104] M. Greiner, O. Mandel, T. Esslinger, T. W. Hänsch, and I. Bloch. Quantum phase transition from a superfluid to a mott insulator in a gas of ultracold atoms. *Nature*, 415:39–44, 2002.

[105] A. Griffin, D. W. Snoke, and S. Stringari. *Bose-Einstein Condensation of Excitons and Biexcitons*. Cambridge University Press, Cambridge, 1995. (editors).

[106] R. Grimm, M. Weidemüller, and Y. B. Ovchinnikov. Optical dipole traps for neutral atoms. *Adv. At. Mol. Opt. Phys.*, 42:95–170, 2000.

[107] V. Gritsev, E. Altman, E. Demler, and A. Polkovnikov. Full quantum distribution of contrast in interference experiments between interacting one dimensional bose liquids. *Nature Phys.*, 2:705 – 709, 2006.

[108] V. Gritsev, E. Demler, M. Lukin, and A.i Polkovnikov. Analysis of quench dynamics of coupled one dimensional condensates using quantum sine gordon model. arXiv:cond-mat/0702343, 2007.

[109] V. Gritsev, A. Polkovnikov, and E. Demler. Linear response theory for a pair of coupled one-dimensional condensates of interacting atoms. arXiv:cond-mat/0701421, 2007.

[110] E. P. Gross. Structure of a quantized vortex in boson systems. *Nuovo Cimento*, 20:454, 1961.

[111] S. Groth. *Development, fabrication, and characterisation of atom chips*. PhD thesis, University of Heidelberg, 2006.

[112] S. Groth, P. Krüger, S. Wildermuth, R. Folman, T. Fernholz, D. Mahalu, I. Bar-Joseph, and J. Schmiedmayer. Atom chips: Fabrication and thermal properties. *Appl. Phys. Lett.*, 85:2980 – 2982, 2004.

[113] A. Günther, M. Kemmler, S. Kraft, C. J. Vale, C. Zimmermann, and J. Fortagh. Combined chips for atom-optics. *Phys. Rev. A*, 71:063619, 2005.

[114] A. Günther, S. Kraft, M. Kemmler, D. Koelle, R. Kleiner, C. Zimmermann, and J. Fortagh. Diffraction of a bose-einstein condensate from a magnetic lattice on a micro chip. *Phys. Rev. Lett.*, 95:170405, 2005.

[115] A. Günther, S. Kraft, C. Zimmermann, and J. Forágh. Atom interferometer based on phase coherent splitting of bose-einstein condensates with an integrated magnetic grating. *Phys. Rev. Lett.*, 98:140403, 2007.

[116] A. Haase. *Trapping Atoms with a Paper Clip*. Diploma thesis, Universität Innsbruck, Freie Universität Berlin, 2000.

[117] A. Haase, D. Cassettari, A. Chenet, B. Hessmo, and J. Schmiedmayer. Trapping neutral atoms with a wire. *Phys. Rev. A*, 64:043405, 2001.

[118] A. Haase, B. Hessmo, and J. Schmiedmayer. Detecting magnetically guided atoms with an optical cavity. *Opt. Lett.*, 31:268 – 270, 2006.

[119] Z. Hadzibabic, P. Krüger, M. Cheneau, B. Battelier, and J. Dalibard. Berezinskii-kosterlitz-thouless crossover in a trapped atomic gas. *Nature*, 441:1118, 2006.

[120] Z. Hadzibabic, S. Stock, B. Battelier, V. Bretin, and J. Dalibard. Interference of an array of independent bose-einstein condensates. *Phys. Rev. Lett.*, 93:180403, 2004.

[121] F.D.M. Haldane. Effective harmonic-fluid approach to low-energy properties of one-dimensional quantum fluids. *Phys. Rev. Lett.*, 47:1840 – 1843, 1981.

[122] John L. Hall. Nobel lecture: Defining and measuring optical frequencies. *Rev. Mod. Phys.*, 78:1279, 2006.

[123] E. Haller. *Microtraps close to atom chip surfaces*. Diplomarbeit, Universität Heidelberg, 2004.

[124] W. Hänsel, P. Hommelhoff, T. W. Hänsch, and J. Reichel. Bose-Einstein condensation on a microelectronic chip. *Nature*, 413:498, 2001.

[125] W. Hänsel, J. Reichel, P. Hommelhoff, and T. W. Hänsch. Magnetic conveyor belt for transporting and merging trapped atom clouds. *Phys. Rev. Lett.*, 86:608, 2001.

[126] W. Hänsel, J. Reichel, P. Hommelhoff, and T. W. Hänsch. Trapped-atom interferometer in a magnetic microtrap. *Phys. Rev. A*, 64:063607, 2001.

[127] W. Happer. Observations of transitions between stationary states in a rotating magnetic field. *Phys. Rev.*, 136:A35, 1964.

[128] S. Haroche, C. Cohen-Tannoudji, C. Audoin, and J. P. Schermann. Modified zeeman hyperfine spectra observed in h^1 and rb^{87} ground states interacting with a nonresonant rf field. *Phys. Rev. Lett.*, 24:861 – 864, 1970.

[129] S. Haupt. *Setup of a New Experiment with Ultracold ^{87}Rb Atoms: Towards Quantum Information Processing on an Atom Chip.* Diploma thesis, Universität Heidelberg, 2003.

[130] D. J. Heinzen. Ultracold atomic interactions. In M. Inguscio, S. Stringari, and C.E. Wieman, editors, *Proceedings of the International School of Physics - Enrico Fermi*, page 351. IOS Press, 1999.

[131] D. Hellweg, L. Cacciapuoti, M. Kottke, T. Schulte, K. Sengstock, W. Ertmer, and J. J. Arlt. Measurement of the spatial correlation function of phase fluctuating bose-einstein condensates. *Phys. Rev. Lett.*, 91:010406, 2003.

[132] D. Hellweg, S. Dettmer, P. Ryyty, J. J. Arlt, W. Ertmer, K. Sengstock, D. S. Petrov, G. V. Shlyapnikov, H. Kreutzmann, L. Santos, and M. Lewenstein. Phase-fluctuations in bose-einstein condensates. *Appl. Phys. B*, 73:781, 2001.

[133] C. Henkel and S. A. Gardiner. Decoherence of Bose-Einstein condensates in microtraps. *Phys. Rev. A*, 69:043602, 2004.

[134] C. Henkel, P. Krüger, R. Folman, and J. Schmiedmayer. Fundamental limits for coherent manipulation on atom chips. *Appl. Phys. B*, 76:173, 2003.

[135] H. F. Hess. Evaporative cooling of magnetically trapped and compressed spin-polarized hydrogen. *Phys. Rev. B*, 34:3476, 1986.

[136] E. A. Hinds, M. G. Boshier, and I. G. Hughes. Magnetic waveguide for trapping cold atom gases in two dimensions. *Phys. Rev. Lett.*, 80:645 – 649, 1998.

[137] E. A. Hinds and I. G. Hughes. Magnetic atom optics: Mirrors, guides, traps, and chips for atoms. *J. Phys. D*, 32:R119, 1999.

[138] E. A. Hinds, C. J. Vale, and M. G. Boshier. Two-wire waveguide and interferometer for cold atoms. *Phys. Rev. Lett.*, 86:1462, 2001.

[139] T.-L. Ho and V. B. Shenoy. Local spin-gauge symmetry of the bose-einstein condensates in atomic gases. *Phys. Rev. Lett.*, 77:2595–2599, 1996.

[140] S. Hofferberth. Experiments with ultracold atoms and bose-einstein condensated in microtraps near surfaces. Master's thesis, University of Heidelberg, 2004.

[141] S. Hofferberth, B. Fischer, T. Schumm, J. Schmiedmayer, and I. Lesanovsky. Radio-frequency-dressed atoms beyond the rotating wave approximation. arXiv:quant-ph/0611240, 2006.

[142] S. Hofferberth, I. Lesanovsky, B. Fischer, J. Verdu, and J. Schmiedmayer. Radio-frequency dressed state potentials for neutral atoms. *Nature Phys.*, 2(10):710–716, 2006.

[143] P. C. Hohenberg. Existence of long-range order in one and two dimensions. *Phys. Rev.*, 158:383, 1967.

[144] P. Hommelhoff, W. Hänsel, T. Steinmetz, T. W. Hänsch, and J Reichel. Transporting, splitting and merging of atomic ensembles in a chip trap. *New J. Phys.*, 7:3, 2005.

[145] C. J. Hood, T. W. Lynn, A. C. Doherty, A. S. Parkins, and H. J. Kimble. The atom-cavity microscope: Single atoms bound in orbit by single photons. *Science*, 287:1457, 2000.

[146] M. Hugbart, J. Retter, F. Gerbier, A. Varon, S. Richard, J. Thywissen, D. Clement, P. Bouyer, and A. Aspect. Coherence length of an elongated condensate: A study by matter-wave interferometry. *Eur. Phys. J. D*, 2005.

[147] A. Imambekov, V. Gritsev, and E. Demler. Distribution functions of interference contrast in low-dimensional bose gases. cond-mat/0612011, 2006.

[148] A. Imambekov, V. Gritsev, and E. Demler. Fundamental noise in matter interferometers. In W. Ketterle M. Inguscio and C.Salomon, editors, *Proceedings of the 2006 Enrico Fermi Summer School on Ultracold Fermi gases*, 2007.

[149] S. Inouye, M. R. Andrews, J. Stenger, H.-J. Miesner, D. M. Stamper-Kurn, and W. Ketterle. Observation of feshbach resonances in a bose-einstein condensate. *Nature*, 392:151–154, 1998.

[150] D. Jaksch, C. Bruder, J. I. Cirac, C. W. Gardiner, and P. Zoller. Cold bosonic atoms in optical lattices. *Phys. Rev. Lett.*, 81:3108, 1998.

[151] J. Javanainen. Oscillatory exchange of atoms between traps containing bose condensates. *Phys. Rev. Lett.*, 57:3164–3166, 1986.

[152] J. Javanainen and M. Wilkens. Phase and phase diffusion of a split bose-einstein condensate. *Phys. Rev. Lett.*, 78:4675–4678, 1997.

[153] J. Javanainen and S. M. Yoo. Quantum phase of a bose-einstein condensate with an arbitrary number of atoms. *Phys. Rev. Lett.*, 76:161–164, 1996.

[154] J. Javaneinen and M. Y. Ivanoc. Splitting a trap containing a bose-einstein condensate: Atom number fluctuations. *Phys. Rev. A*, 60:2351, 1999.

[155] G.-B. Jo, J-H. Choi, C.A. Christensen, T.A. Pasquini, Y.-R. Lee, W. Ketterle, and D.E. Pritchard. Phase sensitive recombination of two bose-einstein condensates on an atom chip. *Phys. Rev. Lett.*, 98:180401, 2007.

[156] G.-B. Jo, Y. Shin, S. Will, T. A. Pasquini, M. Saba, W. Ketterle, D. E. Pritchard, M. Vengalattore, and M. Prentiss. Long phase coherence time and number squeezing of two bose-einstein condensates on an atom chip. *Phys. Rev. Lett.*, 98, 2007.

[157] M. P. A. Jones, C. J. Vale, D. Sahagun, B. V. Hall, C. C. Eberlein, B. E. Sauer, K. Furusawa, D. Richardson, and E. A. Hinds. Cold atoms probe the magnetic field near a wire. *J. Phys. B: At. Mol. Opt. Phys.*, 37:L15, 2004.

[158] B. D. Josephson. Possible new effects in superconductive tunneling. *Phys. Lett.*, 1:251 – 253, 1962.

[159] P. S. Julienne, F. H. Mies, E. Tiesinga, and C. J. Williams. Collisional stability of double bose condensates. *Phys. Rev. Lett.*, 78:1880–1883, 1997.

[160] Y. Kagan, G. V. Shlyapnikov, and J. T. M. Walraven. Bose-einstein condensation in trapped atomic gases. *Phys. Rev. Lett.*, 76:2670–2673, 1996.

[161] J.W. Kane and L. P. Kadanoff. Long-range order in superfluid helium. *Phys. Rev.*, 155:80 – 83, 1967.

[162] M. A. Kasevich. Coherence with atoms. *Science*, 298:1363 – 1368, 2002.

[163] M. A. Kasevich, E. Riis, S. Chu, and R. G. DeVoe. rf spectroscopy in an atomic fountain. *Phys. Rev. Lett.*, 63:612, 1989.

[164] A. Kasper. *Bose-Einstein condensation in a robust microtrap – the combination of wire traps and atom chips*. PhD thesis, Universität Heidelberg, 2003.

[165] A. Kasper, S. Schneider, Ch. vom Hagen, M. Bartenstein, B. Engeser, T. Schumm, I. Bar-Joseph, R. Folman, L. Feenstra, and J. Schmiedmayer. A Bose-Einstein condensate in a microtrap. *J. Opt. B*, 5:S143, 2003.

[166] W. Ketterle, D. S. Durfree, and D. M. Stamper-Kurn. Making, probing and understanding bose-einstein condensates. In *Proceedings of the 1998 Enrico Fermi school on Bose-Einstein condensation in Varenna, Italy*. Academic Press, 1998.

[167] W. Ketterle and D. Pritchard. Trapping and focusing ground-state atoms with static fields. *Appl. Phys. B*, 54:403, 1992.

[168] T. Kinoshita, T. Wenger, and D. S. Weiss. Observation of a one-dimensional tonks-girardeau gas. *Science*, 305:1125–1128, 2004.

[169] M. Köhl, M.J. Davis, C. W. Gardiner, T.W. Hänsch, and T. Esslinger. Growth of bose-einstein condensates from thermal vapor. *Phys. Rev. Lett.*, 88:080402, 2002.

[170] M. Köhl, H. Moritz, T. Stöferle, C. Schori, and T. Esslinger. Superfluid to mott insulator transition in one, two, and three dimensions. *J. Low. Temp. Phys.*, 138:635, 2005.

[171] Christian Koller. Design of an atomchip for the manipulation of internal degrees of freedom in ultra cold rb^{87} atoms. Master's thesis, University of Vienna, 2007.

[172] S. Kraft, A. Günther, H. Ott, D. Wharam, C. Zimmermann, and J. Fortàgh. Anomalous longitudinal magnetic field near the surface of copper conductors. *J. Phys. B*, 35:L469, 2002.

[173] W. Krauth. Quantum monte carlo calculatons for a large number of bosons in a harmonic trap. *Phys. Rev. Lett.*, 77:3695–3699, 1996.

[174] P. Krüger. *Von der Laserdiode Zum Atom Chip: Aufbau Einer Magneto-Optischen Falle und Experimente mit Ultrakalten Atomen in Mikroskopischen Magnetfallen*. Diploma thesis, Universität Innsbruck, Freie Universität Berlin, 2000.

[175] P. Krüger. *Coherent matter waves near surfaces*. PhD thesis, University of Heidelberg, 2004.

[176] P. Krüger, L. M. Andersson, S. Wildermuth, S. Hofferberth, E. Haller, S. Aigner, S. Groth, I. Bar-Joseph, and J. Schmiedmayer. Disorder potentials near lithographically fabricated atom chips. *eprint arXiv:cond-mat/0504686*, 2004.

[177] P. Krüger, X. Luo, M. W. Klein, K. Brugger, A. Haase, S. Wildermuth, S. Groth, I. Bar-Joseph, R. Folman, and J. Schmiedmayer. Trapping and manipulating neutral atoms with electrostatic fields. *Phys. Rev. Lett.*, 91:233201, 2003.

[178] L. D. Landau. Zur theory der energieübertragung - ii. *Phys. Z. Sowjetunion*, 2:46–51, 1932.

[179] A. E. Leanhardt, A. P. Chikkatur, D. Kielpinski, Y. Shin, T. L. Gustavson, W Ketterle, and D. E. Pritchard. Propagation of Bose-Einstein condensates in a magnetic waveguide. *Phys. Rev. Lett.*, 89:040401, 2002.

[180] A. E. Leanhardt, Y. Shin, A. P. Chikkatur, D. Kielpinski, W. Ketterle, and D. E. Pritchard. Bose-Einstein condensates near a microfabricated surface. *Phys. Rev. Lett.*, 90:100404, 2003.

[181] A. J. Leggett. Bose-einstein condensation in the alkali gases. *Rev. Mod. Phys.*, 73:307, 2001.

[182] A. J. Leggett and F. Sols. On the concept of spontaneously broken gauge symmetry in condensed matter physics. *Foundations of Physics*, 21:353–364, 1991.

[183] A. J. Leggett and F. Sols. Comment on *Phase and Phase Diffusion of a Split Bose-Einstein Condensate*. *Phys. Rev. Lett.*, 81:1344–45, 1998.

[184] V. E. Lembessis and D. Ellinas. Optical dipole trapping beyond the rotating wave approximation: the case of large detuning. *J. Opt. B: Quantum Semiclass. Opt.*, 7:319 – 322, 2005.

[185] I. Lesanovsky. Rydberg-Atome in magnetischen Quadrupol-Fallen. Master's thesis, Universität Heidelberg, 2003.

[186] I. Lesanovsky, S. Hofferberth, J. Schmiedmayer, and P. Schmelcher. Manipulation of ultracold atoms in dressed adiabatic rf-potentials. *Phys. Rev. A.*, 74:033619, 2006.

[187] I. Lesanovsky and P. Schmelcher. Magnetic trapping of ultracold rydberg atoms. *Phys. Rev. Lett.*, 95:053001, 2005.

[188] I. Lesanovsky and P. Schmelcher. Quantum states of ultracold electronically excited atoms in a magnetic quadrupole trap. *Phys. Rev. A*, 72:053410, 2005.

[189] I. Lesanovsky, P. Schmelcher, and H. Sadeghpour. Ultra long-range rydberg molecules exposed to a magnetic field. *Journal of Physics B*, 39:L69, 2006.

[190] I. Lesanovsky, J. Schmiedmayer, and P. Schmelcher. Rydberg atoms in magnetic quadrupole traps. *Euro. Phys. Lett.*, 65, 4:478, 2003.

[191] I. Lesanovsky, J. Schmiedmayer, and P. Schmelcher. Electronic structure of atoms in magnetic quadrupole traps. *Phys. Rev. A*, 69:053405, 2004.

[192] I. Lesanovsky, J. Schmiedmayer, and P. Schmelcher. Rydberg atoms in a magnetic quadrupole field. *Journal of Physics B*, 38:S151 – S170, 2005.

[193] I. Lesanovsky, T. Schumm, S. Hofferberth, L. M. Andersson, P. Krüger, and J. Schmiedmayer. Adiabatic radio frequency potentials for the coherent manipulation of matter waves. *Phys. Rev. A*, 73:033619, 2006.

[194] I. Lesanovsky, J. Shmiedmayer, and P. Schmelcher. Rydberg atoms in a magnetic guide. *Phys. Rev. A*, 70:043409, 2004.

[195] I. Lesanovsky and W. von Klitzing. Spontaneous emergence of angular momentum josephson oscillations in coupled annular bose-einstein condensates. *Phys. Rev. Lett.*, 98:050401, 2007.

[196] I. Lesanovsky and W. von Klitzing. Time-averaged adiabatic potentials: Versatile traps and waveguides for ultracold quantum gases. arXiv:cond-mat/0612213, 2007.

[197] M. Lewenstein and L. You. Quantum phase diffusion of a bose-einstein condensate. *Phys. Rev. Lett.*, 77:3489–3493, 1996.

[198] X. Li, H. Zhang, M. Ke, B. Yan, and Y. Wang. A radio-frequency atom chip for trapping atoms in strong-field seeking state. arXiv:physics/0607034 v2, 2006.

[199] E.H. Lieb. Exact analysis of an interacting bose gas. ii. the excitation spectrum. *Phys. Rev.*, 130:1616, 1963.

[200] E.H. Lieb and W. Liniger. Exact analysis of an interacting bose gas. i. the general solution and the ground state. *Phys. Rev.*, 130:1605 – 1616, 1963.

[201] K.K. Likharev. *Dynamics of Josephson junctions and circuits.* Gordon and Breach science publishers, 1986.

[202] X. Liu, K.-H. Brenner, M. Wilzbach, M. Schwarz, T. Fernholz, and J. Schmiedmayer. Fabrication of alignment structures for a fiber resonator by use of deep-ultraviolet lithography. *Appl. Optics*, 44:6857 – 6860, 2005.

[203] F. London. The λ -phenomenon of liquid helium and the bose-einstein degeneracy. *Nature*, 141:643, 1938.

[204] F. London. On the bose-einstein condensation. *Phys. Rev.*, 54:947, 1938.

[205] O. J. Luiten, M. W. Reynolds, and J. T. M. Walraven. Kinetic theory of the evaporative cooling of a trapped gas. *Phys. Rev. A*, 53:381, 1996.

[206] X. Luo, P. Krüger K. Brugger, S. Wildermuth, H. Gimpel, M. Klein, S. Groth, R. Folman, I. Bar-Joseph, and J. Schmiedmayer. An atom fiber for guiding cold neutral atoms. *Optics Lett.*, 29:2145 – 2147, 2004.

[207] J. M. Luttinger. An exactly soluble model of a many-fermion system. *J. Math. Phys.*, 4:1154 – 1162, 1963.

[208] K. W. Madison, F. Chevy, W. Wohlleben, and J. Dalibard. Vortex formation in a stirred bose-einstein condensate. *Phys. Rev. Lett.*, 84:806–809, 2000.

[209] E. Majorana. Atomi orientati incampo magnetico variabile. *Nuovo Cimento*, 9:43, 1932.

[210] L. Mandel and E. Wolf. *Optical Coherence and Quantum Optics.* Cambridge University Press, 1995.

[211] O. Mandel, M. Greiner, A. Widera, T. Rom, T. W. Hänsch, and I. Bloch. Controlled collisions for multiparticle entanglement of optically trapped atoms. *Nature*, 425:937 – 940, 2003.

[212] I. Marino, S. Raghavan, S. Fantoni, S. R. Shenoy, and A. Smerzi. Bose-condensate tunneling dynamics: Momentum-shortened pendulum with damping. *Phys. Rev. A*, 60:487, 1999.

[213] A. G. Martin, K. Helmerson, V. S. Bagnato, G. P. Lafyatis, and D. E. Pritchard. rf spectroscopy of trapped neutral atoms. *Phys. Rev. Lett.*, 61:2431, 1988.

[214] D. C. Mattis and E. H. Lieb. Exact solution of a many-fermion system and its associated boson field. *J. Math. Phys.*, 6:304, 1965.

[215] J. McKeever, A. Boca, A. D. Boozer, J. R. Buck, and H. J. Kimble. Experimental realization of a one-atom laser in the regime of strong coupling. *Nature*, 425:268, 2003.

[216] K. Burnett M.D. Lee, S.A. Morgan. The gross-pitaevskii equation and higher order theories in one-dimensional bose gases. arXiv:cond-mat/0305416, 2003.

[217] C. Menotti, J. R. Anglin, J. I. Cirac, and P. Zoller. Dynamic splitting of a Bose-Einstein condensate. *Phys. Rev. A*, 63:023601, 2001.

[218] C. Menotti and S. Stringari. Collective oscillations of a one-dimensional trapped bose-einstein gas. *Phys. Rev. A*, 66:043610, 2002.

[219] N. D. Mermin and H. Wagner. Absence of ferromagnetism or antiferromagnetism in one- or two-dimensional isotropic heisenberg models. *Phys. Rev. Lett.*, 17:1133, 1966.

[220] H. J. Metcalf. *Laser Cooling and Trapping.* Springer Verlag, Heidelberg Berlin New York, 1999.

[221] M.-O. Mewes, M. R. Andrews, D. M. Kurn, D. S. Durfee, C. G. Townsend, and W. Ketterle. Output coupler for bose-einstein condensed atoms. *Phys. Rev. Lett.*, 78:582–585, 1997.

[222] A. L. Migdall, J. V. Prodan, W. D. Phillips, T. H. Bergeman, and H. J. Metcalf. First observation of magnetically trapped neutral atoms. *Phys. Rev. Lett.*, 54:2596, 1985.

[223] G. J. Milburn, J. Corney, E. M. Wright, and D. F. Walls. Quantum dynamics of an atomic bose-einstein condensate in a double-well potential. *Phys. Rev. A*, 55:4318, 1997.

[224] A. J. Moerdijk, B. J. Verhaar, and T. M. Nagtegaal. Collisions of dressed ground-state atoms. *Phys. Rev. A*, 53:4343–4351, 1996.

[225] B. R. Mollow. Power spectrum of light scattered by two-level systems. *Phys. Rev.*, 188:1969–1975, 1969.

[226] H. Monien, M. Linn, and N. Elstner. Trapped one-dimensional bose gas as a luttinger liquid. *Phys. Rev. A*, 58:R3395, 1998.

[227] C. Mora and Y. Castin. Extension of bogoliubov theory to quasicondensates. *Phys. Rev. A*, 67:053615, 2003.

[228] H. Moritz, T. Stöferle, M. Köhl, and T. Esslinger. Exciting collective oscillations in a trapped 1D gas. *Phys. Rev. Lett.*, 91:250402, 2003.

[229] O. Morizot, Y. Colombe, V. Lorent, H. Perrin, and B. M. Garraway. A ring trap for ultracold atoms. *Phys. Rev. A*, 74:023617, 2006.

[230] T. Mukai, C. Hufnagel, A. Kasper, T. Meno, A. Tsukada, K. Semba, and F. Shimizu. Persistent supercurrent atom chip. arXiv:cond-mat/0702142, 2007.

[231] D. Müller, D. Z. Anderson, R. J. Grow, P. D. D. Schwindt, and E. A. Cornell. Guiding neutral atoms around curves with lithographically patterned current-carrying wires. *Phys. Rev. Lett.*, 83:5194, 1999.

[232] D. Müller, E. A. Cornell, M. Prevedelli, P. D. D. Schwindt, A. Zozulya, and D. Z. Anderson. A waveguide atom beam splitter for laser-cooled neutral atoms. *Opt. Lett.*, 25:1382, 2000.

[233] J. Müller and J. L. Olsen, editors. *Proceedings of the International Conference on High-Tc Superconductors and Materials and Mechanisms of Superconductivity, Interlaken, Switzerland*, volume 153-155C, Pts. I and II. Physica (Amsterdam), 1988.

[234] Frau Muss and Dr. Kröger. Lab rule 3: 10^5 and it will work.

[235] M. Naraschewski, H. Wallis, A. Schenzle, J. I. Cirac, and P. Zoller. Interference of bose condensates. *Phys. Rev. A*, 54:2185–2196, 1996.

[236] M. A. Nielsen and I. L. Chuang. *Quantum Computation and Quantum Information*. Cambridge University Press, Cambridge, 2000.

[237] T. Nirrengarten, A. Qarry, C. Roux, A. Emmert, G. Nogues, M. Brune, J.-M. Raimond, and S. Haroche. Realization of a superconducting atom chip. *Phys. Rev. Lett.*, 97:200405, 2006.

[238] P. Nozières and D. Pines. *The Theory of Quantum Liquids*. Addison-Wesley, Redwood City, CA, 1990.

[239] M. Olshanii. Atomic scattering in presence of an external confinement and a gas of impenetrable bosons. *Phys. Rev. Lett.*, 81:938–941, 1998.

[240] H. Ott, J. Fortagh, G. Schlotterbeck, A. Grossmann, and C. Zimmermann. Bose-Einstein condensation in a surface microtrap. *Phys. Rev. Lett.*, 87:230401, 2001.

[241] B. Paredes, A. Widera, V. Murg, O. Mandel, S. Fölling, J. I Cirac, G. V. Shlyapnikov, T. W. Hänsch, and I. Bloch. Tonks-girardeau gas of ultracold atoms in an optical lattice. *Nature*, 429:277 – 281, 2004.

[242] A. S. Parkins and D. F. Walls. The physics of trapped dilute-gas bose-einstein condensates. *Phys. Rep.*, 303:1–80, 1998.

[243] D. T. Pegg. Misalignment effects in magnetic resonance. *J. Phys. B: At. Mol. Opt. Phys.*, 6(2):241 – 245, 1974.

[244] O. Penrose and L. Onsager. Bose-einstein condensation and liquid helium. *Phys. Rev.*, 104:576, 1956.

[245] S. V. Pereversev, A. Loshak, S. Backhaus, J. C. Davis, and R. E. Packard. Quantum oscillations between two weakly coupled reservoirs of superfluid ^{3}he. *Nature*, 388:449, 1997.

[246] C. J. Pethink and H. Smith. *Bose-Einstein Condensation in Dilute Gases*. Cambridge University Press, 2002.

[247] W. Petrich, M. H. Anderson, J. R. Ensher, and E. A. Cornell. A stable, tightly confining magnetic trap for evaporative cooling of neutral atoms. *Phys. Rev. Lett.*, 74:3352, 1995.

[248] D. S. Petrov. *Bose-Einstein Condensation in Low-Dimensional Trapped Gases*. PhD thesis, University of Amsterdam, 2003.

[249] D. S. Petrov, D. M. Gangardt, and G. V. Shlyapnikov. Low-dimensional trapped gases. *J. Phys. IV*, 116:5–44, 2004.

[250] D. S. Petrov, M. Holzmann, and G. V. Shlyapnikov. Bose-einstein condensation in quasi-2d trapped gases. *Phys. Rev. Lett.*, 84:2551, 2000.

[251] D. S. Petrov, G. V. Shlyapnikov, and J. T. M. Walraven. Regimes of quantum degeneracy in trapped 1D gases. *Phys. Rev. Lett.*, 85:3745, 2000.

[252] D. S. Petrov, G. V. Shlyapnikov, and J. T. M. Walraven. Phase-fluctuating 3D Bose-Einstein condensates in elongated traps. *Phys. Rev. Lett.*, 87:050404, 2001.

[253] L. Pezzé, A. Smerzi, G. P. Berman, A. R. Bishop, and L. A. Collins. Dephasing and breakdown of adiabaticity in the splitting of bose-einstein condensates. *New Journal of Physics*, 7:85, 2005.

[254] W. D. Phillips. Laser cooling and trapping of neutral atoms. *Rev. Mod. Phys.*, 70:721, 1998.

[255] P. W. H. Pinkse, T. Fischer, P. Maunz, and G. Rempe. Trapping an atom with single photons. *Nature*, 404:365, 2000.

[256] L. P. Pitaevskii. Vortex lines in an imperfect bose gas. *Sov. Phys. JETP*, 13:451, 1961.

[257] L. P. Pitaevskii and S.Stringari. Thermal vs. quantum decoherence in double-well trapped bose-einstein condensates. *Phys. Rev. Lett.*, 87:180402, 2001.

[258] A. Polkovnikov. Shot noise of interference between independent atomic systems. *Euro. Phys. Lett.*, 78:10006, 2007.

[259] A. Polkovnikov, E. Altman, and E. Demler. Interference between independent fluctuating condensates. *Proc. Natl. Acad. Sci. USA*, 103:6125 – 6129, 2006.

[260] V. N. Popov. *Functional Integrals in Quantum Field Theory and Statistical Physics*. Reidel, Dordrecht, 1983.

[261] D. Pritchard. Cooling neutral atoms in a magnetic trap for precision spectroscopy. *Phys. Rev. Lett.*, 51:1336, 1983.

[262] I. I. Rabi, N. F. Ramsey, and J. Schwinger. Use of rotating coordinates in magnetic resonance problems. *Rev. Mod. Phys.*, 26:167, 1954.

[263] S. Raghavan, A. Smerzi, and V. M. Kenkre. Coherent oscillations between two weakly coupled bose-einstein condensates: Josephson effects, pi oscillations, and macroscopic quantum self trapping. *Phys. Rev. A*, 59:620, 1999.

[264] A. Rauschenbeutel, G. Nogues, S. Osnaghi, P. Bertet, M. Brune, J. M. Raimond, and S. Haroche. Coherent operation of a tunable quantum phase gate in cavity qed. *Phys. Rev. Lett.*, 83:5166, 1999.

[265] J. Reichel. Microchip traps and Bose-Einstein condensation. *Appl. Phys. B*, 74:469, 2002.

[266] J. Reichel, W. Hänsel, and T. W. Hänsch. Atomic micromanipulation with magnetic surface traps. *Phys. Rev. Lett.*, 83:3398, 1999.

[267] J. Reichel, W. Hänsel, P. Hommelhoff, and T. W. Hänsch. Applications of integrated magnetic microtraps. *Appl. Phys. B*, 72:81, 2001.

[268] S. Richard, F. Gerbier, J. H. Thywissen, M. Hugbart, P. Bouyer, and A. Aspect. Momentum spectroscopy of 1d phase fluctuations in bose-einstein condensates. *Phys. Rev. Lett.*, 91:010405, 2003.

[269] S. Ritter, A. Öttl, T. Donner, T. Bourdel, M. Köhl, and T. Esslinger. Observing the formation of long-range order during bose-einstein condensation. *Phys. Rev. Lett.*, 98:090402, 2007.

[270] A. Röhrl, M. Naraschewski, A. Schenzle, and H. Wallis. Transition from phase locking to the interference of independent bose condensates: Theory versus experiment. *Phys. Rev. Lett.*, 78:4143, 1997.

[271] J. Rottmann. Towards a single atom camera. Master's thesis, University of Heidelberg, 2006.

[272] M. Saba, T. A. Pasquini, C. Sanner ans Y. Shin, W. Ketterle, and D. E. Pritchard. Light scattering to determine the relative phase of two bose-einstein condensates. *Science*, 307:1945, 2005.

[273] M. Schellekens, R. Hoppeler, A. Perrin, J. Viana Gomes, D. Boiron, A. Aspec, and C. I. Westbrook. Hanbury brown twiss effect for ultracold quantum gases. *Science*, 310:638–651, 2005.

[274] David R. Scherer, Chad N. Weiler, Tyler W. Neely, and Brian P. Anderson. Vortex formation by interference of multiple trapped bose-einstein condensates. arXiv:cond-mat/0610187, 2006.

[275] J. Schmiedmayer. Guiding and trapping a neutral atom on a wire. *Phys. Rev. A*, 52:R13, 1995.

[276] J. Schmiedmayer. A wire trap for neutral atoms. *Appl. Phys. B*, 60:169, 1995.

[277] S. Schneider. *Bose-Einstein Kondensation in einer magnetischen Z-Falle*. PhD thesis, Universität Heidelberg, 2003.

[278] S. Schneider, A. Kasper, Ch. Vom Hagen, M. Bartenstein, B. Engeser, T. Schumm, I. Bar-Joseph, R. Folman, L. Feenstra, and J. Schmiedmayer. Bose-Einstein condensation in a simple microtrap. *Phys. Rev. A*, 67:023612, 2003.

[279] D. Schrader, I. Dotsenko, M. Khudaverdyan, Y. Miroshnychenko, A. Rauschenbeutel, and D. Meschede. A neutral atom quantum register. *Phys. Rev. Lett.*, 93:150501, 2004.

[280] F. Schreck, L. Khaykovich, K. L. Corwin, G. Ferrari, T. Bourdel, J. Cubizolles, and C. Salomon. Quasipure bose-einstein condensate immersed in a fermi sea. *Phys. Rev. Lett.*, 87:080403, 2001.

[281] C. Schroll, W. Belzig, and C. Bruder. Decoherence of cold atomic gases in magnetic microtraps. *Phys. Rev. A*, 68:043618, 2003.

[282] T. Schumm. *Bose-Einstein condensates in magnetic double well potentials*. PhD thesis, Université Paris 11, 2006.

[283] T. Schumm, J. Estève, C. Figl, J.-B. Trebbia, C. Aussibal, H. Nguyen, D. Mailly, I. Bouchoule, C. I. Westbrook, and A. Aspect. Atom chips in the real world: the effects of wire corrugation. *Eur. Phys. J. D*, 32:171, 2005.

[284] T. Schumm, S. Hofferberth, L. M. Andersson, S. Wildermuth, S. Groth, I. Bar-Joseph, J. Schmiedmayer, and P. Krüger. Matter wave interferometry in a double well on an atom chip. *Nature Phys.*, 1:57–62, 2005.

[285] M. O. Scully and M. S. Zubairy. *Quantum Optics*. Cambridge University Press, 1997.

[286] S. I. Shevchenko. First and second sound modes of a bose-einstein condensate in a harmonic trap. *Phys. Rev. Lett.*, 80:3985, 1992.

[287] Y. Shin, M. Saba, T. A. Pasquini, W. Ketterle, D. E. Pritchard, and A. E. Leanhardt. Atom interferometry with bose-einstin condensates in a double-well potential. *Phys. Rev. Lett.*, 92:050405, 2004.

[288] Y. Shin, C. Sanner, G.-B. Jo, T. A. Pasquini, M. Saba, W. Ketterle, D. E. Pritchard, M. Vengalattore, and M. Prentiss. Interference of bose-einstein condensates split with an atom chip. *Phys. Rev. A*, 72:021604, 2005.

[289] J. H. Shirley. Solution of the schrödinger equation with a hamiltonian periodic in time. *Phys. Rev.*, 138:B979, 1965.

[290] I. Shvarchuck, Ch. Buggle, D. S. Petrov, K. Dieckmann, M. Zielonkowski, M. Kemmann, T. G. Tiecke, W. von Klitzing, G. V. Shlyapnikov, and J. T. M. Walraven. Bose-einstein condensation into nonequilibrium states studied by condensate focusing. *Phys. Rev. Lett.*, 89:270404, 2002.

[291] A. Smerzi, S. Fantoni, S. Giovanazzi, and S. R. Shenoy. Quantum coherent atomic tunneling between two trapped bose-einstein condensates. *Phys. Rev. Lett.*, 79:4950, 1997.

[292] T. Steinmetz, A. Balocchi, Y. Colombe, D. Hunger, T. W. Hänsch, R. J. Warburton, and J. Reichel. Stable fiber-based fabry-pérot cavity. *Appl. Phys. Lett.*, 89:111110, 2006.

[293] J.A. Stickney and A.A. Zozulya. Influence of nonadiabaticity and nonlinearity on the operation of cold-atom beam splitters. *Phys. Rev. A*, 68:013611, 2003.

[294] T. Stöferle, H. Moritz, C. Schori, M. Köhl, and T. Esslinger. Transition from a strongly interacting 1d superfluid to a mott insulator. *Phys. Rev. Lett.*, 92:130403, 2004.

[295] S. Stringari. Collective excitations of a trapped bose-condensed gas. *Phys. Rev. Lett.*, 77:2360–2363, 1996.

[296] C. V. Sukumar and D. M. Brink. Spin-flip transitions in a magnetic trap. *Phys. Rev. A*, 56:2451, 1997.

[297] I. Teper, Y.-J. Lin, and V. Vuletić. Resonator-aided single-atom detection on a microfabricated chip. *Phys. Rev. Lett.*, 97:023002, 2006.

[298] B. Laburthe Tolra, K. M. O'Hara, J. H. Huckans, W. D. Phillips, S. L. Rolston, and J. V. Porto. Observation of reduced three-body recombination in a correlated 1d degenerate bose gas. *Phys. Rev. Lett.*, 92:190401, 2004.

[299] S. Tomonaga. Remarks on bloch's method of sound waves applied to many-fermion problems. *Prog. Theor. Phys.*, 5:544, 1950.

[300] L. Tonks. The complete equation of state of one, two and three-dimensional gases of hard elastic spheres. *Phys. Rev.*, 50:955, 1936.

[301] J.B. Trebbia, J. Esteve, C. I. Westbrook, and I. Bouchoule. Experimental evidence for the breakdown of a hartree-fock approach in a weakly interacting bose gas. *Phys. Rev. Lett.*, 97:250403, 2006.

[302] P. Treutlein, P. Hommelhoff, T. Steinmetz, T. W. Hänsch, and J. Reichel. Coherence in Microchip Traps. *Phys. Rev. Lett.*, 92:203005, 2004.

[303] P. Treutlein, D. Hunger, S. Camerer, T. W. Hänsch, and J. Reichel. A bose-einstein condensate coupled to a nanomechanical resonator on an atom chip. arXiv:quant-ph/0703199, 2007.

[304] M. Trupke, E. A. Hinds, S. Eriksson, E. A. Curtis, Z. Moktadir, E. Kukharenka, and M. Kraft. Microfabricated high-finesse optical cavity with open access and small volume. *Appl. Phys. Lett.*, 87:211106, 2005.

[305] N. J. van Druten and W. Ketterle. Two-step condensation of the ideal bose gas in highly anisotropic traps. *Phys. Rev. Lett.*, 79:549–552, 1997.

[306] J. Vanier and C. Audoin. *The Quantum Physics of Atomic Frequency Standards.* Adam-Hilger, 1989.

[307] P. Villain, M. Lewenstein, R. Dum, Y. Castin, L. You, A. Imamoglu A., and T. A. B. Kennedy. Quantum dynamics of the phase of a bose-einstein condensate. *Journal of Modern Optics*, 44:1775–1800, 1997.

[308] Christoph vom Hagen. *to be published 2008.* PhD thesis, University of Vienna, 2008.

[309] Y.-J. Wang, D. Z. Anderson, V. M. Bright, E. A. Cornell, Q. D., T. Kishimoto, M. Prentiss, R. A. Saravanan, S. R. Segal, and S. Wu. Atom michelson interferometer on a chip using a bose-einstein condensate. *Phys. Rev. Lett.*, 94(7):090405, 2005.

[310] C. Wei, A. S. M. Windsor, and N. B. Manson. A strongly driven two-level atom revisited: Bloch siegert shift versus dynamic stark splitting. *J. Phys. B: At. Mol. Opt. Phys.*, 30:4877, 1997.

[311] J. Weiner, V. S. Bagnato, S. Zilio, and P. S. Julienne. Experiments and theory in cold and ultracold collisions. *Rev. Mod. Phys.*, 71:1, 1999.

[312] J. D. Weinstein and K. G. Libbrecht. Microscopic magnetic traps for neutral atoms. *Phys. Rev. A*, 52:4004, 1995.

[313] M. White, H. Gao, M. Pasienski, and B. DeMarco. Bose-einstein condensates in rf-dressed adiabatic potentials. *Phys. Rev. A*, 74, 2006. 023616.

[314] N. K. Whitlock and I. Bouchoule. Relative phase fluctuations of two coupled one-dimensional condensates. *Phys. Rev. A*, 68:053609, 2003.

[315] C.E. Wieman, D.E. Pritchard, and D.J. Wineland. Atom cooling, trapping, and quantum manipulation. *Rev. Mod. Phys.*, 71:S253, 1999.

[316] S. Wildermuth. *One-dimensional Bose-Einstein condensates in micro-traps.* PhD thesis, Univserity of Heidelberg, 2005.

[317] S. Wildermuth, S. Hofferberth, I. Lesanovsky, S. Groth, I. Bar-Joseph, P. Krüger, and J. Schmiedmayer. Sensing electric and magnetic fields with bose-einstein condensates. *Appl. Phys. Lett.*, 88:264103, 2006.

[318] S. Wildermuth, S. Hofferberth, I. Lesanovsky, E. Haller, L.M. Andersson, S. Groth, I. Bar-Joseph, P. Krüger, and J. Schmiedmayer. Microscopic magnetic-field imaging. *Nature*, 435:440, 2005.

[319] S. Wildermuth, P. Krüger, C. Becker, M. Brajdic, S. Haupt, A. Kasper, R. Folman, and J. Schmiedmayer. Optimized magneto-optical trap for experiments with ultracold atoms near surfaces. *Phys. Rev. A*, 69:030901, 2004.

[320] M. Wilzbach, A. Haase, M. Schwarz, D. Heine, K. Wicker, X. Liu, K.-H. Brenner, S. Groth, Th. Fernholz, B. Hessmo, and J. Schmiedmayer. Detecting neutral atoms on an atom chip. *Fortschr. Phys.*, 54:746 – 764, 2006.

[321] W. H. Wing. On neutral particle trapping in quasistatic electromagnetic fields. *Prog. Quant. Electr.*, 8:181, 1984.

[322] E. M. Wright, D. F. Walls, and J. C. Garrison. Collapses and revivals of bose-einstein condensates formed in small atomic samples. *Phys. Rev. Lett.*, 77:2158–2161, 1996.

[323] R. Wynands and S. Weyers. Atomic fountain clocks. *Metrologia*, 42:S64 – S79, 2005.

[324] H. Xiong, S. Liu, and M. Zhan. Interaction-induced interference for two independent bose-einstein condensates. *N. J. Phys.*, 8:245, 2006.

[325] C. N. Yang and C. P. Yang. Thermodynamics of a one-dimensional system of bosons with repulsive delta-function interaction. *J. Math. Phys.*, 10:1115, 1969.

[326] I. Zapata, F. Sols, and A. J. Leggett. Josephson effect between trapped bose-einstein condensates. *Phys. Rev. A*, 57:R28, 1998.

[327] C. Zener. Non-adiabatic crossing of energy levels. *Proc. R. Soc. London Ser. A*, 137:696, 1932.

[328] P. Zhang, H. H. Jen, C. P. Sun, and L. You. Angular momentum of a magnetically trapped atomic condensate. *Phys. Rev. Lett.*, 98:030403, 2007.

[329] P. Zhang and L. You. Geometric phase of an atom inside an adiabatic radio frequency potential. arXiv:0704.0476, 2007.

[330] O. Zobay and B. M. Garraway. Two-dimensional atom trapping in field-induced adiabatic potentials. *Phys. Rev. Lett.*, 86:1195–1198, 2001.

[331] O. Zobay and B. M. Garraway. Atom trapping and two-dimensional bose-einstein condensates in field-induced adiabatic potentials. *Phys. Rev. A.*, 69:023605, 2004.

[332] W. H. Zurek. Decoherence, einselection, and the quantum origins of the classical. *Rev. Mod. Phys.*, 75:715 – 776, 2003.

[333] M.W. Zwierlein, J.R. Abo-Shaeer, A. Schirotzek, C.H. Schunck, and W. Ketterle. Vortices and superfluidity in a strongly interacting fermi gas. *Nature*, 435:1047–1051, 2005.